High Efficiency Thin Film Silicon Solar Cells with Novel Light Trapping: Principle, Design and Processing

By

Lirong Zeng

B. S. Materials Physics
University of Science and Technology, Beijing, 1998

M. S. Materials Physics and Chemistry
University of Science and Technology, Beijing, 2001

Submitted to the Department of Materials Science and Engineering in Partial Fulfillment of the Requirements for the Degree of

Doctor of Philosophy in Electronic, Photonic and Magnetic Materials
at the
Massachusetts Institute of Technology

February 2008

Signature of Author: _____
Department of Materials Science and Engineering
December 20, 2007

Certified by: _____
Lionel C. Kimerling
Thomas Lord Professor of Materials Science and Engineering
Thesis Supervisor

Accepted by: _____
Samuel M. Allen
POSCO Professor of Physical Metallurgy
Chair, Departmental Committee on Graduate Students

High Efficiency Thin Film Silicon Solar Cells with Novel Light Trapping: Principle, Design and Processing

By

Lirong Zeng

Submitted to the Department of Materials Science and Engineering
on December 20th, 2007 in Partial Fulfillment of the Requirements for the
Degree of Doctor of Philosophy in Electronic, Photonic and Magnetic Materials

ABSTRACT

One major efficiency limiting factor in thin film solar cells is weak absorption of long wavelength photons due to the limited optical path length imposed by the thin film thickness. This is especially severe in Si because of its indirect bandgap. This thesis invents a novel light trapping scheme, the textured photonic crystal (TPC) backside reflector, which can enhance path length by at least several hundred times the film thickness for sufficient absorption. Physical principles and design optimization of TPC are discussed in detail. Thin film Si solar cells integrated with the new back reflector are successfully fabricated and significant efficiency enhancement is demonstrated.

The new back reflector combines a one-dimensional photonic crystal as a distributed Bragg reflector (DBR) and reflection grating. The DBR achieves near unity reflectivity in a wide omnidirectional bandgap completely covering the wavelengths needing light trapping, and the grating can diffract light into large oblique angles and form total internal reflection against the front surface of the cell. The unique combination of DBR and grating tightly confines light inside the cell, effectively changing the path length from the thickness of the cell to its width.

The back reflector parameters and the antireflection coating are systematically optimized for thin film Si solar cells through simulation and experiments. A 2 μm thick cell can achieve 54% efficiency enhancement using the optimized design.

For proof of concept, the TPC back reflector is integrated with thick crystalline Si solar cells (675 μm thick), which demonstrate external quantum efficiency enhancement up to 135 times in the wavelength range of 1000-1200 nm.

To prove the theory on the intended application, top-contacted thin film Si solar cells integrated with the TPC back reflector are successfully fabricated using Si-on-insulator material through an active layer transfer technique. All cells exhibit strong absorption enhancement, similar to that predicted by simulation. The 5 μm thick cells gained 19% short circuit current density improvement, despite machine problems during fabrication.

The textured photonic crystal back reflector design can be applied directly to single and poly-crystalline Si solar cells, and its principle is broadly applicable to other materials systems.

Thesis supervisor: Lionel C. Kimerling
Title: Thomas Lord Professor of Materials Science and Engineering

Acknowledgement

I would like to take this opportunity to thank many people for their kind help and support during my Ph.D. study at MIT. First, I want to thank my advisor Prof. Kimerling. Kim gave me the opportunity to enter the field of optoelectronics and solar cell research. His guidance and support is invaluable to my research, and I am often impressed by his sharp mind and breadth of knowledge. Almost every discussion with him enlightens me. I enjoyed learning 3.46 from him and T/A'ing this course.

I want to express my deepest gratitude to my research supervisor, Dr. Xiaoman Duan for her guidance and motherly love. Xiaoman has been guiding me on research since the first day I joined EMAT. She taught me how to analyze issues, how to give presentations and revise papers. She always has unique perspectives, not only on research, but also on life. She has been taking me as her daughter, caring about me and teaching me things in every aspect of life. She has created some fundamental changes in me, which will influence me and benefit me for my whole life.

I thank Dr. Yasha Yi for his guidance and help on solar cell research. Yasha led me into the research on solar cell light trapping. His original ideas often impressed me. I would like to thank Dr. Jurgen Michel for his help on PCD measurements, data analysis, and many meaningful discussions. I also want to thank Dr. Ching-yin Hong for her help on processing and for managing the PV project. Ching-yin made most of my PECVD recipes, helped me with i-stepper, and checked all my masks.

I sincerely thank my thesis committee members, Prof. Robert O'Handley, Prof. Emanuel Sachs, and Prof. Eugene Fitzgerald. Bob was my former advisor, and has been caring for me and helping me all the time. I often feel he is like my father. Prof. Sachs is an expert on solar cells. Each discussion with him gives me new insights. He also helped broaden my thesis content. Prof. Fitzgerald has very good intuition on materials, and I have benefited from discussions with him.

Cordial thanks go to Dr. Peter Bermel, my research collaborator, who developed the code for scattering matrix simulations. Whenever I have problems in simulation, he always responds quickly, and he always has solutions. His deep interest in research and warm friendship often touch me. He is the best collaborator I have ever had. I appreciate Dr. Ning-ning Feng's help with coupled wave theory simulations, and learned from him some basics on EM theory.

I deeply appreciate the help from Mr. Bernard A. Alamariu in MTL. He has been helping me enormously on solar cell research. He is not only familiar with processing, but also has deep understanding of physics. We have been discussing each fabrication step and process design. Without Bernard's help, I would not dare to imagine that I could succeed both times, with thick solar cell fabrication and SOI solar cell fabrication, since both were new processes to me.

I am very grateful to my old friend Dr. Jifeng Liu. We came to MIT at the same time. I not only learned from him of courses, but of research. He is the best classmate I have ever had. Not only is he outstanding in both subjects and research, but his willingness to help and kindness are not commonly seen. I also want to thank his sweet wife, Dr. Xiaoxin Wang for her help.

I want to express my deep thanks to my groupmate and friend, Mr. Jae Hyung Yi, who gave me good career advice.

I appreciate the help from many staff members in MTL. Dr. Hanqing Li helped me with process optimization and had many important discussions with me. Dr. Vicky Diadiuk gave me good advice and is always encouraging. Dr. Li-wen Wang not only introduced me to microfabrication, but was a good mentored to me in life. Thank Mr. Robert Bicchieri, Mr. Paul Tierney, Mr. Paul McGrath, Mr. Eric Lim, Mr. Kris Payer, and Mr. Daniel Adams for their help when I encountered problems during processing.

I want to thank a lot of former and current staff members and students in EMAT group. Dr. Mark Beals helped with CMP and offered good suggestions to relieve DBR blistering problem. Dr. Anu Agrawal gave good advice on research. Dr. Anat Eshed helped me with the EMAT sputterer. Dr. David T. Danielson had many meaningful discussions with me on PV related topics. I enjoyed being classmates, colleagues, officemates and lab buddies with him. Dr. Wojtek Giziewicz gave me suggestions on process flow. Mr. Juejun Hu helped me with solar cell measurements. Ms. Samerkhae (Nok) Jongthammanurak has been a good friend, classmate and officemate. Mr. Xiaochen Sun provided information on solar cell testing. Ms. Sarah Bernardis is a sweet officemate. I also enjoy being officemates with Ms. Jing Cheng and Mr. Rong Sun, and had many interesting discussions with them. Mr. Jianfei Wang and Mr. Kevin McComber are good friends. I also want to thank our administrative assistants, Ms. Ellen Weene and Ms. Lisa Page for their help.

Ms. Kathleen R. Farrell, the former Academic Administrator in our Department, encouraged me and helped me a lot during hard times. Ms. Maria Brennan, the International Student Advisor, and Ms. Carol L. Frederick in Barker Library also helped me.

Besides, I thank Mr. Brian McMullen and Dr. Adam Lorenz in Evergreen Solar, Inc. for assistance on solar cell measurements. I appreciate the help from Prof. Steven Brueck, Mr. Andrew Fraunglass, Mr. Alex Raub and Mr. Slava Smolev at University of New Mexico for their help with interference lithography.

I want to thank an old friend, Dr. Yaowu Hao for his help. Yaowu is my alum at University of Science and Technology, Beijing. He helped me adjust to the new environment after I first arrived in the U.S. and often gave me shopping rides. I also thank my close friend Ms. Qiong Wu for her care and support.

Lastly, I want to thank my family for their support. My parents have been caring about me and encouraging me all the time. They worked very hard to give all their children the best education. My brother and sisters also gave me a lot of support. I am also very grateful for the deep love and care from my boyfriend, Mr. Kurt Broderick. Kurt has been my teacher and best friend. He cares about my research and wellbeing. During the phone call every night, we discuss my processing plan and research issues. He gave me a lot of good suggestions and assistance on fabrication and experimental design. During my busiest time, Kurt has been taking care of me, cooking me delicious food, taking me shopping, and being the first reader and editor of my thesis. Without him, I would not have survived the most stressful period before graduation. I am so lucky to have you, honey!

Table of Contents

List of Figures and Tables

CHAPTER 1

Introduction

1.1 Historical overview of solar cells

The key to sustainable development is to maintain a benign cycle between Economy, Environment and Energy [1.1], which requires replacing energy from fossil fuels with clean energy. The finite supply of fossil fuels also demands the development of a replacement energy source. Among all renewable energies, photovoltaics (PV), the direct conversion of sunlight to electricity using semiconductor devices, provides one of the most promising prospects for clean energy for the future. It creates no noise or pollution, is inexhaustible, and available anywhere in the world. Every year, the solar power striking the earth is 1.52×10^{21} KWh, 10,000 times the global power consumption.

To date, the development of solar cells can be divided into several important stages. The first solar cell was made in 1954 at the Bell Laboratories in the U.S., which was based on crystalline Si and had an efficiency of 6% [1.2], and within a few years, the efficiency was increased to 10%. The early solar cells were expensive, and were used as

satellite power supplies. Widespread application of solar cells for terrestrial power supplies received a major driving force from the notorious 1973 oil supply crisis [1.3], which saw numerous research and development institutions built all over the world. Every possible means to reduce cost was tried, as it was recognized that the high costs of PV energy generation was the major hindrance to its widespread application. Besides crystalline silicon, which has been dominating the PV market, other materials such as amorphous Si, III-V and II-VI thin film materials, and organic conductors [1.4] were investigated,. Tandem cells and other multiple bandgap designs were explored as strategies for higher efficiency. From the beginning of 1980s onwards, research had been concentrated on achieving high efficiency due to the recognition that high efficiency is of great importance for cost reduction of the complete system [1.3]. During the 1990s, PV underwent expanded interest, with its economics of scale of PV production driving cost reduction, which in turn opens up new markets [1.4].

Now PV is being used in large-scale power generation, the space industry, consumer products, as well as in supplying power in remote locations and developing countries. The global market of PV has steadily grown at about 35% annually in the last five years. However, cumulative solar energy production still only accounts for less than 0.01% of total global primary energy demand. The premier obstacle for large scale installation of PV systems is its high price. In December 2007, the price of 1KWh of solar electricity costs between 21.37 cents for industrial applications and 37.62 cents for residential use, [1.5], compared to the U.S. Electric Utility average of less than 9 cents per KWh. To be competitive to the mainstream energy, solar electricity must achieve huge cost reductions.

Among current PV technologies, Si solar cells have been dominating due to the abundance of the raw material and the mature manufacturing technology. Laboratory crystalline Si solar cells have achieved record efficiencies of 24.7% [1.6], and commercial cells have efficiencies of around 10-16% [1.7]. In 2004, crystalline Si comprised 88% of the PV cell and module shipments, and amorphous thin film Si shared the balance of the market [1.8]. Fig. 1.1 depicts a plot of the average wafer Si solar dollars per watt module price vs. cumulative installed capacity. It clearly shows that as the installation capacity increases, the module price goes down monotonically. In order to compete with mainstream energy, the key price target is $1/W peak. Suppose a 20% learning rate on cost reduction can be maintained, realizing the targeted price would require an installation capacity of 51,000 MW, which might be realized in the year 2020. However, if a 10% learning rate is assumed, realizing the targeted price would require

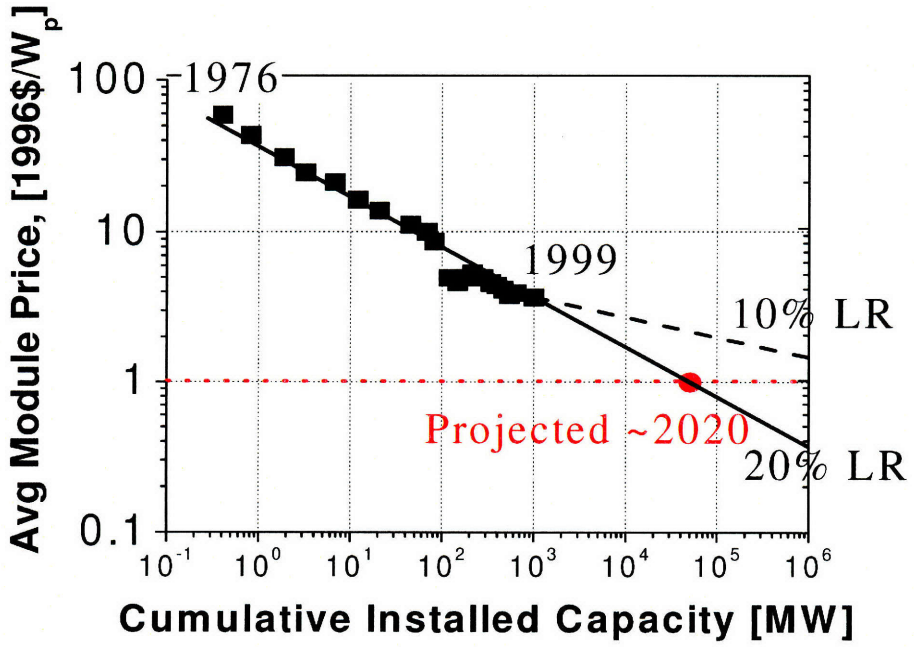

Fig. 1.1 Average crystalline Si solar cell module price vs. cumulative installed capacity [1.9]

more than 1 million MW of cumulative installed capacity. Currently, it seems that our learning rate is saturating. One reason is that approximately 50% of the cost of a crystalline silicon solar cell module is the thick silicon wafers (250-300 μm thick). Worse, because of the fast growth of Si PV industry, there is a worldwide shortage in Si feedstock to meet the planned cell manufacturing capacity expansion. Consequently, the overall PV market growth will be restricted.

1.2 Thin film solar cells

To reduce the cost and facilitate the growth rate of PV market, thin film solar cells (TFSC), where the active layer thickness is on the order of several microns or thinner, are a promising choice. Besides using significantly less material, TFSC allows simpler device processing and manufacturing technology for large-area modules and arrays, enabling a shorter pay-back time [1.1].

Various TFSC materials have been examined [1.10, 1.11]:

(1) Elemental materials: Si, B-doped diamond-like carbon, fullerene films;

(2) Binary alloys/compounds: a-Si:H, GaAs, CdTe, Cu_2S, InP, TiO_2…;

(3) I-III-VI ternaries and related quaternaries: $CuInSe_2$ (CIS), $CuInGaSe_2$(CIGS);

(4) Organic semiconductors: organometallic dyes and polymers.

Among these, major contenders in TFSC market include two materials categories [1.7]: one based on Si, including amorphous Si (a-Si), nanocrystalline and polycrystalline Si (c-Si); the other based on polycrystalline chalcogenide (Group six)

semiconducting compounds. Fig. 1.2 shows the efficiency range of various 2006 thin film modules. The two major contenders will be discussed below.

1.2.1 Si-based technology

a) Single-junction amorphous Si

Amorphous Si solar cells have been available since the early 1980 in consumer products such as calculators and digital watches. The active layer is an a-Si and H alloy, which incorporates 10% atomic H during film deposition to improve the quality of the

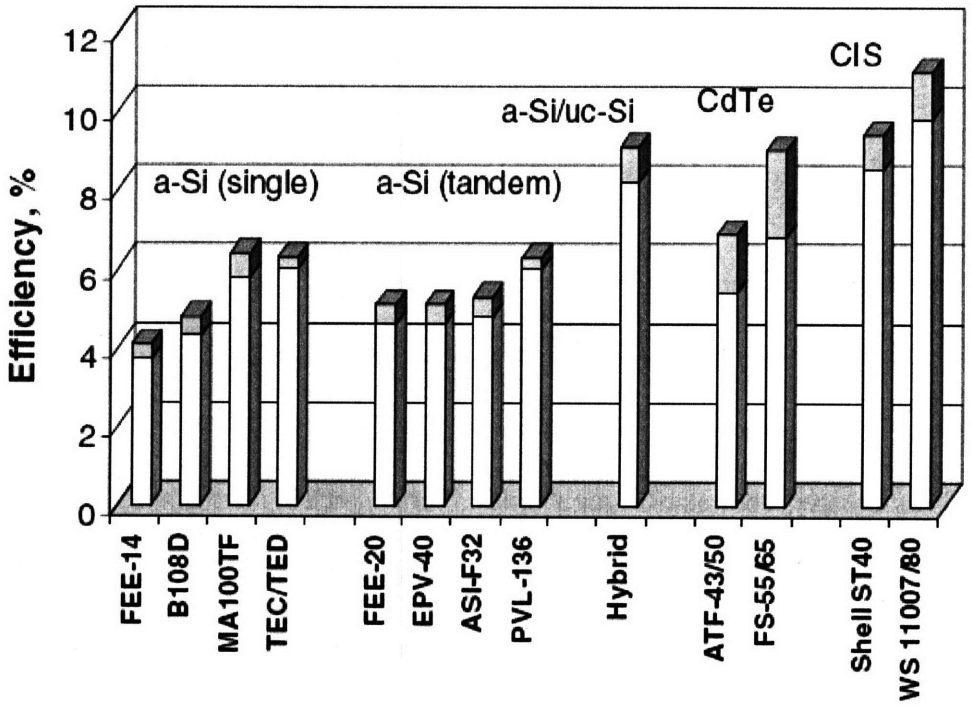

Fig. 1.2 Nominal energy conversion efficiency range of various 2006 thin-film modules (darker top region indicates efficiency range of products meeting specifications) [1.7]

material. Due to the very short diffusion length, p-i-n junction has to be used to extend the absorption layer thicknesses while maintain adequate carrier collection. The configuration of the solar cell can be either superstrate or substrate [1.10]. Fig.1.3. illustrates a cell structure in superstrate configuration. As shown in Fig. 1.2, nominal module efficiency of single-junction a-Si solar cells in 2006 is around 4-6%.

The strength of a-Si technology includes its low processing temperature, enabling module production on flexible and low cost substrates in addition to its reduced materials requirement with an active Si layer of just 1-2 μm due to its inherently high absorption coefficient compared with c-Si; and its use of abundant and environmentally benign Si.

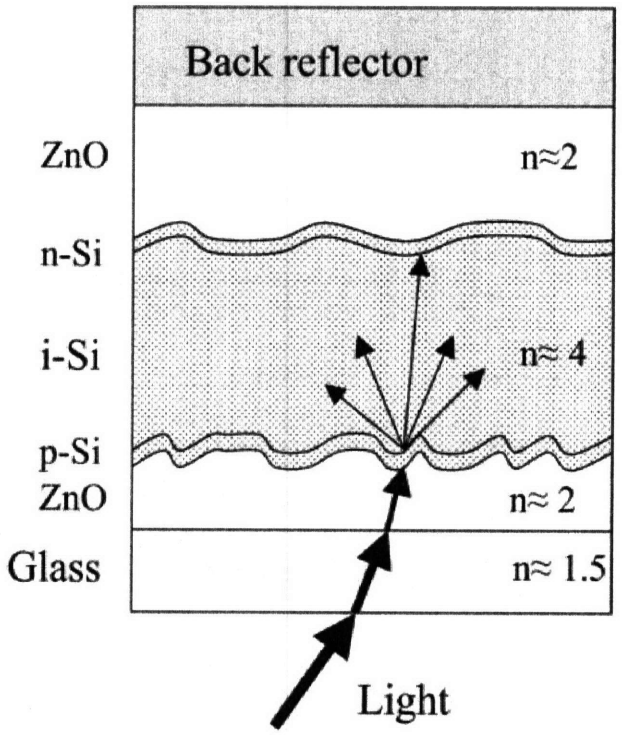

Fig. 1.3 An amorphous Si solar cell with superstrate configuration [1.10]

The drawback is light induced material quality degradation, as the stabilized efficiency after one to two months field exposure is quite low, only 4-6%.

b) Multiple junction amorphous silicon cells

One way to alleviate the decreased efficiency caused by light exposure is to use thinner a-Si and multiple junctions where lower junctions have a smaller bandgap. Fig. 1.4 shows such a structure. Compared to single junction cells, this has increased module efficiency to 8–10%, but the technology otherwise is the same, with its associated advantages and disadvantages.

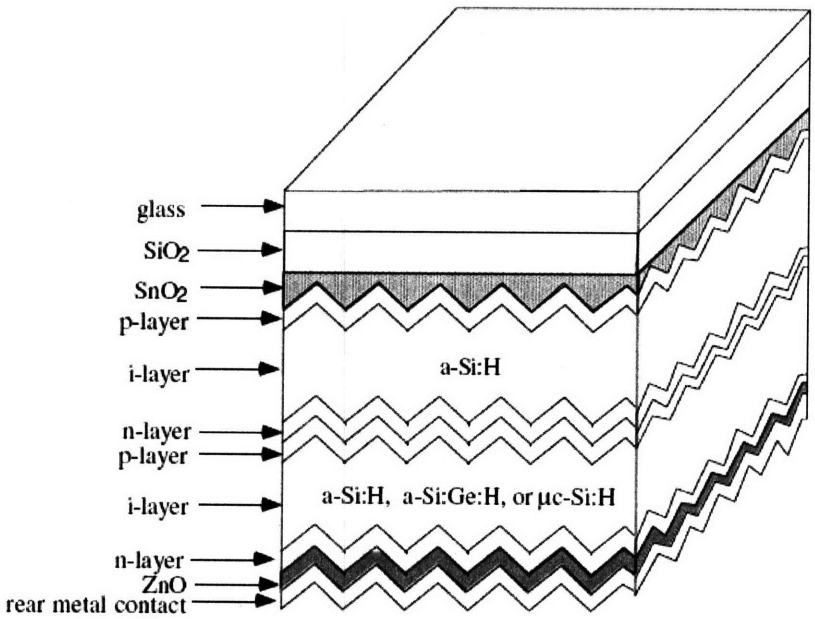

Fig. 1.4 Multiple junction a-Si solar cells

c) Polycrystalline Si solar cells

The polycrystalline Si layer can be made by depositing a-Si followed by high temperature crystallization. The material quality is similar to that of polycrystalline

wafers now dominating the PV market, and it eliminates the stability problem in a-Si. The columnar growth creates grains with height equal film thickness, in contrast to microcrystalline Si films. CSG Solar's crystalline-Si-on-glass technology has reached module efficiency of 9.8% [1.6].

1.2.2 Chalcogenide-based technology

a) Cadmium telluride (CdTe)

Typical device structure consists of a transparent conductive oxide (TCO) layer deposited on glass, a CdS window layer, the CdTe absorber layer, and metal contact, as shown in Fig. 1.5. The major problem with this technology is the toxicity of Cd. Despite of the moderate module efficiency close to 9%, CdTe module is banned in some

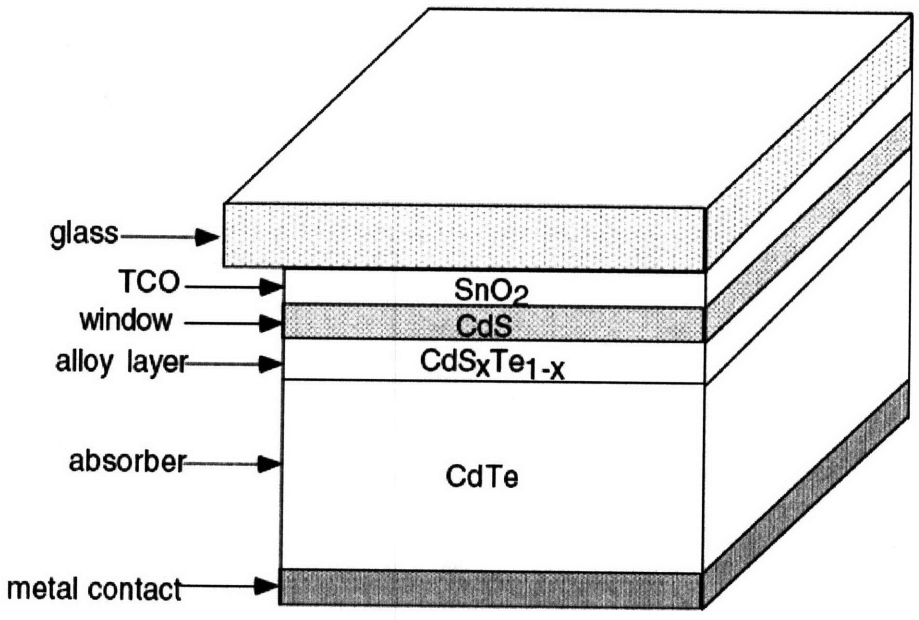

Fig. 1.5 Schematic of a CdTe solar cell [1.7]

countries like Netherlands, and two of the former major manufacturers, BP Solar and Matsushita, have both abandoned the technology due to environmental concerns.

b) Copper-indium diselenide (CIS)

CIS has achieved high laboratory efficiency of 19.5%. Unlike other thin film solar cell technologies which uses glass superstrate, CIS always adopts substrate configuration. As depicted in Fig. 1.6, a Mo layer is deposited on the glass substrate to make an ohmic contact. Besides the CIS absorber layer, there is a CdS window layer and a top layer of TCO. Considerable effort has been undertaken to replace the CdS layer due to the toxicity of Cd, however, the long-term issue is the availability of resources. Both In and Ga reserves on the earth are limited. All known indium reserves can only make enough solar cells with the capacity equal to all present wind generators.

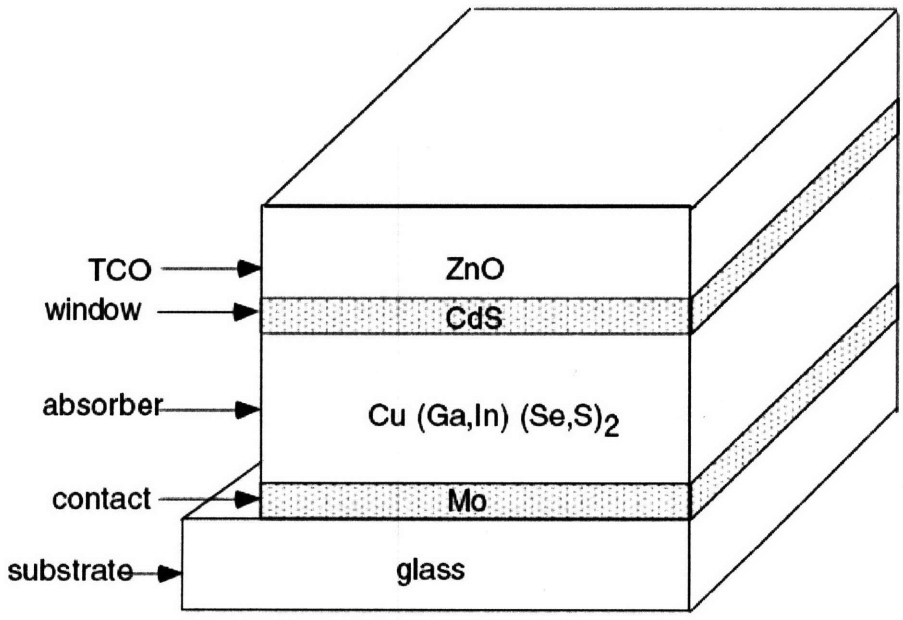

Fig. 1.6 Device structure of a CIS solar cell [1.7]

Based on the above introduction, it is clear that compared to other TFSC technologies, ***thin film Si solar cells are the natural choice*** for future TFSC technology due to their simple manufacturing technology, abundant raw material on the earth, and environmental benignity.

1.2.3 Solar cell efficiency determinants

A solar cell works on the principle of photovoltaics, the conversion of photons to electrons. Its efficiency depends mainly on two aspects: photon absorption, i.e. how many photons are absorbed and converted to free electron-hole pairs, and carrier collection, i.e. how many free carriers successfully reach the electrodes. Fig. 1.7 shows the schematic of a thin film Si solar cell on a ceramic substrate. It has an AR coating, an n^+ Si layer, a

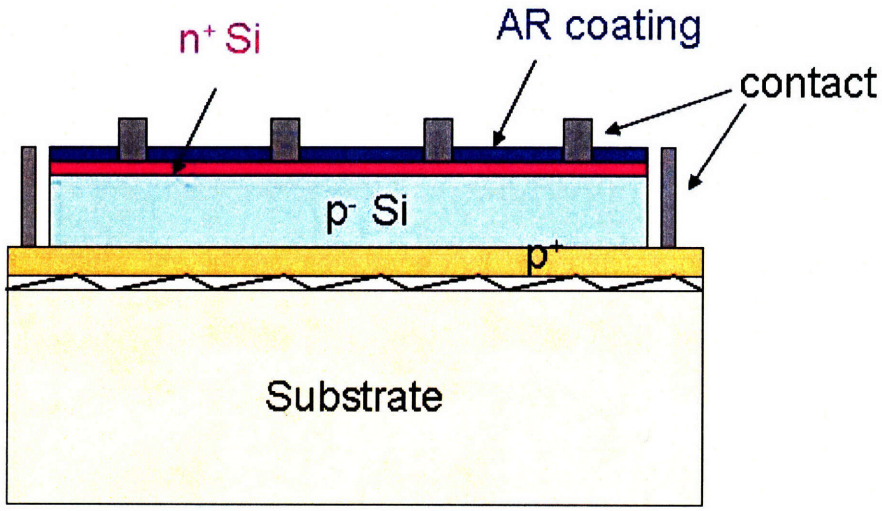

Fig. 1.7 Schematic of a thin film Si solar cell on ceramic substrate with bottom contact in the periphery of the cell

lightly doped p layer as the major layer for photon absorption, and a p^+ bottom layer. There is a textured mirror at the back surface of the cell. Metal fingers are used to contact the n^+ layer, and the bottom p^+ layer is contacted by etching away the periphery of the thin film layers. The factors that determine cell efficiency can be divided into several categories:

a) Materials:

Besides the type of material, there are two factors: device layer thickness, which determines both light absorption and carrier collection, and minority carrier life time τ, which determines carrier collection. τ depends on both bulk lifetime and surface recombination velocity, and determines minority carrier diffusion length.

b) Junction design:

Junction doping can affect free carrier absorption. Doping in the base region also influences minority carrier diffusion length, series resistance, and open circuit voltage. The p-n junction can be vertical as in traditional design, or horizontal. The junction contacting scheme determines both series resistance and shadowing.

c) Light management:

Antireflection coating determines light admission into the cell, while back/front surface texture and backside reflector can influence light absorption by trapping light inside the cell.

These factors are carefully considered in this thesis, with particular attention being paid to light management, through the use of an effective antireflection coating and a new backside reflector, the textured photonic crystal.

1. 3 Light trapping in solar cells

1.3.1 The importance of light trapping in thin film solar cells

Thin film solar cells are attractive because of lower price. However, one common problem for most TFSC is the low power conversion efficiency. For example, Si thin film cells have efficiencies of <10%, far short of the theoretical limit of ~29% for thick Si. Due to the thin film thickness, a large portion of the incident solar photons just penetrate through the solar cell and do not get the chance of being absorbed and converted to electrons. In Si, because of the indirect bandgap, this problem is especially severe.

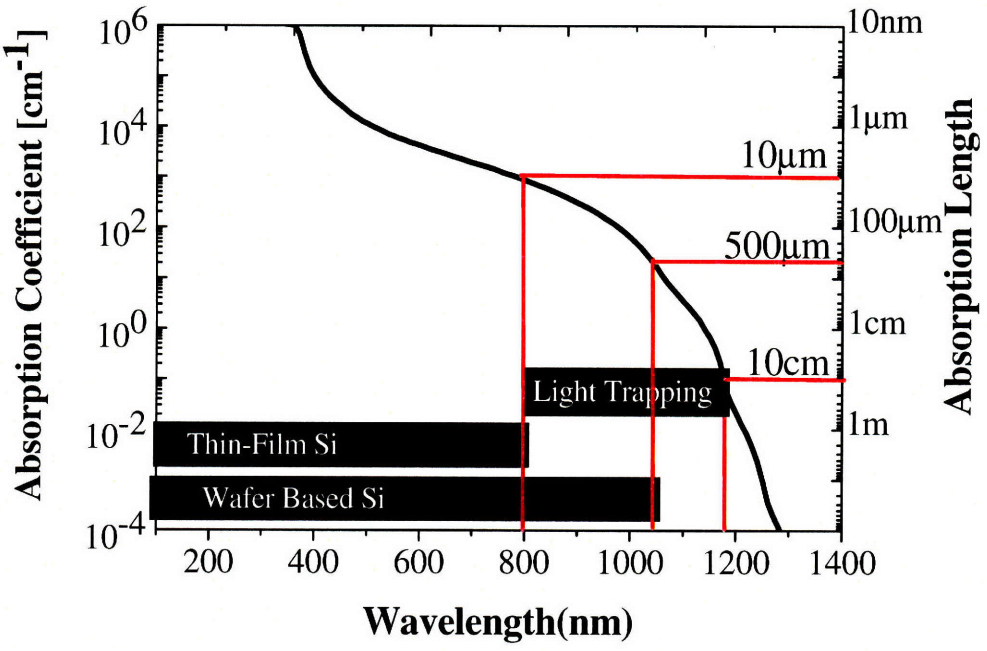

Fig. 1.8 Absorption coefficient and absorption length of Si, showing that thin film Si cells need light trapping in the wavelength range of λ=800-1170 nm

Fig. 1.8 illustrates the absorption coefficient and absorption length vs. wavelength in Si. Due to the indirect bandgap, as the wavelength increases, the absorption coefficient decreases rapidly, leading to very long absorption length L. For example, at λ=800 nm, L≈10 μm. However, when λ approaches the bandgap of Si, L jumps to several mm. Given the thin film thickness on the order of several microns, there is little possibility that these long wavelength photons will be absorbed.

On the other hand, it would be very beneficial to utilize these long wavelength photons that would be otherwise wasted. As indicated in Fig. 1.9, if the absorption cutoff wavelength can be increased from 800 nm to the bandgap wavelength of Si, the short circuit current density can be increased by 65%. The key solution is to enhance the optical path length by trapping light within the solar cell for sufficient absorption.

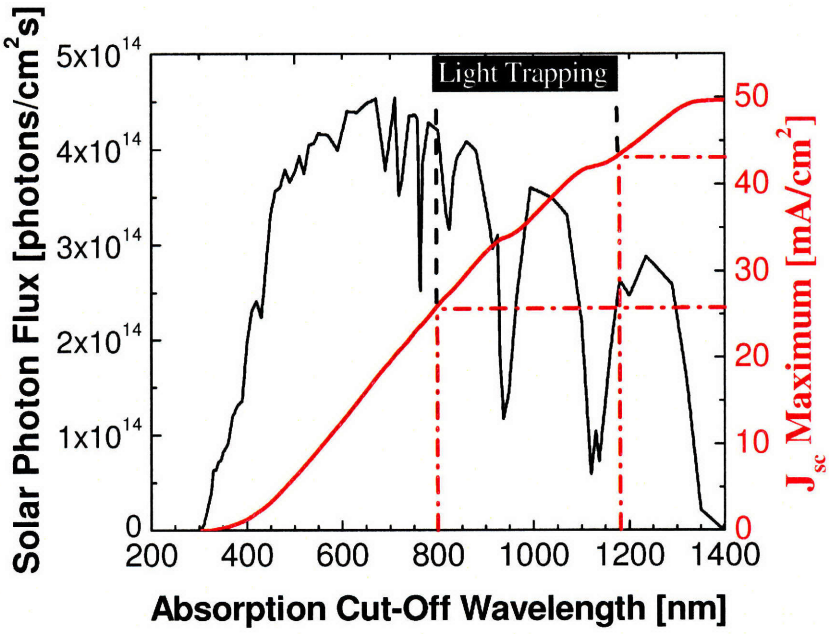

Fig. 1.9 Solar spectrum and absorption cutoff wavelength vs. maximum short circuit current density for Si solar cells

Light trapping is defined as path length enhancement in the bulk regions of the cell. Note that light trapping in a-Si solar cells is also necessary despite stronger absorption than in crystalline Si. The high defect density requires short carrier collection length, therefore a very thin absorber layer, making light absorption insufficient, which in turn makes light trapping important. Light trapping is necessary even in wafer-based Si solar cells. To maximize the open circuit voltage of a solar cell, it is important to minimize free carrier recombination, one effective way of which is to reduce film thickness [1.12]. In order to maintain strong light absorption at the same time, it is necessary to enhance the optical path length by trapping light inside the cell. It is equivalent to increasing the cell thickness, but with the extra advantage of reducing bulk recombination losses, because the minority carriers need to diffuse over a much shorter distance to reach the electrodes.

1.3.2 Light trapping schemes

Light trapping is usually considered in the regime of ray optics where structures are large compared to the wavelength of the light, and light rays with different history do not interfere. In wafer-based Si cells, this is a good approximation as cells are hundreds of microns thick. In structures with micron scale feature sizes, light should be treated as coherent and interference becomes important. In such systems, classical ray tracing methods are no longer valid, and the photogeneration rate can only be deduced from the gradient of the Poynting vector [1.13].

Light trapping is associated with the scattering and reflection of light rays within the cell such that they travel at bigger angles to the surface normal, which can be

considered in terms of the paths taken by light rays inside the cell. One possible figure of merit for light trapping scheme is the path length enhancement factor, which is the ratio of the average path length taken by a beam to the minimum possible path length, the average cell thickness. Typical light trapping schemes include mirrors, randomizing surfaces and textured surfaces.

I. Backside mirrors

A mirror at the back surface of the cell can serve as the simplest light trapping scheme, as shown in Fig. 1.10. The mirror can be implemented by depositing a metal layer at the back surface of the cell, or by growing the active layers on top of a Bragg reflector [1.14, 1.15, 1.16]. The mirror typically reflects more than 95% of the rays impinging on the back surface. The reflected ray is likely to exit the cell at the front surface since the front surface reflectivity is typically low in order to effectively admit

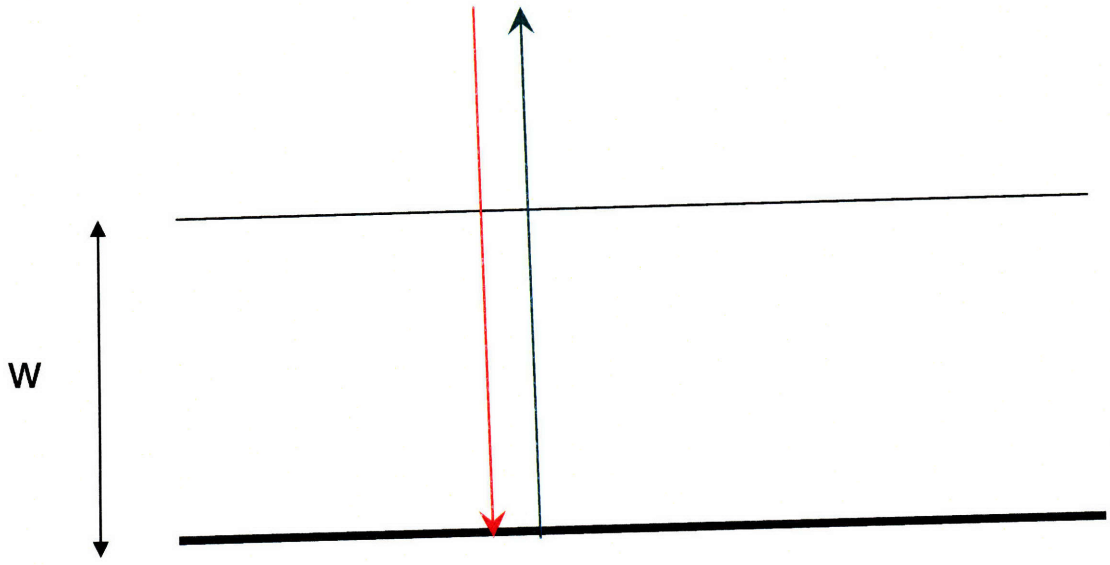

Fig. 1.10 Double optical path length in a cell with a metal back reflector

light into the cell. Therefore, the back side mirror effectively doubles the path length of the light. For an ideal mirror with reflectivity R=1 and ideal front surface with R=0, the path length enhancement factor is 2.

Greater path length enhancement can be achieved by tilting the front or the back surface, or by scattering light within the cell to incur total internal reflection at the front surface.

II. Randomizing surfaces

A roughened surface can scatter or randomize the light upon reflection, changing the angle with which the light strikes the other cell surface. A perfectly randomizing surface, called a Lambertian surface, scatters reflected rays with uniform brightness in all directions in a hemisphere pointing into the cell regardless the original angle of incidence. Fig. 1.11 (a) is a schematic of a light trapping scheme based on internal randomization of light direction. Ray tracing renders a path length enhancement factor of

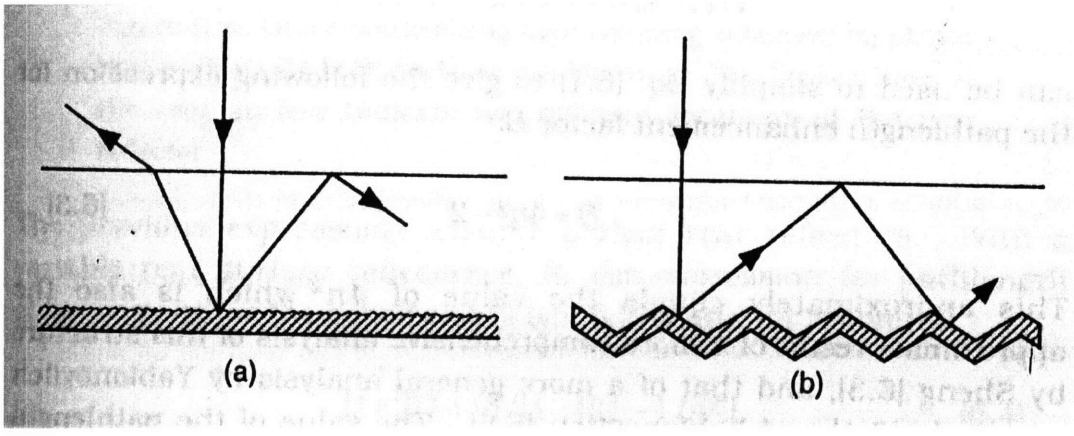

Fig. 1.11 Light trapping schemes based on (a) internal randomization of light direction; (b) regular geometrical structure [1.12]

$$B=4n_s^2-2 \qquad (1.1),$$

where n_s is the refractive index of the semiconductor [1.12]. For Si, this gives $B\approx47$, which demonstrates the potential of light trapping schemes.

If the rear surface is not perfectly reflecting, at each scattering event, a fraction of the light will be lost, reducing the path length enhancement factor to

$$B=2(1+R)/[1-R(1-1/n^2)] \qquad (1.2).$$

This reduction can be considerable due to the big number of reflection events at that surface ($\sim n_s^2$). For Si, R must be >91% to do half as well as the ideal case.

Randomizing surface is useful in indicating the potential of light trapping schemes, but perfectly randomizing surfaces are difficult to realize. Practical schemes usually utilize the geometrical-optical properties of more regular, textured surfaces [1.17].

III. Textured surfaces

The theory of textured surface (geometrical light trapping) is more difficult than randomizing surface. There are both 2D and 3D surface texturing. The former includes creating oblique surface with opposite slopes, forming grooves at the top surface, near-parallel double-sided slat, and holographic gratings [1.18]. The simplest way to realize surface texturing is to tilt one surface relative to the other. Fig. 1.11 (b) is a schematic of a textured surface. If the texturing is symmetrical, at the minimum, only a double pass is achievable. If the texturing is asymmetrical, however, careful choice of the tilt angle can ensure four passes of the light. In general, lower degree of symmetry renders greater degree of light trapping. If surface is textured in two directions, say, by replacing the grooves with pyramids, then the rays are scattered in three dimensions rather than two,

and consequently, light trapping is improved. Among different pyramids, random layout pyramids perform better than regular inverted pyramids, which do better than regular upright pyramids [1.18].

IV. Practical schemes

Typically, reflective back surfaces are prepared by metallizing the back surface of the cell with Al or Au. Reflectivity can further be improved by inserting an oxide layer between semiconductor and metal. However, even with 100% reflective mirrors, this method can at most enhance path length by two times cell thickness.

Front surface texturing in monocrystalline Si can be achieved by wet etching the (100) surface with KOH solution to expose the (111) crystal faces. Actual path length enhancement of over 10, much smaller than the maximum of ~50 has been realized in Si solar cells with roughened surfaces and with pyramidal textures [1.19].

Texturing back surfaces can be realized by growing the active layer on patterned substrates. An alternative is to grow the active layer on gratings [1.20, 1.21, 1.22]. Although gratings can form oblique angles diffractions, they are not effective in preventing huge transmission loss when light is incident on it. Breakthrough in light trapping technique is imperative.

In this thesis, a novel light trapping scheme that utilizes wave optics is developed. It can target the wavelength range that needs light trapping, and enhance the optical path length by several hundred times cell thickness via a textured photonic crystal back reflector, which combines a reflection diffraction grating and a 1D photonic crystal.

1.3.3 Two important light trapping schemes in commercial solar cells

Two light trapping schemes in commercial solar cells are worth special mentioning: laser fired contacts with random pyramids and crystalline Si on glass.

a) Laser fired contact [1.23, 1.24]

This is a back surface contacting scheme developed in Fraunhofer Institute for Solar Energy Systems in Germany. It involves a ~100 nm thick thermal oxide layer inserted between the Si device layer and Al metal layer. By locally firing Al through the oxide into Si, a back surface filed is formed by Al point contacts. The thermal oxide not only passivates the back surface, but also enhances Al reflection. Fig. 1.12 is a schematic of the device structure. This laser fired contact (LFC), together with random pyramids on front surface, entails an efficiency of 17.1% for a cell made of 170 μm thick FZ Si wafer. In Chapter 4, we will compare the light trapping capability of cells with LFC and cells with our invention, textured photonic crystal (TPC) through simulation. As will be shown

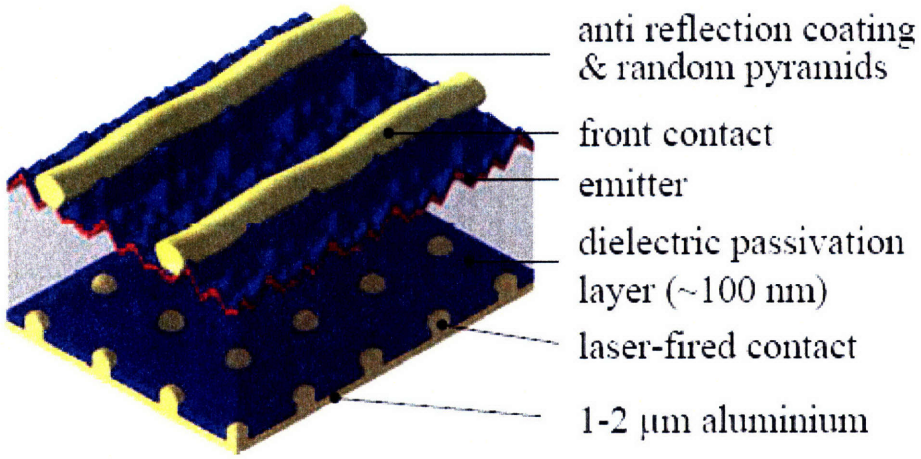

Fig. 1.12 Schematic of a solar cell with laser fired contacts [1.22]

there, for 2 μm thick cells, using TPC can achieve 20% more efficiency enhancement than using LFC.

b) Crystalline Si on glass [1.25, 1.26]

Crystalline Si on glass (CSG) is a thin film PV technology using polycrystalline Si crystallized from amorphous Si as the active layer. It is adopted in a solar cell company, CSG that was founded in 2006 in Germany. By using special light trapping techniques, a 2.2 μm thick cell can reach as high as 9.8% efficiency [1.25]. Fig. 1.13 illustrates the structure of a CSG cell. The light trapping features are textured glass substrate and a rear reflector. The texture is created by dipping glass substrate into a solution with 0.5 μm suspended silica beads, followed by belt dry. Si film is then deposited onto the highly textured substrate, realizing excellent light trapping. A new development is to sand blast glass followed by HF etching [1.25]. Note that another very

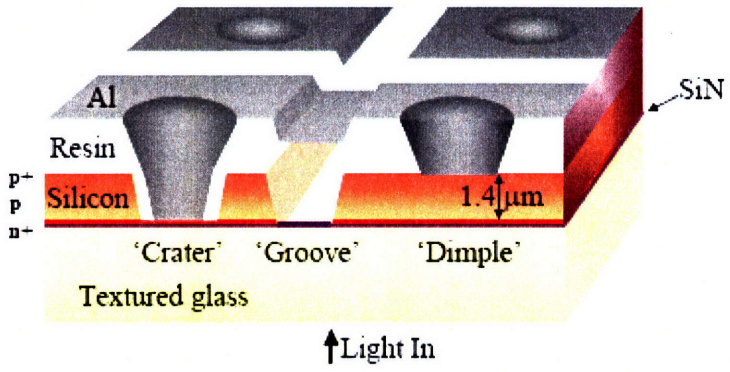

Fig. 1.13 Schematic of a CSG solar cell

important feature to increase optical response, as can be seen from Fig. 1.13, is the shadowless contacting scheme. All the contacts are on the backside of the cell.

Unfortunately, although I have examined all their publications [1.27] carefully, no detailed information on their light trapping scheme was found, making direct quantitative comparison between CSG and our light trapping scheme difficult. We can only compare the efficiency predicted by simulation for our textured photonic crystal (as in chapter 4) and what is experimentally achieved by CSG.

1.4 Outline of this thesis

This thesis focuses on the development and application of a new light trapping scheme, a textured photonic crystal backside reflector.

In chapter 2, the light trapping principle of the textured photonic crystal is discussed, and its two components, DBR and grating, are studied in detail. High index contrast DBR stack material is used to realize wide stopband, omnidirectional reflection. Grating parameters are chosen to cancel 0^{th} order reflection and direct reflected light into first order for large angle diffraction. It is shown, for the first time, that by the unique combination of these two light trapping components, light absorption can be dramatically improved due to the reduced loss from both front and back surface of the solar cell, leading to significant efficiency enhancement.

In Chapter 3, the design, fabrication and characterization of thick crystalline Si solar cells integrated with the textured photonic crystal (TPC) back reflector is presented. Despite of the thick wafers and relatively short minority carrier diffusion length, and non-ideal big grating period, our thick cells exhibited significant absorption enhancement in

the wavelength range between 1000-1200 nm. The maximum external quantum efficiency enhancement factor was as high as 135 times.

In Chapter 4, the design and systematic optimization of the back reflector and antireflection coating parameters by numerical simulation are introduced, using two different methods, coupled wave theory and scattering matrix method. Using the optimized parameters, both methods predict high enhancement of cell efficiency offered by the back reflector, of more than 54% for a 2 μm thick Si solar cell.

Chapter 5 presents the identification of the best antireflection coating for thin film Si solar cells. Optical response, surface passivation capability and dielectric strength are carefully examined for several candidate materials systems through both simulation and experiments. A double-layer AR coating composed of a thin thermal oxide under Si_3N_4 is found to render the highest solar cell efficiency.

Chapter 6 introduces the design, fabrication and characterization of thin film crystalline Si solar cells integrated with TPC back reflectors. An active layer transfer technique is successfully developed to integrate TPC back reflectors with solar cells made of silicon-on-insulator wafers. Solar cells at all device layer thicknesses gained significant efficiency enhancement. The light trapping capability of the TPC back reflector is vividly displayed by the bumps on external quantum efficiency spectra. The short circuit current density gain is close to, or even higher than theoretical predictions.

Chapter 7 summarizes major results and achievements of this thesis, and point out the direction of future work.

References

[1.1] Y. Hamakawa (Ed.), Thin-Film Solar Cells, next generation photovoltaics and its applications, Springer, 2004.
[1.2] D. M. Chapin, C. S. Fuller, and G. L. Pearson, J. Appl. Phys. **25**, 676 (1954).
[1.3] Adolf Goetzberger, Joachim Knobloch and Bernhard Voss, Crystalline Si Solar Cells, John Wiley & Sons, Ltd, Chichester, England, 1998, p2.
[1.4] J. Nelson, The Physics of Solar Cells, Imperial College Press, London, 2003, p4.
[1.5] http://www.solarbuzz.com/SolarPrices.htm.
[1.6] Martin A. Green, Keith Emery, Yoshihiro Hisikawa and Wilhelm Warta, "Solar cell efficiency tables (version 30)", Progress in Photovoltaics, Research and Applications, **15**, 425–430 (2007).
[1.7] Martin A. Green, J Mater Sci: Mater Electron, 18, S15–S19(2007).
[1.8] United States Energy Information Administration website:http://www.eia.doe.gov.
[1.9] Data from: Hugo de Moor, Gerrit Jan Schaeffer, Ad Seebregts, Luuk Beurskens, Michael Durstewitz, Erik Alsema, Wilfried van Sark, Hermann laukamp, Pascal Boulanger and Carlo Zuccaro, 3rd World Conference on Photovoltaic Energy Conversion, May 11-18, 2003, Osaka, Japan, 8P-D5-58, pp. 2624-2627. See also: Gregory Nemet, "Learning Curves for Photovoltaics", on International Energy Agency website: http://www.iea.org/textbase/work/2007/learning/Nemet_PV.pdf, June 2007.
[1.10] K. L. Chopra, P. D. Paulson, and V. Dutta, Prog. Photovolt: Res. Appl. **12**, 69–92 (2004).
[1.11] A. V. Shah, H. Schade ,M. Vanecek, J. Meier, E. Vallat-Sauvain, N.Wyrsch, U. Kroll, C. Droz and J. Bailat, Prog. Photovolt: Res. Appl. **12**,113–142 (2004).
[1.12] Martin A. Green, Silicon Solar Cells, Advanced Principles and Practices, Center for Photovoltaic Devices and Systems, University of New South Wales, Sydney, 1995, p. 92.
[1.13] J. Nelson, The Physics of Solar Cells, Imperial College Press, London, 2003, p273.
[1.14] D.C. Johnson, I. Ballard, K.W.J. Barnham, D.B. Bishnell, J.P. Connolly, M.C. Lynch, T.N.D. Tibbits, N.J. Ekins-Daukes, M. Mazzer, R. Airey, G. Hill and J.S. Roberts, Solar Energy Materials and Solar Cells, **87**, 169 (2005).
[1.15] Y. Shimizu and Y. Okada, Proceedings of the 3rd World Conference on Photovoltaic Energy Conversion, Osaka, Japan, 2003, p781-784.
[1.16] M.Z. Shvarts, O.I. Chosta, I.V. Kochnev, V.M. Lantratov, and V.M. Andreev, Solar Energy Materials and Solar Cells, **68**, 105 (2001).
[1.17] J. Nelson, The Physics of Solar Cells, Imperial College Press, London, 2003, p276.
[1.18]] Martin A. Green, Silicon Solar Cells, Advanced Principles and Practices, Center for Photovoltaic Devices and Systems, University of New South Wales, Sydney, 1995, Chapter 6, Section 6.3.
[1.19] J. Nelson, The Physics of Solar Cells, Imperial College Press, London, 2003, p279 and p282.
[1.20] C. Heine and R. H. Morf, Applied Optics, **34**, 2476 (1995).
[1.21] C. Eisele, C.E. Nebel, and M.Stutzmann, J. Appl. Phys., **89**, 7722 (2001).
[1.22] F. Llopis and I. Tobias, Solar Energy Materials and Solar cells, **87**, 481 (2005).
[1.23] E. Schneiderlöchner, G. Emanuel, G. Grupp, H. Lautenschlager, A. Leimenstoll, S. W. Glunz, R. Preu and G. Willeke, proceedings of the 19th European Photovoltaic Solar Energy Conference, 7-11 June 2004, Paris, France, pp. 447-450.
[1.24] E. Schneiderlöchner, R. Preu, R. Ludemann, and S. W. Glunz, Prog. Photovolt: Res. Appl. , **10**, 29-34 (2002).
[1.25] Mark J Keevers, Trevor L Young, Ute Schubert and Martin A Green, "10% efficient CSG minimodules", from CSG Solar webpage: http://www.csgsolar.com/pages/medias_do.php?lang=en.
[1.26] M.A. Green, P.A. Basore, N. Chang, D. Clugston, R. Egan, R. Evans, D. Hogg, S. Jarnason, M. Keevers, P. Lasswell, J. O_Sullivan, U. Schubert, A. Turner, S.R. Wenham, T. Young, Solar Energy, **77**, 857–863 (2004).
[1.27] http://www.csgsolar.com/pages/medias_do.php?lang=en..

CHAPTER 2

Principle of Light Trapping Using Textured Photonic Crystals

In Chapter 1, the importance of light trapping was addressed. This chapter introduces a breakthrough in light trapping: a textured photonic crystal backside reflector combining reflection grating and distributed Bragg reflector, which can enhance path length by at least several hundred times the cell thickness. First, this novel light trapping scheme is introduced; then its two components, DBR and grating, are studied in detail; and their light trapping capabilities are investigated in terms of light absorption, effective path length enhancement and solar cell efficiency improvement.

2.1 A novel light trapping scheme

The goal of light trapping is to utilize long wavelength photons that would otherwise be lost due to the insufficient optical path length of the thin Si solar cell. In this thesis, a novel light trapping technique, textured photonic crystal, is invented which combines reflection grating and distributed Bragg reflector as a one-dimensional photonic

crystal (*U.S. provisional patent No. 60/645, 766, filed January 19, 2005)*. Figure 2.1 is a schematic of this design. The grating can diffract normally incident light almost parallel to the surface of the cell, increasing the path length by dramatically. Our distributed Bragg reflector (DBR) has an extremely high reflectivity of more than 99.8% over a wide wavelength range, almost completely eliminating reflection loss. Therefore, strong absorption enhancement can be realized.

In the following sections, DBR and grating will be studied in more detail.

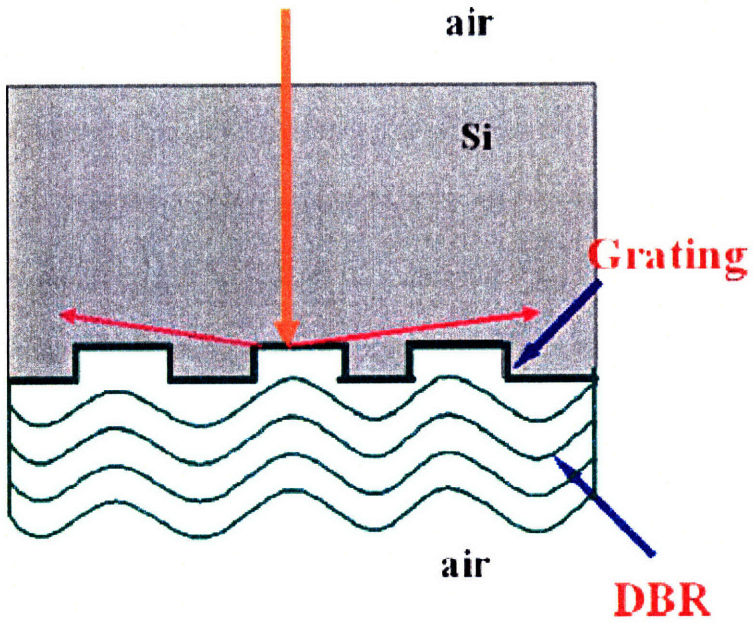

Fig. 2.1 Schematic of our novel light trapping scheme combining reflection grating and distributed Bragg reflector

2.2 DBR:1D photonic crystal high reflectivity mirror

2.2.1 Fundamentals of photonic crystals

Starting 1987, photonic crystals have aroused intensive interest [2.1-2.4]. It is a remarkable invention realized by the combination of optical physics and contemporary microfabrication technologies to control the interaction of radiation fields and matter to mold the flow of light [2.1, 2.3]. These are periodic arrays of materials with different refractive indices, with Fig. 2.2 showing the simplest case where two materials are stacked alternately. The spatial period of the stack is called the lattice constant, as it is analogous to the lattice constant of an ordinary crystal that is composed of periodic array of atoms. For ordinary crystals, it is on the order of angstroms, and for photonic crystals, it is on the order of the wavelength of relevant electromagnetic waves.

There are three major categories of photonic crystals, one-dimensional (1D), two-dimensional (2D), and three-dimensional (3D), depending on the dimensionality of

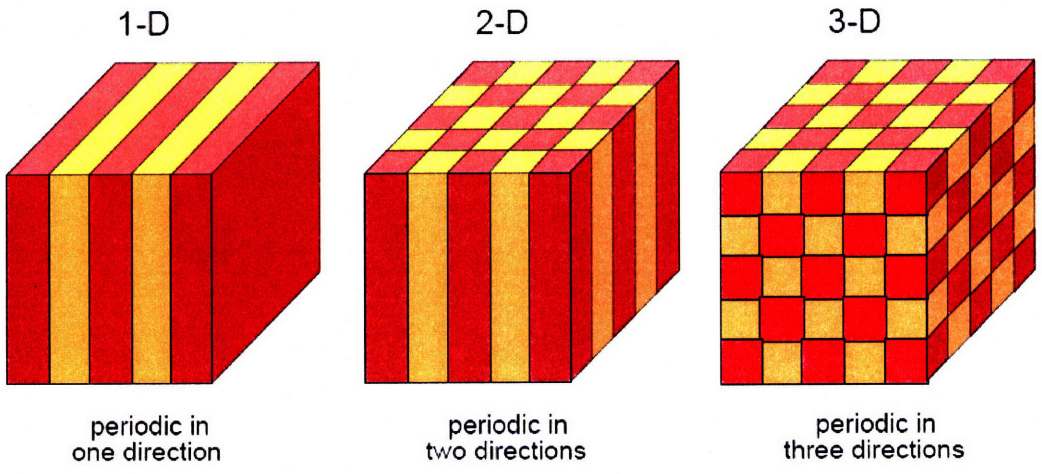

Fig. 2.2 Schematic of 1D, 2D and 3D photonic crystals [2.5]

periodicity, as shown in Fig. 2.2. If a 3D photonic crystal is designed properly, there will be a frequency range where no electromagnetic eigenmode exists. These kind of frequency ranges are called photonic bandgaps, as they correspond to bandgaps of electronic eigenstates in ordinary crystals. To have a complete (for all $\boldsymbol{k}$ vectors and polarizations) photonic band gap, high index contrast ($\Delta n/n$) between the different materials and certain crystal symmetry need to be satisfied. If a disorder is introduced into the regular dielectric structure of the photonic crystal, strongly localized midgap modes may occur, which are called localized defect modes, analogous to the defect states in an ordinary crystal.

Fig. 2.3 shows the schematic of experimentally fabricated 2D photonic crystal

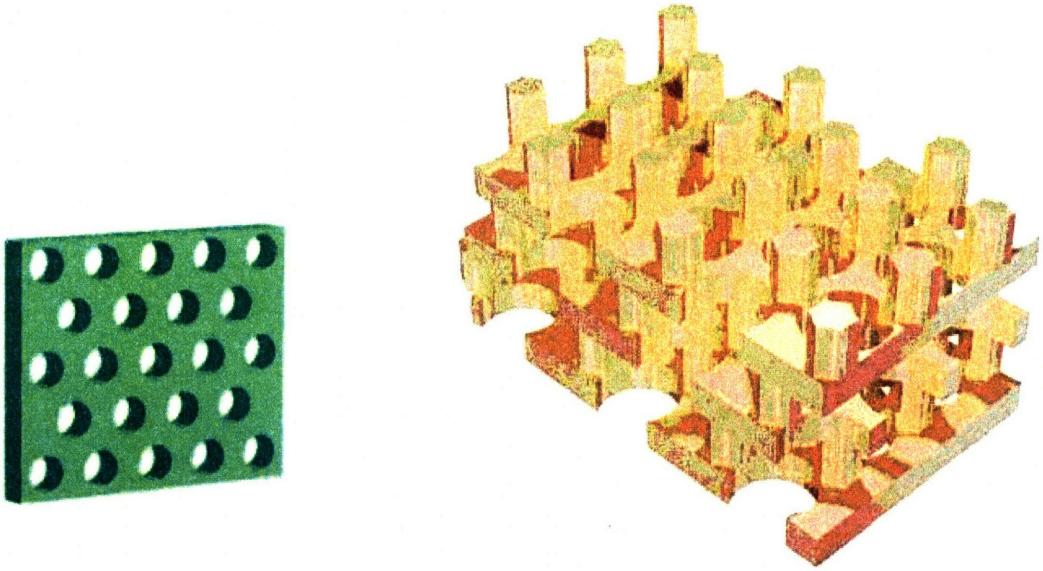

Fig. 2.3 Schematic of experimentally fabricated 2D (a) and 3D (b) photonic crystals [2.5]

slabs and 3D photonic crystals that can be fabricated with a layer-by-layer process. Usually the fabrication of photonic crystals that work in the visible region, especially 3D ones, is quite challenging due to their small lattice constants [2.3]. However, they are pursued because they can have a complete photonic band gap for all angles (omnidirectional bandgap). Recently, omnidirectional photonic band gap structures have been discovered for even one-dimensional photonic crystals, when the index contrast of alternating dielectric layers is high enough and satisfies certain conditions [2.6-2.8]. The high index contrast dielectric layers result in a large photonic band gap for wide angles,

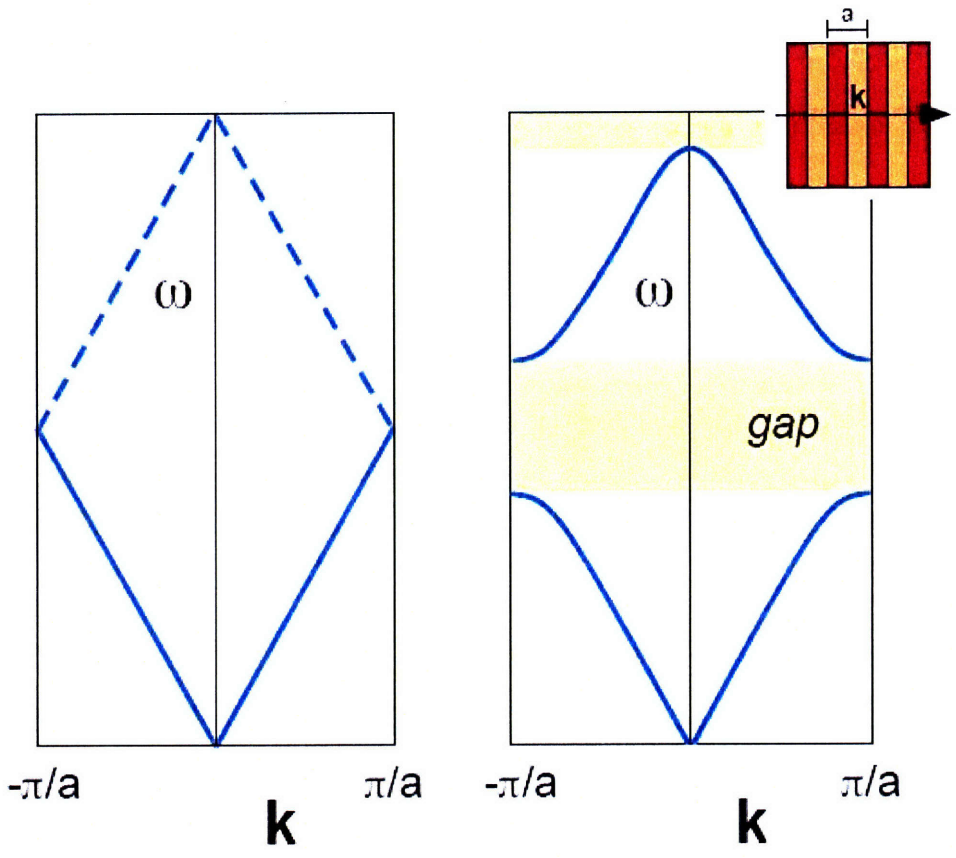

Fig. 2.4 Dispersion relation (band diagram) of (a) left: a uniform one-dimensional medium; (b) right: schematic effect on the bands of a physical periodic dielectric variation, where a gap has been opened by splitting the degeneracy at the k = ±π/a Brillouin-zone boundaries (as well as a higher-order gap at k = 0) [2.5]

leading to the possible realization of an omnidirectional reflector for a 1D system. Fig. 2.4 compares the band diagram of a uniform 1D medium and a 1D photonic crystal.

1D photonic crystals are traditionally called dielectric multilayers and have well-known optical properties [2.9]. For a 1D photonic crystal, incident photons with frequencies in the photonic bandgap (also called stopband) can not propagate through the crystal, and will be completely reflected back. This makes them high reflectivity mirrors. However, as mentioned above, an omnidirectional 1D photonic crystal that is not sensitive to polarization and incident angle is a relatively new finding. The key requirement is high index contrast of the stack materials. In this thesis, we will use 1D Si-based photonic crystal as a high reflectivity mirror for light trapping. In thin film solar cells, a good back reflector should be able to reflect light with high reflectivity across a wide wavelength range needing light tapping, and for wide incidence angles. A 1D photonic crystal with high index contrast has near 100% reflectivity over a wide stopband (photonic bandgap) for a wide range of incidence angles, and thus satisfies all these requirements.

2.2.2 Materials choice for omnidirectional 1D photonic crystals

We find two Si-based materials systems for omnidirectional 1D photonic crystals: Si/SiO_2 (n_1/n_2=3.5/1.46), and Si/Si_3N_4 (n_1/n_2=3.5/2) [2.10, 2.11] as high reflectivity dielectric mirrors. Both materials systems have high index contrast, are easy to fabricate, and have good compatibility to Si. Therefore, they are ideal for light trapping in Si solar cells.

Superior to any other high quality mirror, our 1D photonic crystal has a wide stopband expanding several hundred nanometers with near 100% reflectivity with just a few pairs of stacked materials. For simplicity, from now on, we will call our 1D photonic crystal a **distributed Bragg reflector** (DBR). Both Si/SiO_2 (n_1/n_2=3.5/1.46) and Si/Si_3N_4 (n_1/n_2=3.5/2.0) achieve reflectivity of >99.8% for λ between 800-1100 nm with just a few quarter-wave pairs when light is incident from Si. The high reflectivity of DBR guarantees that almost no light can leak out from the backside of the solar cell. By contrast, for Al backside reflectors commonly used in solar cells, the reflectivity is <80% for Si incidence. For multiple reflections, since the reflection loss scales exponentially with number of reflections, the difference in reflectivity makes a huge difference in terms of reflection loss.

Our DBR stack is composed of alternating layers of these two Si-based materials systems. The key parameters of a DBR stack are the Bragg wavelength λ_B and number of quarter wave pairs u. λ_B determines the thickness of the high and low index layers through

$$t_{hi,lo} = \frac{\lambda_B}{4n_{hi,lo}} \qquad (2.1),$$

where n_{hi}, n_{lo} are the indices of the two stack materials. The DBR reflectivity at the stopband center λ_B can be approximately calculated [2.13] from

$$R_{SBC} = \left(\frac{1-(n_{lo}/n_{hi})^{2u}}{1+(n_{lo}/n_{hi})^{2u}}\right)^2 \qquad (2.2),$$

where u is the number of quarter wave pairs as mentioned before. The stopband width $\Delta\lambda_{SB}$ can be obtained analytically [2.12] from

$$\Delta\lambda_{SB} = \frac{2\lambda_B(n_{hi} - n_{lo})}{\pi n_{eff}} \qquad (2.3),$$

where

$$n_{eff} = 2(\frac{1}{n_{hi}} + \frac{1}{n_{lo}})^{-1} \qquad (2.4).$$

Accurate calculation of DBR reflectivity and stopband width requires numerical simulation.

For Si_3N_4/Si DBR, just 7 pairs can reach reflectivity of 99.96%, whereas for SiO_2/Si, due to a higher index contrast, only 5 pairs can achieve 99.98% reflectivity. More pairs will not appreciably increase reflectivity, except that the reflectivity spectrum will show more square-shaped photonic bandgap closer to theoretical prediction for a 1D photonic crystal. Adjusting the central wavelength λ_B will move the stopband and alter the band width.

Fig. 2.5 illustrates the simulated reflectivity of a 10- pair SiO_2/Si DBR stack using transfer matrix calculation. The central wavelength is set as 900 nm so that the stop band covers the entire wavelength range that needs light trapping. Fig. 2.6 displays the measurement results on 8 pairs of SiO_2/Si DBR stack, with λ_B=1000 nm. As we can see, the measurement follows simulation well given their different λ_B and number of pairs.

In solar cell applications, the omnidirectional property of DBR is important because on average 15% of the sun light is diffuse and incident onto the solar cell in all angles [2.13]. Fig. 2.7 shows the simulated reflectivity of a 10-pair SiO_2/Si DBR stack with λ_B=900 nm, at three incidence angles 0°, 45° and 89°. It demonstrates that increased incidence angle leads to increased reflectivity and a slight blue shift of the stop band. It

also shows that the omnidirectional stop band is >500 nm wide. Therefore, our DBR is good for all incidence angles.

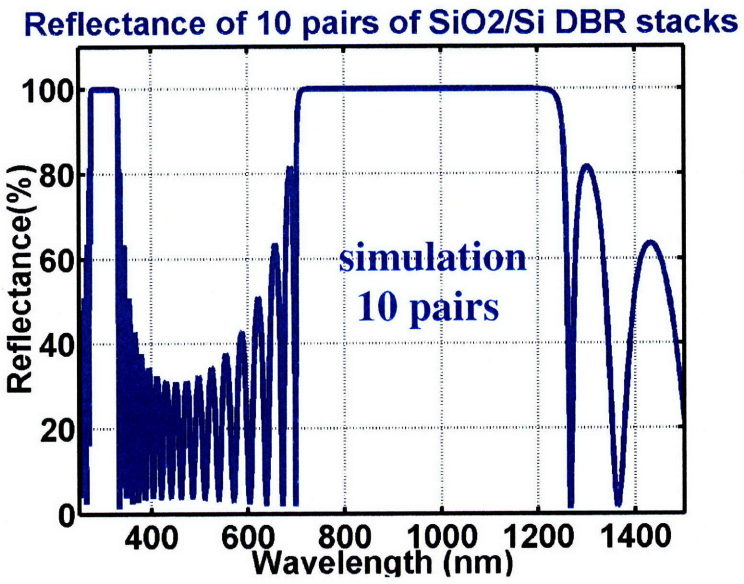

Fig. 2.5 Simulated reflectivity of a 10 pair-SiO_2/Si DBR stack

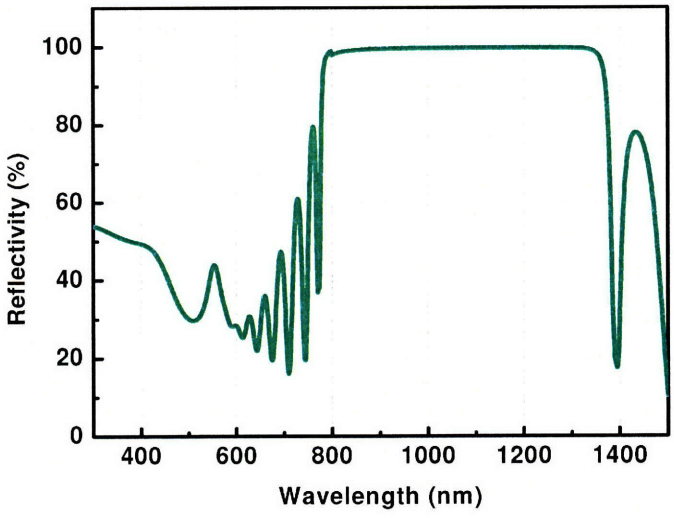

Fig. 2.6 Measured reflectivity of a 8-pair SiO_2/Si DBR stack

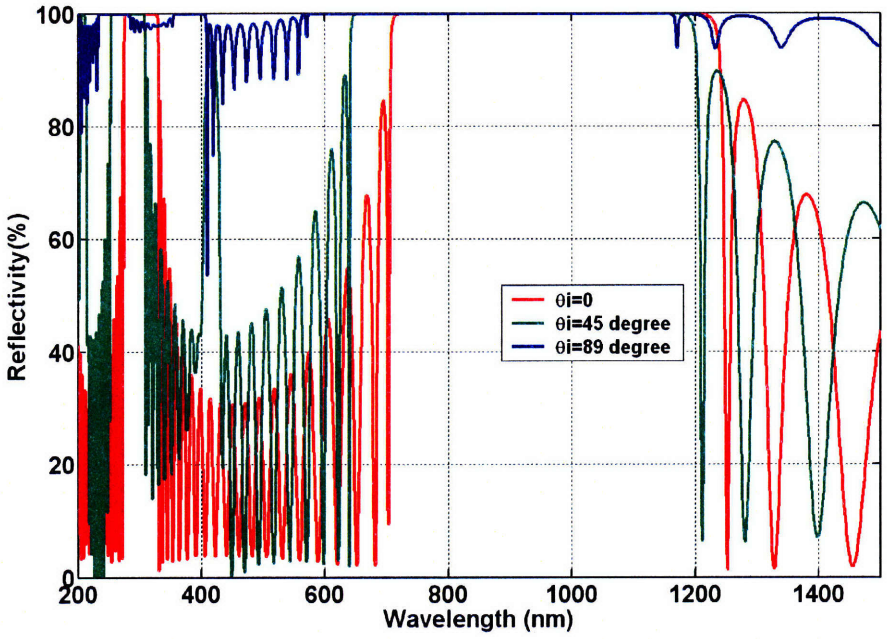

Fig. 2.7 Simulated reflectivity of a SiO_2/Si DBR stack composed of ten quarter-wave pairs with a Bragg wavelength at 900 nm, at three incidence angles onto the DBR.

2.2.3 DBR thermal stability

DBR can be deposited via sputtering, evaporation, or more commonly, as in our experiments, plasma enhanced chemical vapor deposition (PECVD). In PECVD, the temperature is less than 450° during deposition. However, during device processing, it is very likely that there will be high temperature steps after DBR deposition, like dopant anneal (~ 1000 °C for 30 min) and thermal oxidation in device fabrication, as will be seen in our thin film Si solar cell fabrication presented in Chapter 6. Since DBR is composed of multiple layers that might have accumulated stress or interlayer diffusion during high temperature processing, there is a concern as to whether it will crack due to thermal stress, or lose its superior optical properties, perhaps via densification and an increase in the refractive index.

To study this problem, and also as process development for our future thin film Si solar cell processing presented in Chapter 6, 8 pairs of alternating Si/ SiO_2 DBR and Si/Si_3N_4 DBR with λ_B=1000 nm were deposited using PECVD on several Si wafers. Since nitride is known to be less forgiving in high temperature applications than SiO_2, maybe having higher stress, a test was performed on Si/Si_3N_4 DBR first. It was put into an annealing tube at 800°C for 1 hour in N_2 ambient. After it was taken out of the annealing tube, the originally shiny DBR surface became completely dim. Inspection under the microscope showed that small cracks created across the wafer surface. Therefore the rest of the test was focused on the Si/ SiO_2 DBR. The studying method was to simulate high temperature steps by tube annealing the DBR stack in N_2 ambient and measure reflectivity change afterward. Two kinds of experiments were performed:

First, a wafer with Si/ SiO_2 DBR was annealed at 1000°C for 3.5 hours in N_2 atmosphere to evaluate the influence of thermal stress. After coming out of the annealing tube, significant color change on the film surface was observed. The originally light blue color became reddish, but with no film cracking, and the stack surface was still shiny and of uniform color.

Second, another wafer with Si/ SiO_2 DBR was cut into pieces and annealed under two different thermal conditions:

Sample 1: 1050°C for 1 hour, followed by 775°C for 1 hour, and then 1000°C for 1.5 hours. This is to simulate the high temperature process design including wafer bonding, LPCVD Si_3N_4 deposition, thermal oxidation, and dopant anneal. The higher temperatures are assumed to render more solid processing and device performance.

Sample 2: 800°C for 4 hours, followed by 775°C for 1 hour. This is the low temperature alternative in case our DBR fails high temperature processing under the conditions sample 1 experienced.

Sample 3: no anneal.

Both Sample 1 and 2 looked fine after coming out of the annealing tube, other than a slight color change. These three samples, together with the Si/ SiO_2 DBR wafer annealed at 1000°C for 3.5 hours, which is now designated as Sample 4, were brought for reflectivity measurements using a high resolution spectrometer. The reflection spectra of each sample is shown in Fig. 2.8. The discontinuity at λ=800 nm is due to the change of detector. Detailed information about key parameters of DBR performance is listed in Table 2.1.

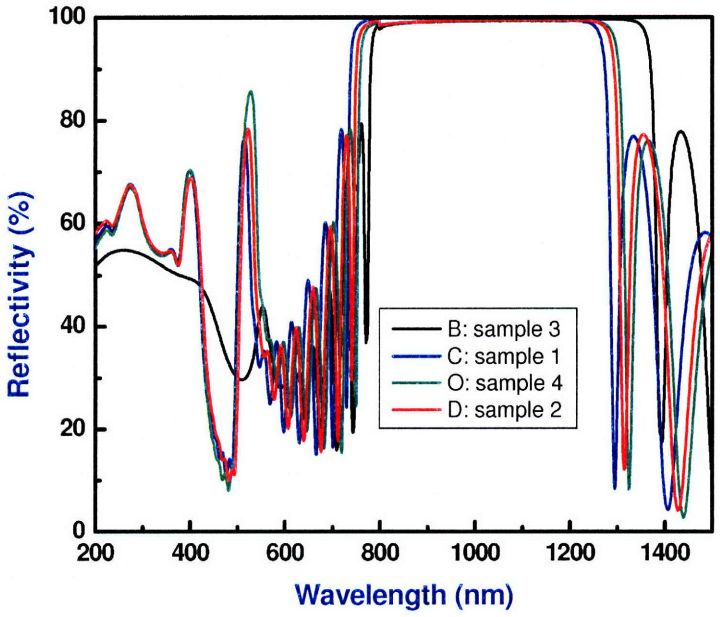

(a) full spectra

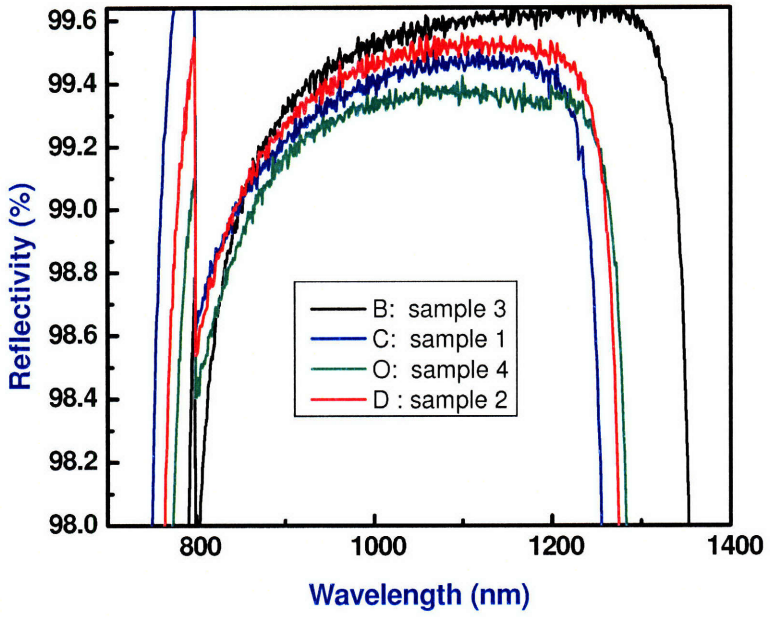

(b) Enlarged view of stopband

Fig. 2.8 (a) and (b): Reflection spectra of Si/SiO_2 DBR after different anneal

Table 2.1 DBR parameters change after anneal under different conditions

Sample #	Anneal condition	Stopband central λ (nm)	Stopband width $\Delta\lambda_{SB}$ (nm)	Reflectivity @ 1100 nm (%)
1	1050°C/1 hr + 775°C/1 hr + 1000°C/1.5 hr	939.4	504.9	99.46
2	800°C/4 hr + 775°C/1 hr	955.5	510.4	99.56
3	No anneal	1000.1	560.4	99.61
4	1000 °C/3.5 hr	965.4	508.9	99.38

From Fig. 2.8 and Table 2.1, we observe that under all thermal conditions:

1. the stopband reflectivity drops slightly, by 0.05% to 0.23 %;
2. the stopband width (photonic bandgap) shrinks by around 50 nm;
3. the stopband central wavelength (λ_B) blue shifts by 26 to 34.7 nm.

The shift of λ_B is possibly due to the densification and refractive index change of the stack material. Because $\lambda_B=4nt$, if the film becomes thinner due to densification, λ_B will become smaller. We see that the difference between Samples 1 and 2, which underwent the high and low thermal budget extremes for our future thin film solar cell fabrication, are small in all aspects considered in Table 2.1. Therefore, we can conclude that Si/SiO_2 DBR is quite stable both mechanically and optically under a high thermal budget. We can safely use the high temperature process design for solid processing and better device performance.

2.3 Grating for strong light bending

In the previous section, we studied the 1D photonic crystal (DBR), which is one of the two central components of our new light trapping scheme: textured photonic crystal. In this section, we will now study the other component, diffraction grating.

2.3.1 Grating basics

Diffraction grating is an old concept that has been known for over 150 years [2.14]. Whenever a traveling wave encounters a periodic obstruction with dimension similar to its wavelength, energy is scattered into different discrete directions which are called diffraction orders. Such a periodic structure is referred to as a diffraction grating. Historically, due to their importance in spectroscopic instruments, gratings have received considerable and sustained research.

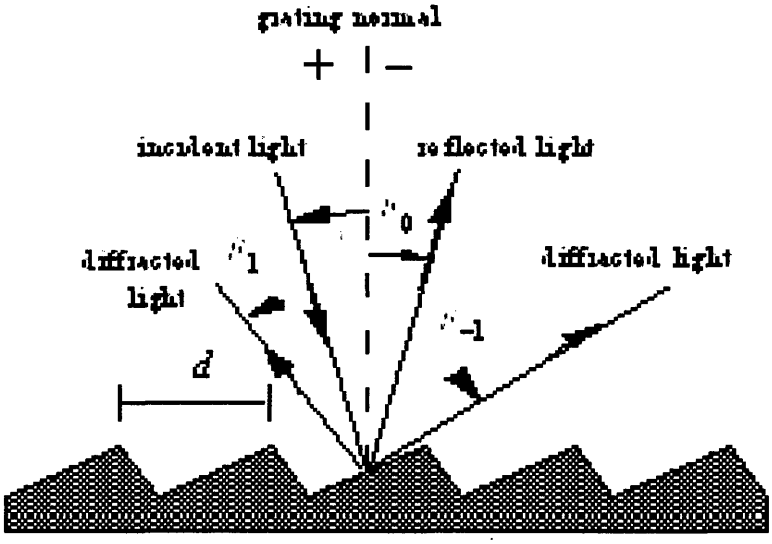

Fig. 2.9 Diagram explaining grating equation

I. Grating properties [2.15]

The famous property of gratings to diffract light into clearly distinctive directions is expressed in grating equation

$$m\lambda = p(\sin\alpha + \sin\beta) \qquad (2.5),$$

where m is the diffraction order, λ is the wavelength, p is the grating period, α and β are the angles between the incident (and diffracted) wave directions and the normal to the grating surface. Fig. 2.9 illustrates this relation. When m=0, specular reflection occurs, and all wavelengths superimpose. When $m\neq 0$, for the same incidence angle α, different λ are diffracted into different directions, and are angularly separated.

For a diffraction order to propagate and carry energy away from the grating, the diffraction angle β must satisfy

$$|\sin\beta| < 1 \qquad (2.6).$$

Diffraction orders with numbers m such that Eq. (2.6) are satisfied are called propagating orders, and those that fail to do so are called evanescent orders, and they can only be detected within a distance a few wavelengths away from the grating surface. Evanescent orders are essential in waveguide and fiber gratings.

Grating Eq. (2.5) only gives the diffraction direction. Another important property about gratings is their diffraction efficiency, the physical quantity that characterizes how the energy from the incident field is distributed among the different orders. It is defined as the ratio between the energy flow of a particular order in a direction perpendicular to the grating surface and the corresponding flow of the incident wave through the same surface. There is no simple way to describe grating efficiency behavior. For gratings with period p much longer than the wavelength λ, the diffraction efficiency can be estimated with Fraunhofer approximations. When p is reduced to near λ, Fraunhofer approximations no longer hold, and grating efficiency must be analyzed with numerical methods. Several rules can help with grating efficiency analysis.

The first one is "energy balance criterion": the sum of efficiencies of all the propagating orders must equal the intensity of the incident light minus the losses. The second one is the "reciprocal theorem": if grating is used under the same conditions as in Fig. 2.9, but with the angle of incidence and diffraction exchanged, the grating efficiency in the diffraction order considered remains unchanged. The third one is about "perfect blazing". The property of gratings to concentrate the diffracted light into a certain order is called blazing. For gratings with fine periods which only support two orders, the 0^{th} and 1^{st} orders, the grating groove depth can be optimized to suppress the 0^{th} order regardless the grating profile.

II. Types of diffraction gratings

Gratings can be divided into many types with different criteria:

(1) amplitude and phase gratings: the former is supposed to change only the amplitude of the incident light in different groove regions and the latter only change the phase;

(2) reflection and transmission gratings: they work in either reflection or transmission regimes;

(3) symmetrical and blazed gratings: depending on whether the shape of the grating groove is symmetrical or characterized by a triangular groove shape with 90° apex angle;

(4) ruled, holographic and lithographic gratings: depending on the way they are fabricated;

(5) waveguide gratings, fiber gratings, etc., depending on their applications.

2.3.2 Grating parameters selection for large angle diffraction

For a plane reflection grating with rectangular cross section, there are three structural parameters: the grating period p, depth h, and duty cycle f, which is defined as the ratio between the width of the plateau to the spacing between adjacent plateaus. For plane reflection gratings in general, two major factors determine their grating efficiency: the ratio between the wavelength and the grating period, i.e. λ/p, and the ratio between the grating depth and the period h/p. The next factor is the shape of the groove [2.16].

For lamellar gratings (a type of symmetrical gratings) that consists of ridges with rectangular cross section and a duty cycle of 0.5, there is an important property [2.17]: if

the height of the ridge is designed such that the optical path difference between the rays reflected (or transmitted) at the top and on the bottom is $\lambda/2$, the 0^{th} order at this λ may be eliminated, and an equally strong +1 and -1 orders appear at either side.

Since gratings can diffract light, if integrated into the back side of the solar cell, it can elongate the optical path length by forming large angle diffraction. Based on the grating properties above, we choose to use lamellar gratings with a rectangular cross section and duty cycle 0.5 for light trapping in solar cells. The grating period p is set to be close to λ_g/n_{Si} where λ_g is the bandgap wavelength of Si, and n_{Si} is the refractive index of Si. The grating depth is set to be around $\lambda_g/4(n_{Si}-n_{Ex})$, where n_{Ex} is the refractive index of the exit medium, such that in the case of normal incidence, the incident light and 0^{th} order reflection will have a phase shift of π, and thereby cancel each other, leaving only +1 and -1 orders diffracted into large oblique angles, as shown in Fig. 2.10.

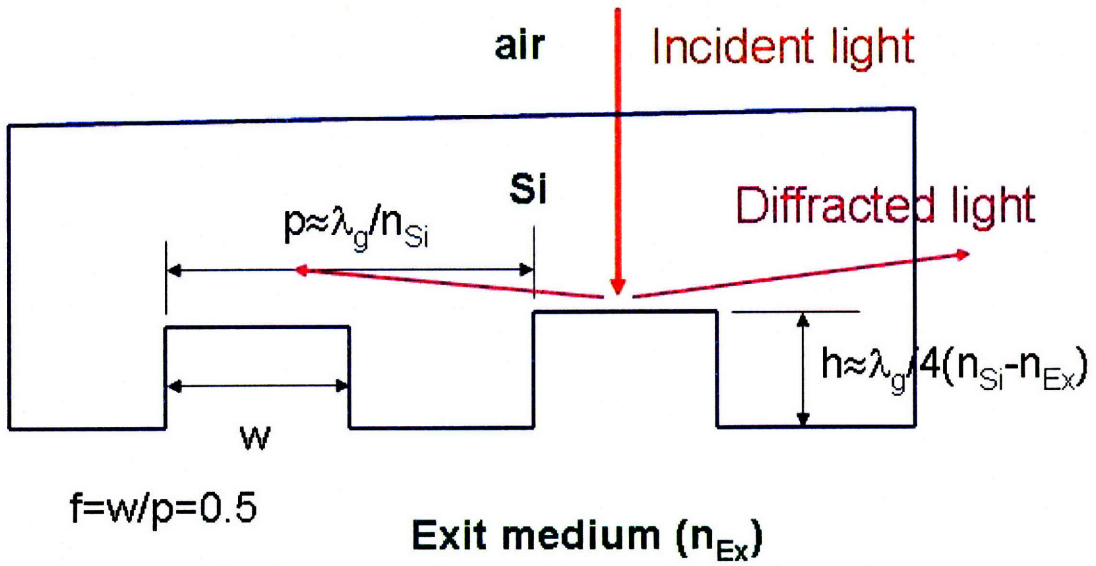

Fig. 2.10 Grating parameters selection for large angle diffraction in a Si solar cell

The parameter choice above can be explained in more detail. From grating Eq. (2.5), when $p \approx \lambda/n_{Si}$ (note that when light is incident from a medium with refractive index n, the wavelength λ becomes λ/n, and therefore the grating period needs to be adjusted accordingly), under normal incidence, both 0^{th} order and ± 1 order diffraction can occur. Usually 0^{th} order diffraction is the strongest. It will be reflected back in the normal direction, while the ± 1-order will be diffracted to almost parallel to the grating surface. If the etch depth $t \approx \lambda/4(n_{Si}-n_{Ex})$, the 0^{th} order diffraction will be strongly canceled, leaving only ± 1-order diffraction, bent by near 90° from the original path. The grating period is set to be around λ_g/n_{Si} because photons near the Si bandgap are effective in converting optical energy into electrical energy due to reduced thermal loss.

For wavelengths different from the grating period, ± 1-order diffraction angle increases with λ according to Eq. (2.5). Photons with λ from 800 nm-1100 nm all need light trapping due to the long absorption length. The corresponding light diffraction angle varies from 47° to 90° for this λ range. Since at λ=310nm, the diffraction angle already reaches 16.6°, the critical angle of Si, wavelengths longer than this will encounter total internal reflection when the light impinges on the front surface of the cell. Therefore, light will be reflected back into the cell for further absorption. Consequently, large angle diffraction increases light absorption not only by having a big oblique diffraction angle, but also by reducing the transmission loss from the front surface of the cell.

Fig. 2.11 illustrates the diffraction angle vs. wavelength calculated from Eq. (2.5). It is clear that large angle diffraction occurs for λ between 800-1100 nm, far above the total internal reflection angle between Si and air. To experimentally verify the strong light bending, the diffraction behavior of a 1.5 μm period grating etched 375 nm deep

into a Si wafer was measured using the setup in Fig. 2.12. Note that the grating period was scaled from the designed 1.1 μm/n_{Si} to 1.5 μm due to air incidence and light source

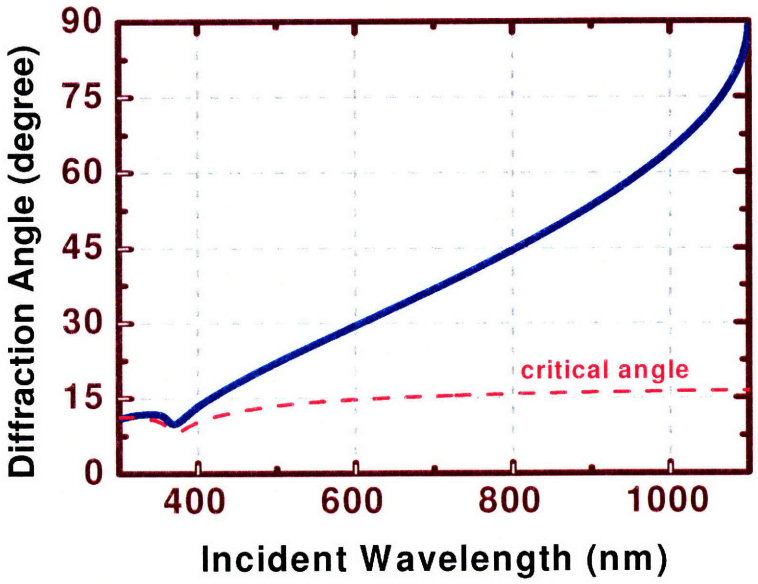

Fig. 2.11 Calculated diffraction angle vs. wavelength for a Si grating with period λ_g/n_{si} when light is incident from Si

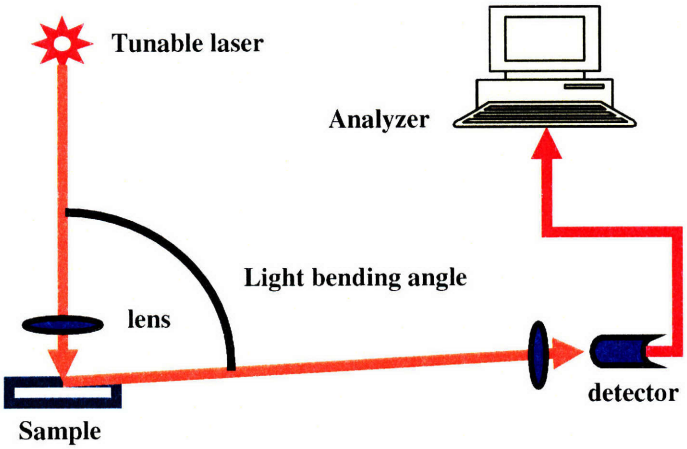

Fig. 2.12 Experimental setup for grating light bending measurement

limitations. The etch depth was also modified from 1.1 μm/4n_{Si} to 1.5 μm/4 for the same reason. A 1.5 μm tunable laser shone monochromic light onto the grating. The direction and intensity of the reflected light were detected by a rotating detector, which was connected to an analyzer. Fig. 2.13 shows the measurement results. The reflection intensity was normalized to the reflected intensity when light is incident from air onto a planar Si surface. It is clear that not only is large angle diffraction up to 84° realized, but also that most of the energy goes into the first order diffraction.

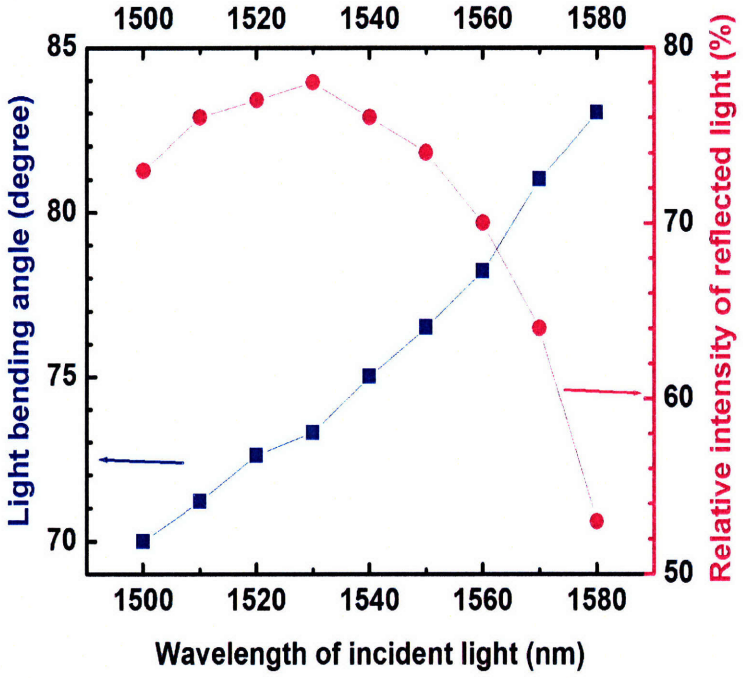

Fig. 2.13 Measured strong light bending by a 1.5 μm period grating

2.3.3 Grating fabrication

Submicron period gratings for light trapping in our solar cells can be formed using interference lithography or nanoimprint lithography. Interference lithography is a

simple maskless process which exposes photoresist with the interference fringes of two laser beams. It provides an inexpensive, large-area capability, enabling numerous applications in nanotechnology [2.18], including nanoscale epitaxial growth for semiconductor heterostructures, nanomagnetics, nanophotonics, and nanofluidics for biological separations.

Fig. 2.14 is a schematic of the setup of a Lloyd's Mirror Interferometer. It consists of a laser with a set of lenses, and a mirror placed perpendicular to the sample holder. The UV beam from the laser illuminates both the mirror and the sample. Part of the light is reflected from the mirror and interferes with the portion of the beam that is directly incident on the sample. This interference will generate a line pattern with a period given by

$$p = \frac{\lambda}{2\sin\theta} \qquad (2.7),$$

where λ is the wavelength and θ the angle between the incidence light and the sample normal. The grating period can be conveniently adjusted by rotating the sample holder-mirror fixture, and the accuracy can be within a few nanometers. Figs. 2.15 and 2.16 are

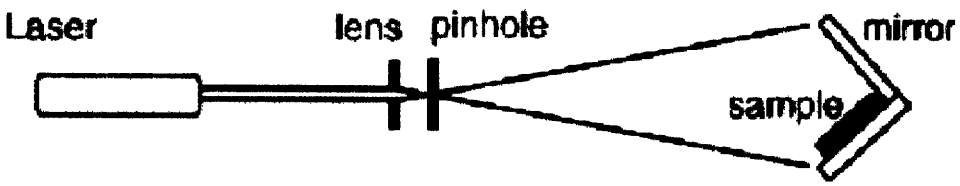

Fig. 2.14 Schematic of the setup of a Lloyd's Mirror Interferometer

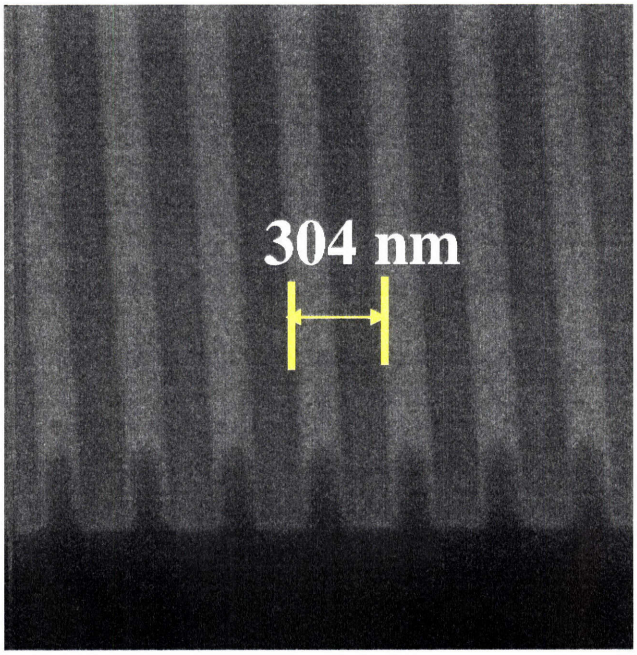

Fig. 2.15 SEM picture of a 1D grating with 304 nm period fabricated using interference lithography

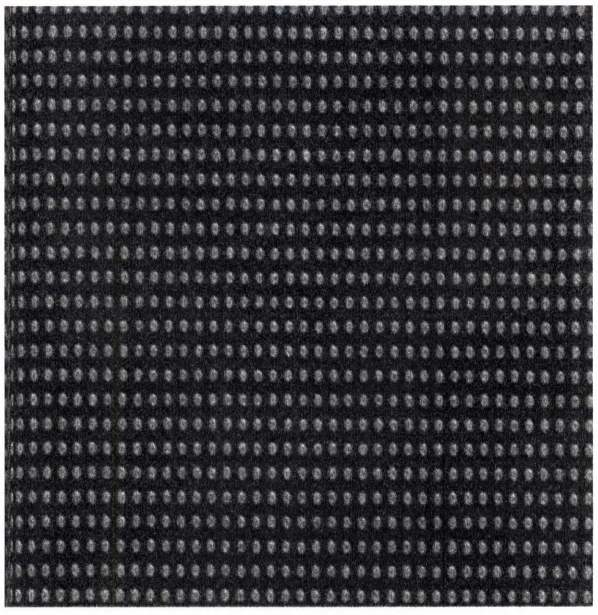

Fig. 2.16 SEM picture of a 2D grating with 289nm period fabricated using interference lithography

SEM pictures of 1D and 2D gratings fabricated at University of New Mexico using the Fresnel Corner Cube Mirror Interferometric Lithography tool.

Nanoimprint lithography is an emerging technology of high throughput and potentially low cost [2.19, 2.20]. It transfers the desired pattern from a template to the substrate. The process flow is shown in Fig. 2.17. The template can be made with e-beam and interference lithography, or even advanced stepper projection lithography.

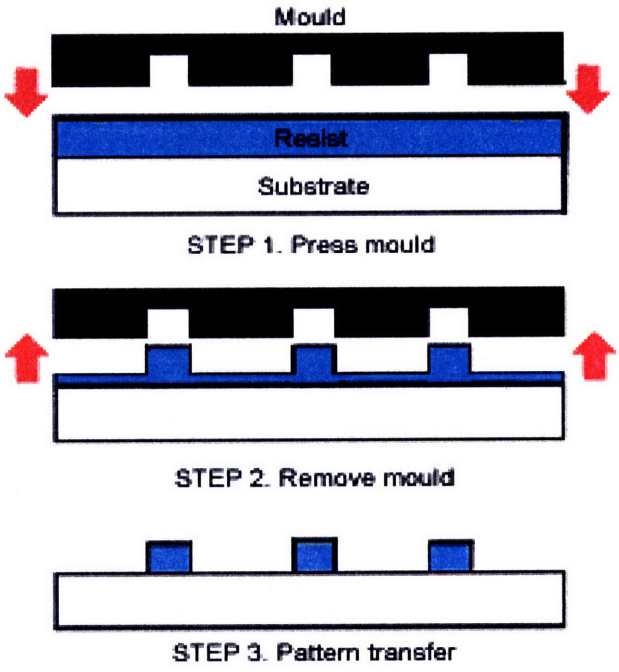

Fig. 2.17 Process flow of nanoimprint lithography

2.4 Textured photonic crystal as a new backside reflector

2.4.1 Intuitive understanding

In the previous two sections, we have learned of the strong light trapping properties of DBR and gratings. However, if they are used alone, each will have

problems, as illustrated in Figs.2.18 and 2.19. If only DBR is used, 70% of the light will be lost when it is reflected to the front surface of the cell due to the natural transmission from Si to air. On the other hand, if the grating is used alone, 70% of the light will leak out from the back surface due to low reflection. Therefore, it is best to use them together, as shown in Fig. 2.18, i.e., making a textured photonic crystal by forming the grating and

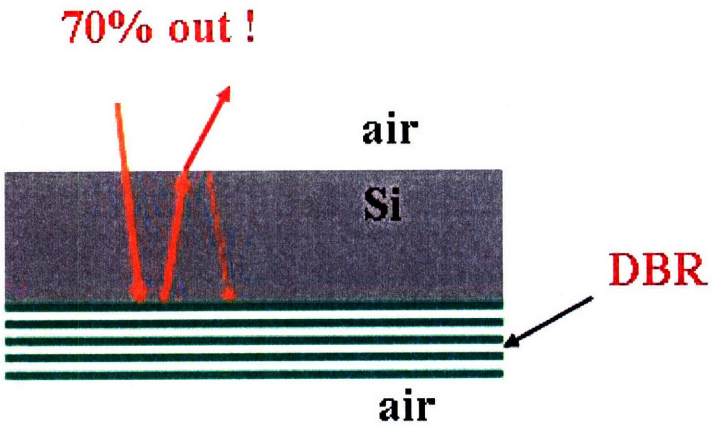

Fig. 2.18. Transmission loss from the front side when DBR is used alone

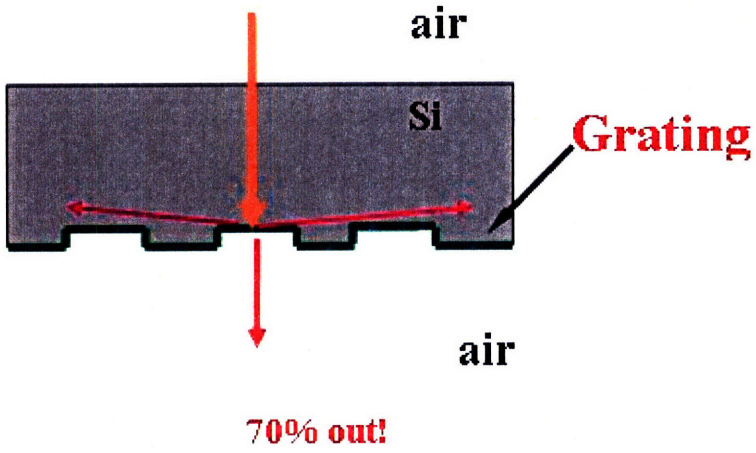

Fig. 2.19 Transmission loss form the back side when grating is used alone

depositing DBR at the back surface of the cell. This way, DBR eliminates transmission loss at the backside of the cell, and the grating not only forms large angle diffraction, but also induces total internal reflection at the front surface of the cell. By the unique combination of DBR and grating, light will be tightly trapped inside the cell, effectively changing the path length from the thickness of the cell to its lateral dimension. Huge solar cell efficiency improvement can be achieved.

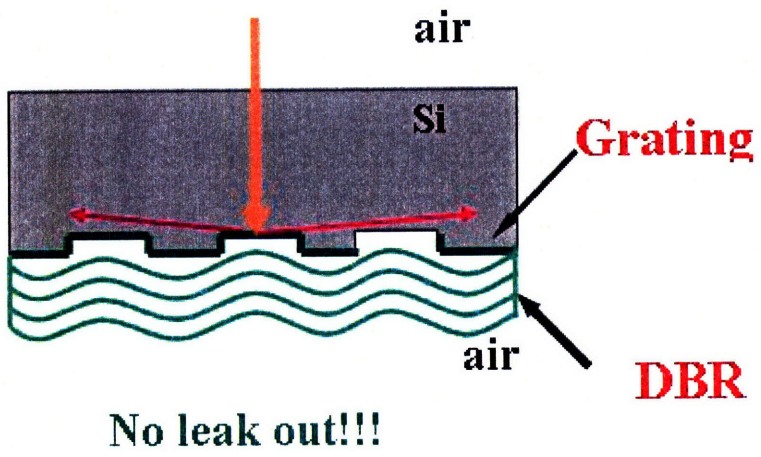

Fig. 2.20 By integrating both grating and DBR onto the solar cell, the transmission loss from both the back and front surface of the cell is greatly reduced

2.4.2 Absorption spectrum

Since the purpose of light trapping is to enhance the absorption of long wavelength photons, besides the intuitive pictures in the previous section, a more insightful way to understand the principle of light trapping of textured photonic crystal (TPC) is to inspect the absorption spectrum. Below we will study the simulated

absorption spectra of solar cells at two active layer thicknesses: 5 μm and 2 μm, with the following back structures as shown in Fig. 2.21:

(a) Reference cell:

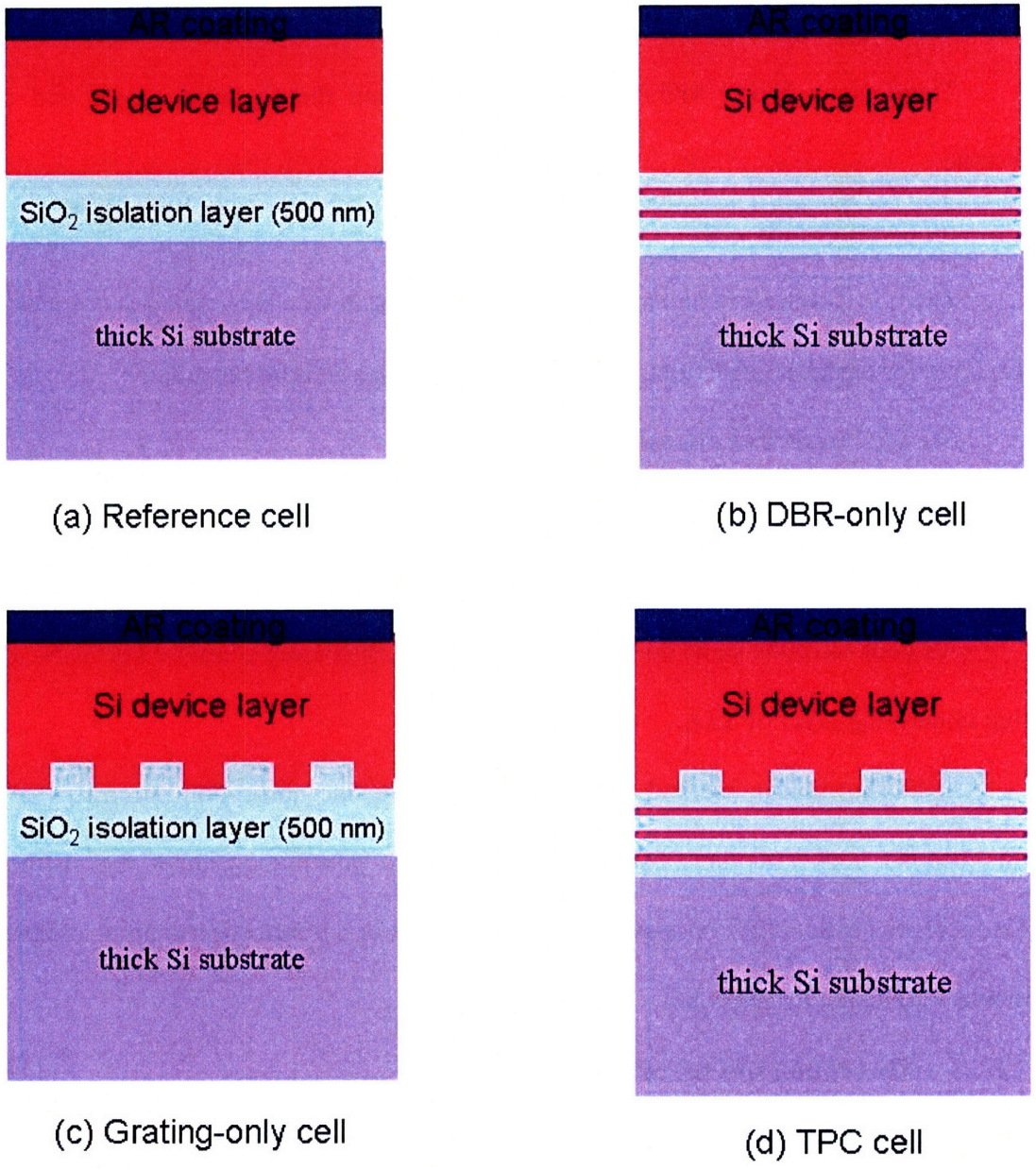

Fig. 2.21 Schematic of solar cells with different back structures for absorption simulation

There is no DBR or grating at the backside of the cell, except a 500 nm thick SiO_2 layer to electrically isolate the device layer from the thick Si substrate. Note that the substrate can be glass or ceramics, and that will not affect the absorption of the device layer.

(b) DBR-only cell:

There is an 8-pair SiO_2/Si DBR stack between the Si device layer and the substrate.

(c) Grating-only cell:

There is a grating etched at the backside of the Si device layer and a 500 nm thick SiO_2 layer for electrical isolation between the device layer and the substrate.

(d) TPC (textured photonic crystal) cell:

Besides the grating, there is an 8-pair SiO_2/Si DBR stack between the Si device layer and the substrate.

All cells have the same double-layer antireflection coating composed of Si_3N_4 and a thin underlying layer of SiO_2.

Scattering matrix method was used to calculate the absorption spectra of cells with different back structures listed above. For more information about this method, please refer to section 4.3 in Chapter 4. The parameters of antireflection coating and back structures are listed in Table 5.8.

I. Absorption spectra of 5 μm thick cells

Fig. 2.22 depicts the individual absorption spectrum of 5 μm thick solar cells under normal incidence. Fig. 2.23 illustrates all the absorption spectra in one combined figure for easier comparison. Obviously, at $\lambda<500$ nm, all the cells with different back structures

have overlapping absorption curves, because short wavelength photons will not be able to "see" the back structure. For λ>500 nm, the curves start to show very different shapes. The reference cell has the smoothest shape, and small inference peaks start to appear from λ=630 nm onward. The DBR-only cell displays stronger interference peaks, and starts at a shorter wavelength (~λ=510 nm). The grating-only cell starts to have small absorption peaks at around λ=590 nm, and the peaks heighten for λ>800 nm.

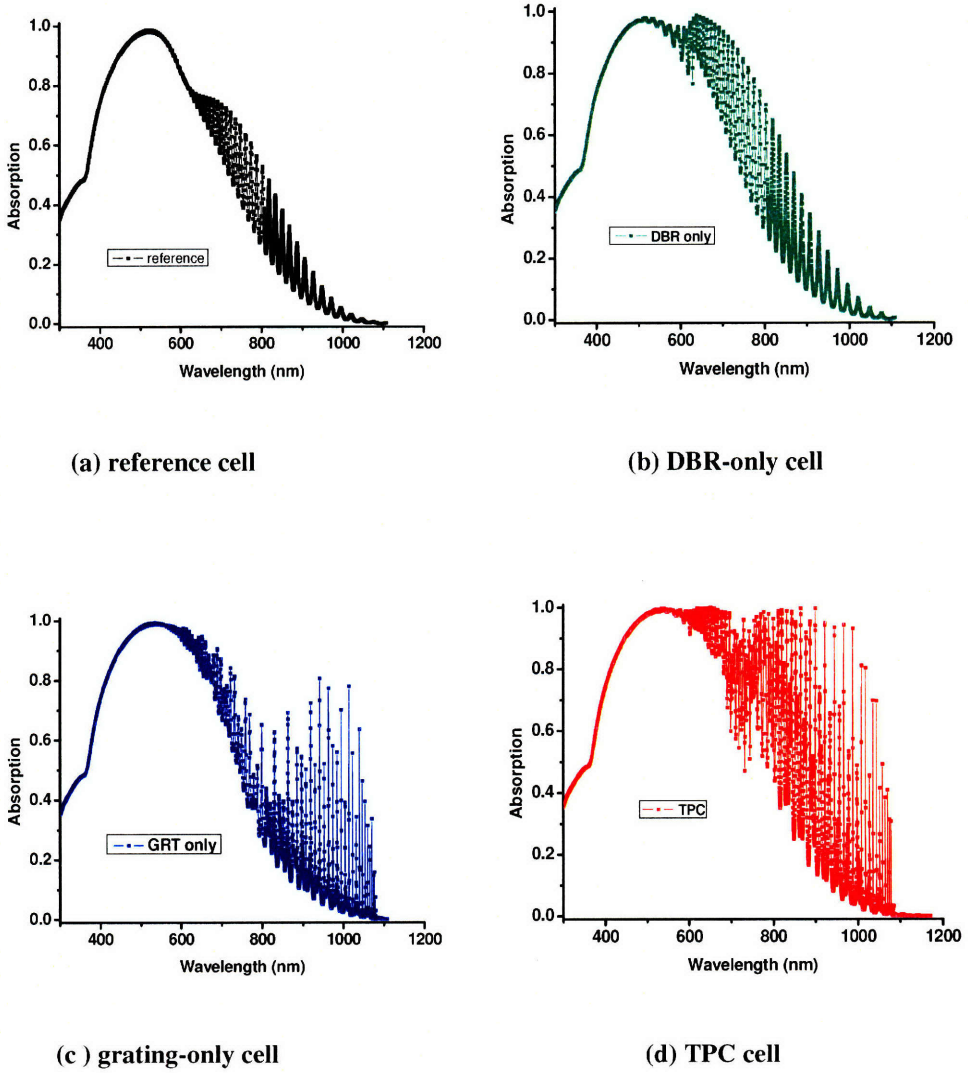

(a) reference cell **(b) DBR-only cell**

(c) grating-only cell **(d) TPC cell**

Fig. 2.22 Individual absorption spectrum of 5 μm thick cells with different back structures

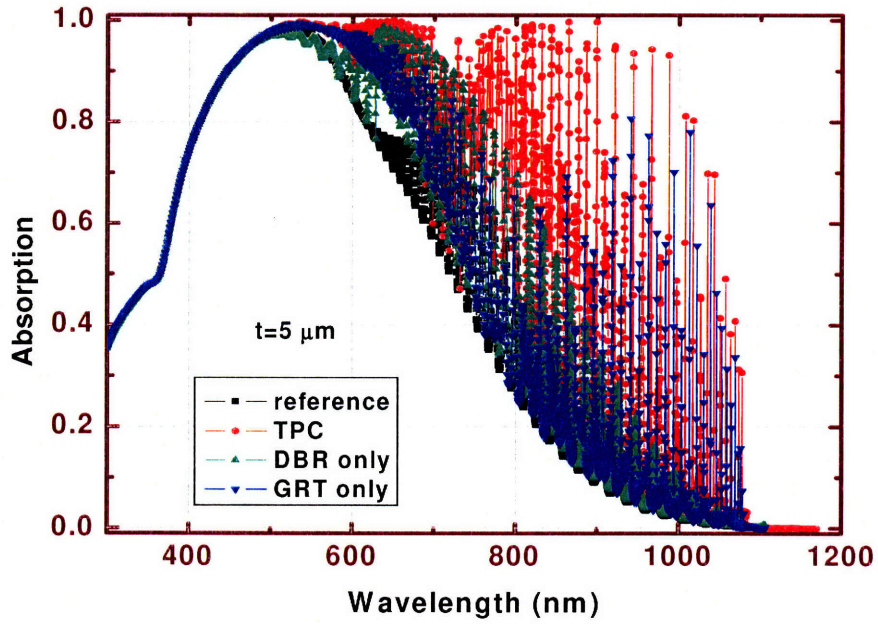

Fig. 2.23 Combined absorption spectra of 5 μm thick cells with different back structures

In general, the absorption curve of the grating-only cell is higher than that of the reference cell. The TPC cell has almost a square shape due to very dense and strong absorption peaks. At around λ= 900 nm, when the reference cell only has ~15% absorption, the TPC cell can still absorb near 100% of the incident photons.

To see the difference more clearly, Fig. 2.24 shows an enlarged view of Fig. 2.23 in the wavelength range of 850-960nm. On the spectrum of the reference cell, periodic interference peaks occur, and peak height monotonically decreases as λ increases. The interference peaks can be understood using a simple analytical model. If an active layer thickness t is considered, constructive interference happens when the round-trip phase change is a multiple of 2π, rendering the resonance condition

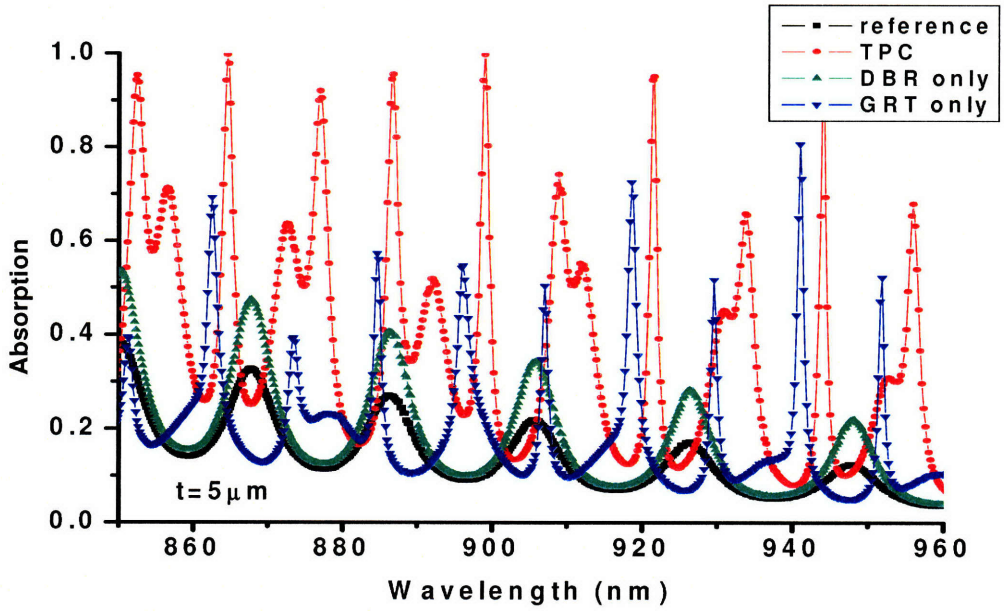

Fig. 2.24 Absorption spectra between 850-960 nm of 5 μm thick cells with different back structures

$$k = \frac{\pi l}{t} \qquad (2.8),$$

where k is the wave vector, and l is an integer. Since $k = \frac{2\pi n}{\lambda}$, where n is the refractive index of the device layer, this gives the peak position

$$\lambda_l = \frac{2nt}{l} \qquad (2.9).$$

Eq. (2.9) implies that peak spacing increases as wavelength increases, corresponding to decreasing mode number l. This is verified in Fig. 2.22(a): as λ increases, increasing peak spacing makes individual peaks discernable. The decreasing peak height with increasing wavelength is due to decreasing absorption coefficient.

The DBR-only cell also exhibits periodic interference peaks, at exactly the same positions as the reference cell, but with bigger peak height due to enhanced reflection.

There are 6 peaks for both the reference cell and DBR-only cell between λ=850-960 nm. The grating-only cell demonstrates a strong diffraction effect: there are more peaks (a total of 10) compared to the reference and DBR-only cell, the peak positions are different, and peak intensity does not decrease as λ increases. In the case of normal incidence, compared to a planar surface with just a perpendicular wave vector $k_{\perp} = \frac{\pi l}{t}$, the grating introduces a lateral component

$$k_{\parallel} = \frac{2\pi s}{\Lambda} \qquad (2.10)$$

to the wave vector, equal to a reciprocal lattice vector of the grating [2.21], where s is the diffraction order, and Λ is the grating period. Therefore,

$$k = \sqrt{(\frac{\pi l}{t})^2 + (\frac{2\pi s}{\Lambda})^2} \qquad (2.11).$$

Consequently, the wavelength of the diffracted mode is

$$\lambda = \frac{2\pi n}{k} = \frac{2\pi n}{\sqrt{(\frac{\pi l}{t})^2 + (\frac{2\pi s}{\Lambda})^2}} \qquad (2.12),$$

which is different from the peak positions in Eq. (2.9). The fact that the peak intensity of grating-only cell does not decrease as λ increases is because large angle diffraction elongates the path length, which compensates for the decreasing absorption coefficient as λ becomes longer.

In Fig. 2.24, the TPC cell exhibits the most interesting curve: it not only has many more peaks, but the peaks are much higher than those of the first three kinds of cells discussed. In the wavelength range depicted, the TPC cell demonstrates 10 major peaks,

slightly shifted from the 10 diffraction peaks of the grating-only cell; and 6 secondary peaks, corresponding to the 6 interference peaks of the DBR-only cell. Its absorption spectrum is an enhanced combination of DBR-only and grating-only cells as the major peaks are much stronger than those of the grating-only cell, and the secondary peaks are also much stronger than those of the DBR-only cell. The powerful combination of DBR and grating renders near 100% absorption at long wavelengths where the reference cell has very weak absorption. For instance, at λ=921 nm, the absorption of TPC cell is 95%, while the reference cell only has 10% absorption. The increased peak number and enhanced peak height render much bigger area under the curve, enabling strong cell efficiency enhancement.

II. Absorption spectra of 2 μm thick cells

It is beneficial to see how the absorption spectrum changes as cell thickness changes. Fig. 2.25 illustrates individual absorption spectrum of 2 μm thick cells with the same differing back structures. Fig. 2.26 shows the spectra in a combined figure. As can be seen, the individual spectrum looks like that of 5 μm thick cells, but the spectra start to differ at a shorter wavelength, 440 nm instead of 500 nm, as shorter wavelength photons can "see" the back structure due to reduced device layer thickness. More insights can be gained from the enlarged view in Fig. 2.27. Compared to 5 μm thick cells, there are many fewer peaks because peak spacing is inversely proportional to cell thickness. In the wavelength range between 850-950 nm, the reference cell has two interference peaks with decreasing height as λ increases, because of the reduced absorption coefficient. The DBR-only cell also has two peaks at the same locations, but with bigger peak height due

to the enhanced reflection. The grating-only cell shows four diffraction peaks, much higher, but narrower than those of the DBR-only cells. The TPC cell exhibits 4 major peaks similar to the diffraction peaks of the grating-only cell, but with stronger height; and 2 secondary peaks like those of the DBR-only and reference cells, again, at a bigger height. An interesting observation is that although the height of the secondary

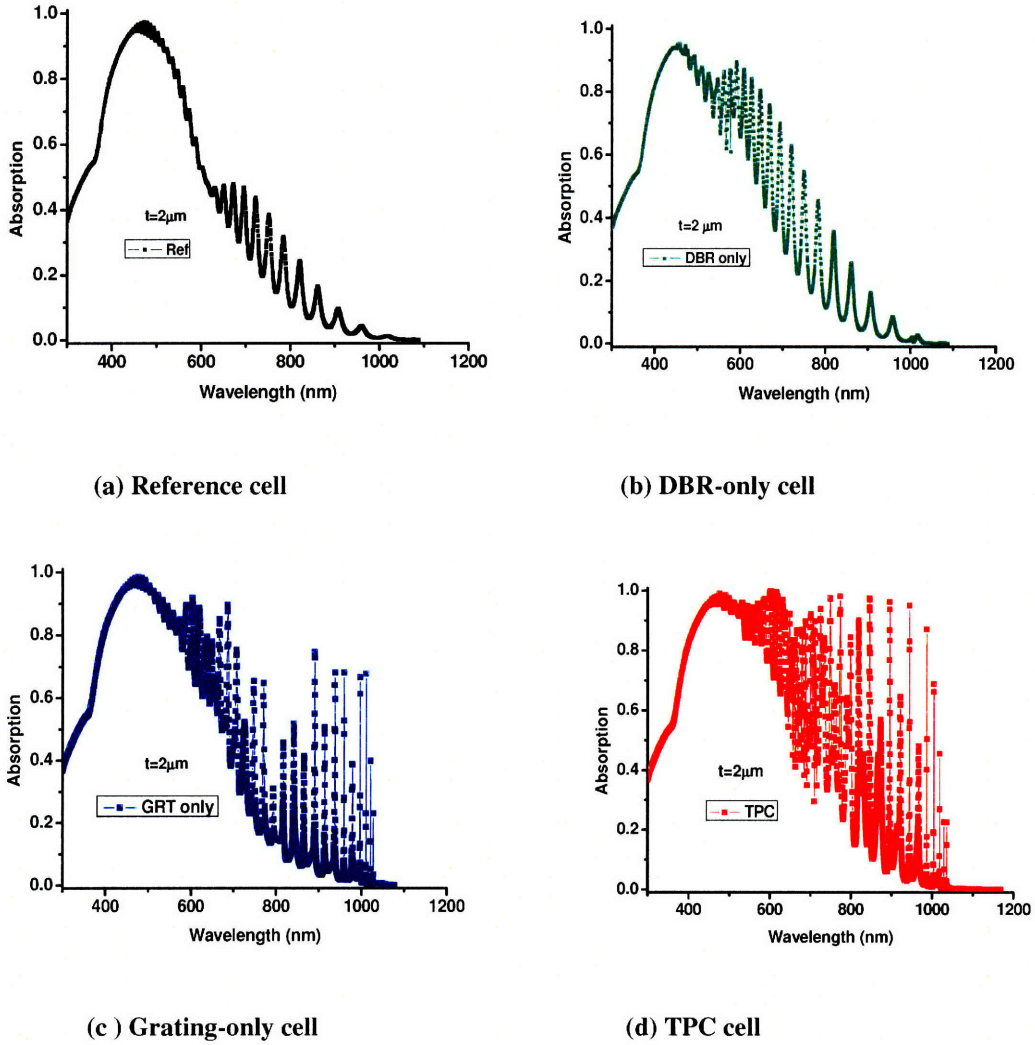

(a) Reference cell **(b) DBR-only cell**

(c) Grating-only cell **(d) TPC cell**

Fig. 2.25 Individual absorption spectrum of 2 μm thick cells with different back structures

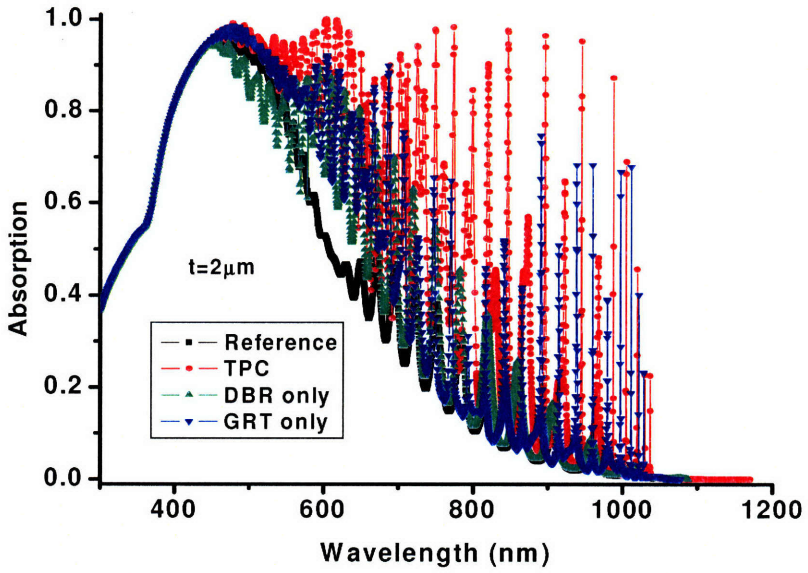

Fig. 2.26 Combined absorption spectra of 2 μm thick cells with different back structures

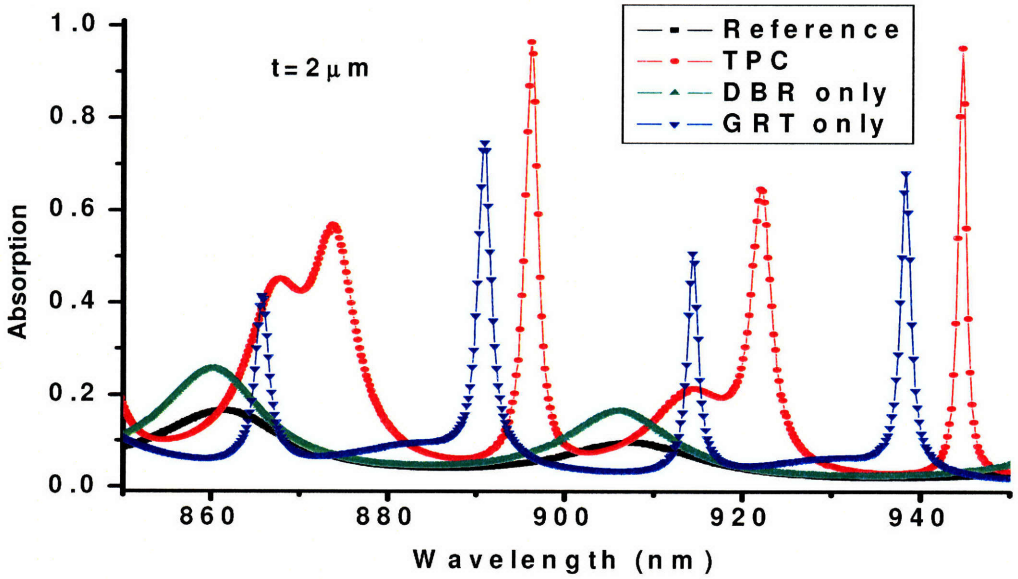

Fig. 2.27 Absorption Spectra between 850-950 nm of 2 μm thick cells with different back structures

interference peaks decreases with wavelength, the major diffraction peaks can be very high even at long wavelengths.

2.4.3 Effective path length enhancement

As mentioned in section 1.3.2 in Chapter 1, path length is not a valid concept for thin solar cells due to strong interference effect. However, to get an intuitive feel of how our back reflector compares to other light trapping schemes, it is helpful to define an effective path length L_{eff} for a certain wavelength λ based on absorption A. From

$$A(\lambda) = 1 - e^{-\alpha(\lambda)L} \qquad (2.13),$$

One can get

$$L_{eff}(\lambda) = \frac{\log_e(1 - A(\lambda))}{-\alpha(\lambda)} \qquad (2.14).$$

Comparing the L_{eff} of solar cells with the same thickness, but different back structures will provide an effective path length enhancement factor.

I. 5 μm thick cells

Fig. 2.28 illustrates the effective path length vs. wavelength for 5 μm thick cells with the different back structures. For λ<500 nm, the curves for cells with different back structures overlap, corresponding to their overlapping absorption spectra. In general, for the grating-only cell and the TPC cell, L_{eff} increases as λ increases, a desirable feature as longer wavelength light has smaller absorption coefficient and needs longer path length. The TPC cell reaches a maximum L_{eff} of 541.1 μm at λ=1035 nm, when the reference cell has an L_{eff}=3.7 μm. Fig. 2.29 is an enlarged view of Fig. 2.28 in the range of λ=850-960 nm. The curves look very similar to the absorption spectra depicted in Fig. 2.24,

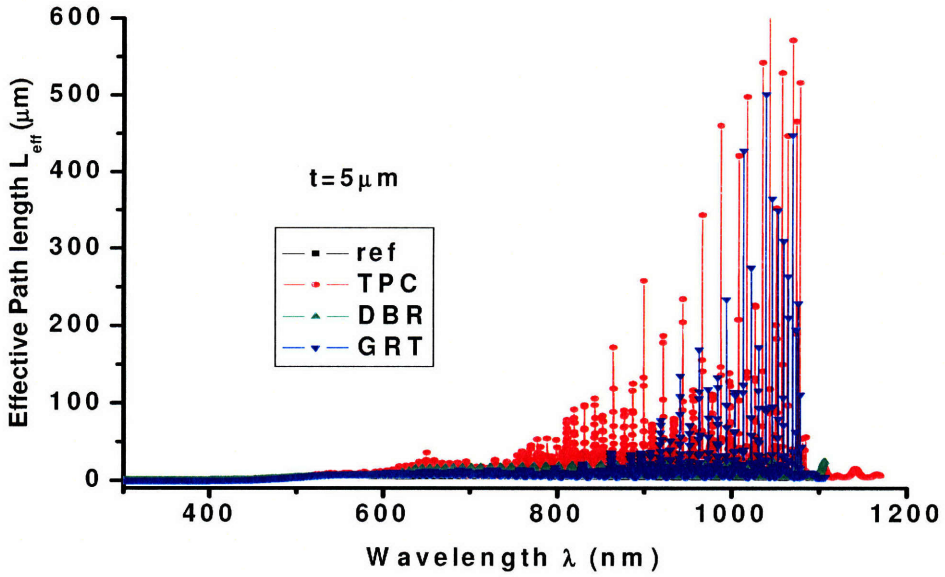

Fig. 2.28 Effective path length vs. wavelength for 5 μm thick cells with different back structures

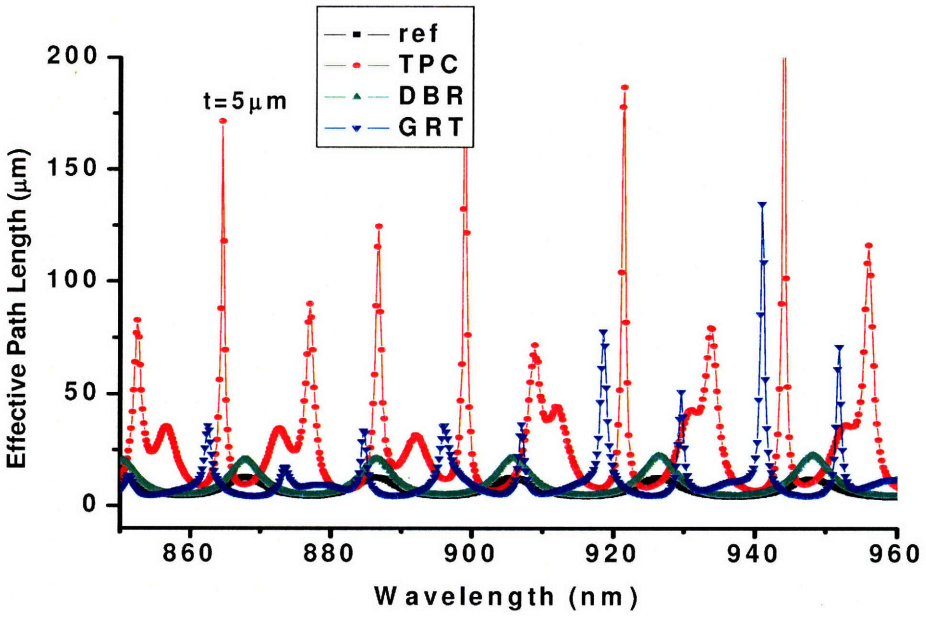

Fig. 2.29 Effective path length vs. wavelength for λ between 850-960 nm for 5 μm thick cells with different back structures

except that for the reference cell and the DBR-only cell, the peak height remains constant vs. wavelength, a verification that the decreasing peak strength vs. wavelength in Fig. 2.24 is indeed due to the decreasing absorption coefficient as λ increases. The peak height is at around 22.3 μm for the DBR-only cell and 12.6 for the reference cell.

Fig. 2.30 shows the effective path length enhancement factor vs. wavelength relative to the reference cell in the wavelength range of 890-1050 nm. The curves look like Fig. 2.29, with strong periodic peaks for grating and TPC cells. The TPC cell achieves a path length enhancement factor of 145 at λ=1035 nm. The advantage of TPC is clear: by using a wave optics approach with feature sizes comparable to wavelength, one can target the weakly absorbed long wavelength photons and enhance the path length by hundreds of times. In the simulation, the calculation was set to stop at a certain cutoff

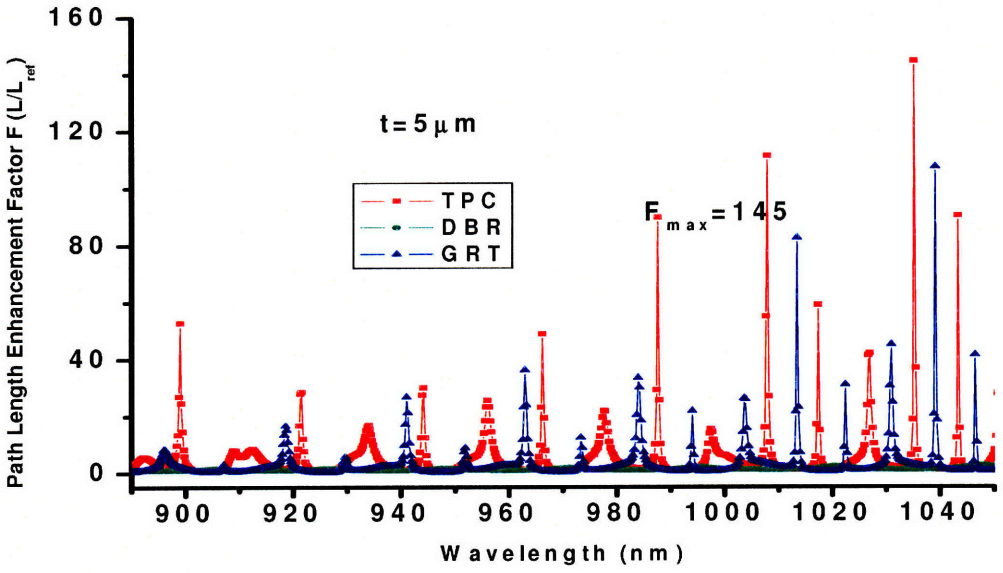

Fig. 2.30 Effective path length enhancement factor vs. wavelength for 5 μm thick cells with different back structures

wavelength where further calculation will make a contribution to the cell efficiency of less than 0.01% (absolute efficiency). From Fig. 2.23, we can see that while the calculation for TPC cell goes to 1170 nm, it stops at 1106 nm for the reference cell. If the calculation goes further for the reference cell, one can imagine that the path length enhancement would be very high, maybe way more than 1000 times because if a finite number (TPC cell path length) is divided by a number near zero (reference cell), the result can be infinitely large.

II. 2 μm thick cells

Figs. 2.31 and 2.32 depict the effective path length and path length enhancement factor for 2 μm thick cells with different back structures. Like 5 μm thick cells, generally

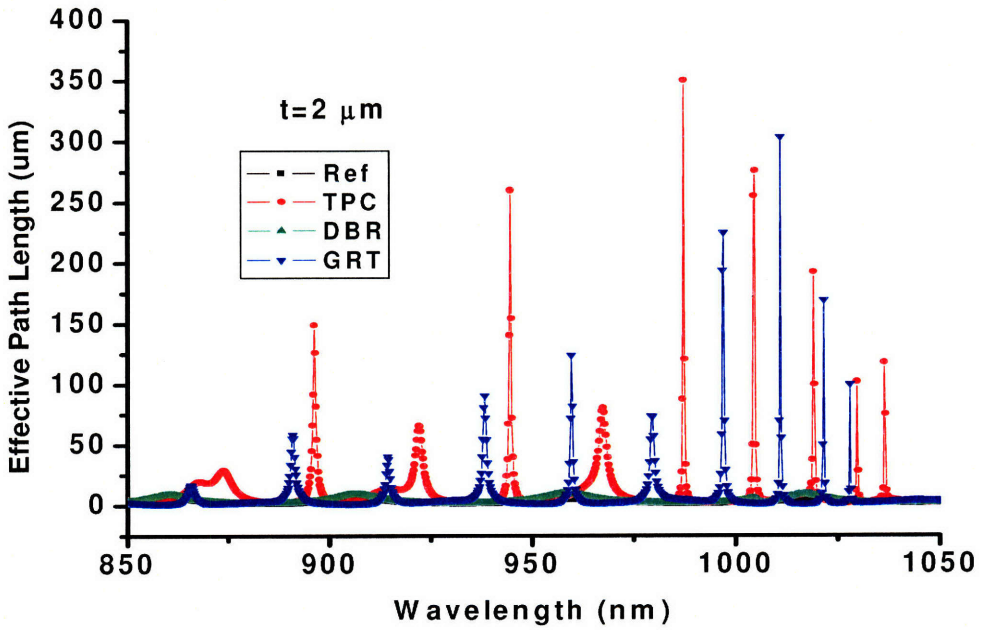

Fig. 2.31 Effective path length vs. wavelength for 2 μm thick cells with different back structures

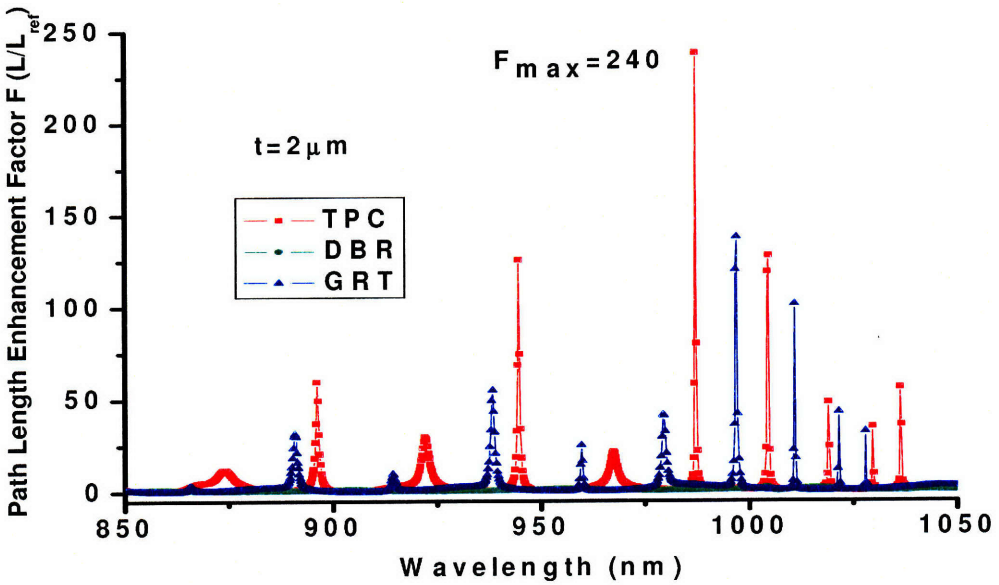

Fig. 2.32 Effective path length enhancement factor vs. wavelength for 2 μm thick cells with different back structures

speaking, more path length enhancement is achieved as λ increases, with a maximum path length enhancement factor of 240 realized at λ=987 nm.

2.4.4 Solar cell efficiency enhancement

In the previous section, we borrowed the concept of path length enhancement from ray optics. As evident from the figures there, different wavelengths get different path length enhancement. Shorter wavelength photons generally do not need much path length enhancement, and, each wavelength has different solar photon flux under AM1.5 spectrum. Therefore, a more meaningful benchmark in judging the effectiveness of a light trapping scheme for thin film cells would be solar cell efficiency, which considers the collective effect of photon absorption at all wavelengths above the bandgap wavelength. Table 2.2 lists cell efficiencies at 2 and 5 μm device layer thicknesses obtained from

scattering matrix simulation, with the structural parameters listed in Table 5.7. Also listed is the relative efficiency enhancement rendered by different back structures. For details on how the efficiency is calculated, please refer to Section 4.3.1 in Chapter 4.

Table 2.2 Calculated solar cell efficiency with different back structures

Cell thickness (μm)	**Reference cell efficiency η_{ref}**	**DBR-only cell**		**Grating-only cell**		**TPC cell**	
		Efficiency η (%)	$\frac{\eta-\eta_{ref}}{\eta_{ref}}$ (%)	Efficiency η (%)	$\frac{\eta-\eta_{ref}}{\eta_{ref}}$ (%)	Efficiency η (%)	$\frac{\eta-\eta_{ref}}{\eta_{ref}}$ (%)
2	10.56	12.13	14.9	12.83	21.5	15.55	47.3
5	14.93	16.48	10.4	16.34	9.4	19.33	29.5

Table 2.2 demonstrates that although both DBR and grating enhances cell efficiency significantly, when they are combined, the efficiency enhancement is much more than the sum of the efficiency enhancement provided by each of them. Also obvious is that thinner cell acquires more efficiency enhancement, due to the wider wavelength range where absorption can be enhanced. A 2 μm thick cell can obtain 47.3% efficiency enhancement when a textured photonic crystal back reflector is used.

It is noteworthy that using two-dimensional gratings in TPC instead of 1D gratings can increase cell efficiency further because light can be diffracted in two perpendicular directions, especially if the grating periods in the two directions are set such that the diffraction in x direction enhances absorption mainly in one certain wavelength range and the diffraction in y direction enhances absorption in another wavelength range, as confirmed by our recent publication [2.21].

References

[2.1] John D. Joannopoulos, Robert D. Meade, Joshua N. Winn, Photonic Crystals: Molding the Flow of Light, Princeton University Press, Princeton, 1995.

[2.2] Steven G. Johnson, J.D. Joannopoulos, Photonic Crystals: The Road from Theory to Practice, Kluwer Academic Publishers, Boston,/Dordrecht/London, 2002.

[2.3] Kazuaki Sakoda, Optical properties of photonic crystals, second edition, Springer, Berlin, 2005, Chap.1.

[2.4] K. Inoue, K. Ohtaka (Eds.), Photonic Crystals: Physics, Fabrication and Aplications, Springer, Berlin/Heidelberg/New York, 2004. .

[2.5] S. G. Johnson and J. D. Joannopoulos, "Introduction to Photonic Crystals: Bloch's Theorem, Band Diagrams, and Gaps (But No Defects)", MIT (2003), p. 5, available at http://ab-initio.mit.edu /photons/tutorial/photonic-intro.pdf.

[2.6] J. N. Winn, Y. Fink, S. Fan, and J. D. Joannopoulos, Opt. Lett., **23**, 1573 (1998).

[2.7] Y. Fink, J. N. Winn, S. Fan, C. Chen, J. Michel, J. D. Joannopoulos, and E. L.Thomas, Science 282, 1679 (1998).

[2.8] D. N. Chigrin, A. V. Lavrinenko, D. A. Yarotsky, and S. V. Gaponenko, Appl. Phys.A, 68, 25 (1999).

[2.9] A. Yariv, P. Yeh, Optical Waves in Crystals, Wiley, New York, 1984, Chap. 6.

[2.10] L. Zeng, Y. Yi, C. Hong, X. Duan and L. C. Kimerling, Mater. Res. Soc. Symp. Proc., **862**, 381(2005).

[2.11] L. Zeng, Y. Yi, C. Hong, B. A. Alamariu, J. Liu, N. Feng, X. Duan, and L. C. Kimerling, Appl Phys. Lett., **89,** 111111 (2006).

[2.12] C. W. Wilmsen, H. Temkin, and L. A. Coldren (Eds.) Vertical-Cavity Surface-Emitting Lasers: Design, Fabrication, Characterization, and Applications, Cambridge University Press, Cambridge, 1999, p. 72.

[2.13]J. Nelson, The Physics of Solar Cells, Imperial College Press, London, 2003, pp. 22 and 264.

[2.14] M.C. Hutley, Diffraction Gratings, Academic Press Inc., London, 1982.

[2.15] Erwin G. Loewen, Evgeny Popov, Diffraction gratings and Applications, Marcel Dekker, Inc.,New York, Basel, Hong Kong, 1997, Chapter 2.

[2.16] Erwin G. Loewen, Evgeny Popov, Diffraction gratings and Applications, Marcel Dekker, Inc.,New York, Basel, Hong Kong, 1997, p. 72.

[2.17] Erwin G. Loewen, Evgeny Popov, Diffraction gratings and Applications, Marcel Dekker, Inc.,New York, Basel, Hong Kong, 1997, p. 60.

[2.18] S. R. J. Brueck, Proceedings of the IEEE, Vol. 93, NO. 10, October 2005, pp. 1704-1721.

[2.19] L. Jay Guo, in Quantum Dots, Nanoparticles, and Nanoclusters II, edited by Diana L. Huffaker, Pallab K. Bhattacharya, Proceedings of SPIE, Vol. **5734** (SPIE, Bellingham, WA, 2005), p.53.

[2.20] Michael D. Stewart and C. Grant Willson, MRS Bulletin, Vol. **30**, December 2005, p. 947.

[2.21]Peter Bermel, Chiyan Luo, Lirong Zeng, Lionel C. Kimerling, and John D. Joannopoulos, Optics Express, Vol. 15, No. 25, 16986 (2007).

CHAPTER 3

Thick Crystalline Si Solar Cells Integrated with Textured Photonic Crystal Backside Reflectors

In Chapter 2, we introduced the light trapping principle of textured photonic crystal (TPC) composed of a diffraction grating and distributed Bragg reflector. We have seen that both the grating and DBR have strong light trapping capabilities individually. And together, they work even more potently. Whether in reality this is true needs experimental verification. To prove the concept, we fabricated thick crystalline Si solar cells integrated with TPC, and the resulting efficiency enhancement is promising. This chapter will present this work.

3.1 Thick crystalline Si solar cell design

3.1.1 Materials selection

In order to eliminate materials quality issues and make the optical effects from the back reflector prominent, we choose crystalline Si wafers as our starting material. They are (100) oriented, double-side polished, with diameter 6 inch. The dopant is boron, because p-type doping means minority carriers are electrons, and their much higher mobility compared to holes translates to longer diffusion length according to the Einstein relation

$$\frac{D}{\mu} = \frac{kT}{q} \qquad (3.1),$$

where D is the diffusion constant. The diffusion length is determined by

$$L_D = \sqrt{D\tau} \qquad (3.2),$$

where τ is the minority carrier lifetime.

In terms of substrate doping density, since heavy substrate doping will increase free carrier absorption and minority carrier recombination, and too light doping will increase series resistance significantly, we choose a substrate resistivity of 1.5 Ohm-cm, corresponding to a doping level ~$1x10^{16}/cm^3$. Wafer thickness is 675 μm, the most commonly available.

3.1.2 Antireflection coating and back reflector design

The antireflection coating (ARC) and back reflector are the key light managing components in a solar cell. Thermal oxide will be used as ARC material due to its excellent surface passivation property. The thickness d is determined to be 110 nm,

targeting a reflection minimum wavelength of $\lambda c=4n_{SiO2}d=640$ nm where the solar spectrum has strong intensity.

Four types of back reflectors will be implemented:

a. grating only;

b. DBR only;

c. grating plus DBR;

d. no back reflector for reference.

For grating a., there are three parameters to determine: period, etch depth, and duty cycle, which is the ratio of the plateau width of a grating over the period. Our desired grating period is $\lambda_g/n_{Si}\approx 314$ nm, where λ_g is the bandgap of Si. Etch depth will be $\lambda/4n_{Si}$ such that normally incident light can be strongly bent by 47°(at λ=800 nm) to 90° (at $\lambda=\lambda_g$), which far exceeds the critical angle of total internal reflection of Si (16.6°). However, due to the limited resolution of the lithography system available in MIT cleanroom (0.5 μm, equivalent to a minimum grating period of 1 μm), a grating period of 1.1 μm will be used, with a duty cycle at 0.5.

Two types of DBR will be used: Si/Si_3N_4 (n_1/n_2=3.5/2) and Si/SiO_2 (3.5/1.46). A Bragg wavelength of 1000 nm is adopted, which means a layer thickness of 71nm for Si, 125 nm for Si_3N_4, and 171 nm for SiO_2. 8 bilayers (16 layers in total) will be used for each kind of DBR.

3.1.3 Top-contacted lateral p-i-n junction design

Given that DBR is a dielectric stack and not conducting, using traditional solar cell top and bottom contacting scheme would be difficult in our situation. To tackle this

problem, lateral p-i-n junctions will be employed, with interdigitated top contacts. Each doped region width will be 10 μm wide, and the distance between adjacent doped regions is 40 μm. Cell size varies from 1 mm^2 to 36 mm^2.

The contact metal will be 1 μm thick Al-2%Si, with finger width 6 μm, corresponding to a shadowing of 15.3%, including bus lines and contact pads.

3.2 Solar cell fabrication

Fig. 3.1 shows the process flow for wafers with both grating and DBR on the back. The starting material is 675 μm thick double-side polished Si wafers. There are 6 photolithography steps. Major steps include:

(1) thermal oxidation (wet) for antireflection coating and surface passivation;

(2) alignment marks formation by patterning and etching into the thermal oxide;

(3) ion beam implantations to form lateral p-i-n junctions;

Wafers were first patterned with p-implantation mask and sent out to a commercial vendor for boron implantation with the following specification: energy 50 KeV, dose $2x10^{15}/cm^2$, 7 degree tilt. After stripping of the photoresist and piranha clean, they were patterned with n-type implantation mask and sent out again for phosphor implantation with the following specification: 100 KeV, $7x10^{15}/cm^2$, 7 degree tilt. Then the wafers were annealed at 1000°C for 30 minutes to activate the dopants. Given the substrate doping level, this will render a junction depth of 0.8-1 μm.

(4) grating formation;

Then the wafers were flipped, and grating was patterned and etched into Si on the

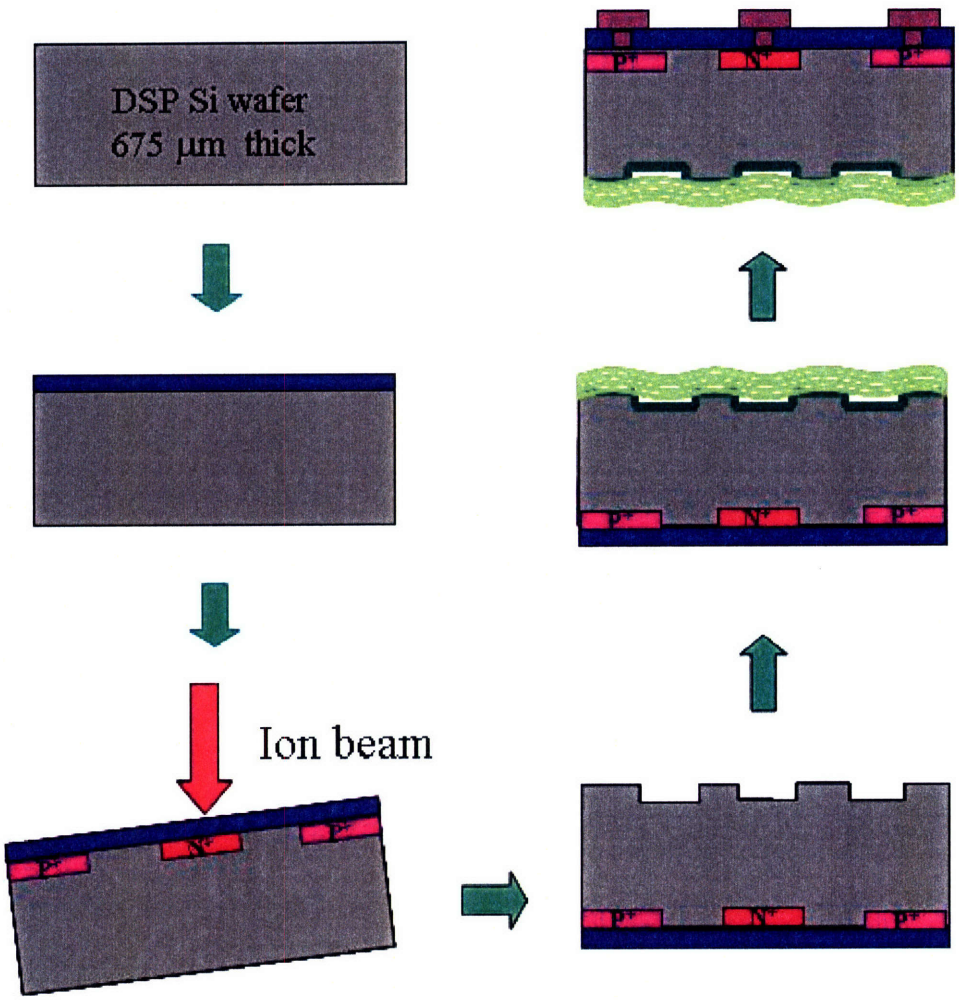

Fig. 3.1 Process flow of thick crystalline Si solar cells

backside of the wafers using reactive ion etching.

(5) DBR deposition;

8 pairs of Si/SiO_2 or Si/Si_3N_4 DBR were deposited using plasma enhanced chemical vapor deposition (PECVD).

(6) contact window opening;

The wafers were then flipped again for front side processing. By patterning and etching the oxide with BOE (buffered oxide etch), contact window was opened in the AR coating oxide.

(7) Metal deposition and etching.

As the last step, 1 μm thick Al-2% Si was sputtered, patterned and etched using RIE to form metal lines and contact pads.

For wafers with grating or DBR only, step (5) or (4) was omitted; for those without back structure, both steps were omitted.

3.3 Solar cell characterization [3.1]

3.3.1 Imaging

Fig. 3.2 shows the optical top view of the solar cells. The thick horizontal lines are bus lines, and the vertical thin lines are metal fingers. Since the focus of the work in this chapter is the back reflector, imaging the back reflector is important. Fig. 3.3 is a cross sectional TEM (XTEM) image of a Si/SiO_2 DBR stack on the backside of a solar cell, showing uniform deposition of the layers. Fig. 3.4 shows the XTEM image of a back structure combining DBR and grating. The bottom black part is Si grating. The grating looks quite ideal with good sidewall and surface. The DBR over Si grating exhibits a very uniform layer stack of Si and SiO_2 with smooth interfaces between the layers. The DBR looks very flat over the valley Si and becomes wavy above the plateau, just nicely following the Si grating.

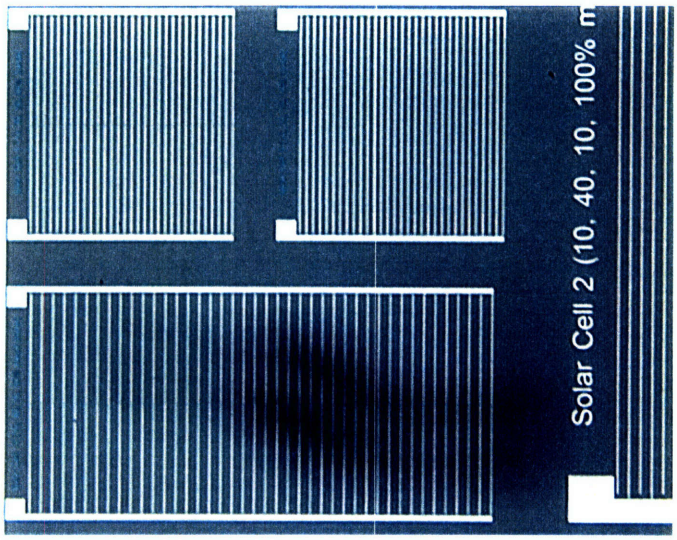

Fig. 3.2 Optical top view of solar cells in different sizes

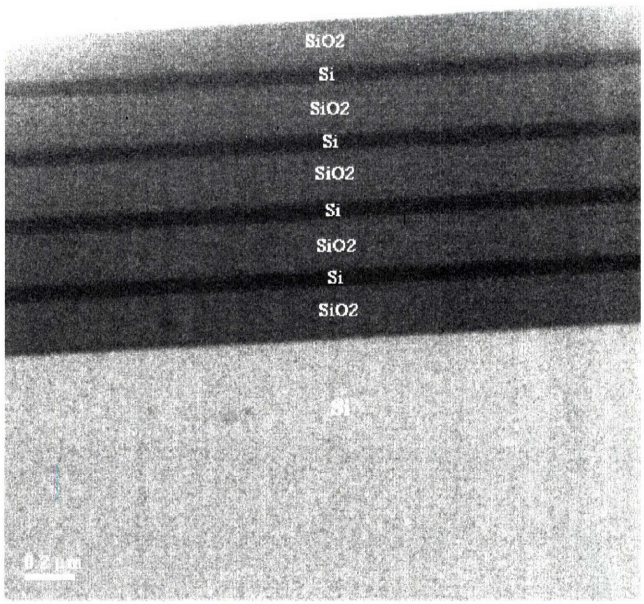

Fig. 3.3 cross sectional TEM image of a Si/SiO_2 DBR stack

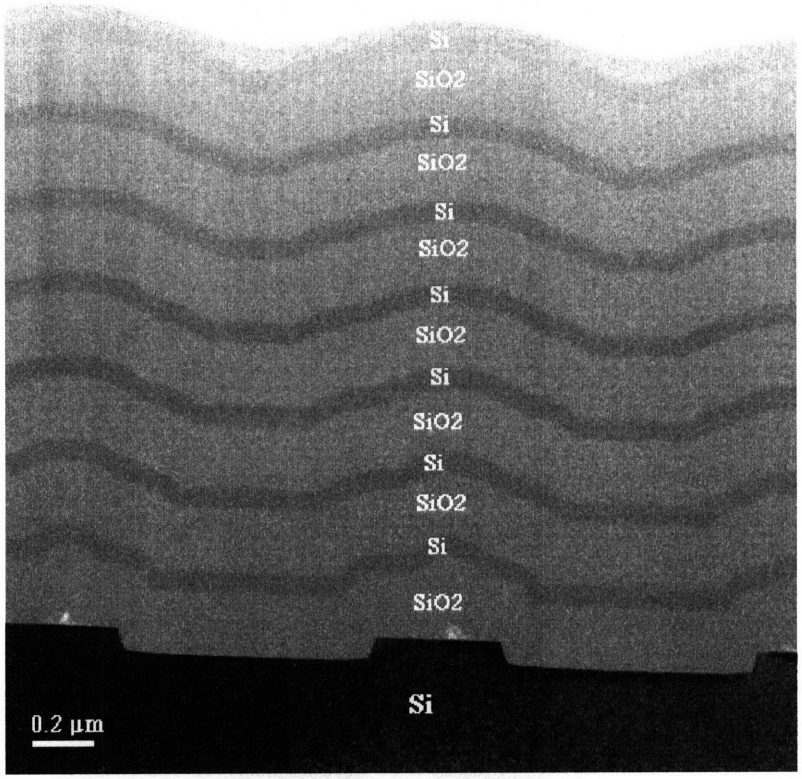

Fig. 3.4 Cross sectional TEM image of a grating with Si/SiO_2 DBR stack

3.3.2 Dark I-V measurements

The solar cells showed good rectifying behavior in the dark. They display reverse bias current of tens of nano amps or less under -2V bias, and have a breakdown voltage of over 50 Volts. The forward bias current usually exceeds 100 mA at 1V bias. As an example, Fig. 3.5 illustrates the dark I-V curve of a solar cell (36 mm^2) with Si/SiO_2 DBR plus grating. The reverse bias current at -2 V is 34.6 nA, corresponding to a current

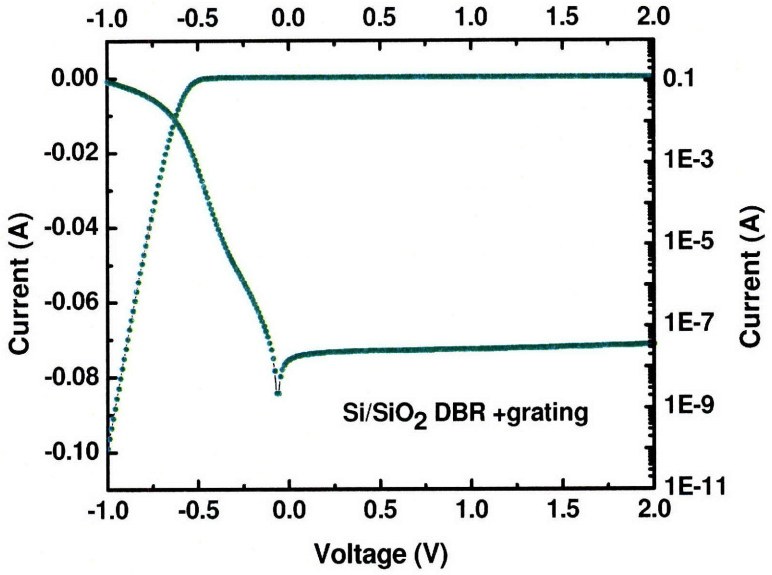

Fig. 3.5 Dark I-V curve of a solar cell with both Si/SiO_2 DBR and grating

density of $9.6x10^{-8}$ A/cm^2 if we divide the current directly by the cell area (note that our cells have top contacts).

3.3.3 External quantum efficiency measurements [3.2]

External quantum efficiency (EQE) was measured using a Hewlett-Packard 4145A semiconductor analyzer, with the light source being a halogen lamp coupled to an H20 IR Jobin Yvon monochromator.

In the wavelength range between 300-1000 nm, there is no obvious difference between the EQE curves of wafers with different back structures. However, starting at λ=1000 nm, wafers with different back structures exhibit appreciable difference, as shown in Fig. 3.6. All the back reflectors enhance absorption, with Si_3N_4/Si DBR plus grating offers the most enhancement. To make comparing easier, the EQE enhancement

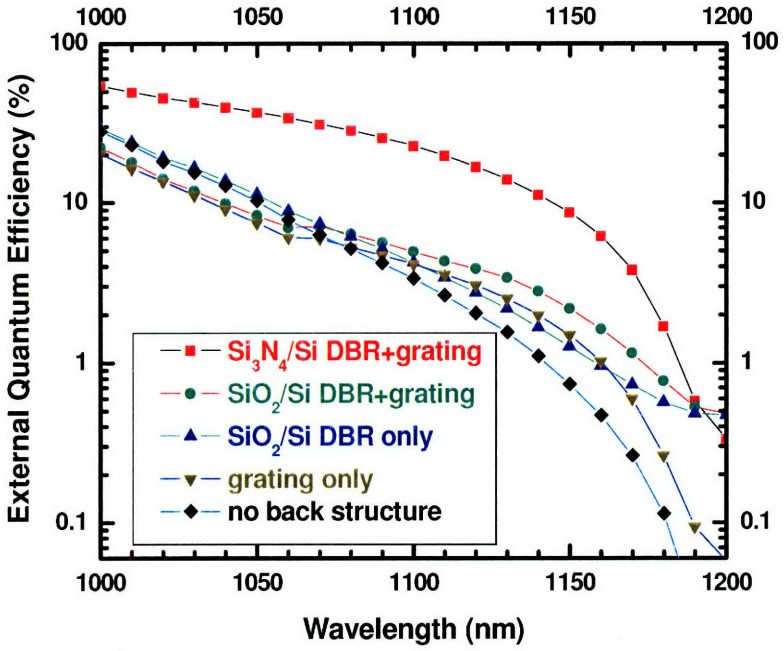

Fig. 3.6 External quantum efficiency of wafers with different back structures for λ>1000 nm

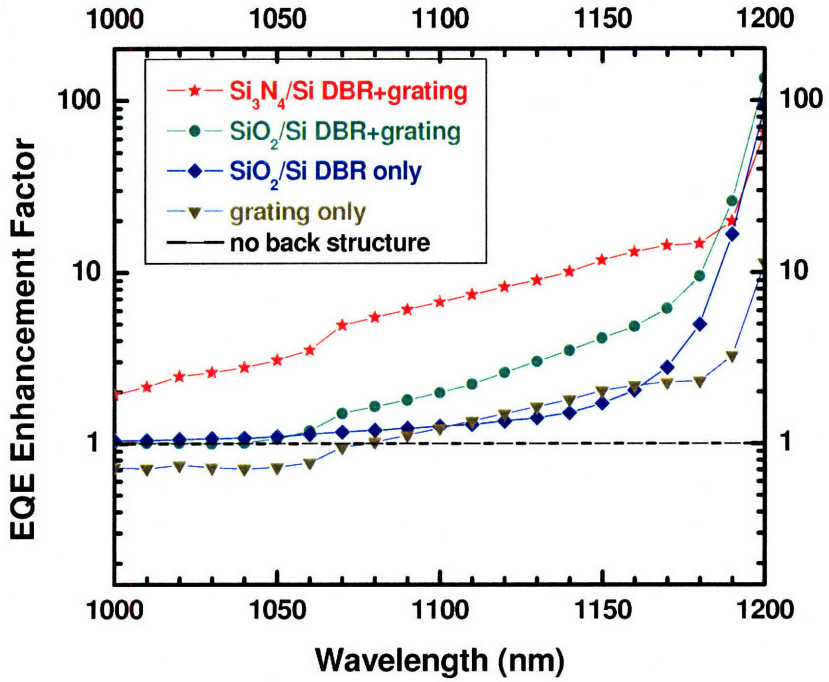

Fig. 3.7 EQE enhancement factor of wafers with different back structures for λ>1000 nm

factor for the various cells is calculated and depicted in Fig. 3.7. The flat black line at the bottom represents the reference cell. The EQE enhancement is obvious. The enhancement factor (EF) increases as λ increases, as it should, because light trapping is more effective for longer λ. The highest EF reaches 135 time by Si_3N_4/Si DBR plus grating at λ=1200 nm. Interestingly, for λ<1070 nm, the "grating only" cell has a lower EQE than the reference cell without back structure. This should be due to the surface damage caused by dangling bonds created during dry etching of the grating, which increased the surface recombination velocity. For λ>1070 nm, the EQE enhancement due to the light trapping by the grating dominates the surface recombination effect, and EF monotonically increases and reaches 11.4 times at 1200 nm. In order to fully utilize the path length enhancement capability of the grating, better back surface passivation is needed to counteract the side effect caused by grating etching.

3.3.4 I-V measurements under sun simulator

Solar cell power conversion efficiency was measured using the sun simulator in Evergreen Solar, Inc. under AM1.5 conditions. Fig. 3.8 displays the J-V curves of cells with different back structures. Note that due to our lateral p-i-n junction configuration, the current density is converted to current per illuminated area, which is more meaningful. It can be seen that all back reflectors increase cell efficiency appreciably. Although they all have similar Voc of ~620 mV and a fill factor of around 77%, cells with back structures show higher Jsc than do the cells without back structures. The cell with Si_3N_4/Si DBR plus grating has the highest Jsc of 27.5 mA/cm^2, compared to the reference cell which has a Jsc of 23.3 mA/cm^2. This corresponds to an overall efficiency increase

from 11.1% to 13.2%, meaning a relative increase ($\Delta\eta/\eta$) of 19%. The absolute efficiency increase ($\Delta\eta$) is 2.1%.

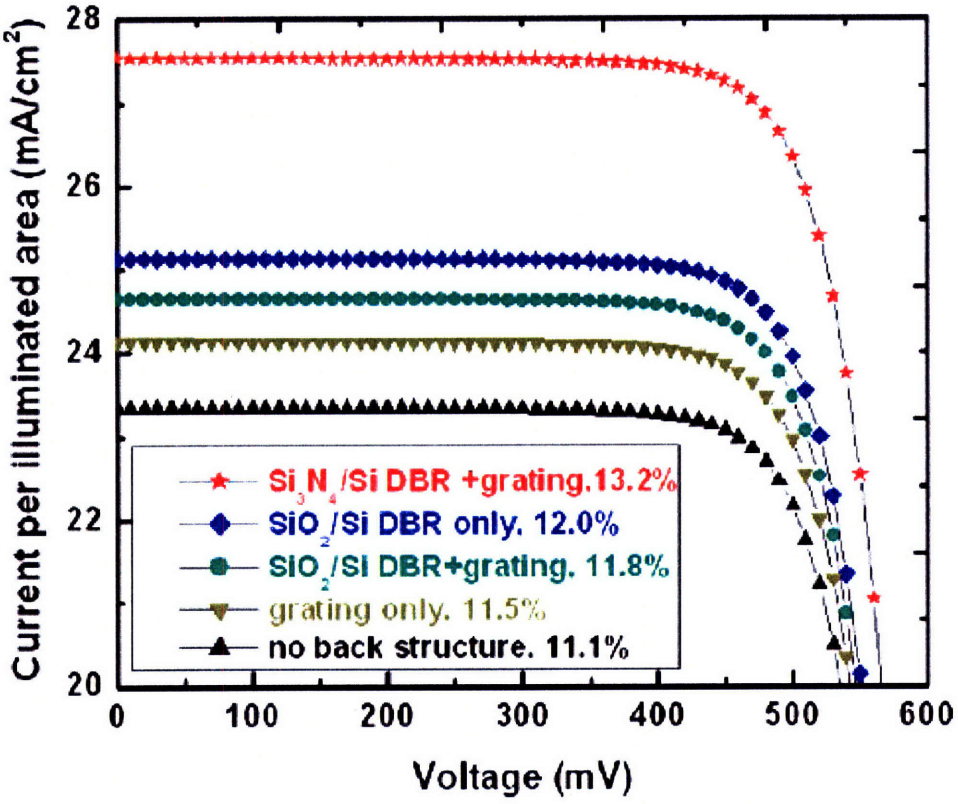

Fig. 3.8 J-V curves of solar cells with different back structures under the sun simulator

Note that the huge cell thickness (675 μm) severely limited the absolute efficiency, and affected $\Delta\eta$ as well. Photoconductance decay measured a bulk minority carrier life time of only 18 μ seconds, corresponding to a diffusion length of 230 μm at the base doping level. This is especially severe in our case because our cells have both n and p contacts at the top surface, so the influence from short diffusion length is especially serious. Most of the carriers generated within the bottom 2/3 thickness of the cell will recombine before they can reach the top contacts. The thick cell also limited the EQE

enhancement wavelength to a narrow window beyond 1000 nm. Nevertheless, our results have shown that despite of the thick wafer and relatively short diffusion length, significant efficiency enhancement has been achieved by integrating the textured photonic crystal backside reflector to the cell. More efficiency enhancement can be achieved for thinner cells and by using finer grating period.

References

[3.1] L. Zeng, Y. Yi, C. Hong, B. A. Alamariu, J. Liu, X. Duan, and L. C. Kimerling, Mater. Res. Soc. Symp. Proc. Vol 891, EE06-06, 2006.
[3.2] L. Zeng, Y. Yi, C. Hong, B. A. Alamariu, J. Liu, N. Feng, X. Duan, and L. C. Kimerling, Appl Phys. Lett., 89, 111111 (2006).

CHAPTER 4

Design Optimization of Textured Photonic Crystal Backside Reflector for Crystalline Thin Film Si Solar Cells

In chapter 3, we presented the design, fabrication and characterization of thick Si solar cells integrated with textured photonic crystal (TPC) back reflector for proof of concept. In this chapter, we will consider applying TPC to thin film Si solar cells, which is its intended application. The back reflector design will be systematically optimized for crystalline thin film Si solar cells through simulation. We will do simulation first using coupled wave theory, and secondly using scattering matrix method. Then the results from these two methods will be compared.

4.1 The necessity of design optimization in thin film Si solar cells

For thin film solar cells, the design we used earlier for thick cells needs to be modified in order to achieve high efficiency. There are two major reasons, which can be understood by the aid of Fig. 4.1.

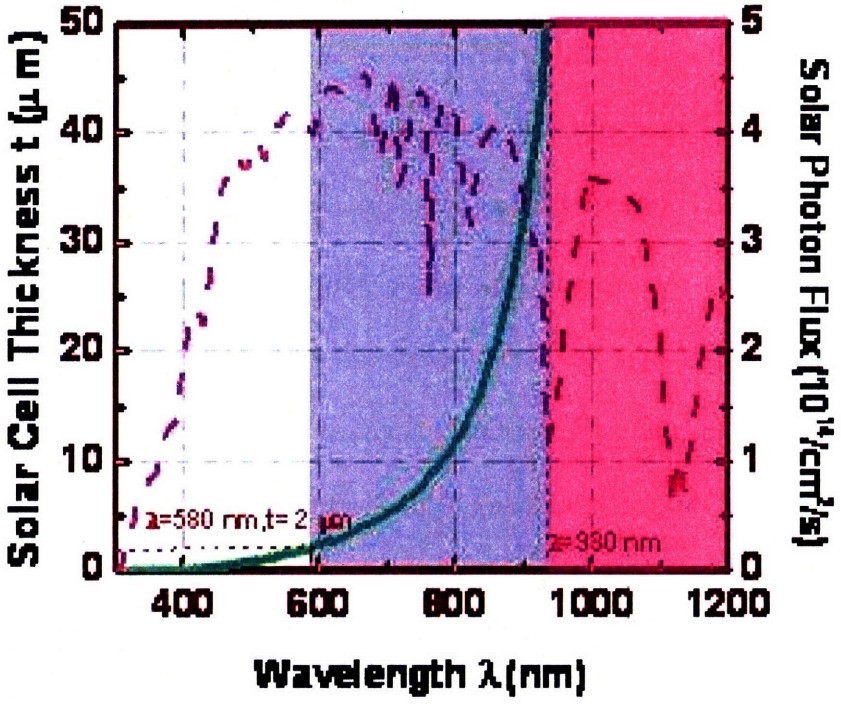

Fig. 4.1 Solar spectrum and solar cell thickness vs. absorption cutoff wavelength

The following equation expresses the short circuit current density

$$J_{sc} = \int_{\lambda_1}^{\lambda_2} qA(\lambda)s(\lambda) \qquad (4.1),$$

where q is the electron charge, A(λ) is the absorption at a certain wavelength, and s(λ) is the incident solar photon flux at that wavelength. J_{sc} is an integration of absorption

weighted by $s(\lambda)$ over a wide spectral range, and as seen in Fig. 4.1 by the dashed purple curve, $s(\lambda)$ varies significantly with respect to wavelength. So the first reason thin cells' TCP needs modifying to achieve high solar cell efficiency is we not only need strong absorption, but also need to strategically place the strong absorption points in areas of high solar flux. This optimization necessitates simulation.

The second reason we have to modify the TCP is that when thin film solar cell thickness decreases, the spectral range needing light trapping increases. The green curve in Fig. 4.1 indicates the relation between solar cell thickness and absorption cutoff wavelength. For a 50 μm thick cell, its thickness corresponds to the absorption length of 980 nm light, meaning that the pink shaded region needs light trapping. While for a 2 μm thick cell, the cutoff wavelength decreases to 580 nm, therefore, both the gray and pink region need light trapping. We expect there will be different optimizations of the back reflector design depending on the cell thickness, with thinner cells having a broader spectrum needing to be accommodated by the back reflector.

Furthermore, an important question that is remaining is: what is the maximum efficiency gain that this new back reflector, the textured photonic crystal, can give us? Again, this requires design optimization by simulation.

4.2 Coupled Wave Theory

4.2.1. General simulation approach with coupled wave theory

Coupled wave theory is a good tool for grating calculations [4.1-4.3]. Assuming the incident sun light as a plane wave, the reflection at the top surface of the solar cell and the transmission at the bottom surface of the cell can be calculated by Rigorous

Coupled Wave Analysis (RCWA). Due to the periodicity of the grating, both the fields and refractive index in each layer of the solar cell structure can be expanded to Fourier series in terms of grating period [4.4]. To simplify the calculation, we chose the coordinate system as shown in Fig. 4.2.

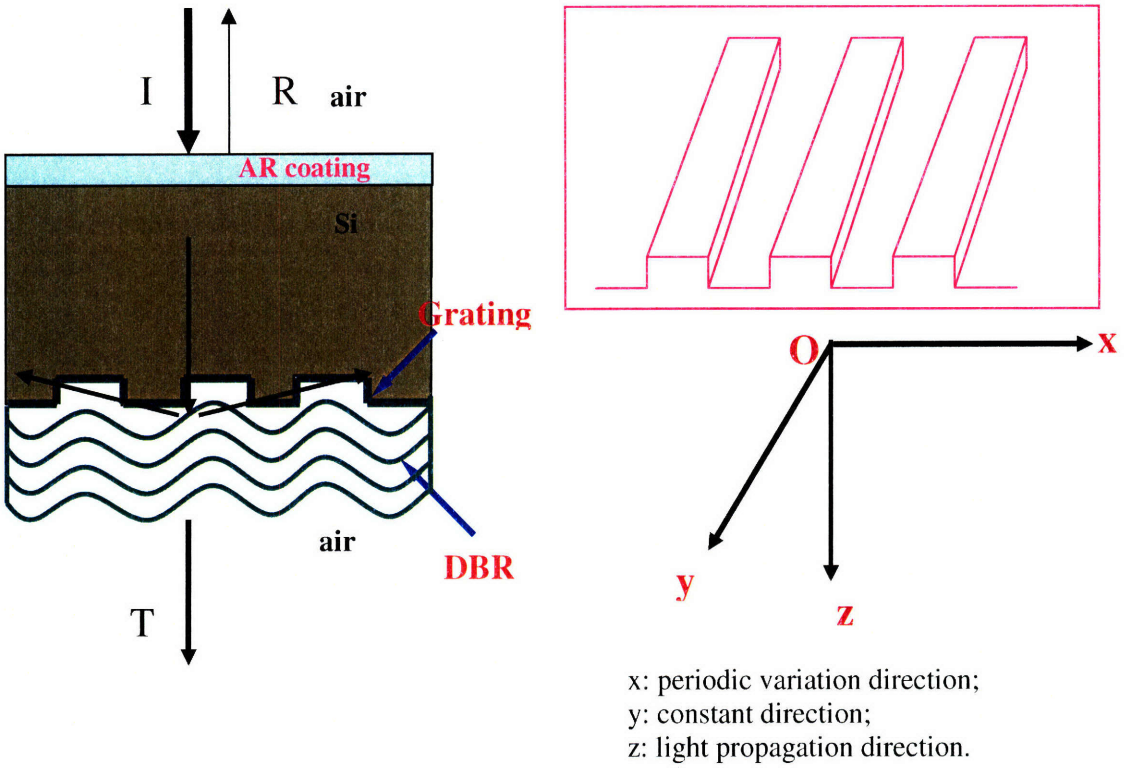

Fig. 4.2 The choice of coordinate system in coupled wave theory simulation. Left figure: schematic of solar cell; right figure: grating with coordinate system based on it.

The calculation starts with the three-dimensional Hemholtz equation

$$(\nabla^2 + k^2)\vec{E} = 0 \qquad (4.2).$$

Since $\vec{E}$ is constant in the y direction, Eq. (4.2) becomes a 2D partial differential equation

$$(\frac{\partial^2}{\partial x^2} + \frac{\partial^2}{\partial z^2} + n^2 k_0^2)E = 0 \qquad (4.3).$$

Assuming TE mode, solve for $E_x(x,y,z)$

$$(\frac{\partial^2}{\partial x^2}+\frac{\partial^2}{\partial z^2}+n^2k_0^2)E_x=0 \qquad (4.4).$$

Next expand E_x and n into Fourier series in terms of grating period p

$$E_x=\sum_{m=-\infty}^{+\infty}E_m e^{jk_{xm}x}=\sum_{-\infty}^{+\infty}E_m e^{j\frac{2\pi}{p}mx} \qquad (4.5),$$

$$n^2=\sum_{l=-\infty}^{+\infty}n_l^2 e^{j\frac{2\pi}{p}lx} \qquad (4.6).$$

Substituting Eqs. (4.5) and (4.6) into Eq. (4.4) renders a 1D ordinary differential equation

$$-(m\frac{2\pi}{p})^2E_m+\frac{d^2}{dz^2}E_m+n_l^2k_0^2\otimes E_m=0 \qquad (4.7)$$

for each order of k_x, with m$\in(-\infty, +\infty)$.

Eq. (4.7) can be rewritten as

$$\frac{d^2}{dz^2}E_m+[n_l^2k_0^2\otimes E_m-(m\frac{2\pi}{p})^2E_m]=0 \qquad (4.8).$$

Let $$\frac{d^2}{dz^2}E_m=-C_uE_m \qquad (4.9)$$

with solution $$E_m=E_0e^{\pm\sqrt{C_u}z}=A_{mu}e^{-\sqrt{C_u}z}+B_{mu}e^{\sqrt{C_u}z} \qquad (4.10),$$

where C_u is unique for each layer, with u being the layer label.

Plugging Eq. (4.10) into Eq. (4.5) leads to

$$\begin{aligned}E_{xu}&=\sum_{m=-\infty}^{+\infty}E_m e^{jk_xx}=\sum_{m=-\infty}^{+\infty}(A_{mu}e^{-\sqrt{C_u}z}+B_{mu}e^{\sqrt{C_u}z})e^{j\frac{2\pi}{p}mx}\\&\approx\sum_{m=-M}^{+M}(A_{mu}e^{-\sqrt{C_u}z}+B_{mu}e^{\sqrt{C_u}z})e^{j\frac{2\pi}{p}mx}\end{aligned} \qquad (4.11),$$

where M is the truncation number.

The next step is to match boundary conditions. First, the tangential component of $\vec{E}$ field is continuous at each interface between two layers,

$$E_{xu} = E_{x(u+1)} \qquad (4.12).$$

Second, since the incident field is known and there is no reverse propagation field in the exit medium (the last layer of our structure), for the 1st layer, A_{m1}'s are known, and for the last layer, B_{mN}'s=0. Matching the boundary conditions will result in a matrix equation, and the field components can be obtained by solving the equations [4.1], [4.2]. We can in turn obtain reflection R and transmission T. The absorption A at a certain wavelength is simply

$$A(\lambda)=1-R(\lambda)-T(\lambda) \qquad (4.13).$$

However, for multilayered structures, the field matching becomes very complicated. We resort to coupled modal transmission lines (MTLs) to simplify this issue. It transforms the layered structure into a series of coupled modal transmission lines, associates the eigenvalues of the coefficient matrix with the propagation constants and characteristic impedances [4.3], and expresses the fields in terms of the voltages and currents of the MTLs. The reflection and transmission at the top and bottom surfaces can be calculated accordingly. Eq. (4.13) gives the absorption at a certain wavelength.

Solar cell efficiency can be calculated from

$$\eta = \frac{J_{sc} V_{oc} FF}{P_{in}} \qquad (4.14),$$

where J_{sc} is the short circuit current density, V_{oc} is the open circuit voltage, FF is the fill factor, and P_{in} is the incident solar power density, which equals 0.1 W/cm^2 under AM1.5 solar spectrum [4.6]. J_{sc} is determined by light absorption and carrier collection

$$J_{sc} = \int_{\lambda_1}^{\lambda_2} qA(\lambda)s(\lambda)\eta_c \qquad (4.15),$$

where $q=1.60\times10^{-19}$ C is the electron charge; $A(\lambda)$ is the absorption at a particular wavelength acquired from Eq. (4.13); $s(\lambda)$ is the incident solar photon flux in units of $cm^{-2}s^{-1}$; η_c is a phenomenological factor representing carrier collection efficiency mainly affected by surface recombination and solar cell material quality. Our previous measurements on crystalline Si solar cells show that an average η_c of > 90% can be realized. Here, we assume a relatively conservative η_c of 85%. The integration is taken from λ_1=300 nm to λ_2=1200 nm.

Voc can be obtained from

$$V_{oc} = \frac{kT}{q}\ln(\frac{J_{sc}}{J_{s0}}+1) \qquad (4.16),$$

where k is the Boltzmann's constant, T = 300 K, q is electron charge, and J_{s0} is the diode reverse bias saturation current. According to [4.6], the smallest J_{s0} for Si at 300 K is around 1×10^{-15} A/cm^2. Here, we take $J_{s0}=1.5 \times 10^{-15}$ A/cm^2. Regarding fill factor, choosing the load appropriately can render a reasonable FF= 80% [4.6]. In addition, a 5% shadowing from the electrodes is assumed in our calculation.

Fig. 4.3 is a more abstract schematic showing the simulated solar cell structure, labeling the thickness and refractive index of each layer. It consists of an antireflection coating with index n_{AR} and thickness t_{AR}; an active silicon layer with index n_c and thickness t_c; and a back reflector combining a diffraction grating and a DBR stack. The grating has period p, plateau width w, and etch depth t_g. The DBR stack is composed of 8 pairs of SiO_2 (n_l=1.46 and $t_l= \lambda_B/4n_l$) and Si (n_h=3.5 and $t_h= \lambda_B/4n_h$) double layers with λ_B

being the Bragg wavelength of the DBR. As shown in Fig. 3.4, if the grating is formed before DBR deposition, the layers will be wavy, which is very hard to simulate. To simplify the calculation, grating valleys are filled with SiO_2, which has a flat surface and an extra thickness $t_b=t_l$ above the grating. The refractive index of this buffer layer is set to be n_b = 1.46. The active silicon layer has the real part of its refractive index set as 3.5, and its absorption coefficient is obtained from Reference [4.5]. The structural parameters to be optimized in the following sections include AR coating index and thickness, grating period p, etch depth t_g, and duty cycle F=w/p, and DBR central wavelength λ_B.

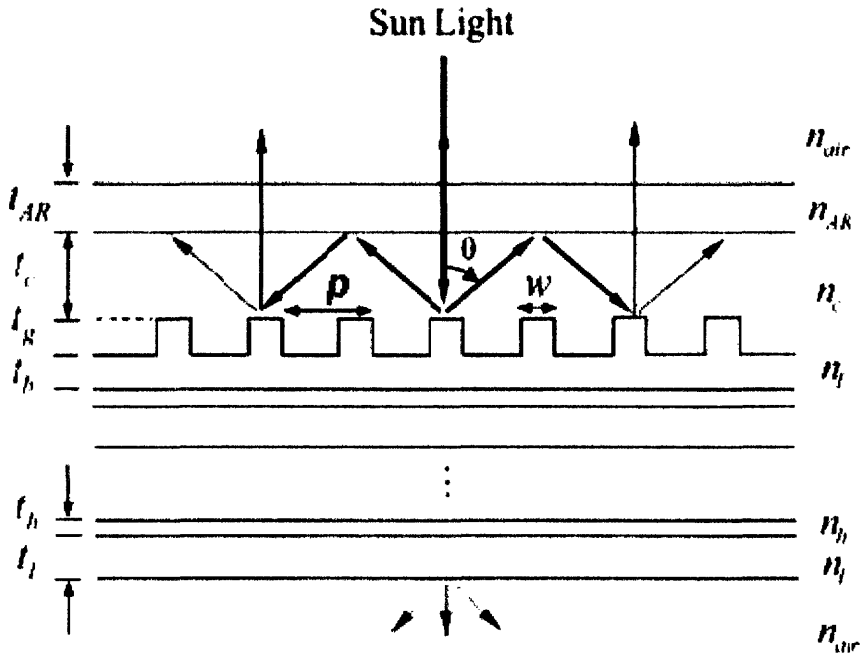

Fig. 4.3 A schematic showing the simulated solar cell structure and the parameters needing optimization [4.4]

4.2.2 Light trapping structure design optimization

In this section, we will present a comprehensive study of the light trapping structure in Fig. 4.3, and demonstrate the significant solar cell efficiency enhancement gained by optimizing the design parameters.

I. AR coating

AR coating determines light admission into the solar cell. It is well known that an effective AR coating (ARC) for a certain wavelength λ_c has the thickness

$$t_{AR} = \frac{\lambda c}{4 n_{AR}} \qquad (4.17),$$

where n_{AR} is the refractive index of the ARC. For Si solar cells, we are dealing with a very wide spectral range: 300 nm-1200 nm. For a certain ARC material, it is hard to achieve low reflectivity in such a wide wavelength range. Therefore, it is important to select a optimal central wavelength λ_c so that low reflection is realized in the interested wavelength range, leading to the highest solar cell efficiency. Here we need to determine two parameters regarding ARC: the material, hence n_{AR}, and the central wavelength λ_c. We will solve this problem in two steps. First, determine the optimal λ_c, then find the best ARC material (n_{AR}). In the simulation, we fix the grating period of the back reflector to be $p = 797nm$, grating depth $t_g = 199nm$, duty cycle F=0.5, and the Bragg wavelength of the DBR is set as $\lambda_0 = 850nm$ with a stopband around 500 nm wide.

Fig. 4.4 (a) illustrates the calculated solar cell efficiency vs. λ_c, which determines ARC thickness through Eq. (4.17). Three ARC refractive indices are considered: 1.46, 1.88, and 2.20, which can be associated to three different materials: SiO_2, SiO_xN_y, and

Si_xN_y. For two different Si thicknesses t_c=5 μm and 10 μm, all three indices exhibit the highest cell efficiency at the same λ_c=576 nm.

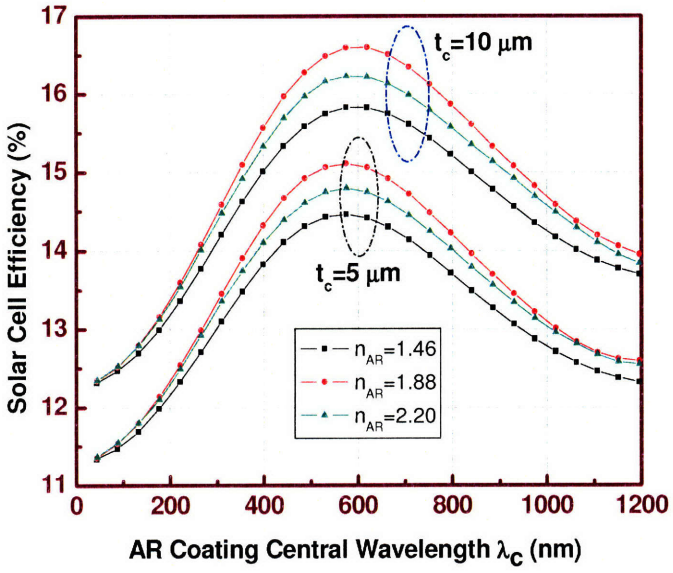

Fig. 4.4 (a) ARC thickness optimization through the optimization of ARC central wavelength ($\lambda_c = 4t_{AR}n_{AR}$).

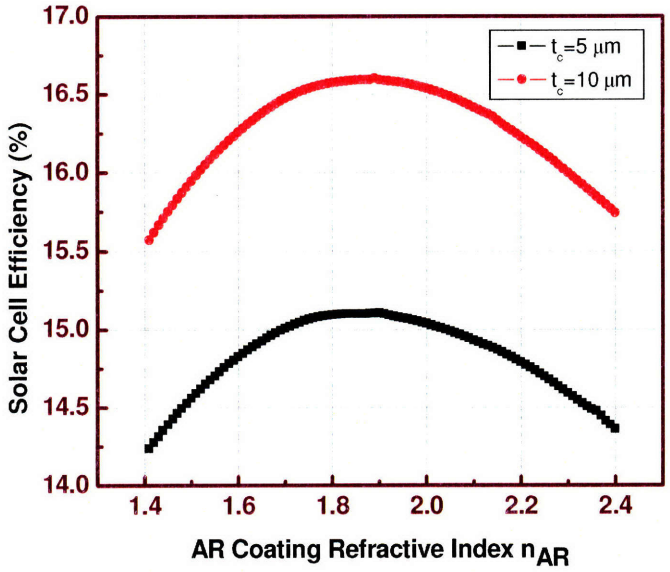

Fig. 4.4 (b) ARC refractive index optimization

Fig. 4.4 (b) shows the optimization of n_{AR} with λ_c=576 nm. For cells 5 and 10 μm thick, the same n_{AR}=1.88 renders the highest cell efficiency η. Note n_{AR}=1.88 is close to the theoretical prediction $n_{AR} = \sqrt{n_c} = \sqrt{3.5} = 1.87$ where n_c is the refractive index of Si in the infrared range.

II. Diffraction grating

Grating plays a critical role in enhancing the optical path length by bending light into large diffraction angles. The grating equation

$$m\lambda = pn(\sin\alpha + \sin\beta) \qquad (4.18)$$

specifies the diffraction angle β for incidence angle α at incident wavelength λ, where m is the diffraction order, p is the grating period, n is the refractive index of the grating. Besides grating period, grating depth and duty cycle are two important parameters determining grating performance. Figs. 4.5 (a) through (c) illustrate the optimization of these parameters.

Fig. 4.5(a) shows two efficiency maxima for each cell thickness, located at p≈400 and 800 nm, respectively, with the peak at 800 nm higher. With p=800 nm, at the incident wavelength λ=800 nm, Eq. (4.18) gives a 1st order diffraction angle of β=16.6°, which equals the critical angle of total internal reflection from Si to air, meaning that the 1st order reflected light from the grating will form total internal reflection when it impinges on the front surface of the solar cell, thereby being reflected back into the cell for further absorption. At λ=1.1 μm, β=23.1°. Note that with the smaller grating period p=400 nm, Eq. (4.18) renders bigger diffraction angles, e.g. at λ=1.1 μm, the 1st order diffraction angle β increases to 51.8°. Intuitively, bigger diffraction angle will lead to longer path

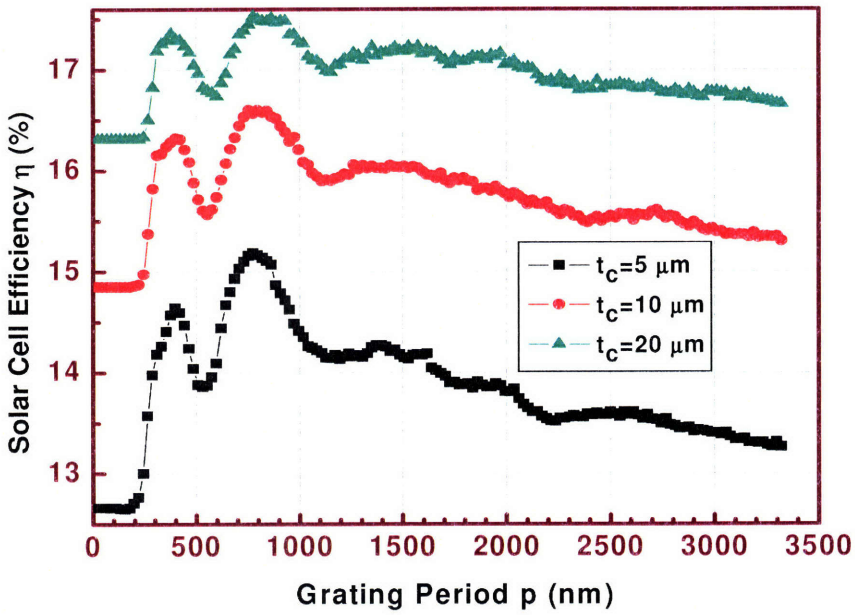

Fig. 4.5 (a) Grating period optimization

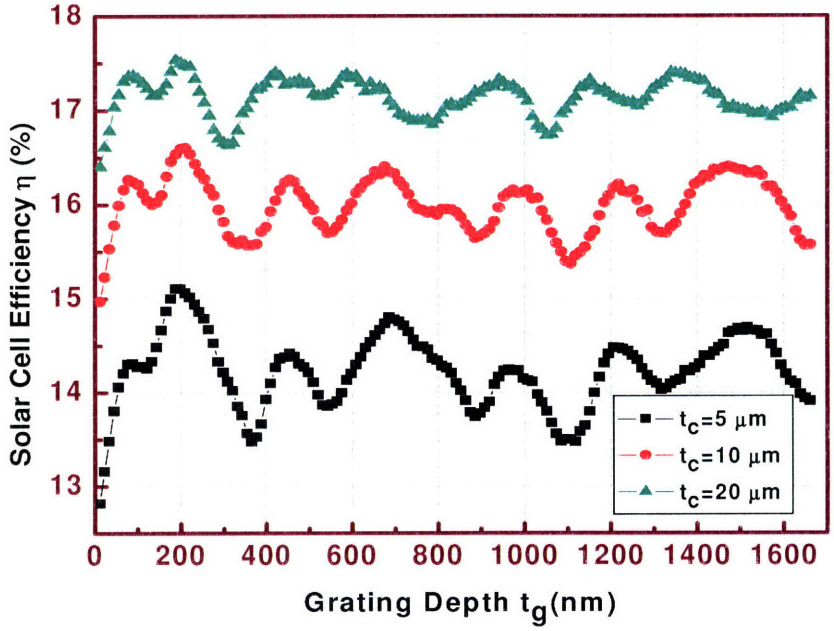

Fig. 4.5 (b) Grating depth optimization

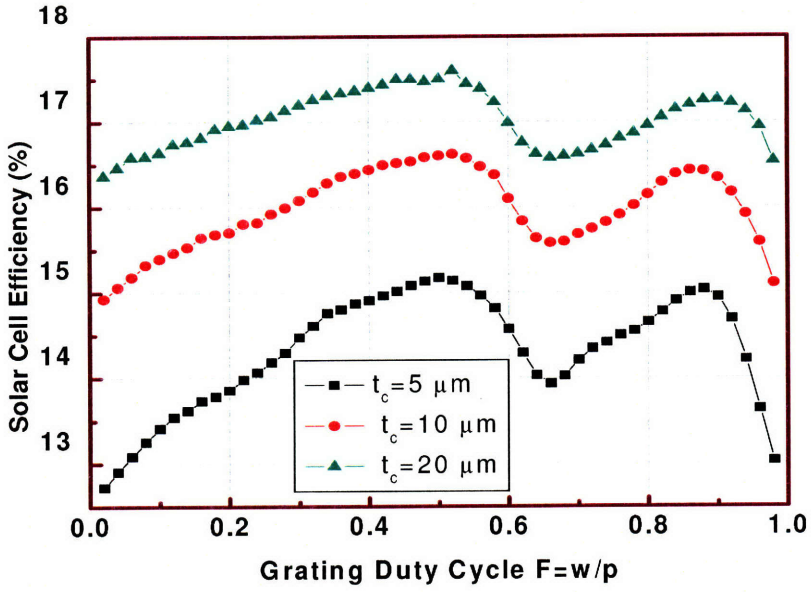

Fig. 4.5 (c) Grating duty cycle optimization

length, hence higher cell efficiency. However, Fig. 4.5 (a) seems to contradict this. Actually, the grating equation gives the phase information, but does not tell the grating efficiency, i.e., how much energy goes into each diffraction order, which can only be solved numerically. It is found that bigger diffraction angles come with smaller diffraction efficiency (less energy). Consequently, large diffraction angles do not necessarily contribute more to solar cell efficiency.

Fig. 4.5 (b) demonstrates that solar cell efficiency oscillates when grating depth varies, and has a maximum at $t_g \approx 200$ nm for all three cell thicknesses. Careful inspection of the figure reveals that the relative efficiency variation is within 18% regardless of t_g, with the thinner cells having greater variations of efficiency than the thicker cells.

Fig. 4.5 (c) illustrates that the optimal duty cycle is F=0.5, and there is another peak at 0.88 with slightly lower efficiency. However, cell efficiency drops rapidly when F deviates from 0.88, making 0.5 the better choice.

III. DBR

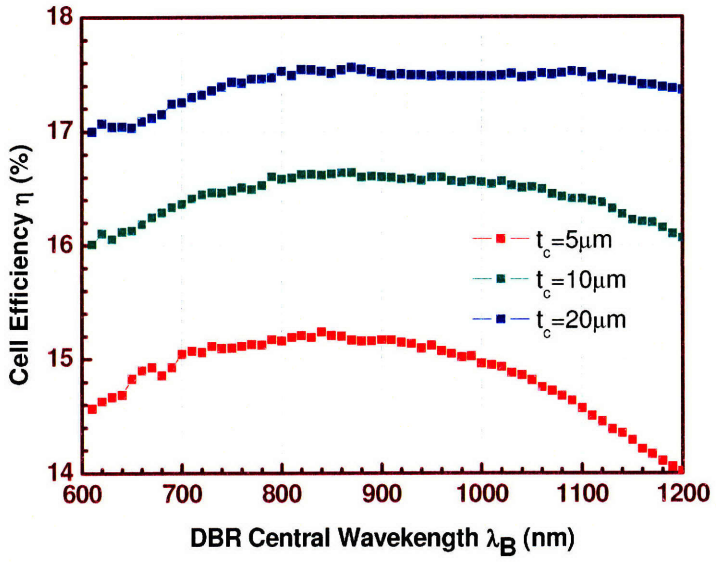

Fig. 4.6 DBR Bragg wavelength optimization

In addition to the grating, the DBR is another very important light trapping component, which reflects light that is transmitted through the grating back into the cell for further absorption. The thickness of each DBR stack layer is simply a quarter-wave $\lambda_B/4n_{h,l}$ where $n_{h,l}$ is the index of the high or low index material. In this simulation, the DBR material is set as Si/SiO_2, and the number of DBR pairs (bilayers) is set as 8, so the only parameter to optimize is DBR central wavelength λ_B. Fig. 4.6 depicts cell efficiency vs. λ_B. Cell efficiency peaks at λ_B= 850 nm for all three active layer thicknesses, 5, 10,

and 20 μm. Thinner cells are more sensitive to λ_B, because they have a bigger spectral range needing path length enhancement.

Table 4.1 summarizes the optimized parameters of ARC, grating and DBR. The achievable efficiency with the optimized design is presented in Table 4.2.

Table 4.1 Optimized parameters of light trapping structures for thin film Si solar cells

AR coating central wavelength λ_c (nm)	AR coating Index n_{AR}	Grating period p (nm)	Grating depth t_g (nm)	Grating duty cycle (F=w/p)	DBR Bragg wavelength λ_B (nm)
576	1.88	800	200	0.5	850

4.2.3 Contribution from light trapping components

To understand the contribution from each of the light trapping components: ARC, DBR and grating, to cell efficiency improvement, cell efficiencies with different optimized light trapping structures are calculated. Table 4.2 presents these results for 5 different cell thicknesses t_c. As can be seen, when t_c=1 and 2 μm, the maximum efficiency with both ARC and textured photonic crystal (TPC, i.e. DBR+grating) are more than twice the value obtained without any light trapping structure. Fig. 4.7 is a more detailed plot, showing cell efficiency vs. thickness for three different cases: no light trapping structure, ARC only, and ARC plus TPC. It is obvious that for cells thinner than 10 μm, the back structure is the major factor in improving efficiency; when cell thickness

Table 4.2 Solar cell efficiency using optimal design parameters at different cell thicknesses

Cell Thickness t_c (μm)	Cell Efficiency η_0 (%) / No ARC, no back structure	Cell Efficiency η_1 (%) / ARC only	Cell Efficiency η_2 (%) / ARC + TPC
1	4.48	5.98	9.46
2	6.08	8.28	12.24
5	8.34	11.47	15.17
10	9.87	13.60	16.64
100	12.93	17.64	18.88

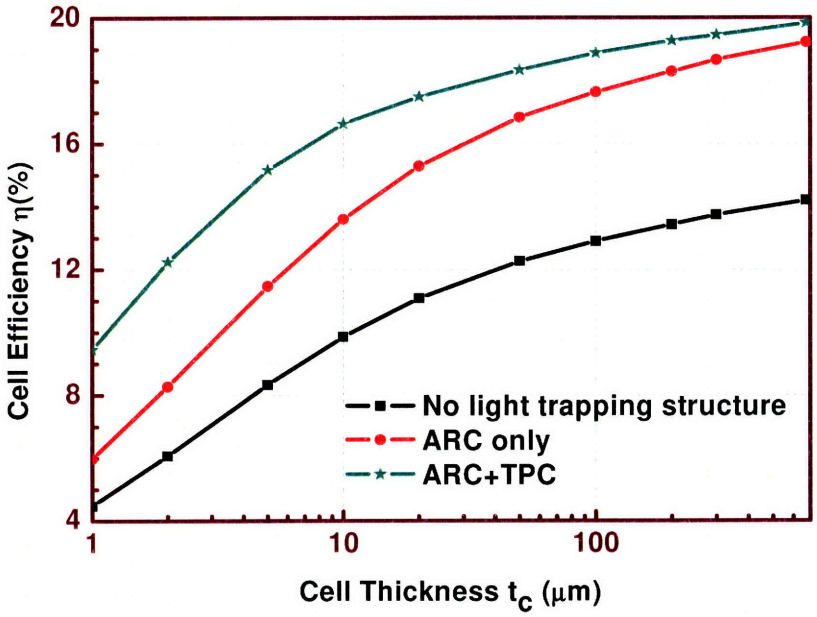

Fig. 4.7 Solar cell efficiency vs. thickness with different light trapping structures

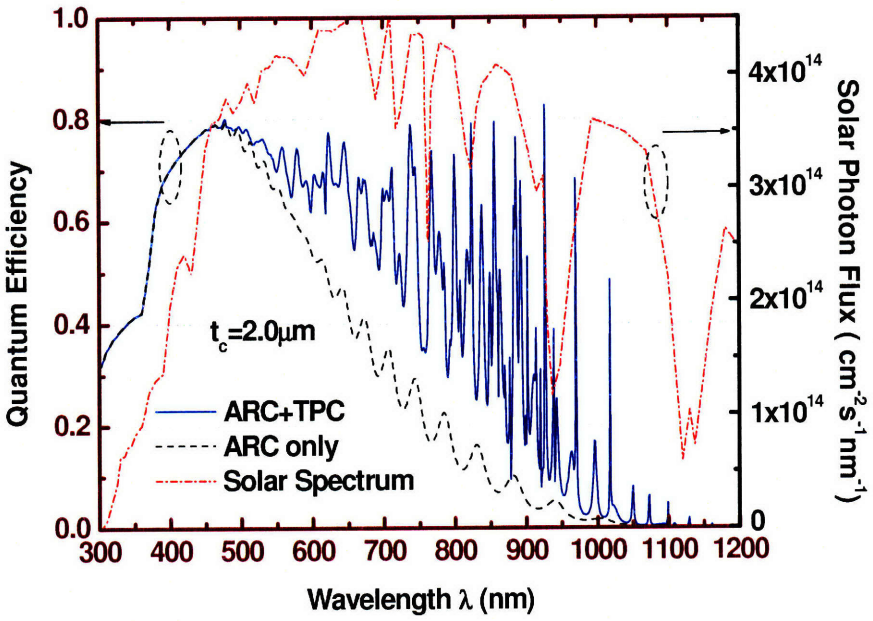

Fig. 4.8 (a) Quantum efficiency of 2 μm thick Si solar cells with and without back reflector

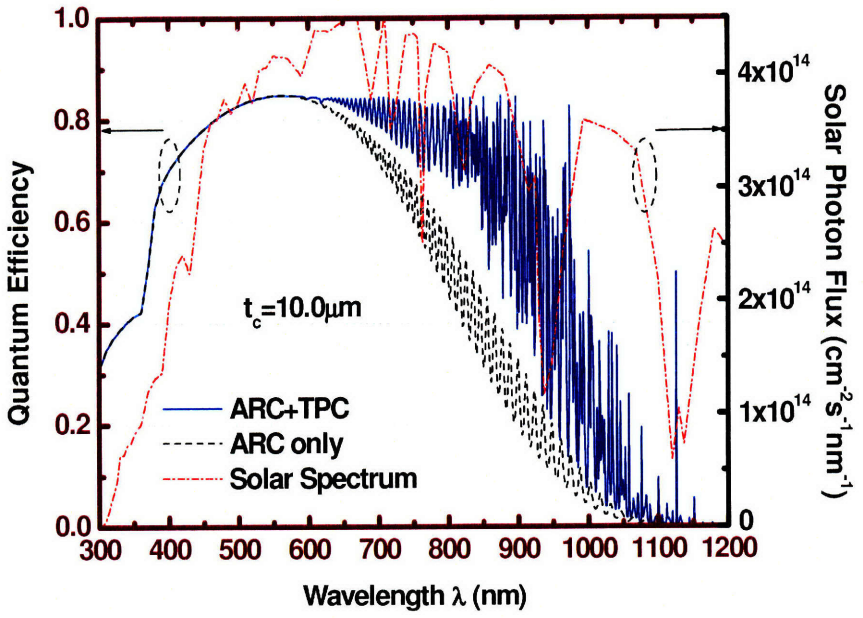

Fig. 4.8 (b) Quantum efficiency of 10 μm thick Si solar cells with and without back reflector

exceeds 10 μm, the back reflector contribution decreases rapidly. This decrease can be understood by inspecting the quantum efficiency (absorption times the collection efficiency η_c= 85%) spectra in Fig. 4.8. It shows that for thinner cells (t_c=2 μm), the TPC back reflector renders significant absorption enhancement in the wide wavelength range between 450-1100 nm, where most of the incident solar photon flux is concentrated, while for the thicker cell (t_c=10 μm), the absorption enhancement window shrinks to 650-1100 nm, and the strong enhancement portion happens to overlap with one of the major dip regions in solar spectrum at around 850-1000 nm.

To study the role of the two components of the TPC back reflector: DBR and grating in more detail, Fig. 4.9 plots the cell efficiency with different light trapping components, at different device layer thicknesses. Table 4.3 summaries the relative contribution from each light trapping component. It clearly demonstrates that at all

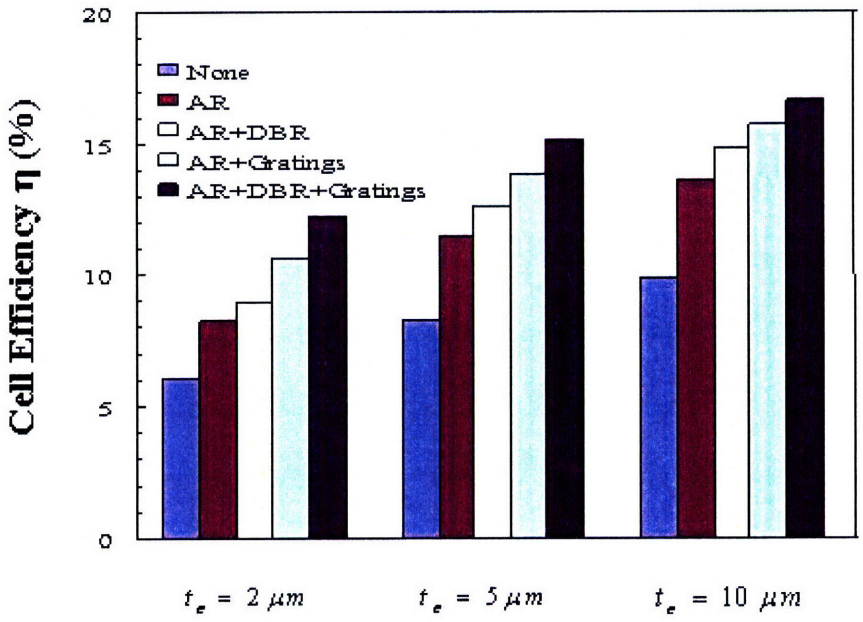

Fig. 4.9 Solar cell efficiency with different light trapping components at different thicknesses

Table 4.3 Contribution from each light trapping component to total efficiency enhancement

Cell Thickness t_c (μm)	Total Efficiency enhancement (%)	Contribution from AR (%)	Contribution from DBR (%) (%)	Contribution from Grating (%)
2	101	36	11	54
5	82	37	15	30
10	69	37	13	19

thicknesses, grating contributes more than DBR to the total efficiency enhancement. And at t_c<10 μm, when the cell gets thinner, the contribution from grating increases rapidly, while that from DBR and ARC is almost constant. When t_c=2 μm, the total efficiency enhancement is as high as 101%, out of which grating contributes 54%, DBR only contributes 11%, and ARC 36%. This is probably because DBR by itself can at most double path length, while grating bends light into large oblique angles, increasing path length by much more than two times cell thickness, which is especially important for thinner devices.

4.2.4 The influence of incidence angle

In the aforementioned simulation, normal incidence was assumed. However, the incidence angle of the sun light is not always normal to the cell surface due to diffuse light. On average, around 15% of the sun light is diffuse [4.7], impinging onto the solar cell from all angles. Therefore, it is worthwhile to study how the light trapping structure performs at oblique incidence. Fig. 4.10 illustrates cell efficiency vs. incidence angle for three different cell thicknesses, at the optimized light trapping parameters. As expected, cell efficiency decreases as incidence angle increases, due to increased reflection. However, even at 50° incidence, cell efficiency is still around 80% of the value under

normal incidence. The possible reason is that Si has high index relative to air, light incident at all angles onto Si will be directed into a small cone within 16.6° to the surface normal, before it impinges on the back reflector.

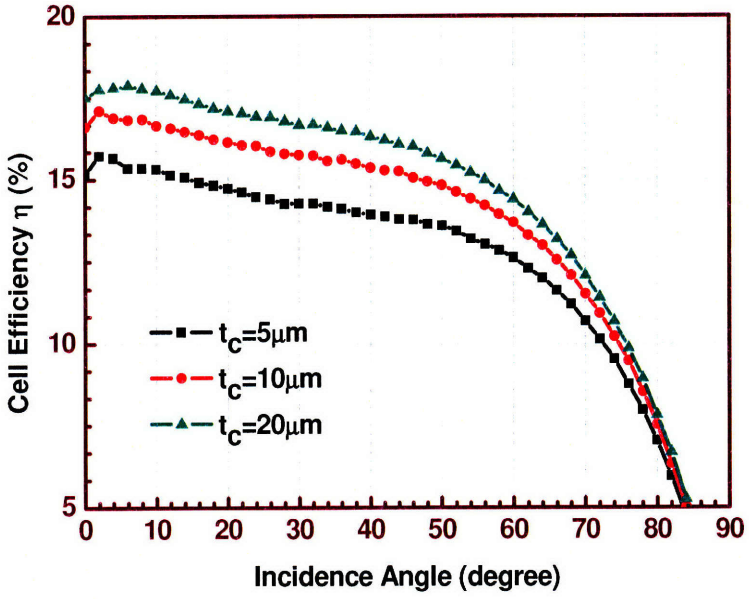

Fig. 4.10 Cell efficiency vs. incidence angle for solar cells with optimized light tapping structures

4.3 Scattering Matrix Method

In section 4.2, we presented the design optimization of the light trapping structures using coupled wave theory. It is a little surprising that the optimal parameters of the back reflector and AR coating do not change as cell thickness varies. Quite often, simulation results not only depend on the model used, but related to the inherent assumptions of the simulation method. To be sure, it is beneficial to check the simulation results with another method. In this section, we will simulate the solar cell structure with scattering matrix method and optimize the same design parameters. In the next section we

will compare the results from coupled wave theory with those from scattering matrix method.

4.3.1 General approach of scattering matrix method simulation [4.8]

Scattering matrix (S-matrix) method [4.9-4.11] is an approach closely related to transfer matrix. Fig. 4.11 shows the solar cell structure we simulated using this method. From top to bottom, it has an AR coating with thickness C; an active Si layer with thickness t; a diffraction grating at the bottom of the device layer, with period P, etch depth E, and duty cycle F=V/P, where V and P are the valley width and grating period, respectively; a DBR stack composed of SiO_2 and Si quarter-wave pairs, with period B;

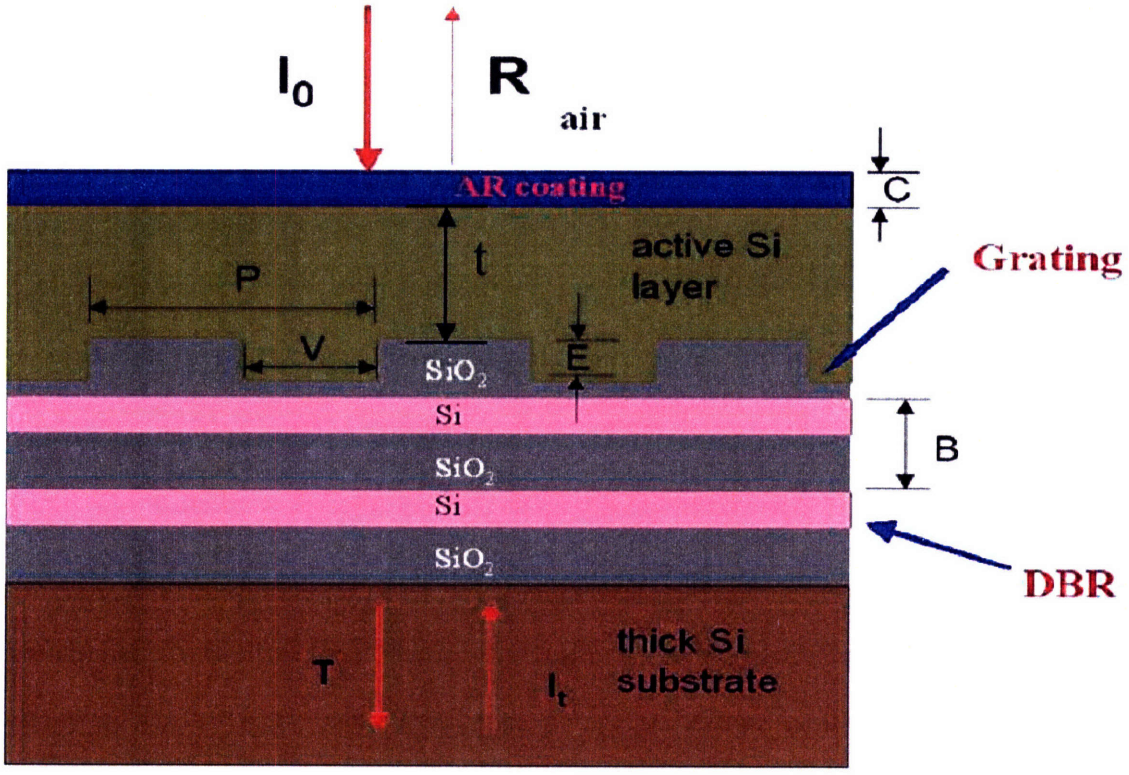

Fig. 4.11 Schematic of the solar cell structure in scattering matrix method simulation

and a thick Si substrate, taken as semi-infinite. Actually the substrate could also be glass or ceramics without affecting the simulation results. We choose Si because that is what we will use in our future experiments as detailed in Chapter 6, as Si is the default material allowed to be processed in most cleanrooms, including those here at MIT. We set the ARC material to be thermal oxide for this TPC chapter because it provides excellent surface passivation to Si, which is especially important for thin film solar cells, and because it is a stable process not needing further characterization, therefore is well suited as a reference material. As an aside, chapter 5 of this thesis is devoted to ARC optimization: there we determine we will use a double-layer ARC composed of Si_3N_4 and a thin layer of thermal oxide for our experimental thin cells. The parameters to be optimized in this section with thermal oxide are: ARC thickness C, grating period P, etch depth E, duty cycle F, DBR Bragg wavelength λ_B, which determines its period B through

$$B = \frac{\lambda_B}{4}\left(\frac{1}{n_h} + \frac{1}{n_l}\right) \qquad (4.19),$$

where n_h and n_l are the refractive index of the high (Si) and low (SiO_2) dielectric in the DBR stack. The influence of number of DBR quarter-wave pairs will also be examined.

The simulation approaches are:

(1) decompose the entire solar cell structure into uniform layers in the z direction;

(2) calculate the Fourier transform of the dielectric function of each layer;

(3) using the periodicity of the cell structure, specifically, the period of the grating, transform the **E** and **H** fields into Fourier series in each layer;

(4) use Maxwell's equations to derive the S-matrix, which relates fields in the adjacent layers at a certain wavelength;

(5) compose the whole S-matrix;

(6) find reflection R and transmission T by applying boundary conditions: the incident intensity I_0 is known, and the reverse propagating light intensity in the substrate I_t=0. The absorption A=1-R-T for a given wavelength;

(7) repeat for all wavelengths that may be absorbed by the solar cell;

(8) finally, obtain the solar cell efficiency through the absorption spectrum and solar photon flux by identifying the maximum power point on the J-V curve

$$J = \int_{\lambda_1}^{\lambda_2} qA(\lambda)s(\lambda)d\lambda - \frac{q(n^2+1)E_g{}^2kT}{4\pi^2\hbar^3c^2}\exp(\frac{qV-E_g}{kT}) \qquad (4.20),$$

where q is the electronic charge, A(λ) is the absorption at a certain wavelength λ, s(λ) is the incident solar photon number at this λ under AM 1.5 conditions, n is the average refractive index of the semiconductor, and Eg is its bandgap. The first term in Eq. (4.20) represents short circuit current density

$$J_{sc} = \int_{\lambda_1}^{\lambda_2} qA(\lambda)s(\lambda)d\lambda \qquad (4.21),$$

and the second term considers radiative recombination loss [4.12, 4.13]. Voc is obtained by setting J=0 in Eq. (4.20). And by setting $\frac{d(JV)}{dV} = 0$, one can find the maximum output power point (V_m, J_m). The fill factor is

$$FF = \frac{J_m V_m}{J_{sc} V_{oc}} \qquad (4.22).$$

Finally the power conversion efficiency of the solar cell is

$$\eta = \frac{J_{sc} V_{oc} FF}{P_{in}} \qquad (4.23),$$

where P_{in}=0.1 W/cm^2 is the incident solar energy per unit area under the AM1.5 spectrum.

To get quantitative information on efficiency improvement rendered by the back reflector and optimized ARC, we also calculated the efficiency of reference cells with the same device layer thickness t, but no grating or DBR. The schematic of a reference cell is shown in Fig. 2.21 (a). Compared to the solar cell structure shown in Fig. 4.11, it has a SiO_2 ARC with fixed thickness at 120 nm, and a 500 nm thick SiO_2 layer between the active layer and the substrate for electrical isolation. In this simulation, for cells of a certain thickness t, the figure of merit for design parameter optimization is taken as the efficiency enhancement offered by the solar cell with optimized structural parameters compared to the reference cell, with the absolute value defined as η-η_{ref}, and the relative one as $\frac{\eta - \eta_{ref}}{\eta_{ref}}$. Note that in the efficiency calculation, no shadowing is considered, and other than radiative recombination loss, the photogenerated carriers are assumed to be fully collected by the electrodes.

The active Si layer is treated as a medium with complex dielectric constant that depends on wavelength, as obtained from Ref. [4.14]. The refractive index of Si in DBR is set to be 3.5, and that of SiO_2 in the ARC, DBR and the isolation layers is set to be 1.46. The standard solar spectrum is acquired from Ref. [4.15].

Fig. 4.12 illustrates the optimization sequence. It starts with grating etch depth E, then grating period P, followed by DBR Bragg wavelength λ_B, ARC thickness C, and grating duty cycle F. When optimizing a certain parameter, other parameters are held constant at approximately the values shown in Table 4.4. Then using this set of optimized parameters, we calculate the efficiency enhancement relative to the reference cell, and repeat the optimization sequence until the efficiency enhancement stops increasing.

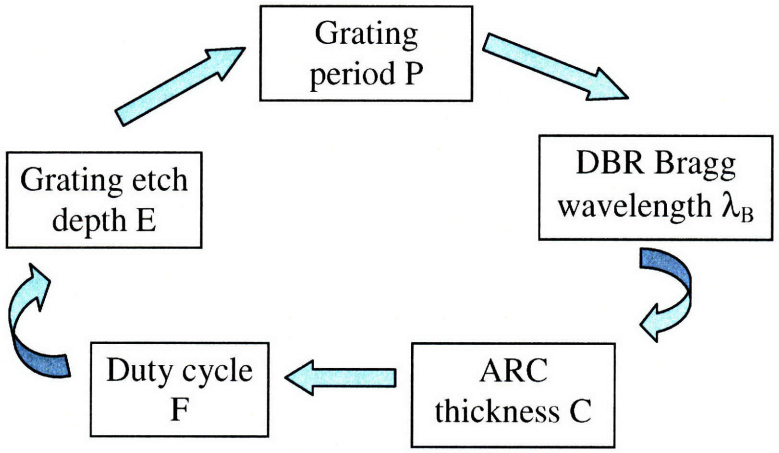

Fig. 4.12 Optimization sequence using scattering matrix method

Fifteen Si/SiO_2 DBR quarter-wave pairs are used during the parameter optimization, then the number of bilayers is reduced to eight to calculate the final efficiency enhancement, because this is the number of pairs we will use in future experimental work. It is found that cell efficiency stays almost the same compared to 15-pair DBR. Actually, as will be shown in Fig. 4.17, cell efficiency starts to saturate when the number of DBR bilayers increases to 6. Design parameters are optimized for four cell thicknesses: 2, 5, 20 and 50 μm.

To check the validity of our simulations with the scattering matrix approach, finite-difference time domain (FDTD) method [4.16] has been use for several simulations with perfectly matched boundary layers [4.17]. Generally, the results agree well, but since the FDTD method is much slower for the same resolution, it is not used for most simulations.

4.3.2 Design parameters optimization

I. Grating

There are three grating parameters to optimize: etch depth, period, and duty cycle. Fig. 4.13 shows the grating etch depth vs. absolute cell efficiency enhancement relative to the reference cell at different cell thicknesses. As the cell becomes thinner, the optimum etch depth decreases, changing from 115 nm for a 50 μm thick cell to 56 nm for a 2 μm thick cell, less than half of the former value. For 50 and 20 μm thick cells, the cell efficiency does not change much for etch depth E around the optimal value, while 5 and 2 μm thick cells are more sensitive to the variation of E and shows obvious peaks.

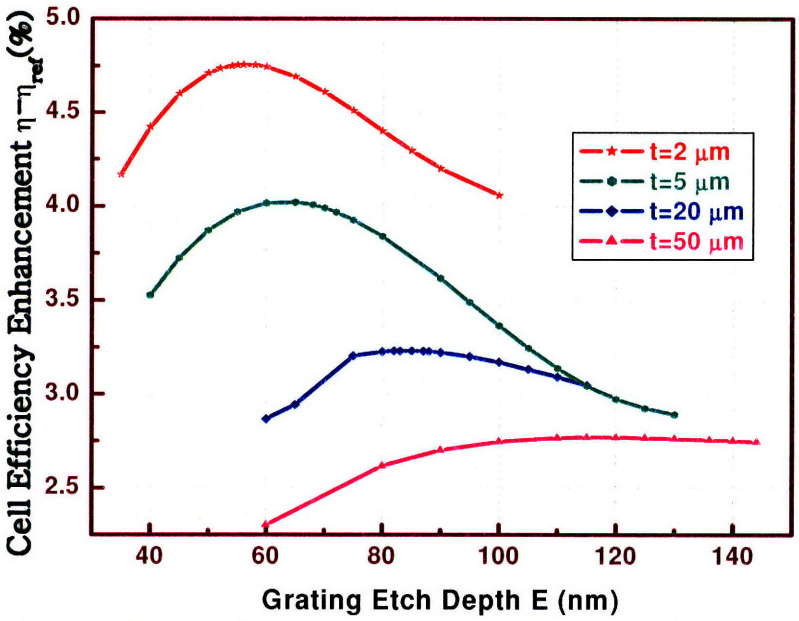

Fig. 4.13 Grating etch depth optimization

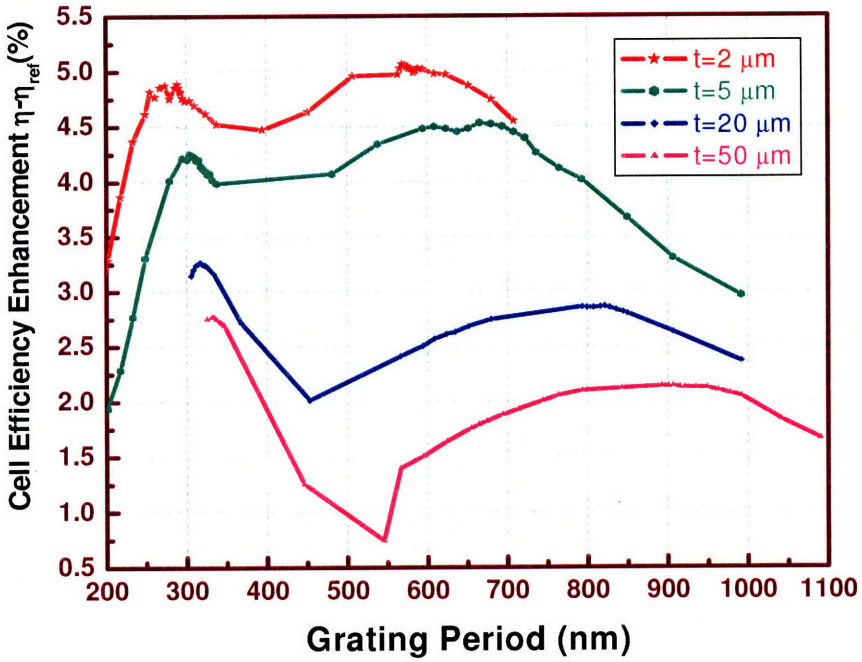

Fig. 4.14 Grating period optimization

Fig. 4.14 depicts grating period variation vs. cell efficiency enhancement. A distinctive feature is that for each cell thickness t, there are two maxima on the curve between 200 and 1100 nm. The first maximum is located around 300 nm, and corresponds to the first order diffraction. The second maximum varies from 569 nm for a 2 um thick cell to 907 nm for a 50 um thick cell, corresponding to second order diffraction. As with etch depth, both maxima decrease as cell becomes thinner. For t=50 and 20 um, the first maximum is obviously higher than the second one (>0.4%). As t decreases, the second maxima increases, and becomes slightly higher than the first ones for t=5 and 2 um. It seems that for all cell thicknesses, having a grating period corresponding to the first order diffraction is a good choice. Note that at each thickness,

since the efficiency of our reference cell is fixed due to the fixed structural parameters, the variation in absolute efficiency enhancement equals the variation of the absolute efficiency of the cell being optimized.

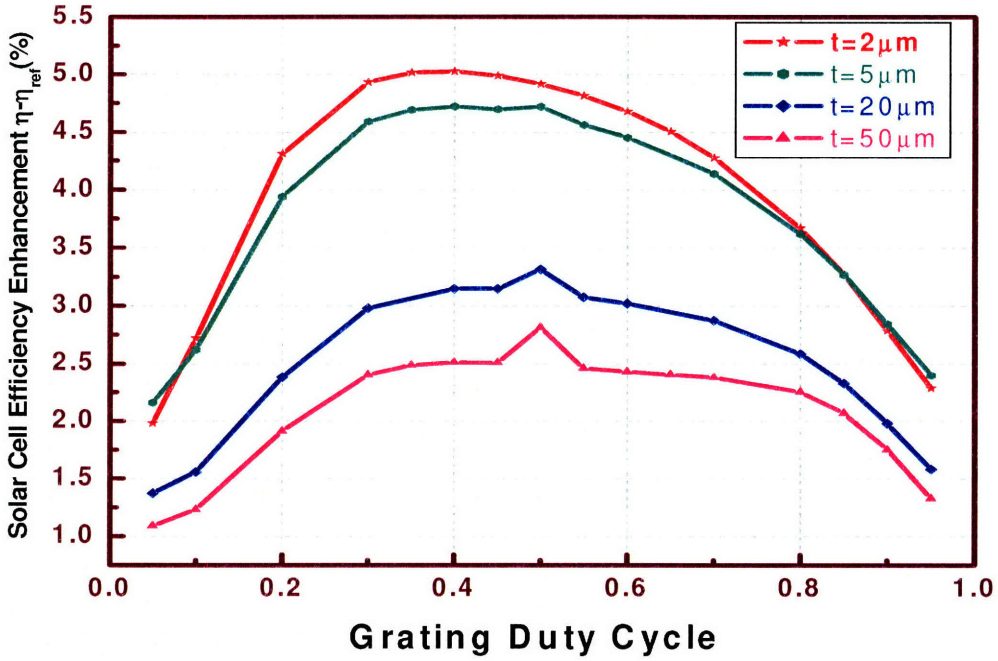

Fig. 4.15 Grating duty cycle optimization

Fig. 4.15 illustrates the influence of grating duty cycle F on cell efficiency. For both 50 and 20 μm thick cells, there is a sharp peak located at F=0.5. For t=5 μm, cell efficiency equals at F=0.4 and 0.5, while for t=2 μm, F=0.4 renders a slightly higher efficiency (0.11%). Since at t=5 and 2 μm, the efficiency improvement when F is slightly shifted from 0.5 is very small, we will take F=0.5 as the optimum value for all cell thicknesses. The optimal value of F=0.5 can be explained by the fact that diffraction strength is proportional to the Fourier component of the grating period, which is

maximized with an equal amount of high and low dielectric in the grating-that corresponds to a duty cycle of 0.5.

II. DBR

Two parameters determine the reflectivity of DBR: Bragg wavelength "B" and the number of quarter-wave pairs (bilayers). B determines the central location of the photonic band gap, i.e., which wavelength range will have the highest reflectivity. Fig. 4.16 illustrates the optimization of B. As with grating etch depth and period, we see that as the cell becomes thinner, the optimal B decreases, and changes from 853 nm for t=50 μm to 721 nm for t=2μm.

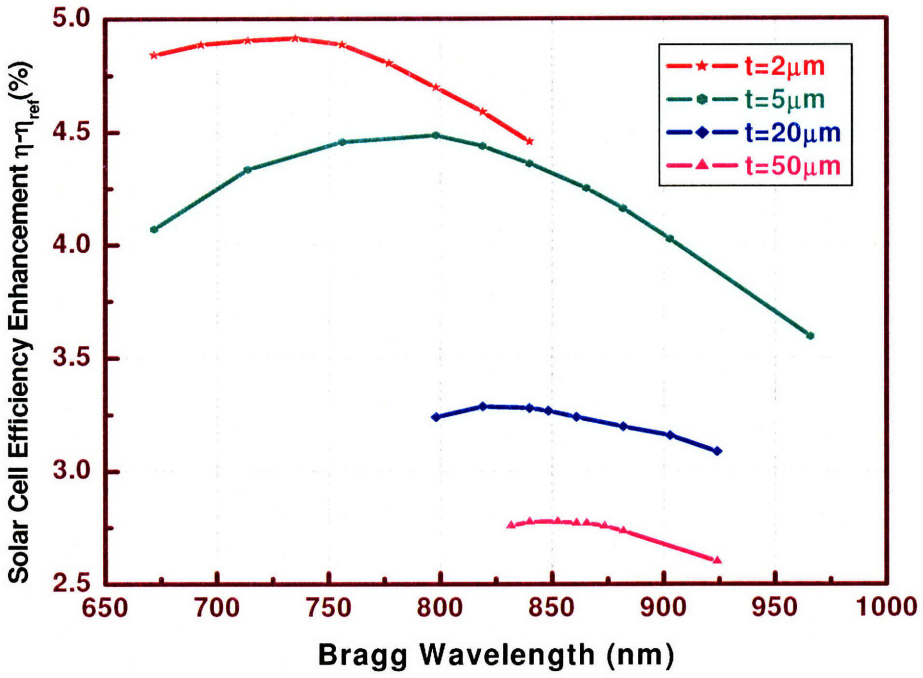

Fig. 4.16 DBR Bragg wavelength optimization

For a fixed Bragg wavelength, although intuitively more DBR bilayers will render higher reflectivity and a wider stopband, it is only significant when the number of DBR bilayers is below a certain value. Above that value, the reflectivity will saturate and stay almost constant at near 100%, and adding more DBR layers will not improve cell efficiency further. Fig. 4.17 depicts the absolute cell efficiency enhancement compared to the reference cell vs. number of SiO_2/Si DBR bilayers, for cells with optimized ARC and back reflector parameters as listed in Table 4.4. Clearly, for all cell thicknesses illustrated, adding two DBR bilayers to the grating increases cell efficiency significantly; but when

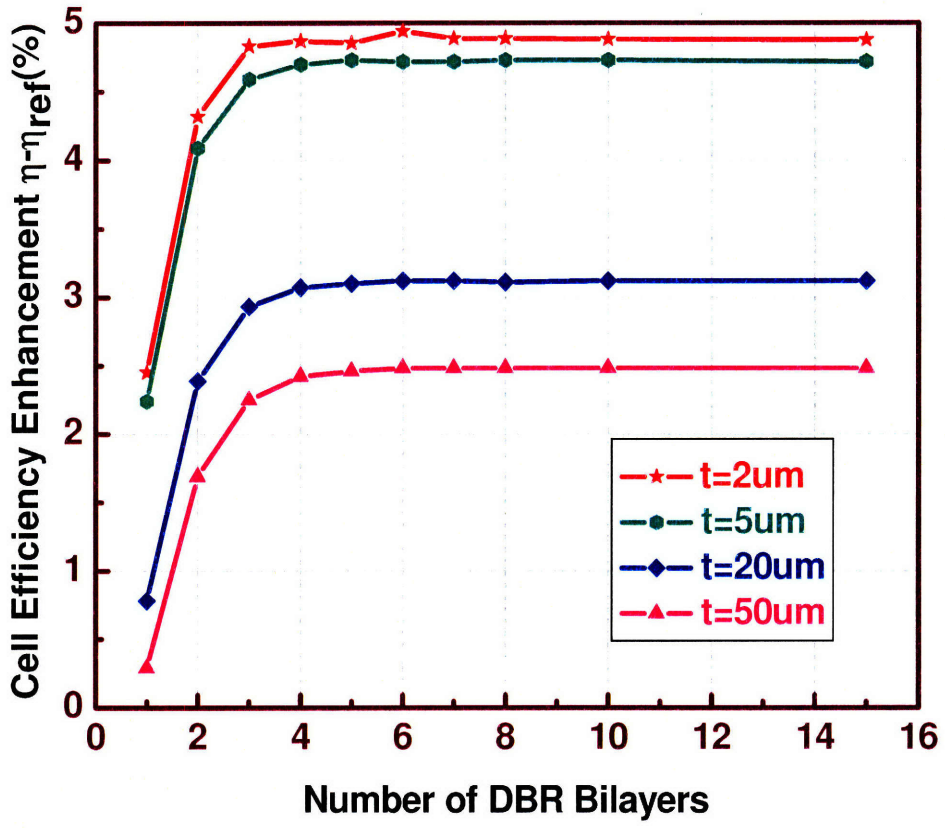

Fig. 4. 17 Cell efficiency enhancement vs. number of SiO_2/Si DBR bilayers

more layers are added, η increases at a slower rate, and reaches the maximum value at around 6 bilayers, and stays constant afterwards.

III. AR coating thickness

Fig. 4.18 depicts the variation of SiO_2 ARC thickness vs. cell efficiency enhancement. Again, it decreases as cell becomes thinner, and is reduced from 108 nm for t=50 μm to 92nm for t=2μm, corresponding to a change of the reflection minimum ($\lambda_c=4tn_{SiO2}$, ARC central wavelength) decrease from 631 nm to 537 nm.

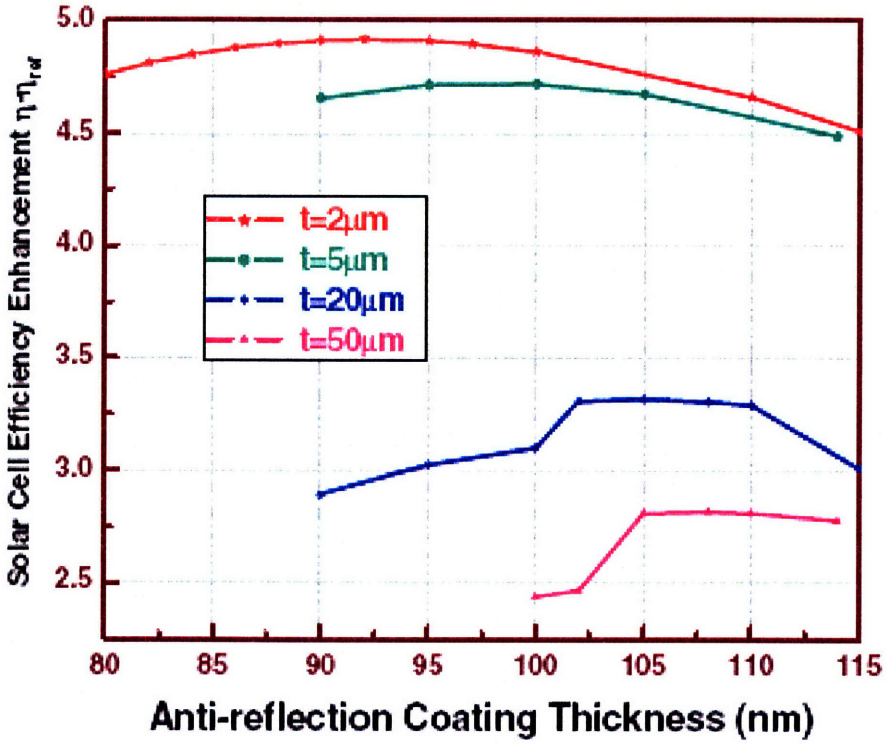

Fig. 4.18 ARC thickness optimization

The optimized parameters together with the absolute cell efficiency and enhancement are summarized in Table 4.4.

Table 4.4 Optimized solar cell design for different cell thicknesses

Solar cell thickness t (μm)	Grating etch depth (nm)	Grating period (nm)	Grating duty cycle	DBR Bragg wavelength (nm)	AR coating thickness (nm)	Optimized cell efficiency η_{opt} (%)	Reference cell efficiency η_{ref} (%)	$\frac{\eta_{opt}-\eta_{ref}}{\eta_{ref}}$ (%)
2	56	289	~0.5	721	92	14.4	9.5	52.8
5	65	304	~0.5	798	100	17.9	13.2	35.8
20	85	317	0.5	819	105	21.9	18.6	17.8
50	115	334	0.5	853	108	23.7	20.9	13.5

Note: the reference cell has an AR coating of 120 nm thick SiO_2, and has a 500 nm thick SiO_2 between the active layer and the substrate for electrical isolation. The optimized cells have 8 bilayers of SiO_2/Si DBR.

IV. Understanding the parameter variation vs. cell thickness

The trend of the variation of optimized parameters vs. cell thickness is vividly depicted in Fig. 4.19, which clearly shows that as cell becomes thinner, all the optimized

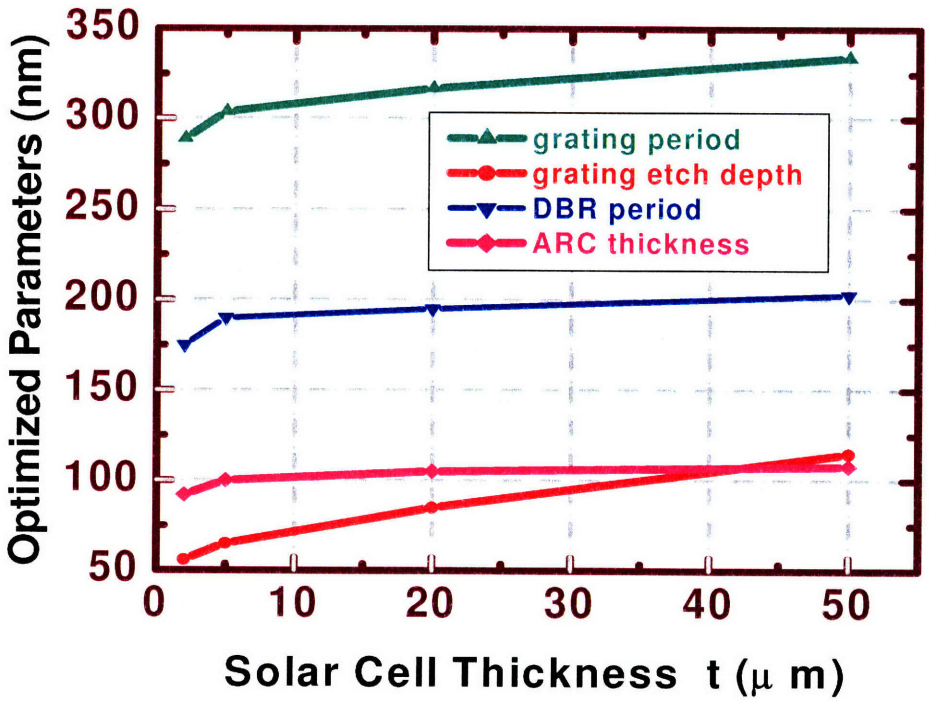

Fig. 4.19 The variation of optimized parameters vs. cell thickness

parameters decrease, except for duty cycle (not shown in the figure), which stays almost constant at 0.5. For t≥5 μm, the variation is linearly; for t<5 μm, the slope is sharper. The decrease of parameters vs. cell thickness can be explained by the fact that due to the monotonical decrease of absorption length of Si as wavelength becomes shorter (see Fig. 4.1), thinner cells have a lower limit of wavelength range that can benefit from light trapping. This can be seen clearly from the absorption spectra of 50 and 5 μm thick solar cells shown in Figs. 4.20 and 4.21.

In both figures, in the regions of enhanced absorption, strong resonance peaks occur periodically. These modes are created by grating diffraction [4.18], and confined within the device layer by total internal reflection. Their spacing is inversely proportional to the cell thickness, so more densely spaced modes are seen in Fig. 4.20 for a 50 μm thick cell than in Fig. 4.21 for a 5 μm thick cell. Compared to the reference cell, strong absorption enhancement starts at λ=800 nm for 50 μm thick cell with optimized back reflector; while significant enhancement starts at λ=580 nm for 5 μm thick cell. Once it has been determined that light trapping should start at shorter wavelength for thinner cells, due to the scale-invariance of Maxwell's equations, all the back-reflector parameters should decrease accordingly.

For example, from the grating equation $m\lambda = pn(\sin\alpha + \sin\beta)$, one can see that in order to achieve the same diffraction angle β for the same incidence angle α and diffraction order m, the period p should be proportional to the diffraction wavelength λ. Etch depth decrease can be understood by writing a simple expression for the cancellation of 0th order reflection

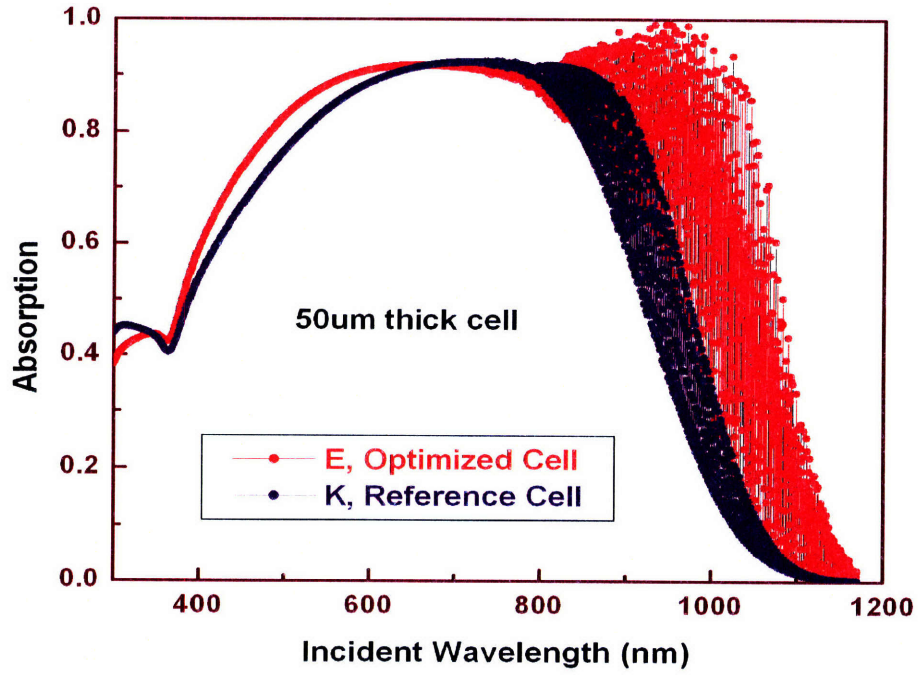

Fig. 4.20 Absorption spectra of 50 μm thick cells

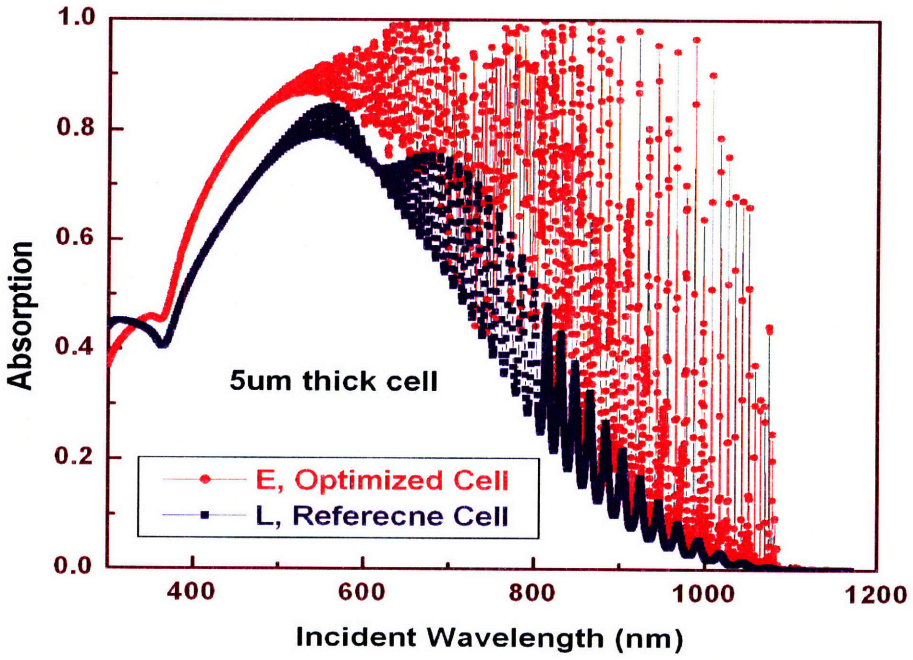

Fig. 4.21 Absorption spectra of 5 μm thick cells

$$E = \frac{\lambda}{4(n_{Si} - n_{SiO_2})} \qquad (4.23).$$

DBR Brag wavelength has to decrease as well because in thinner cells, the stopband needs to cover a wider spectral range starting at shorter λ. Finally, ARC thickness decreases because it is beneficial to preferentially admit photons into the cell which can be well absorbed.

Fig. 4.22 shows efficiency enhancement vs. cell thickness. Both relative and absolute efficiency enhancement increase as cell becomes thinner. For a 2 μm thick cell, the relative efficiency enhancement is as high as 53%. The higher efficiency gain of thinner cells can be easily understood as thinner cells have a wider wavelength range that can benefit from light trapping, and a lower baseline efficiency of the reference cells.

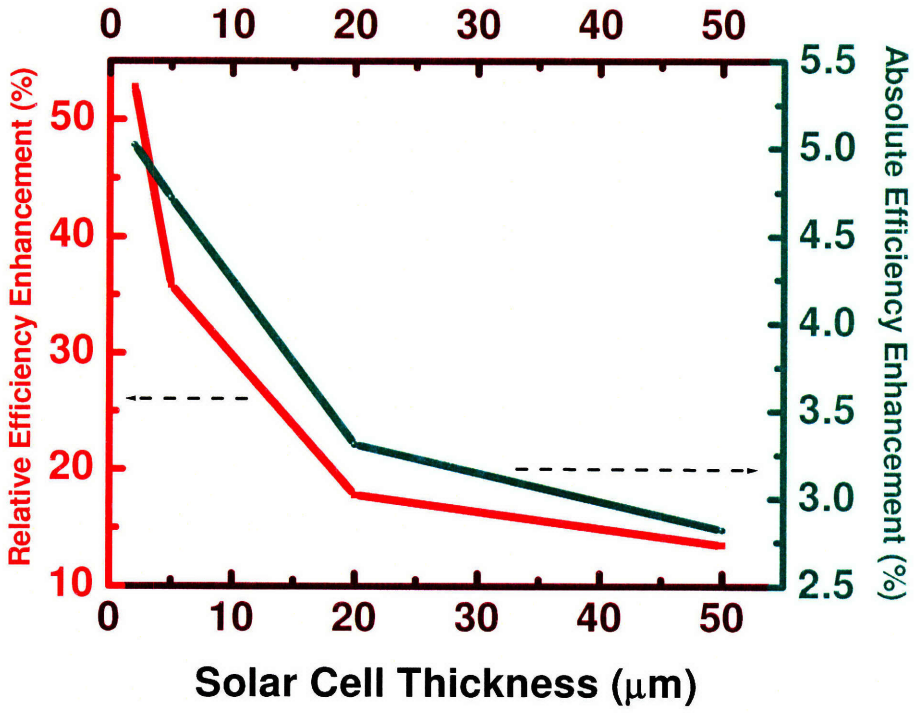

Fig. 4.22 Efficiency enhancement using optimized design vs. solar cell thickness

4.3.3 Efficiency enhancement by light trapping components

To study the relative importance of DBR and grating, besides reference cell and TPC cell (DBR+grating), cell efficiencies with DBR-only and grating-only back structures are also calculated. Schematic structures of these cells are shown in Fig. 2.21. All the cells at the same device layer thickness have the same optimized antireflection coating as identified in Chapter 5 and listed in Table 5.8. The grating and DBR parameters are the optimized values in Tables 4.4 and 5.8. Table 4.5 lists cell efficiency with different back structures. Figs. 4.23 and 4.24 are graphic displays of the table. In order to understand the importance of antireflection coating and compare with coupled wave theory simulation results, efficiencies of "bare" cells are also calculated and shown in Fig. 4.23. They have otherwise identical structure as the reference cell, except that the antireflection coating is removed.

Table 4.5 Efficiency of solar cells with different back structures at different thicknesses

Cell thickness (μm)	Cell efficiency η and relative efficiency enhancement						
	Reference	DBR-only		GRT-only		TPC	
	η_{ref}	η(%)	$\frac{\eta-\eta_{ref}}{\eta_{ref}}$(%)	η(%)	$\frac{\eta-\eta_{ref}}{\eta_{ref}}$(%)	η(%)	$\frac{\eta-\eta_{ref}}{\eta_{ref}}$(%)
2	10.56	12.13	**14.87**	12.83	**21.50**	15.55	**47.25**
5	14.93	16.48	**10.38**	16.34	**9.44**	19.33	**29.47**
20	20.48	21.51	**5.03**	20.83	**1.71**	23.39	**14.21**
50	22.76	23.62	**3.78**	23.08	**1.41**	25.1	**10.28**

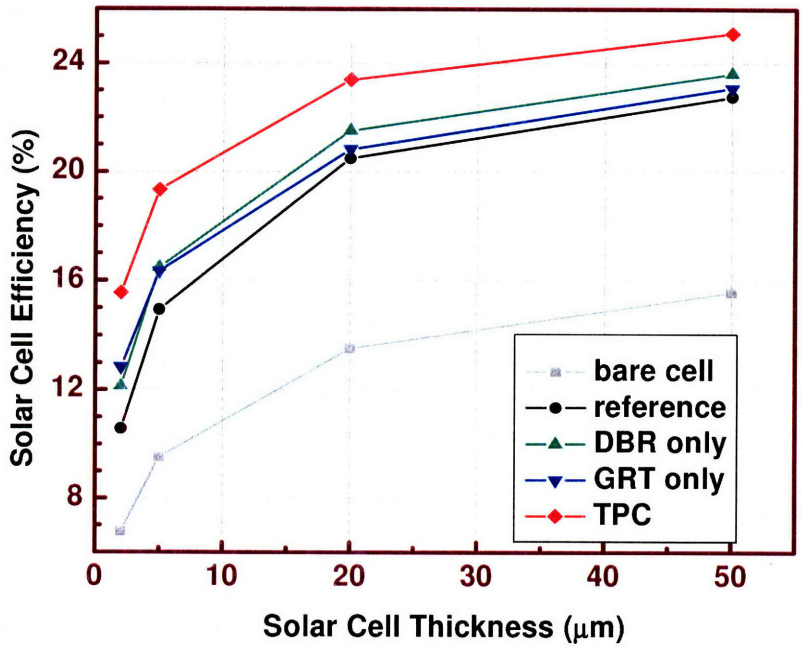

Fig. 4.23 Solar Cell efficiency vs. thickness with differing back structures

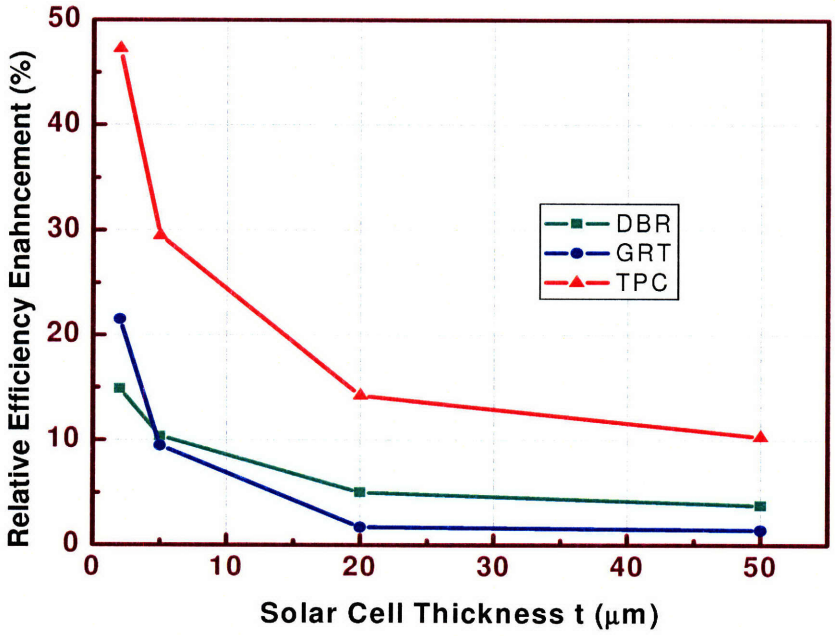

Fig. 4.24 Efficiency enhancement by DBR and grating relative to reference cell

Obviously, DBR, grating and TPC all enhance cell efficiency more as cell becomes thinner. For cell thickness t≥5 μm, DBR gains more efficiency enhancement than grating does, and for thinner cells, grating achieves more enhancement. Intuitively, this is because in thinner cells, the large angle diffraction may entail more light absorption than the high reflectivity of DBR does. When they are combined together, TPC acquires more enhancement than the sum of the enhancement by DBR and grating, which can be easily understood from the absorption spectra in Section 2.4.2 in Chapter 2.

As seen from Fig. 4.23, adding an antireflection coating to a bare cell increases cell efficiency by more than 46% (relative).

4.3.4 Comparison to other light trapping schemes

In section 1.3.3 of Chapter 1, we introduced a commercially adopted light trapping scheme-laser fired contact (LFC). It has an Al back reflector and an oxide layer between the device Si layer and the Al reflector to enhance reflection. In this section, we will compare the efficiency enhancement by textured photonic crystal (TPC) and LFC.

The efficiencies of 2 μm thick Si solar cells with 70 nm thick antireflection coating (refractive index n=1.91) and different back reflectors, TPC and LFC, are calculated using scattering matrix method. No shadowing is considered, and carrier collection efficiency is assumed to be 100%.

In LFC cell efficiency simulation, the Al layer thickness is considered semi-infinite, as a few micron thick Al has strong absorption and will not allow any light to penetrate through it. For fair comparison, the first thing is to optimize the back oxide thickness. As shown in Fig. 4.25, there are two oxide thicknesses giving peak efficiencies:

85 nm and 300 nm, with the efficiency at 85 nm slightly higher. Therefore, we will use the efficiency at this oxide thickness to compare with the efficiencies given by other back reflectors.

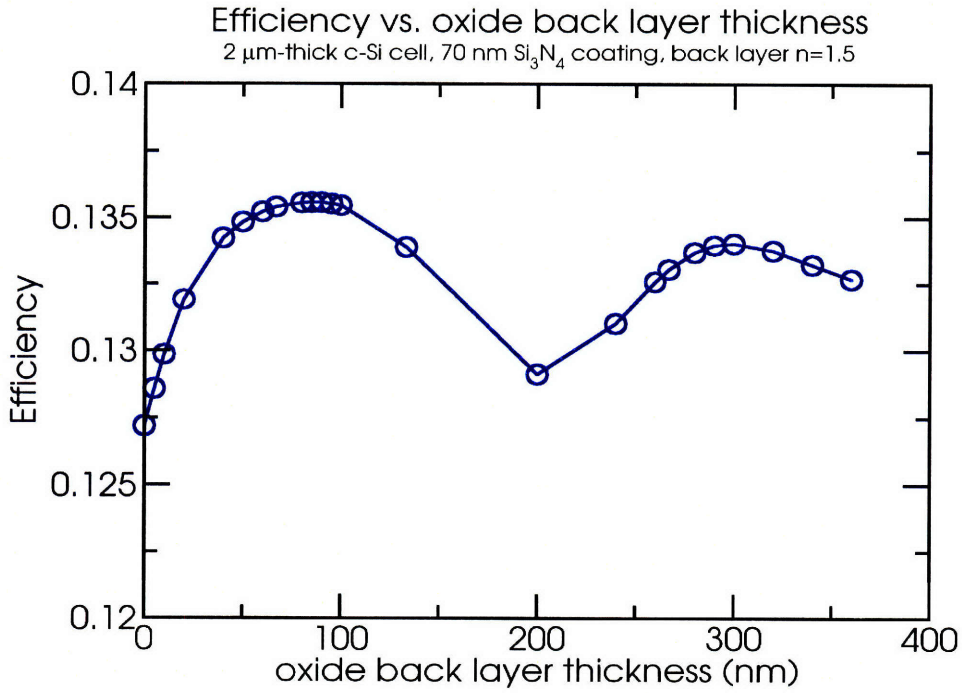

Fig. 4.25 Back oxide layer thickness optimization for cells with laser fired contact

Fig. 4.26 illustrates the efficiencies of 2 μm thick Si solar cells with different back reflectors. Seven types of back reflectors are considered: no back reflector, Al only, Al with 85 nm oxide, perfect metal (an imaginary material with 100% reflectivity at all incident wavelengths), DBR plus 1D grating, and DBR plus 2D grating. It shows that Al alone only improves absolute cell efficiency by 3.3%, corresponding to a relative increase of 35%. Apparently, adding an oxide layer almost turns the lossy metal (Al has strong

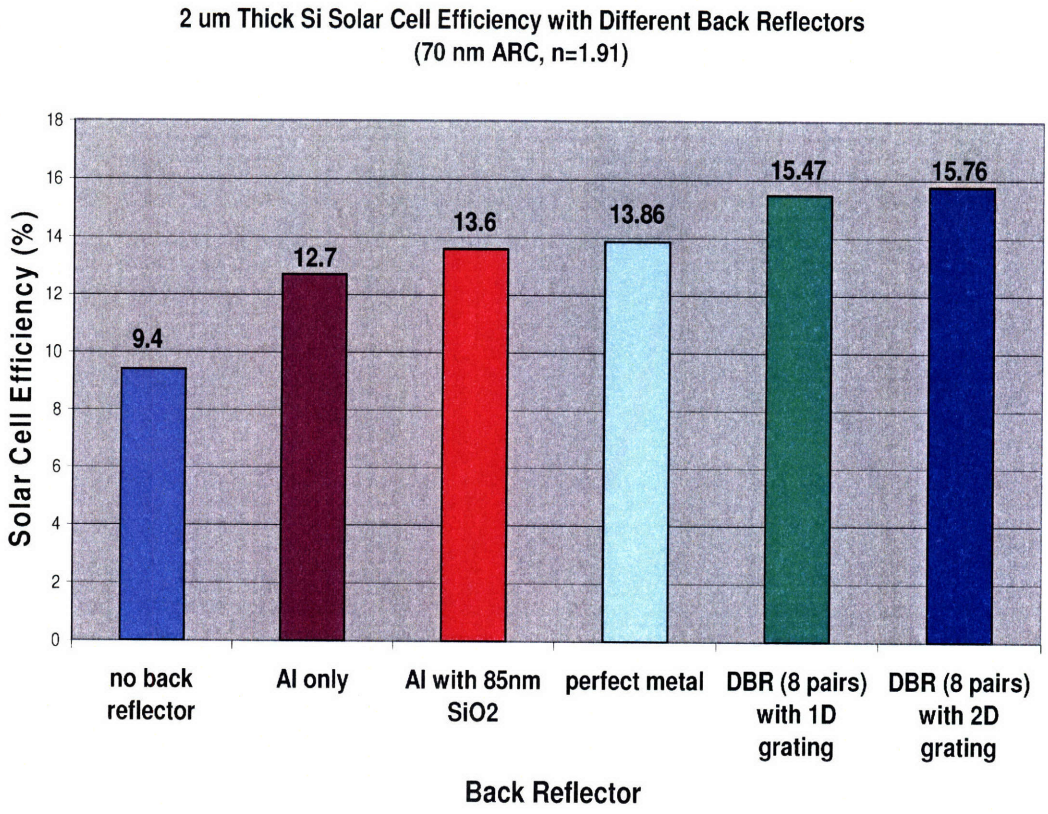

Fig. 4. 26 Efficiencies of 2μm thick Si solar cells with different back reflectors

absorption) into a perfect metal, and increases absolute cell efficiency by 4.7% (relative enhancement 45%) compared to the reference cell having no back reflector. However, our TPC back reflector gains significantly more efficiency enhancement: an 8-pair DBR plus 1D grating gains absolute efficiency enhancement of 6.1%, corresponding to a relative enhancement of 65%. If a 2D grating is used with DBR, the efficiency enhancement will be even higher (relative enhancement 68%).

The superiority of TPC back reflector over LFC can be best understood by inspecting the absorption spectra of the corresponding solar cells. As shown in Fig. 4.27,

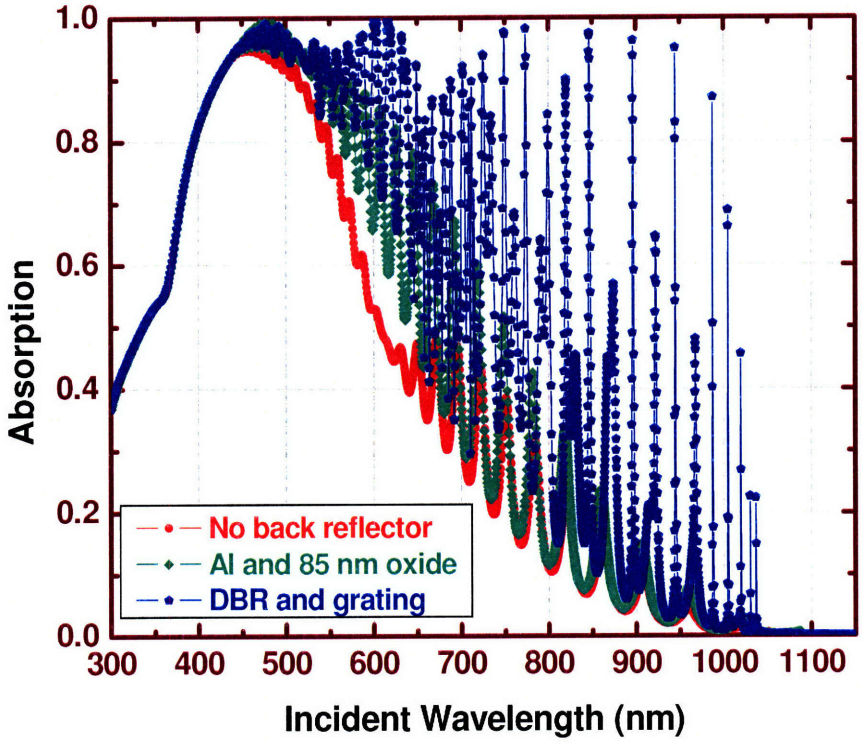

Fig. 4.27 Comparison of absorption spectra of 2 μm thick solar cells with laser fired contact and texture photonic crystal back reflectors

although at short wavelengths, the absorption spectra overlap, for λ>450nm, huge difference occurs, with TPC cell demonstrating much stronger and closely spaced absorption peaks, which do not decrease as wavelength increases.

4.3.5 Cell efficiency when actual parameters deviate from design values

The efficiency listed in Table 4.4 is obtained from the optimal ARC and back reflector parameters. During fabrication, there will be deviation from the ideal parameters, which will affect cell efficiency. Its influence can be easily estimated from the design

optimization figures in Section 4.3.2. Deviations shown in Table 4.6 result in efficiency reductions of only 0.2% (relative reduction ≈1.4%) for a 2 μm thick cell.

Table 4.6 Design parameters variation allowed for absolute cell efficiency reduction of 0.2% from the maximum value

Parameter	Grating depth	Grating period	Duty cycle	Bragg wavelength λ_B	ARC thickness*
Allowed variation	30 nm	50 nm	0.16	100 nm	30 nm

Note: SiO_2 ARC is considered here. If Si_3N_4/SiO_2 ARC is used as shown in Chapter 5, the allowed thickness variation will be 15 nm.

As the parameters have quite some latitude to deviate from the ideal values without major degradation in efficiency, normal fabrication tool accuracy is sufficient for this manufacturing. For example, grating etch depth and period can be easily controlled to within a few nanometers using RIE (reactive ion etching) and interference lithography, respectively. Duty cycle can be carefully optimized by adjusting the exposure time in interference lithography. Using PECVD machines, 4 nm thickness accuracy is easy to realize, so the allowed 100 nm Bragg wavelength variation for a DBR stack, which corresponds to layer thickness change of 7 nm for Si and 17 nm for SiO_2, can be easily controlled. For ARC, thermal oxide growth and LPCVD Si_3N_4 deposition is normally accurate to a couple of nanometers.

4.4 Comparison between results from coupled wave theory and scattering matrix method

In the previous two sections, using two different methods, coupled wave theory (CWT) and scattering matrix method (SMM), we systematically optimized the design parameters of crystalline thin film Si solar cells integrated with textured photonic crystal back reflector. Both methods showed that as cells become thinner, the efficiency enhancement that can be obtained from the optimized back reflector and antireflection coating increases. While CWT predicts a relative efficiency enhancement of 65% due to the back reflector (Table 4.3) for a 2 μm thick cell with an ARC material having refractive index 1.88 (possible SiOxNy), SMM calculations yields a relative enhancement of 53% using a SiO_2 ARC. As we will see in Chapter 5, with a double-layer ARC composed of Si_3N_4 and a thin underlying layer of SiO_2 (thermal oxide), an efficiency enhancement of 54% is predicted by SMM. The absorption spectra shown in Figs. 4.8, 4.20 and 4.21 are also quite similar. Both theories gave the same optimum grating duty cycle of 0.5.

In terms of design parameters for the back reflector, however, the two methods showed different results. First, CWT achieves maximum cell efficiencies with a grating period around 800 nm and etch depth 200 nm, seemingly using the 2nd order diffraction, and SMM obtains an optimal grating period of around 300 nm at a much shallower etch depth, utilizing the 1st order diffraction. Secondly, CWT does not show any obvious parameter variation relative to cell thickness, while all the parameters in SMM decrease for thinner cells. Besides the difference in grating parameters, DBR Bragg wavelength is fixed at 850 nm in CWT, but varies from 720-850 nm in SMM depending on cell

thickness, and the ARC central wavelength is 576 nm from CWT, and 530-630 nm from SMM. This could be attributed to several reasons: (a) In CWT, the active Si layer has a fixed real part of dielectric constant, 3.5, while SMM adopts a varying value when the wavelength differs. (b) In CWT, the solar cell substrate is air, while in SMM, a Si substrate is assumed because in real experimental fabrication, thin film Si must have a substrate. However, the influence from the substrate should be small given that in DBR most of the optical field is confined in the first layer of the stack material. Different substrate may render different grating etch depth. (c) CWT has been used before in grating study, while SMM has been a good method to solve multiple-layered structures. (d) CWT is usually applied to system with weak absorption, and how well it applies to a Si device layer that is supposed to be absorbing is unknown.

Another difference is that CWT shows that at all cell thicknesses, grating contributes more to cell efficiency improvements than DBR, while SMM demonstrates that for cells no thinner than 5 μm, DBR gains more efficiency enhancement than grating. SMM also verifies that the efficiency enhancement by DBR and grating combined is much more than the sum of the enhancement from the two components individually. This is reasonable as optical components may not display linear summation in their function.

Before application to the simulation presented in this chapter, we verified CWT method by duplicating some results on gratings in literature; and confirmed the SMM approach by simulating several solar cell structures using FDTD. Which method is more reasonable is yet to be studied further and verified by experiments.

Before concluding this chapter, it is noteworthy that in both CWT and SMM simulations, the simulated solar cell structures, as shown in Figs. 4.3 and 4.11, assume

flat DBR, although in experiments, if grating is formed before DBR deposition, the DBR will naturally be wavy due to the underlying uneven topography of grating, as shown clearly in Fig. 3.4 in Chapter 3. The extra periodicity in the plane of DBR films may contribute to light trapping by forming oblique angle reflection. Actually, as will be seen in Chapter 6, in our experimental work on thin film Si solar cells, wavy DBR plus grating back reflector outperforms flat DBR plus grating at all film thicknesses. However, simulation including this wavy DBR is quite challenging given the periodicities that already occur in grating and flat DBR (1D photonic crystal). Therefore, for future work, it would be beneficial to find a way to simulate solar cells with wavy DBR plus grating back reflectors and guide practice in order to take full advantage of TEXTURED photonic crystal light trapping capability.

References

[4.1] M. G. Moharam and T. K. Gaylord, J. Opt. Soc. Amer., vol. 71, no. 7, pp. 811–818, Jul. 1981.
[4.2] D. P. Pai and K. A. Awada, J. Opt. Soc. Amer. A, Opt. Image Sci., vol. 8, no. 5, pp. 755–762, May 1991.
[4.3] T. Tamir and S. Zhang, J. Lightw. Technol., vol. 14, no. 5, pp. 914–927, May 1996.
[4.4] Ning-ning Feng, Jurgen Michel, Lirong Zeng, Jifeng Liu, Ching-Yin Hong, Lionel C. Kimerling, and Xiaoman Duan, IEEE Transactions on electron Devices, vol. 54, no. 8, pp. 1926-1933, August 2007.
[4.5] C. Herzinger, B. Johs, W. McGahan, J. Woollam, and W. Paulson, J. Appl. Phys., vol. 83, no. 6, pp. 3323–3336, Mar. 1998.
[4.6] S. M. Sze, Physics of Semiconductor Devices, 2nd ed. Hoboken, NJ: Wiley, 1981, ch. 14, pp. 790–808.
[4.7] J. Nelson, The Physics of Solar Cells, Imperial College, London, 2003, pp. 22 and 264.
[4.8] Lirong Zeng, Peter Bermel, Yasha Yi, Ning-ning Feng, Bernard A. Alamariu, Ching-yin Hong, Xiaoman Duan, John Joannopoulos, and Lionel C. Kimerling, Mater. Res. Soc. Symp. Proc. Vol. 974, CC02-06, 2007.
[4.9] D. Y. K. Ko and J. C. Inkson, Phys. Rev. B **38**, 9945 (1988).
[4.10] M. Auslender and S. Hava, Optics Letters, **21,** 1765 (1996).
[4.11] D. Whittaker and I. Culshaw, Phys. Rev. B **60**, 2610 (1999).
[4.12] W. Shockley and H. J. Queisser, J. Appl. Phys. **32**, 510 (1961).
[4.13] C. Henry, J. Appl. Phys. 51, 4494 (1980).
[4.14] C. Herzinger, B. Johs, W. McGahan, J. Woollam, and W. Paulson, J. Appl. Phys. **83**, 3323 (1998).
[4.15] ASTMG173-03, Standard Tables for Reference Solar Spectral Irradiances: Direct Normal and Hemispherical on 37 degree Tilted Surface, ASTM International, West Conshohocken, Pennsylvania, 2005.

[4.16] K. S. Yee, IEEE Trans. Attennas Propag. AP-14, 302 (1966).
[4.17] J. Berenger, J. Comp. Phys. **114**, 185 (1994).
[4.18] Peter Bermel, Chiyan Luo, Lirong Zeng, Lionel C. Kimerling, and John D. Joannopoulos, Optics Express, Vol. 15, No. 25, 16986 (2007).

CHAPTER 5

Identification of the Best Antireflection Coating for Thin film Si Solar Cells

Although in both Chapters 3 and 4, thermal oxide was used as an antireflection coating (ARC) for good surface passivation, in terms of optical response, SiO_2 is not the best choice due to its low refractive index. In this chapter, we will examine the different materials choice and identify the best ARC for thin film Si solar cells

5.1 General requirements for solar cell antireflection coating

The front surface dielectric coating plays an important role in determining solar cell performance. Although each of the three most commonly used metallization schemes, namely evaporated metal contacts, screen printing, and buried contact, has different requirements [5.1], there are inherent common requirements, as well. These include:

1) reduction of reflection;

2) providing surface passivation, especially for thin film solar cells;

For buried-contact solar cells, the dielectric coating has to be

3) insulating as well to allow selective plating of metal contacts.

Since our back reflector is not conducting due to the dielectric distributed Bragg Reflector (DBR) stack, we choose interdigitated top contacts, not one of the three metallization schemes just mentioned. Top contact cells have the same three general requirements, with the additional requirement of allowing maximum light admission into the cell by minimizing the metallization area. As with buried contact solar cells, the dielectric coating must also be an insulator, to prevent shorting between the p and n regions.

5.1.1 Low reflection

The reflectivity at the interface between two media is determined by their refractive indices n_0 and n_s. In the simplest case of planar surfaces, at normal incidence, the light is reflected with probability

$$R = \left(\frac{n_0 - n_s}{n_0 + n_s} \right)^2 \qquad (5.1).$$

For air incidence, $n_0=1$, and since most semiconductors have indices n_s equal 3-4 at visible wavelengths, around 30-40% of the light normally incident from free space onto the semiconductor surface will be reflected. To reduce reflection, a thin layer of dielectric film with refractive index n_1 satisfying $n_0<n_1<n_s$ can be applied to the surface of semiconductor and serve as an antireflection coating (ARC) [5.2].

To achieve minimum reflection loss at a certain incident wavelength λ_0, ARC should have an index n_1 satisfying

$$n_1 = \sqrt{n_0 n_s} \qquad (5.2),$$

and thickness t determined by

$$t=\lambda_0/4n_1 \qquad (5.3),$$

For air incidence, although $n_0=1$ is constant, the solar spectrum is wide, and the wavelengths that can possibly be absorbed by Si range from 300 nm to near 1.2 μm, and the refractive index of Si, n_s, varies significantly in this wavelength range, as shown in Fig. 5.1. Therefore, index match at one wavelength does not mean high light admission over the entire solar spectrum. Meanwhile, the well-admitted light needs to be well-absorbed by the semiconductor, i.e., adequate internal quantum efficiency (IQE) is necessary. This relation can be best embodied by the following expression of short-circuit current density

$$\begin{aligned} J_{SC} &= q\int_{\lambda_{min}}^{\lambda_{max}} (1-R(\lambda)-A(\lambda))N_{ph}(\lambda)IQE(\lambda)d\lambda \\ &= q\int_{\lambda_{min}}^{\lambda_{max}} T(\lambda)N_{ph}(\lambda)IQE(\lambda)d\lambda \end{aligned} \qquad (5.4),$$

where $R(\lambda)$ is the wavelength dependant reflectivity of ARC, $A(\lambda)$ is its absorption in the case where it absorbs in the UV region of the solar spectrum. $T(\lambda)$ is its transmission. N_{ph} (λ) is incident solar photon flux at that wavelength. Clearly, J_{sc} is an integrated effect of ARC reflection and semiconductor absorption over the whole solar spectrum. Therefore, optimization of ARC is a quite complicated issue. Careful simulation which takes solar

cell efficiency as the ultimate indicator is necessary in order to identify the best ARC material and thickness.

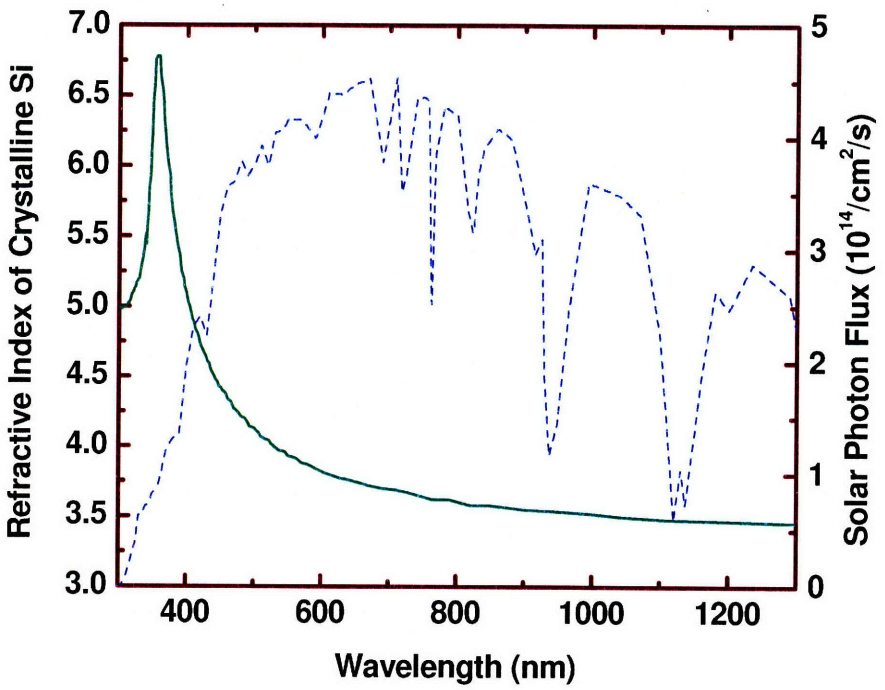

Fig. 5.1 Refractive index of crystalline Si and solar photon flux vs. wavelength (AM1.5)

Compared to single layer ARC, ARC composed of two or more thin films can render improved reflectivity over a range of wavelengths. However, due to cost considerations and sensitivity to angle of incidence, multiple layers are generally not used except on some high efficiency cells. The layer indices should increase consecutively from air (n_0) to first coating (n_1) to second coating (n_2) and to semiconductor (n_s)[5.2], i.e.

$$n_0 < n_1 < n_2 < n_s. \qquad (5.5).$$

For single incident wavelength, zero reflectivity is achieved when both films have quarter-wave thickness and satisfies

$$(\frac{n_2}{n_1})^2 = \left(\frac{n_s}{n_0}\right). \qquad (5.6).$$

5.1.2 Good surface passivation

Due to the termination of periodic crystalline structure, there are many dangling bonds and defects at the semiconductor surface, which create bandgap states and serve as free carrier traps. For thin film solar cells, high quality surface passivation is more important compared to bulk solar cells. It not only determines carrier collection efficiency, and thereby directly affects J_{sc}; it also determines solar cell dark reverse saturation current density J_0, which influences V_{oc} through

$$V_{oc} = \frac{nKT}{q}\ln(\frac{J_{sc}}{J_0} + 1) \qquad (5.7),$$

where n is the diode ideality factor. Good surface passivation is essential to realize small J_0 and high V_{oc}.

In solar cells, surface passivation can be achieved either by reducing the defect density at the surface, or by reducing the number of excess minority carriers reaching the surface, and thereby reducing the effective surface recombination velocity [5.3]. The former can be achieved by growing a layer of SiO_2, or by hydrogen termination of dangling bonds. The latter can be accomplished by introducing a region of higher doping. Techniques using this approach include inversion layer passivation, back or front surface fields, and floating junction passivation. Besides low reflectivity, a good ARC should also afford good surface passivation.

5.1.3 Good insulator

For top-contacted solar cells, ARC must be insulating in order to prevent shorting the p and n contacts. This is also a requirement for buried-contact solar cell, a high-efficiency bulk solar cell developed at the University of New South Wales in the mid-1980s and later commercialized by BP Solar, in order to selectively plate nickel and copper contacts into the heavily doped grooves [5.1].

5.1.4 Commonly used ARC materials for Si solar cells

From Fig. 5.1, it is obvious that the refractive index of Si is above 3.5 for all wavelengths below 1.2 μm. Eq. (5.2) renders an ARC refractive index of $n_1>1.87$. A wide variety of dielectrics have been tried as ARC on Si solar cells [5.1], including silicon dioxide (SiO_2), LPCVD (Si_3N_4) and PECVD silicon nitride (a-SiN_x:H), silicon oxynitride (SiON), cerium dioxide (CeO_2), zinc sulphide (ZnS), titanium dioxide (TiO_2), zinc oxide [5.4], tantalum oxide [5.2], and electrochemically formed porous Si [5.5, 5.6]. Among these, the more commonly used materials are SiO_2, Si_3N_4, a-SiN_x:H [5.1]. SiON also aroused some attention due to its tunability of refractive index.

Thermally grown SiO_2 has been widely used in laboratory-scale processing and in the development of buried-contact solar cells due to its ease of fabrication, excellent surface passivation capability and very good electrical insulation, but its low refractive index ($n_1\approx1.46$) makes it only appropriate as a rudimentary ARC, and it barely offers any ARC benefit once the solar cell is encapsulated under ethyl vinyl acetate (EVA) and glass, both of which have a refractive index around 1.5 over most of the solar spectrum.

LPCVD Si_3N_4 exhibits a refractive index n_1=2.0-2.2 over λ=300-1200 nm and therefore works much better as an ARC for encapsulated Si solar cells than SiO_2. It is also an excellent electrical insulator. However, the major drawback of Si_3N_4 is that it affords little or no surface passivation of the silicon surface [5.7]. LPCVD Si_3N_4 contains less than 3 atomic % hydrogen. Due to the high film deposition temperature (700-800°C), hydrogen will out-diffuse during the deposition process, causing the film to lose its surface passivation capacity.

While LPCVD Si_3N_4 exhibits quite stable properties, those of PECVD deposited films (a-SiN_x:H) vary significantly, depending on the deposition system, process conditions, and gas composition. Its index can be tuned from 1.95 to 2.3 [5.1], and offers good antireflection properties. When not subjected to high-temperature processing, a-SiN_x:H films can provide excellent surface passivation due to very high fixed positive charge density, which produces an inversion layer at p-type silicon surface [5.8], and can provide bulk passivation of crystallographic defects in multi-crystalline Si as well owing to its high hydrogen concentration (25-40 atomic % hydrogen). However, the electronic benefits are hard to retain during lengthy high-temperature processing. Furthermore, because of the low deposition temperature (<450°C) and high hydrogen concentration, a-SiN_x:H films are usually not as dense as LPCVD Si_3N_4 films. Pinholes and micro-cracks which can cause short circuit defect are often observed in these films, and blistering effects can also occur due to the large hydrogen content [5.9].

The refractive index of SiON can be tuned in a wide range, from 1.46 of SiO_2 to more than 2.0 of Si_3N_4, by changing the ratio of nitrogen: oxygen (N:O). Unfortunately, application of SiON to Si solar cells as ARC demonstrated low V_{oc} and J_{sc} due to poor-

quality surface passivation and its low refractive index (n≈1.7) [5.10]. However, since material quality can vary depending on deposition conditions, and the index can be tuned to be higher, it is still worth while to do some study on this material.

From the discussion above, it seems desirable to combine the electronic benefits of thermal SiO_2 and the optical and other advantages of Si_3N_4. There were tests done using an insulation layer of SiO_2 (50 nm) under SiN [5.3], with results of improved surface passivation by the SiO_2, but at the cost of increased reflection. Besides single-layer ARC, double-layer ARC based on PECVD SiO_2/SiN [5.3], SiO_2/Si_3N_4 [5.11] and SiO_2/TiO_2 [5.12] were also tried, with SiO_2 as a top layer due to index match requirements.

Since adding more layers to ARC increases complexity and the sensitivity to angle of incidence [5.2], in this thesis, we will focus on single-layer ARC based on SiO_2, Si_3N_4, and SiON, and double-layer ARC composed of Si_3N_4 or SiON with a thin passivation thermal oxide layer, denoted as Si_3N_4/SiO_2 and $SiON/SiO_2$. For the passivation oxide, our major goal is to identify the minimum thickness which can offer adequate surface passivation without hampering the optical properties. In the following sections, we will examine these five materials systems in terms of optical response, surface passivation capability and dielectric breakdown voltage.

5.2 Optical response simulation

This section examines the optical response of five materials systems: SiO_2, Si_3N_4, SiON, Si_3N_4/SiO_2, and $SiON/SiO_2$ by scattering matrix simulation. For each ARC material, we will identify the optimal thickness for highest efficiency, and then compare

the highest efficiencies given by the differing materials. 100% carrier collection efficiency is assumed to make optical effects prominent and back reflector parameters are fixed at the optimal values obtained from scattering matrix simulation in Chapter 4.

Figs. 5.2 and 5.3 illustrate the dispersion curves of SiO_2 and Si_3N_4 [5.13]. For photons with wavelengths 300 nm $<\lambda<$ 1.2 μm, i.e., energies 1.03 eV$<$ E $<$4.1 eV, the refractive index of Si_3N_4 is between 2.0 and 2.16 and that of SiO_2 is between 1.45 and 1.49 [3]. Due to the small dispersion and the limit in accurate film thickness control (will be explained later, at the end of section 5.2.1), in our simulation, the indices of SiO_2 and Si_3N_4 are taken as 1.46 and 2.0. As for SiON, a former graduate student in our research group, Dr. Victor Nguyen, developed PECVD recipes for several SiO_xN_y films with indices from 1.67 to 1.895 at λ=633nm. Since higher index is desirable, we will only consider the film with n=1.895. Fig. 5.4 shows the fitted dispersion curve of SiON based on Cauchy Equations. Since for 400 nm $<\lambda<$ 1.2 μm (1.03 eV$<$ E $<$3.1 eV), 1.88 $<$n $<$1.95, taking the average gives n=1.91. Photons with λ<400nm are not considered in the averaging here for two reasons: first, in solar spectrum, this portion of photon flux is very low; and second, the external quantum efficiency is often limited by surface recombination, therefore the admitted photons can not be well utilized by the solar cell.

Four different solar cell thicknesses: 2, 5, 20 and 50 μm will be considered. For each solar cell thickness, we will simulate solar cell efficiency with the flowing ARC structures:

(1) SiO_2 -only ARC;

(2) Si_3N_4-only ARC;

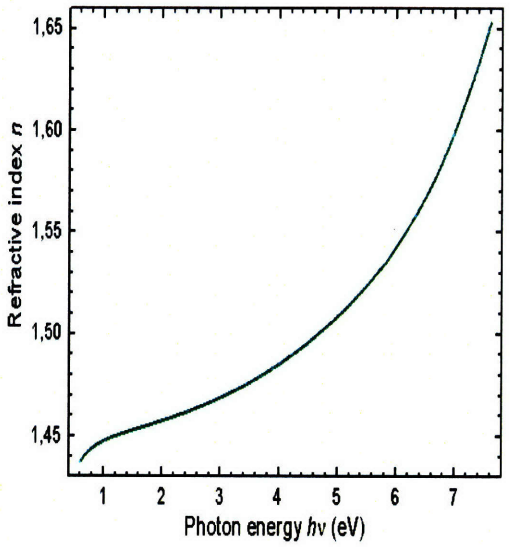

Fig. 5.2 Dispersion curve of SiO_2 [5.13]

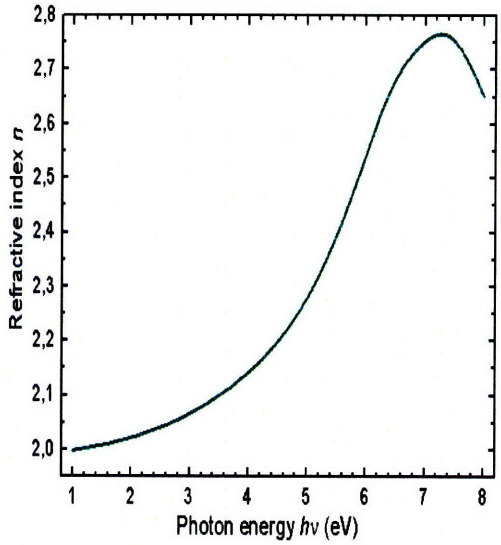

Fig. 5.3 Dispersion curve of Si_3N_4 [5.13]

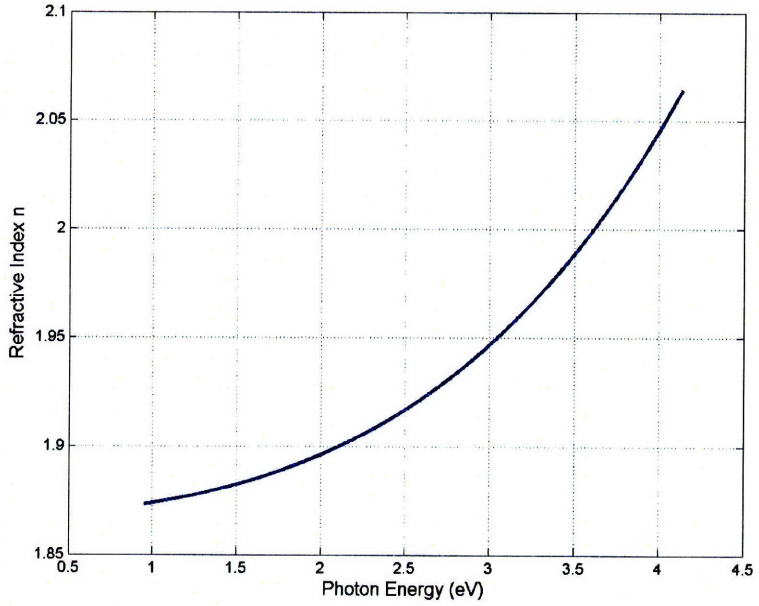

Fig. 5.4 Fitted dispersion curve of SiON film with n=1.895 @ λ=633nm. n and k data courtesy of Dr. Victor Nguyen [5.14]

(3) Si_3N_4 ARC with a thin SiO_2 passivation layer, abbreviated as Si_3N_4/SiO_2 double ARC;

(4) SiON-only ARC;

(5) SiON ARC with a thin SiO_2 passivation layer, abbreviated as $SiON/SiO_2$ double ARC.

For simulations (3) and (5) above, the Si_3N_4/SiO_2 and $SiON/SiO_2$ double ARC, we will follow a three-step procedure:

a) fix SiO_2 thickness at 4nm, which is the smallest thickness for adequate surface passivation, and adjust Si_3N_4 or SiON thickness;

b) fix Si_3N_4 or SiON thickness at the optimal thickness found above, and vary SiO_2 thickness;

c) vary SiO_2 and Si_3N_4 or SiON thicknesses simultaneously: scan SiO_2 thickness, and for each SiO_2 thickness, calculate the corresponding Si_3N_4 or SiON thickness and the solar cell efficiency.

In the following sections, we will show the detailed simulation procedure of the 5 μm thick cell as an example, and present the simulation results of cells at the other three thicknesses.

5.2.1 ARC simulation for 5 μm thick Si solar cells

Figs. 5.5 through 5.8 depict how the ARC thickness influences Si solar cell efficiency for cells with a 5 μm thick active device layer. Figs. 5.5 and 5.6 show that for a single-layer ARC made of SiO_2 or Si_3N_4, there is an optimal thickness, 100 nm for SiO_2 and 70 nm for Si_3N_4, which renders highest cell efficiency. It is obvious that simply by

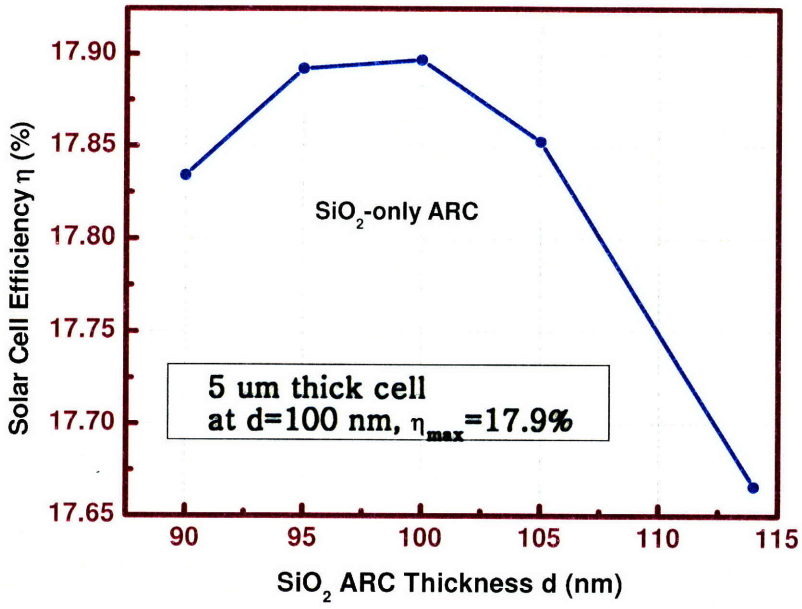

Fig. 5.5 Solar cell efficiency vs. SiO_2 antireflection coating thickness for Si solar cells with a 5 μm thick active layer

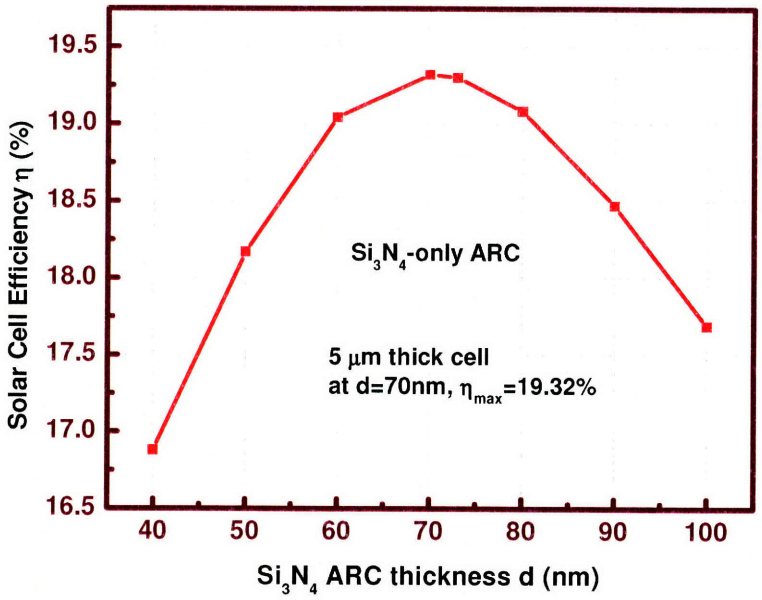

Fig. 5.6 Solar cell efficiency vs. Si_3N_4 antireflection coating thickness for Si solar cells with a 5 μm thick active layer

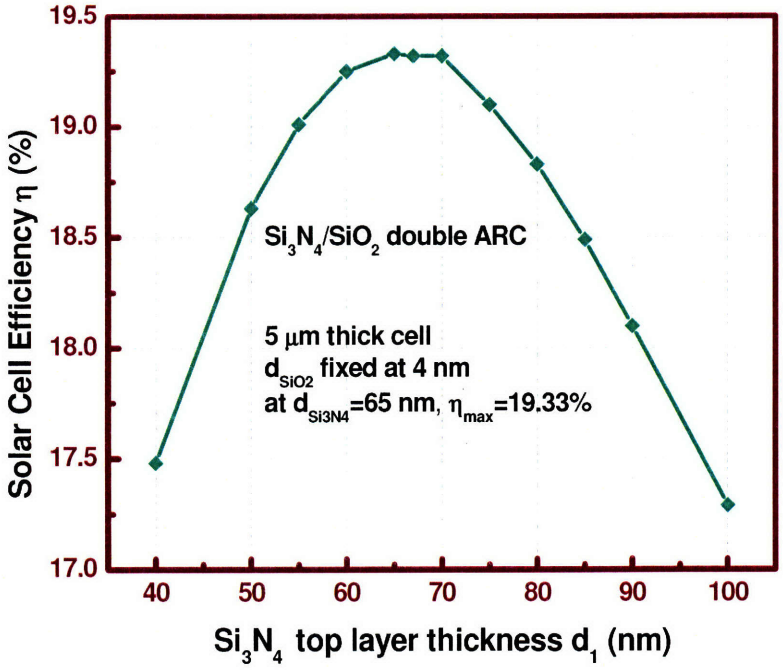

Fig. 5.7 Solar cell efficiency vs. Si_3N_4 top layer thickness of a Si_3N_4/SiO_2 double-layer antireflection coating for Si solar cells with a 5 μm thick active layer. The bottom SiO_2 layer thickness is fixed at 4 nm

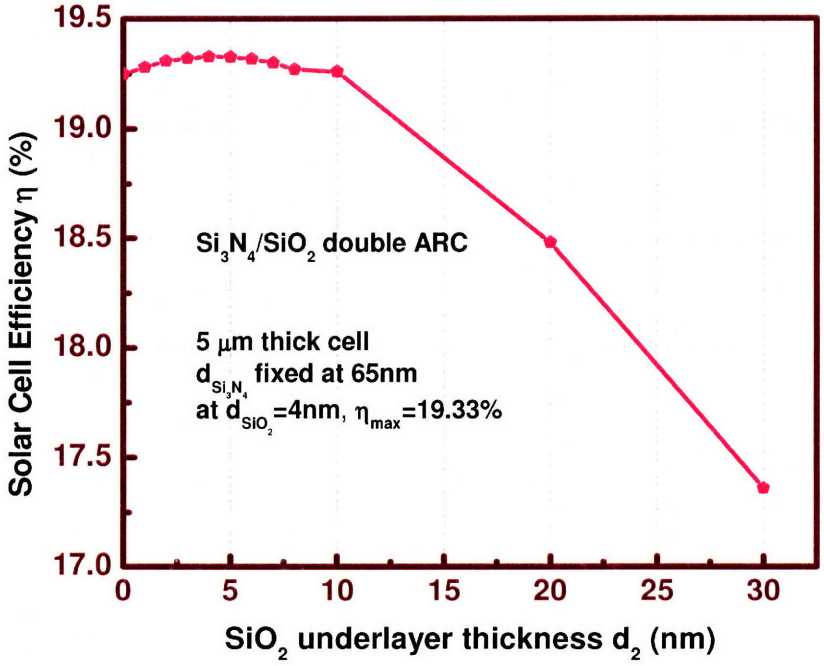

Fig. 5.8 Solar cell efficiency vs. SiO_2 bottom layer thickness of a Si_3N_4/SiO_2 double-layer antireflection coating for Si solar cells with a 5 μm thick active layer. The top Si_3N_4 layer thickness is fixed at 65 nm

changing the ARC from SiO_2 to Si_3N_4, cell efficiency η can be increased from 17.9% to 19.32%, an absolute increase of 1.42%. Fig. 5.7 shows that for Si_3N_4/SiO_2 double ARC, when the SiO_2 underlayer thickness d_2 is fixed at 4 nm, there is a prominent peak at a Si_3N_4 top layer thickness d_1=65 nm, giving η=19.33%. Fig. 5.8 indicates that when d_1 is fixed at 65 nm, η first increases slightly when d_2 is increased from zero, and reaches a peak value of 19.33% at d_2=4 nm, and then starts to drop slowly. For $0<d_2<8$ nm, η is almost flat. When d_2 is further increased, η decreases rapidly. With a 30 nm thick SiO_2 underlayer, η=17.36%, much lower than cells with a single-layer optimized SiO_2 ARC.

Since d_1=65 nm and d_2=4 nm may not be the optimal combination, η with simultaneously changing d_1 and d_2 is also calculated, as shown in Table 5.1. Because Fig. 5.6 shows an optimal thickness of 70 nm for a single-layer Si_3N_4 ARC, for Si_3N_4/SiO_2 double ARC with a SiO_2 thickness d_2, the corresponding Si_3N_4 thickness d_1 is

$$d_1 = 70 - \frac{n_2 d_2}{n_1} \qquad (5.8),$$

Table 5.1 Simulated Si solar cell efficiency for cells with 5 μm thick active layer and Si_3N_4/SiO_2 double layer antireflection coating

Bottom layer SiO_2 thickness d_2 (nm)	Top layer Si_3N_4 thickness d_1(nm)	Solar cell efficiency η
0	70	19.32
4	**67**	**19.32**
8	64	19.29
10	63	19.26
20	55	19.09
30	48	18.82

where n_1 and n_2 are the refractive index of Si_3N_4 and SiO_2, respectively. $\frac{n_2 d_2}{n_1}$ denotes the equivalent thickness of Si_3N_4 for a SiO_2 layer with thickness d_2, which should be deducted from the optimal thickness of 70 nm. Table 5.1 shows that when SiO_2 thickness exceeds 4 nm, even if Si_3N_4 thickness is adjusted accordingly, cell efficiency decreases. At d_2=30 nm and d_1=48 nm, η drops to 18.82%. Note that this efficiency is still much higher than the case where d_2=30 nm with d_1 fixed at 65 nm (η=17.36%).

Figs. 5.9 through 5.11 display the simulation results with SiON and SiON/SiO_2 double ARC. For single-layer SiON ARC, the highest efficiency of 19.28% is achieved at d=76nm. For SiON/SiO_2 double ARC, when SiO_2 is 4 nm thick and d_1=70 nm,

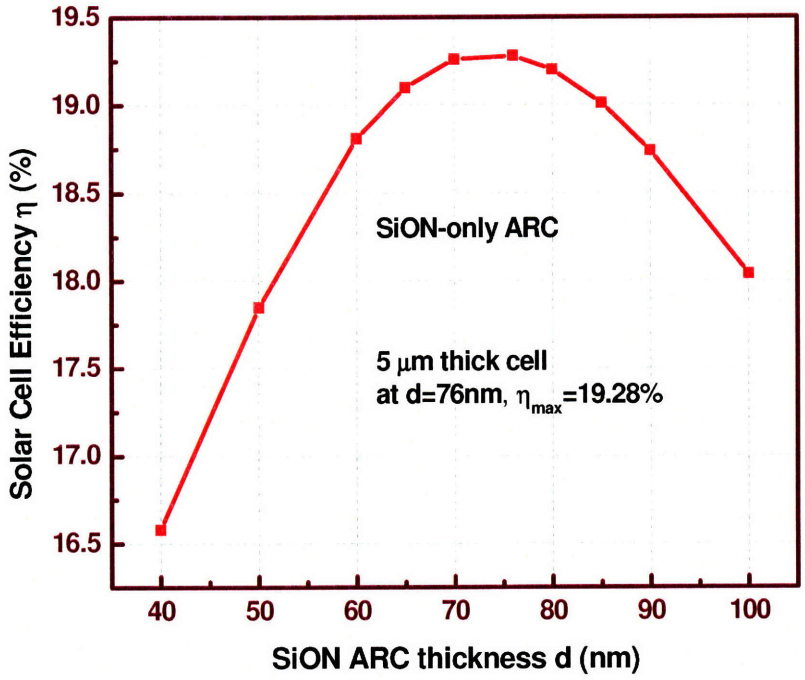

Fig. 5.9 Solar cell efficiency vs. SiON antireflection coating thickness for Si solar cells with a 5 μm thick active layer

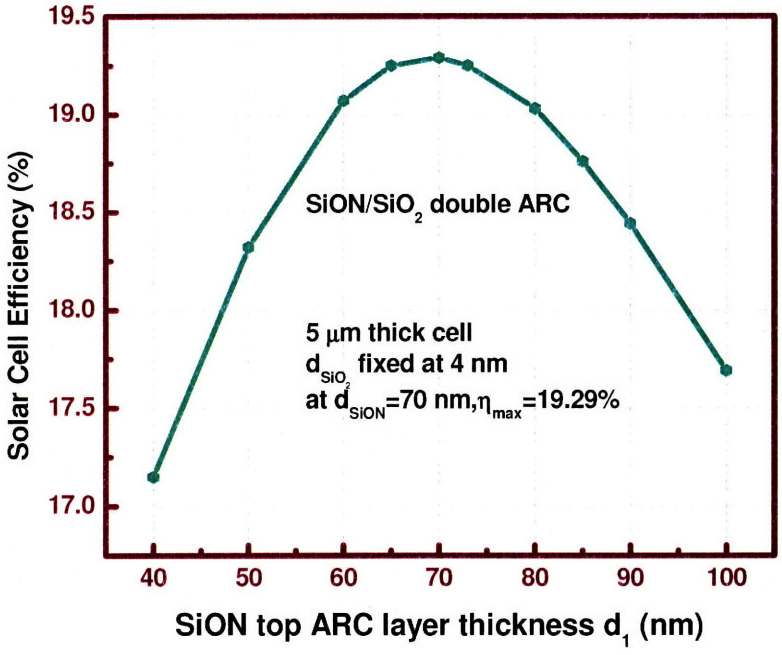

Fig. 5.10 Solar cell efficiency vs. SiON top layer thickness of a SiON /SiO_2 double-layer antireflection coating for Si solar cells with a 5 μm thick active layer. The bottom SiO_2 layer thickness is fixed at 4 nm

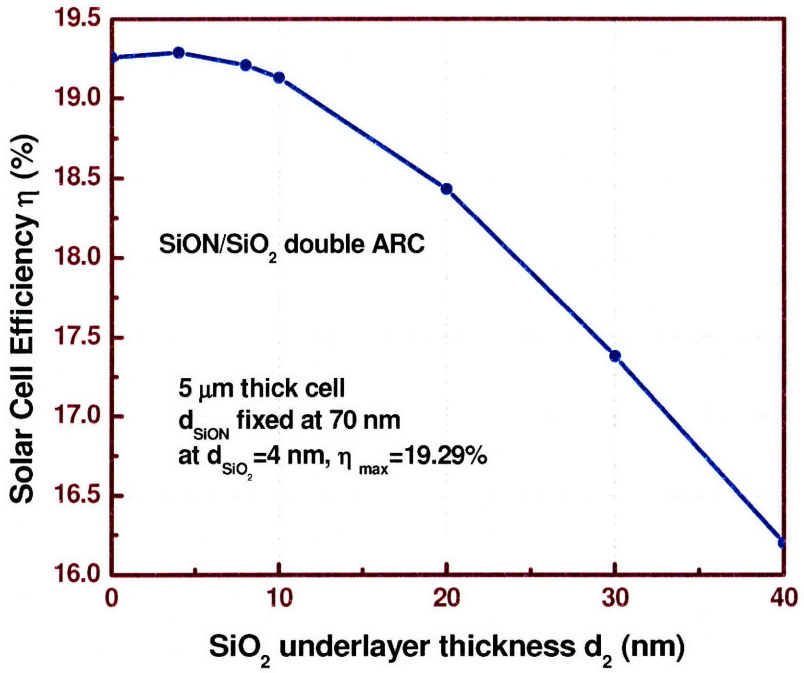

Fig. 5.11 Solar cell efficiency vs. SiO_2 bottom layer thickness of a SiON/SiO_2 double-layer antireflection coating for Si solar cells with a 5 μm thick active layer. The top SiON layer thickness is fixed at 70 nm

η_{max}=19.29%, with η decreasing continuously as SiO_2 thickness increases. Table 5.2 shows the variation of cell efficiency while SiON and SiO_2 layer thicknesses change simultaneously. Except for rows with d_2=0 and 4nm, where d_1 is fixed intentionally at 70 nm, as SiO_2 thickness changes, the resulting SiON thickness, calculated from Eq. (5.8) with 70 replaced with 76, and with n_1=1.91, is shown. At d_2=4 nm, cell efficiency is the highest.

Table 5.2 Simulated Si solar cell efficiency for cells with 5 μm thick active layer and SiON/SiO_2 double layer antireflection coating

Bottom layer SiO_2 thickness d_2 (nm)	Top layer SiON thickness d_1(nm)	Solar cell efficiency η
0	70	19.26
4	**70**	**19.29**
8	70	19.21
10	68	19.19
20	61	18.96
30	53	18.70
40	45	18.46

Table 5.3 Antireflection coating simulation results for 5 μm thick Si solar cells

ARC material	Optimal ARC thickness d (nm)	Solar cell efficiency η (%)
SiO_2	100	17.90
Si_3N_4	70	19.32
Si_3N_4/ SiO_2 double layer	**65/4**	**19.33**
SiON	76	19.28
SiON/ SiO_2 double layer	70/4	19.29

Table 5.3 summarizes the simulation results for 5 μm thick Si solar cells. Among all five materials systems, Si_3N_4/ SiO_2 double layer ARC with d_1=65 nm and d_2=4 nm renders the highest cell efficiency, just above that of the single-layer Si_3N_4 ARC.

Earlier in section 5.1, we mentioned that in the simulation, one reason to set the index of SiON at an average value of 1.91 instead of more precise one-to-one n-λ correspondence is due to the limit of accurate film thickness control. This is because for the optical properties of a film, an important quantity is the equivalent optical path length, n times d, where n is the refractive index, and d is the film thickness. To maintain a certain equivalent optical path length, if n changes, d needs to change accordingly. Assume that nd=C, where C is a constant. Taking derivative of both sides of the equation, one gets

$$\frac{\Delta n}{n} = -\frac{\Delta d}{d} \qquad (5.9).$$

Suppose n=1.91 and d=76 nm, a variation of n from 1.88 to 1.95 renders Δn=0.07, and Eq. 5.9 gives $|\Delta d|$=2.78 nm. Therefore, in order to make the accurate n-λ correspondence meaningful, one must be able to control the film thickness within 2.78 nm. This is difficult to achieve with a PECVD machine, whose deposition velocity is often above 4 nm/s, and the thickness variation on one film often exceeds 4 nm, too. Thus to simplify simulation, n of SiON is set at 1.91.

5.2.2 ARC simulation for Si solar cells at other thicknesses

Following the same procedure as with 5 μm thick Si solar cells, scattering matrix simulation was done on cells with active layer thicknesses at 2, 20 and 50 μm. Tables 5.4 through 5.6 summarize the results. The following conclusions can be made:

(i) SiO_2 ARC gives the lowest cell efficiency;

(ii) Si_3N_4, Si_3N_4/SiO_2, SiON, and SiON/ SiO_2 ARC render similar efficiencies;

(iii) Si_3N_4 and Si_3N_4/ SiO_2 double layer with a SiO_2 thickness of 4 nm provide the highest efficiency, slightly higher than that from SiON and SiON/ SiO_2 ARC.

As shown in Fig. 5.12, as the cell becomes thicker, for Si_3N_4/ SiO_2 double ARC, the optimal Si_3N_4 top layer thickness increases. This is because the optimal ARC thickness is determined by the interference effect contributed by the entire solar cell structure, including the active layer (and back structure), not just the ARC material.

Table 5.4 Antireflection coating simulation results for 2 μm thick Si solar cells

ARC material	Optimal ARC thickness d (nm)	Solar cell efficiency η (%)
SiO_2	92	14.43
Si_3N_4	67	15.54
Si_3N_4/ SiO_2 double layer	**60/4**	**15.55**
SiON	70	15.51
SiON/ SiO_2 double layer	65/4	15.52

Table 5.5 Antireflection coating simulation results for 20 μm thick Si solar cells

ARC material	Optimal ARC thickness d (nm)	Solar cell efficiency η (%)
SiO_2	105	21.92
Si_3N_4	77	23.36
Si_3N_4/ SiO_2 double layer	**70/4**	**23.39**
SiON	80	23.35
SiON/ SiO_2 double layer	77/4	23.34

Table 5.6 Antireflection coating simulation results for 50 μm thick Si solar cells

ARC material	Optimal ARC thickness d (nm)	Solar cell efficiency η (%)
SiO_2	108	23.71
Si_3N_4	75	25.10
Si_3N_4/ SiO_2 double layer	**72/4**	**25.11**
SiON	80	25.09
SiON/ SiO_2 double layer	75/4	25.09

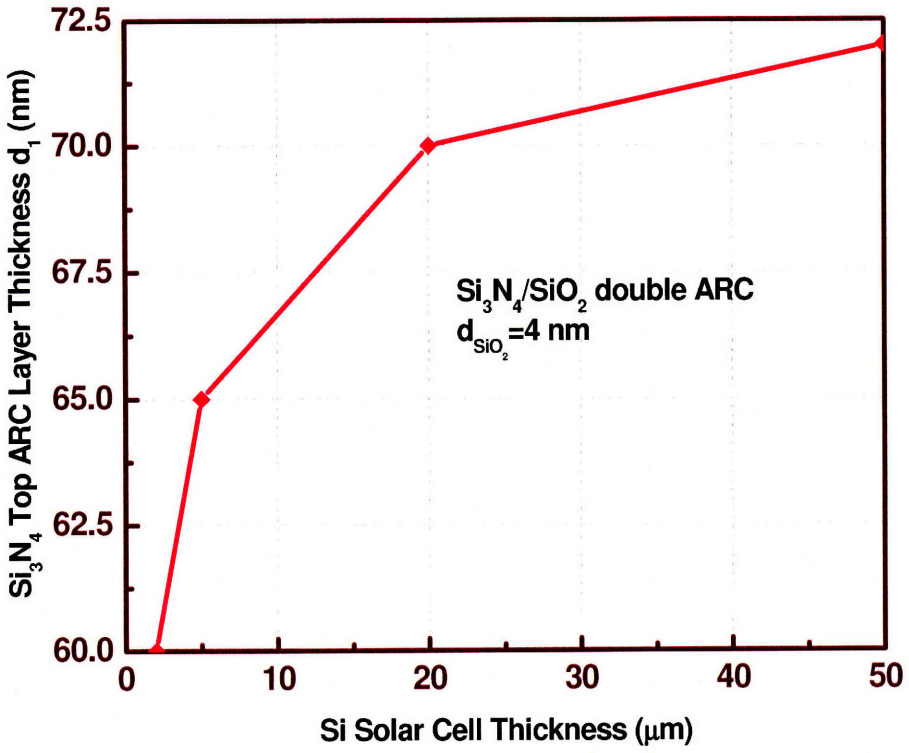

Fig. 5.12 Optimal Si_3N_4 top layer thickness vs. Si active layer thickness for solar cells with Si_3N_4/SiO_2 double layer antireflection coating

To choose an ARC material to be used on the solar cells we are going to fabricate, there are some practical considerations as well as theoretical ones. SiON does not seem to be the best choice, as it offers no optical advantage over Si_3N_4, nor were its electrical properties well characterized on the PECVD tool at MTL, the MIT cleanroom fabrication facility where the solar cells in this thesis are made. Victor Nguyen has been the only one to develop or use a PECVD recipe for SiON, and that was more than two years ago. He studied the optical properties of SiON for waveguide applications, and no electrical research was performed. Moreover, the PECVD machine has been suffering from serious blistering problems for months this year, as will be discussed in detail in Chapter 6 on silicon on insulator (SOI) solar cell fabrication. Given these limitations, in the following

chapters on surface passivation and dielectric strength study, we will not be considering SiON.

Si_3N_4 and Si_3N_4 with a thin passivation layer have similar optical responses, so should we bother to grow this thin thermal oxide? Can adding the 4 nm thick SiO_2 offer much more surface passivation? Sections 5.3 and 5.4 will answer this question.

5.3 Surface passivation study

Besides good antireflection properties, an ARC should also provide sufficient surface passivation; otherwise what is gained optically may be lost electrically due to poor collection of photogenerated carriers.

5.3.1 Photoconductance decay as a surface probe

Surface states are allowed electronic states caused by dangling bonds due to the abrupt termination of periodic crystalline lattice, defects and impurities. They are recombination centers. Ways to passivate them include termination of dangling bonds by atomic hydrogen and chemical reactions with halogens [5.15]. HF can provide excellent surface passivation to Si by terminating the surface with H atoms. Creating electrical potential which repels minority carriers away from the surface is also an effective way to passivate the surface.

Surface recombination depends on how fast carriers reach the surface due to drift and /or diffusion and how fast they recombine via surface recombination centers. The degree of surface passivation is quantified by surface recombination velocity S, which is one of the major determinants of minority carrier lifetime. Usually the effective minority

carrier life time τ_{eff} has two components: bulk lifetime τ_b and surface lifetime τ_s, and satisfies this equation from reference [5.16]

$$\frac{1}{\tau_{eff}} = \frac{1}{\tau_b} + \frac{1}{\tau_s} \qquad (5.10).$$

If the bulk lifetime τ_b is the same for wafers passivated by different means, the difference in τ_{eff} will tell the difference in τ_s, which has the following relation with S:

At low S,

$$\frac{1}{\tau_{eff}} = \frac{1}{\tau_b} + \frac{2S}{d} \qquad (5.11);$$

For large S (S→∞),

$$\frac{1}{\tau_{eff}} = \frac{1}{\tau_b} + \frac{D_n \pi^2}{d^2} \qquad (5.12),$$

and τ_{eff} is independent of S. For polished Si surfaces, high S starts at ~10^4 cm/s [5.15].

For semiconductors with large bulk lifetimes ($\tau_b \geq 1$ ms), Eq. (5.11) gives

$$\frac{1}{\tau_{eff}} = \frac{2S}{d} \qquad (5.13),$$

or equivalently

$$S = \frac{d}{2\tau_{eff}} \qquad (5.14).$$

When both S and τ_b are large, Eq. (5.12) simplifies to

$$\tau_{eff} = \frac{d^2}{D_n \pi^2} \qquad (5.15),$$

indicating that the effective lifetime is just the average time it takes the carriers to arrive at the semiconductor surface.

Photoconductance decay (PCD) is a sensitive means to measure minority carrier lifetime. During PCD measurements, free carriers are injected into the semiconductor by shining a beam of light onto the sample, and then the decay time τ_{eff} of minority carriers is measured. When the bulk lifetime is held constant, the change in lifetime τ_{eff} tells the surface quality difference. We will use contactless RF-PCD to examine the surface passivation capability of different films mentioned in section 5.2 for ARC applications.

5.3.2 Sample preparation for photoconductance decay measurements

To measure τ_{eff} of samples with different antireflection coatings, 14 prime Si wafers were taken out of the same cassette. They are 625±15 μm thick, (100) orientated, boron doped, ρ=5-15 Ω-cm, corresponding to a doping level of $1\text{-}3x10^{15}/cm^3$.

After RCA clean, the following 7 types of samples were prepared, two wafers for each type:

(i) thick thermal oxide (107 nm): 800°C, 3 hours, dry oxidation;

(ii) thin thermal oxide (8.1 nm): 800°C, 95 minutes, dry oxidation;

(iii) thinner thermal oxide (4.5 nm): 800°C, 30 minutes, dry oxidation;

(iv) thick LPCVD Si_3N_4 (60 nm): LPCVD, 775°C, 26 minutes deposition time;

The reaction for stoichiometric Si_3N_4 with n=2.0 is:

$$3SiH_2Cl_2 + 5NH_3 \Longrightarrow Si_3N_4 + NH_4Cl + 5HCl + 6H_2$$

Si_3N_4 and NH_4Cl are in solid phase, with Si_3N_4 depositing on hot surfaces and NH_4Cl condensing on cold vacuum lines. This process includes long temperature ramp and stabilization times, which can be counted as annealing. The process recipe temperature

budget is as follows: start at 600°C, ramp up from 600°C to 700°C in 34 minutes, then go up to 775°C in 20 minutes, stabilize at 775°C for 20 minutes, followed by 11 minutes gas stabilization, then film deposition at 775°C for the input deposition time, and finally 60 minutes slow ramp down to 600°C before boat out.

(v) thin Si_3N_4 (10 nm): LPCVD, 775°C, ~4 minutes;

Same reaction as (iv).

(vi) thick Si_3N_4 (60 nm) on thin thermal oxide (8.1 nm);

Oxide was grown in the same boat as wafers in type (ii), and nitride was deposited in the same boat as wafers in type (iv).

(vii) thick Si_3N_4 (60nm) on thinner thermal oxide (4.5 nm);

Oxide was grown in the same boat as wafers in type (iii), and nitride was deposited in the same boat as wafers in type (iv).

For these 7 types of wafers, oxide or nitride was grown or deposited on both sides of the wafers. The reason why samples with 8 nm thick thermal oxide layer were prepared is that from the simulation results in section 5.2, optically, a Si_3N_4/SiO_2 double layer ARC with a 8 nm thick oxide underlayer renders almost the same solar cell efficiency as the double layer with 4 nm thick oxide, and we suspect that a 8 nm oxide layer will provide better surface passivation than 4 nm oxide and lead to higher cell efficiency.

5.3.3 PCD measurement results

During PCD measurements, a UV beam was shined directly onto front surfaces of the samples, and the average was taken for the lifetimes of the two samples of each type.

Fig. 5.13 displays the measurement results. Both of the Si_3N_4/SiO_2 double layers and the thick thermal oxide coated wafers have lifetimes of more than 500 μs. τ_{eff} of the 10 nm thick nitride film coated sample is not shown because it is below the detection limit (< 10 μs) of our PCD tool.

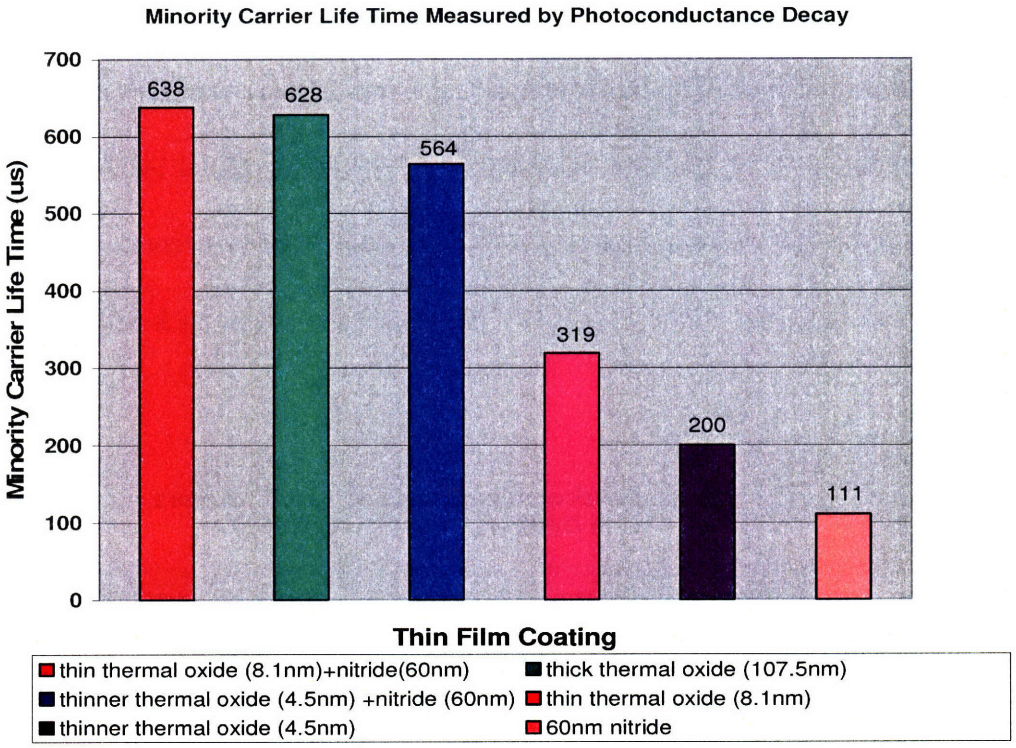

Fig. 5.13 Minority carrier lifetime of Si wafers with different dielectric coatings measured by photoconductance decay

In order to calculate the surface lifetime and surface recombination velocity, one must know the bulk life time. Since all the 14 wafers were from the same cassette, we assume that their bulk lifetime is the same. To measure τ_b, two bare Si wafers were drawn from the same cassette. During PCD measurements, the two wafers were soaked in 49% HF solution while the UV beam was shone on the top surface. HF can render high quality passivation to Si surface by terminating the dangling bonds with atomic hydrogen [5.15].

Therefore, the measured τ_{eff} will be taken as the approximate bulk life time τ_b. PCD measured a τ_b (τ_{eff}) of 74 μs, which is shorter than the τ_{eff} of wafers coated with all kinds of films except the 10 nm thick Si_3N_4. According to Eq. (5.10), τ_b should be longer than τ_{eff}. Given that all the wafers in Fig. 5.13 underwent high temperature anneal during film deposition, which can increase bulk lifetime by metal gettering and defect density reduction, after the first PCD measurements, the two bare Si wafers were annealed at 800°C for 3 hours in N_2 ambient, and soaked in HF for a second PCD measurement, which caused the lifetime to jump to 2.6 ms. To calculate surface recombination velocity, a τ_b=1 ms is assumed for all the 7 types of films except the 10 nm thick Si_3N_4.

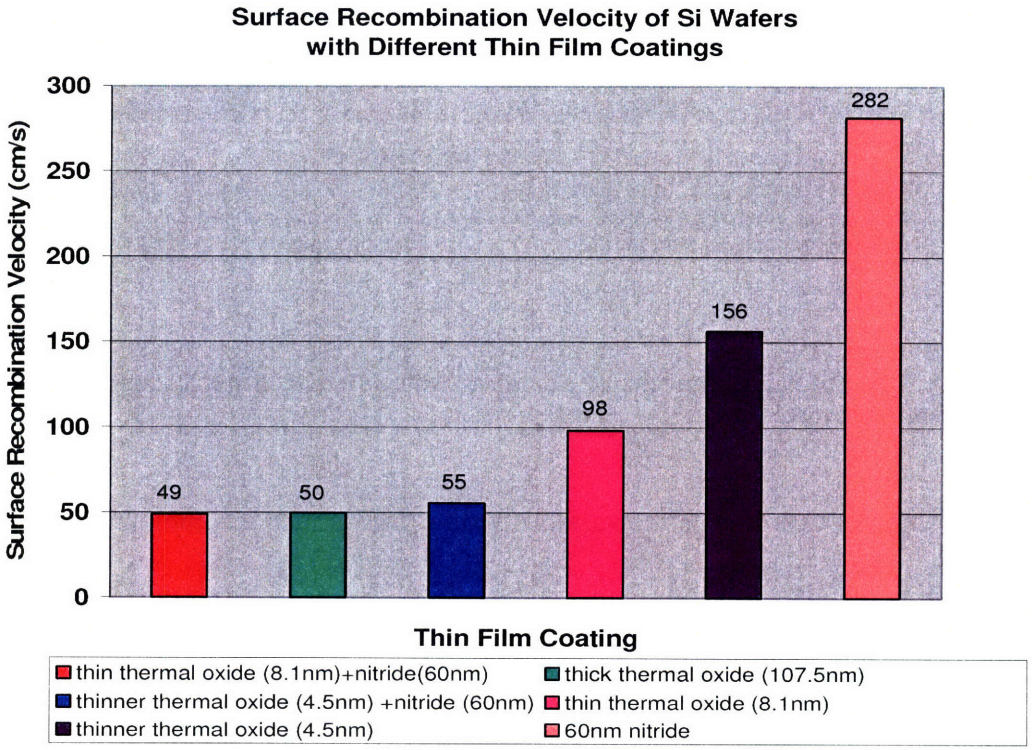

Fig. 5.14 Approximate surface recombination velocity of Si wafers with different dielectric coatings

The calculated surface recombination velocity S from Eq. (5.13) is shown in Fig. 5.14. Three kinds of films, namely Si_3N_4/SiO_2 (60 nm/8.1 nm), 107.5 nm thick thermal oxide, and Si_3N_4/SiO_2 (60 nm/4.5 nm) all have a low S of around 50 cm/s. The double-layer Si_3N_4/SiO_2 (8.1 nm) renders the best surface passivation, even better than the 107.5 nm thick thermal oxide. Si_3N_4/SiO_2 (4.5 nm) has slightly higher S than the thick thermal oxide. Both thin oxide films, 8.1nm and 4.5 nm, exhibit higher S than the thick one, but still lower than 60 nm Si_3N_4. This verifies that it is well worth it to have a thin thermal oxide layer underneath LPCVD nitride as the antireflection coating.

5.4 Dielectric strength study

The antireflection coating on top-contacted solar cells must be insulating in order to prevent shorting between p and n regions. The quality of a material as an insulator is measured by dielectric strength. It is defined as the maximum electric field strength that the material can withstand without experiencing failure of its insulating properties. Theoretical dielectric strength is an intrinsic property of the bulk material and depends on the geometry of the material and the electrodes with which the electric field is applied. Since dielectric materials usually contain small defects, the practical dielectric strength is usually smaller than the intrinsic dielectric strength for ideal, defect free material. Thin films of dielectrics can exhibit higher dielectric strength than thicker samples of the same material [5.17].

The dielectric strength of some samples prepared in Section 5.3.1 was tested using I-V probes. First, any insulator on the backside of the wafers was removed by reactive ion etch. Then the wafers were placed onto an I-V probe station with voltage applied to

the top surface of the dielectric using a probe, and backside contact was made to the bare Si via a metallic vacuum chuck. The voltage was increased slowly until the current started to increase abruptly. The voltage at this point was recorded as the breakdown voltage. The dielectric strength was calculated by dividing the breakdown voltage by the film thickness. The measurement results are shown in Table 5.7. It should be noted that the results here can only be used as rough estimation: accurate measurements necessitate deposition of a metal layer on top of the dielectric and patterning the metal into small mesas, and then placing the probe on top of the metal. This can be done either by depositing metal first, and patterning later using photolithography, or by depositing metal through a shadow mask. Placing the probe directly on top of the dielectric can cause

Table 5.7 Dielectric strength of certain thin film coatings on Si wafers

Film	Film thickness (nm)	Breakdown voltage	Nominal breakdown field (MV/cm)
Si_3N_4, not annealed	60	70	11.3
Si_3N_4, annealed	60	120	19.4
SiO_2, not annealed	107.5	100	9.3
Si_3N_4/SiO_2 double layer, not annealed	60/8.1	80	11.4
Si_3N_4/SiO_2 double layer, annealed	60/8.1	300	42.8

Note: anneal was done at 800°C for 3 hours.

penetration into the film and possible concentration of electric filed at the tip of the probe, and therefore is not an accurate method. Nevertheless, it can still give good indication on whether the dielectric is a good insulator. The very thin films of oxide and nitride prepared in section 5.3 were not tested due to the increased error of the probe method when the films are too thin.

We observe the following from Table 5.7:

1) All films exhibit high dielectric strength, near or over 10 MV/cm, which is sufficient to insulate P and N regions;

2) Si_3N_4 has higher dielectric strength than thermal oxide;

3) Si_3N_4/SiO_2 double layer has the highest dielectric strength;

4) After anneal, breakdown field of both nitride and oxide increases. This is close to what will happen to the device wafers due to dopant anneal (950°C, 20 minutes) and metal sinter (400°C, 30 minutes) after the formation of ARC.

5.5 Conclusion and design parameters update

In this chapter, we studied the antireflection coating on Si solar cells systematically. Five materials systems were considered in terms of optical response, surface passivation and insulation properties. Optical response simulation showed that Si_3N_4 and Si_3N_4/SiO_2 renders higher solar cell efficiency than either the SiO_2 or SiON coatings. Si_3N_4/SiO_2 and thick thermal SiO_2 provide much better surface passivation than does Si_3N_4. All the coatings exhibit high dielectric strength, with Si_3N_4/SiO_2 double ARC having the highest. Therefore, Si_3N_4/SiO_2 double ARC made of a Si_3N_4 layer and an

underlying thin thermal oxide layer (4-8 nm thick) has the best overall performance and will be chosen for thin film solar cell fabrication in the subsequent chapters.

Now it is time to update Table 4.4 with the best AR coating identified in this chapter along with the corresponding cell efficiency. In Table 5.8, the reference cells have a single layer ARC made of 70 nm Si_3N_4, and the optimized cells all have a double-layer ARC consisting of Si_3N_4 and an underlying layer of 4 nm thick thermal SiO_2.

Table 5.8 Optimized solar cell design with double-layer AR coating for different cell thicknesses

Parameters/ Cell efficiency		**Solar cell thickness**			
		2 μm	**5 μm**	**20 μm**	**50 μm**
Grating	Etch depth (nm)	56	65	85	115
	Period (nm)	289	304	317	334
	Duty cycle	~0.5	~0.5	0.5	0.5
DBR	Bragg wavelength (nm)	721	798	819	853
	Number of bilayers	≥6	≥6	≥6	≥6
AR coating thickness	Si_3N_4 top layer (nm)	60	65	70	72
	SiO_2 underlayer (nm)	4 - 8	4 - 8	4 - 8	4 - 8
Optimized cell efficiency η_{opt} (%)		15.55	19.33	23.39	25.10
Reference cell efficiency η_{ref} (%)		10.11	14.28	19.83	22.54
Efficiency enhancement $\frac{\eta_{opt} - \eta_{ref}}{\eta_{ref}}$ **(%)**		53.8	35.4	18.0	11.4

Note: all the reference cells have a 70 nm thick single-layer AR coating, and the optimized cells have a double-layer ARC made of a Si_3N_4 layer and a thermal SiO_2 underlayer.

An update of Fig. 4.19, optimized design parameters vs. cell thickness, is shown in Fig. 5.15. As with other parameters depicted in the figure, the thickness of Si_3N_4 ARC top layer has linear variation, although smaller, for cell thickness above 5 μm, with the slope becoming steeper when cell thickness is below 5 μm, probably due to the strong interference effect in thinner cells. Fig. 5.16 illustrates efficiency enhancement vs. cell thickness with the optimized design in Table 5.7. It is very similar to Fig. 4.22. For a 2 μm thick cell, using the optimized design, the relative efficiency enhancement is as high as 54%, and the absolute efficiency enhancement is 5.44%, compared to 4.92% with the SiO_2-only ARC.

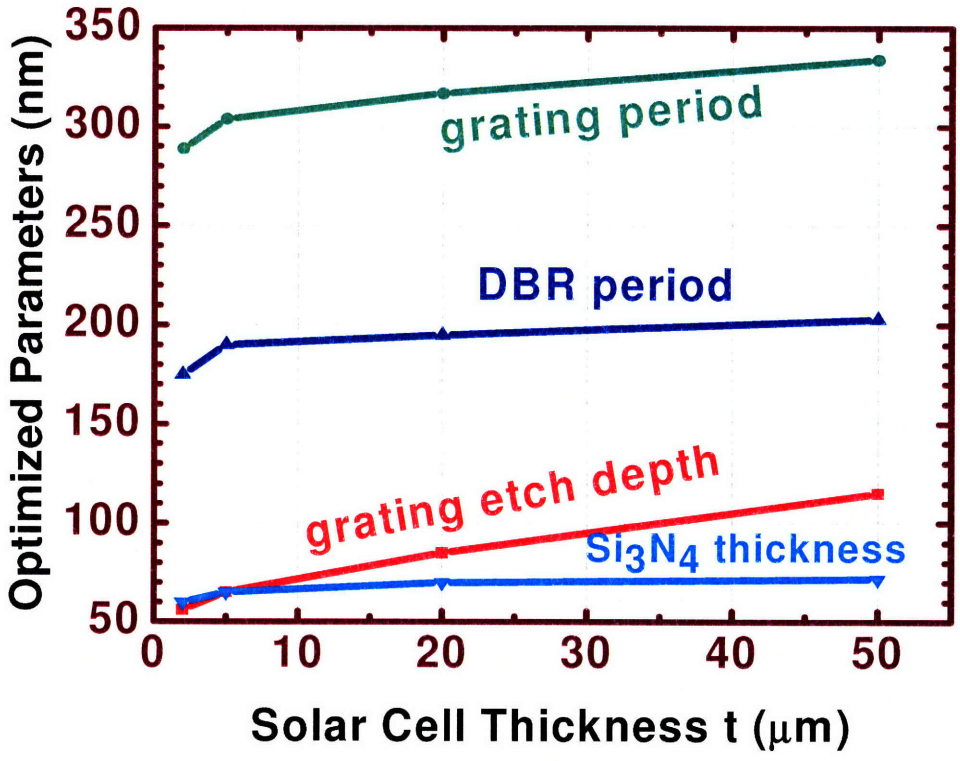

Fig. 5.15 Optimized design parameters for thin film Si solar cells with Si_3N_4/SiO_2 double-layer AR coating and textured photonic crystal backside reflector. Not shown: grating duty cycle remains at 0.5 and the thermal SiO_2 underlayer of AR coating is 4 nm for all cell thicknesses

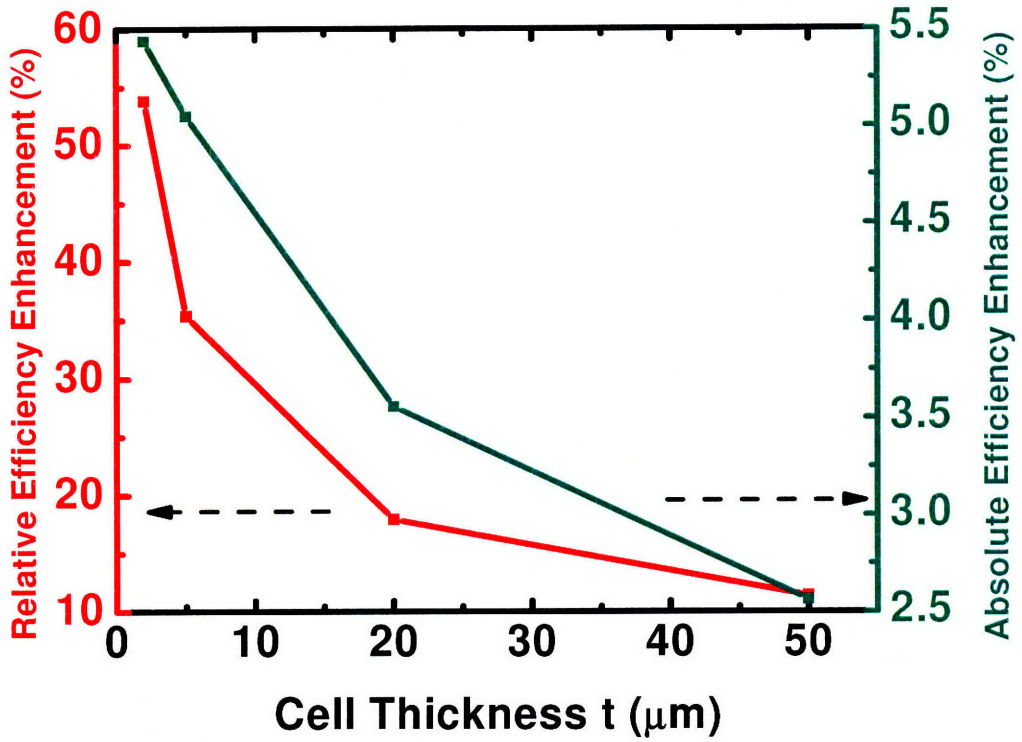

Fig. 5.16 Efficiency enhancement by cells with optimized design compared to reference cells at different cell thicknesses

References

[5.1] B. S. Richards, Prog. Photovolt: Res. Appl. **12**, 253 (2004).
[5.2] Jenny Nelson, *The Physics of Solar Cells*, Imperial College Press, London, 2003, p. 258.
[5.3] B. Vogl, A. M. Slade, C. B. Honsberg, J. E. Cotter, S. R. Wenham, Proceedings of the 28th IEEE photovoltaic Specialists Conference, 327 (2000) .
[5.4] Takashi Minemoto, Takahiro Mizuta, Hideyuki Takakura, and Yashihiro Hamakawa, Solar Energy Materials and Solar Cells, **91**, 191 (2007).
[5.5]A. Prasad, S. Balakrishnan, S.K. Jain, J. Electrochem. Soc. **129**, 596 (1982).
[5.6] B.C. Chakravarty, Jyoti Tripathi, A. K. Charma, R. Kumar, K.N. Sood, S. B. Samanta, S. N. Singh, Solar Energy Materials and Solar Cells, **91**, 701 (2007).
[5.7] S. Arimoto, M. Nakatani, Y. Nishimoto, H. Morikawa, M. Hayashi, H. Namizaki, K. Namba, Proceedings of the 28th IEEE photovoltaic Specialists Conference, 188 (2000) .
[5.8] S. Dauwe, J. Schmidt, A. Metz, R. Hezel, Proceedings of the 29th IEEE Specialists Conference, 162 (2002).

[5.9] W. Soppe, A. Weeber, H. De Moore, W. Sinke, T. Lauinger, R. Auer, B. Lenkeit, A. Aberle, Proceedings of the 2nd World Conference on Photovoltaic Energy Conversion, 1558 (1998).
[5.10] A.U. Ebong, M. Taouk, C. B. Honsberg, S. R. Wenham, Solar Energy Materials and Solar Cells, **40** , 183 (1996).
[5.11] Gee-Keun Chang, Materials Science Forum, **449-452**, 1013 (2004).
[5.12] K. L. Jiao and W. A. Anderson, Solar Cells, **22**, 229 (1987).
[5.13] http://www.ioffe.ru/SVA/NSM/nk/index.html.
[5.14] Victor T. Nguyen, *Efficient power coupling to waveguides in high index contrast systems,* Ph.D. Thesis, Massachusetts Institute of Technology, 2006.
[5.15] Hichem M'Saad, The Role of Surface and Bulk Perfection in the Processing and Performance of Crystalline Si, Ph.D. Thesis, Massachusetts Institute of Technology, 1994.
[5.16] K. L. Luke and L. J. Cheng, J. Appl. Phys. **61**, 2282 (1987).
[5.17] N. Klein, and H. Gafni, IEEE Transactions on Electron Devices, Vol. ED-13, No. 12, P 281 (1966).

CHAPTER 6

Si-on-insulator Solar Cells Integrated with Textured Photonic Crystal Backside Reflector

In Chapters 4 and 5, we presented the design of the textured photonic crystal (TPC) back reflector and antireflection coating for thin film crystalline Si solar cells. Our next step is to experimentally verify the design optimization by fabricating thin film Si solar cells for testing. This chapter will focus on the design, processing and characterization of thin film solar cells made of silicon-on-insulator material integrated with the texture photonic crystal back side reflector, and compare the experimental results with simulation.

6.1 Si-on-insulator solar cell design

6.1.1 Materials choice

Although the optimized design in Chapters 4 and 5 can be applied to both single crystalline and poly crystalline Si solar cells, in order to make optical effects obvious and avoid complications due to materials quality issues, we decided to use Si-on-insulator (SOI) as our device active layer. To see design parameter variation at differing cell thickness, three thicknesses of SOI wafer device layer are chosen: 5, 20 and 50 μm, which correspond to the absorption lengths of 690, 860, and 935 nm photons, as shown in Fig. 6.1. The wafers are 6 inch in diameter, and the device layer is (100) oriented, boron doped, with resistivity between 2 and 4 Ω-cm, corresponding to doping levels of $8x10^{15}$

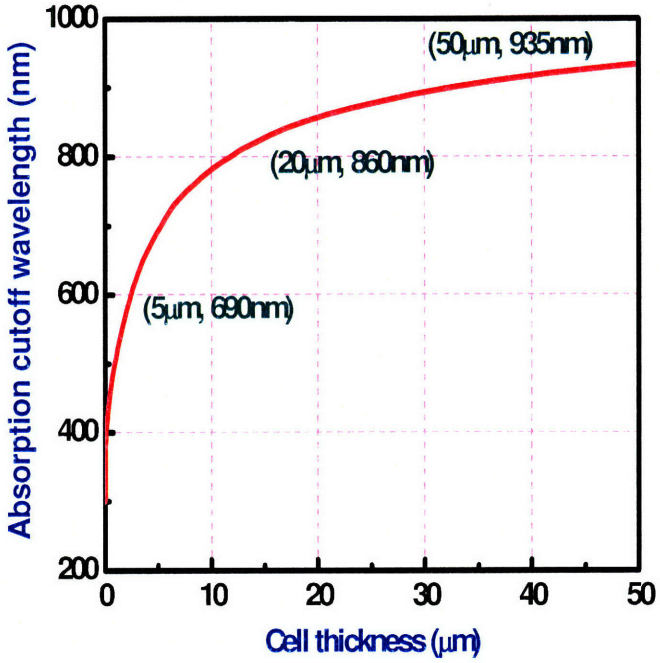

Fig. 6.1 Si solar cell thickness vs. absorption cutoff wavelength

to 4 x10^{15} /cm^3. The buried oxide is 0.5 μm thick, and the handle wafer is 600 μm thick, with the same doping and orientation as the device layer.

6.1.2 Back reflector and antireflection coating design

Three types of back reflector designs will be used for each of the three cell thicknesses:

Type I, grating plus wavy DBR and Type II, grating plus flat DBR

Both 1D and 2D gratings will be made for Type I reflectors, with the period in x and y directions held equal in the 2D structures. During fabrication, if the grating is etched before DBR deposition, then the DBR will be wavy due to the underlying topography of grating, as seen in Fig. 3.4. However, due to the complexity of simulation involving wavy DBR, simulation was only performed on grating plus flat DBR. To accurately compare between simulation and experiments, and to verify whether the extra periodicity of wavy DBR in the plane of quarter-wave films enhances path length, we will also make 1D flat, Type II, DBRs on top of the gratings.

For type I and II back reflectors, the optimal parameters from simulations in Chapters 3 and 4 will be used. A big difference from thick Si solar cell fabrication in Chapter 3 is that gratings will have the designed period of ~300 nm. SiO_2/Si DBR will be used, as the Si_3N_4/Si DBR might crack due to high tensile film stresses. In contrast to our previous thick solar cell fabrication, this back reflector will be formed in the early stage of the process flow, and the DBR will need to withstand high temperature steps in the subsequent ARC deposition and dopant anneal.

Type III: no back reflector as reference.

There will not be any deliberate reflector for the reference cell, but there will be a 500 nm thick SiO_2 layer underneath the Si device layer for electrical insulation, which may have some reflector effect.

For solar cells with the same device layer thickness, but different back reflectors, the same double-layer antireflection coating composed of a thin thermal oxide and an LPCVD Si_3N_4 top layer, as identified in Chapter 5, will be employed. Table 6.1 lists the back reflector and ARC parameters.

Table 6.1 Design parameters used for SOI solar cell fabrication

Cell thickness (μm)	Grating			SiO_2/Si DBR		Double-layer AR Coating	
	Period (nm)	Etch depth (nm)	Duty cycle	Bragg wavelength (nm)	Number of pairs	Si_3N_4 thickness (nm)	SiO_2 thickness (nm)
5	304	65	0.5	798	8	65	4
20	317	85	0.5	819	8	70	4
50	334	115	0.5	853	8	72	4

6.1.3 Finger spacing design

Because DBR is not conducting, we will use interdigitated top contacts and lateral p-i-n junctions, same as in the fabrication of thick solar cells presented in Chapter 3. For

top contacts, one of the most important parameters is the distance d_f between the adjacent p and n regions, which is the width of the intrinsic, undoped region. A short distance will render better carrier collection and smaller series resistance, but also means more shadowing. A good design should be based on minority carrier diffusion length L_D, and make $d_f<L_D$.

Our SOI wafers came from the vendor in three different boxes, with wafers in the same box having the same thickness. It is supposed that wafers with the same thickness have similar materials quality. Prior to any processing, an RF photoconductance decay (PCD) measurement was performed on two of the 5 μm thick SOI wafers, trying to determine diffusion length through minority carrier life time. The wafers were immersed in 49% HF solution during the measurement, and the PCD is supposed to detect the bulk minority carrier life time τ_b. However, the signal was below the detection limit of our RF-PCD system, 10 μs, and even after annealing at 800°C for 3 hours, still no signal was detected. This may mean that the top or bottom surface of the device layer has poor quality, or the bulk is problematic. We can, however, estimate the diffusion length assuming different minority carrier life time τ_{eff}. The p-type doing of 4-8x10^{15}/cm^3 has electron mobility of around 1290 cm^2/V-s [6.1]. According to Einstein relation

$$\frac{D}{\mu}=\frac{kT}{q} \qquad (6.1),$$

at 300K, the electron diffusion constant D is ~ 33.5 cm^2/s. From

$$L_D=\sqrt{D\tau_{eff}} \qquad (6.2),$$

when τ_{eff}=5 μs, the diffusion length L_D=130 μm; for τ_{eff}=1 μs, L_D=58 μm; and at τ_{eff}=100 ns and 10 ns, the corresponding L_D=18 μm and 5.8 μm, respectively.

Due to the possible wide variation of diffusion length, in order to make working devices out of these unknown wafers, layout of the solar cell is carefully designed, as will be detailed below.

Each wafer has a unique back reflector design mentioned in section 6.1.2. On each wafer, there are identical dice, each die having 14 different solar cells. The cells can be divided into two groups with active areas either 40 mm^2 or 4 mm^2. In each cell, the doped p and n region width equals, and the distance d_f between adjacent p and n regions is constant.

(i) The 40 mm^2 cells:

There are 10 such big cells. In each cell, every doped region is 10 or 20 μm wide. Each metal line is 7 μm wide. Among the cells, the distance d_f between adjacent p and n regions varies gradually from 20 μm, through 100 μm, up to 500 μm, corresponding to shadowing from 23.3% to 1.3%. Since the distance between the metal lines (fingers) is only a few microns less than d_f, from now on, we will call d_f finger spacing, which is more intuitive.

(ii) The 4 mm^2 cells:

There are 4 such small cells. Each doped region is 6 μm wide, and has finer spacing, varying from 3 to 20 μm. These cells have heavy shadowing of 19% to 66%.

6.1.4 Metal line thickness and width design

To reduce shadowing and keep series resistance low at the same time, it is wise to use narrow and thick metal lines. We will use 2 μm thick Al-2%Si on all cells, at 7 and 5.5 μm width, for the big and small cells, respectively.

6.2 SOI solar cell fabrication

6.2.1 Process flow

To integrate the textured photonic crystal back reflector with SOI solar cells, we developed an active layer transfer technique. Fig. 6.2 illustrates major processing steps for type I cells with back reflector composed of both grating and wavy DBR. The major steps are: back surface field formation, back reflector fabrication, chemical mechanical polishing (CMP) and wafer bonding, removal of original handle wafer, and front side processing including AR coating and junction formation and metallization. For type II cells with flat DBR plus grating, an extra step is inserted between steps 3 and 4: after grating etch, a thick SiO_2 layer is deposited, which is then made flat by CMP, before the deposition of other DBR layers. For type III reference cells, steps 3 and 4 are replaced by a 700 nm thick SiO_2 layer deposition. In the following sections, the major processing steps will be presented in detail.

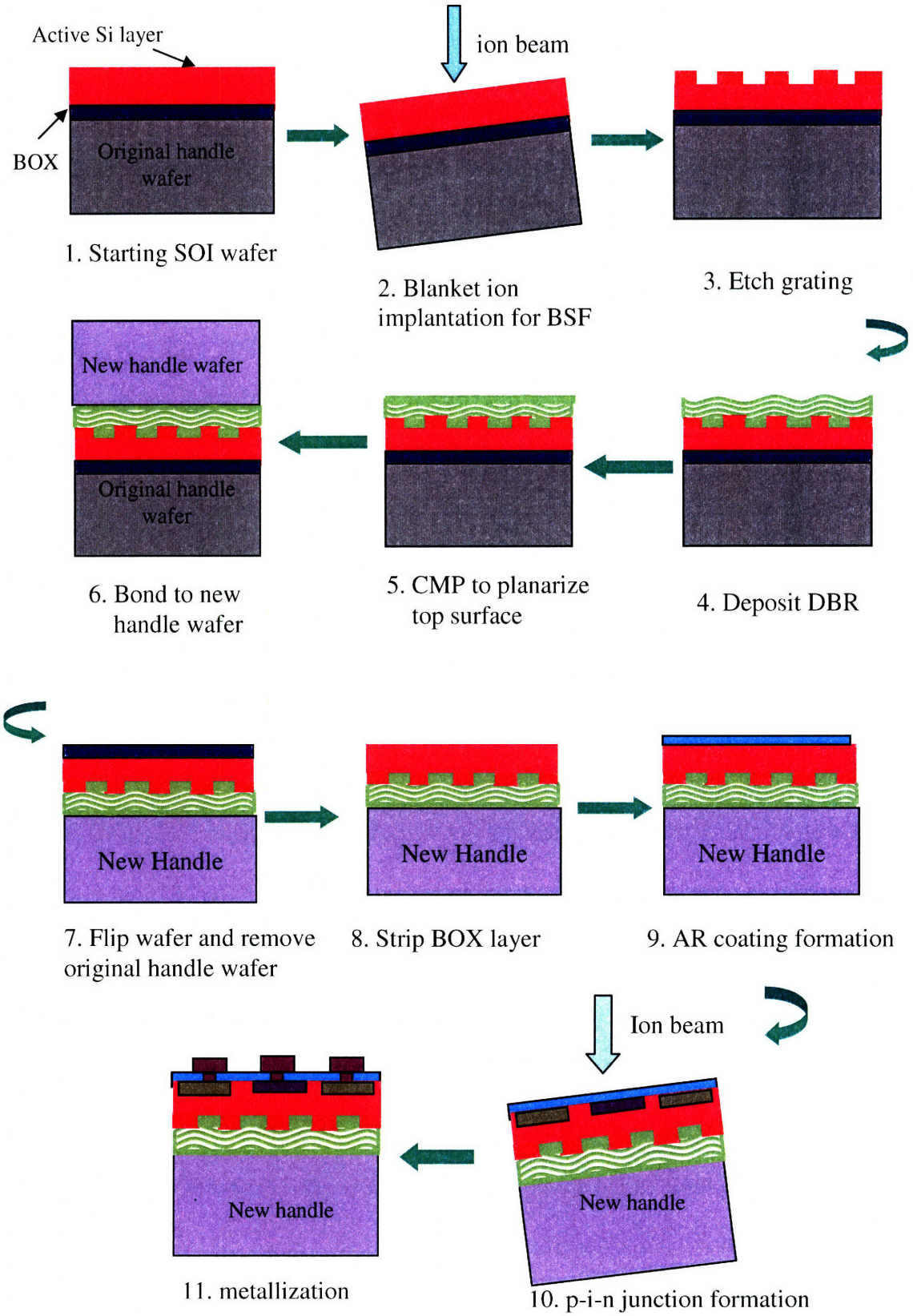

Fig. 6.2 Process flow of SOI solar cells with grating plus wavy DBR back reflector

6.2.2. Back surface field formation

Since there are three different SOI device layer thicknesses, and three different back reflector designs within each thickness, to avoid confusion during wafer handling, a unique letter was scribed with a diamond scriber on the backside of each original handle wafer, near the flat, before any processing.

All the wafers were then sent out for ion implantation with the following specifications: boron, energy 25 keV, dose 3E14/cm^2, 7 degree tilt. This corresponds to a doping level of 2x10^{19}/cm^3, and junction depth of 0.8 μm.

6.2.3. Back reflector fabrication

Back reflector fabrication will include both grating formation and DBR deposition. The grating lithography was performed by interference lithography, in the Center of High Technology Materials at University of New Mexico, at the Nanoscience @ UNM facility, a member of the National Nanotechnology Infrastructure Network. As mentioned in Chapter 2, by the interference of two laser beams, a periodic interference fringe is created without a mask. The grating period can be easily changed by adjusting the incidence angle of the laser beam.

The laser source was the third harmonic (355 nm) output from a Coherent Infinity 40-100 pulsed Nd:YAG laser, operating at a frequency of 60 Hz. Output energy was 50 mJ, and exposure time varied from 12 to 20 seconds. The exposure used the Fresnel Corner Cube Mirror Interferometric Lithography setup. Since the window where the laser beam can make uniform exposure is less than 2x2 inch^2, manual step and repeat

enabled the formation of 9 dice in the center of the wafer in three rows, with the size 1.1x1.1 inch^2 each.

After the grating lithography, the wafers were shipped back to MIT cleanroom Microsystems Technology Laboratories (MTL) for further processing.

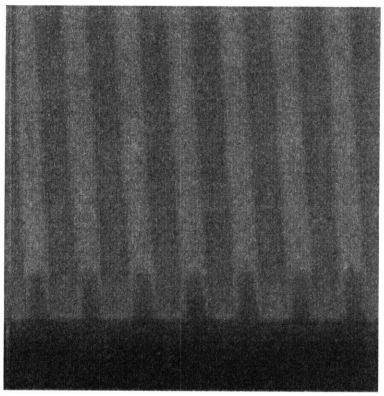

Fig. 6.3 (a) SEM picture of a grating with period 304 nm, after photoresist develop, before etching

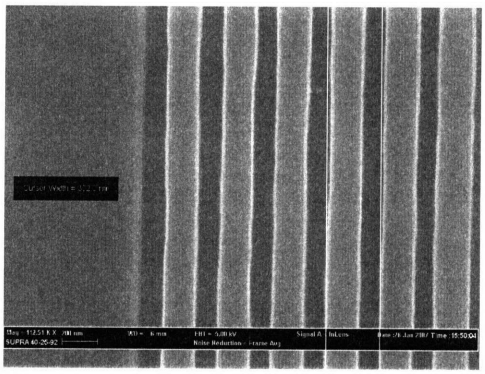

Fig. 6.3 (b) SEM picture of a grating with period 302 nm, after ARC and Si etching

Fig. 6.3 are SEM pictures of a grating formed by interference lithography, before and after etching. After etching, the period was 302 nm, only 2 nm off the designed 304 nm for 5 μm thick solar cells, but the duty cycle is around 0.37, further from our desired value of 0.5.

For type I and II wafers, after grating formation, a 4 nm thick thermal oxide layer was grown on top of the grating, as a second effort to reduce back surface recombination, in addition to back surface field implantation. For type I wafers, this thin oxide layer will serve as part of the first SiO_2 layer in SiO_2/Si DBR. For type II wafers, after thermal oxide growth, a 400 nm thick SiO_2 layer was deposited using plasma enhanced chemical vapor deposition (PECVD), after which this deposited oxide layer was planarized and thinned down to around 150 nm using chemical mechanical polishing (CMP).

Then both type I and II wafers had 8 pairs of SiO_2/Si layers deposited using PECVD, plus a 400 nm thick SiO_2 top layer to be used to CMP planarize the top surface and prepare for wafer bonding.

For type III reference wafers, a 4 nm thick thermal oxide layer was also grown after back surface field formation, followed by the deposition of a 700 nm thick PECVD SiO_2 layer, which replaces steps 3 and 4 in Fig. 6.2.

6.2.4 CMP and wafer bonding

In order to bond two wafers together, the bonding interface must be smooth. High quality wafer bonding requires a root-mean square surface roughness <1 nm [6.2]. For type I wafers, the top surface of the 400 nm thick SiO_2 on top of DBR is wavy due to the grating underneath, which has etch depth of ≥ 56 nm; and for type all wafers the surface of deposited SiO_2 layer is not smooth enough for wafer bonding, requiring a CMP to smooth the wafers before bonding.

I. Anneal before wafer bonding

Wafer bonding generally involves two steps: first, press together two wafers to be bonded to form Van der Waals bonds between them; then anneal at high temperature to form permanent covalent bonds. During process trial for wafer bonding, Si wafers with CMP smoothened PECVD oxide were attempted to be bonded to bare Si wafers but it failed more than half of the time, and increasing the anneal temperature from 600°C to 1000°C actually decreased the yield. It turned out that there was outgassing from the deposited SiO_2 during anneal, as CVD oxide is relatively porous and large amount of

hydrogen and some other by-products or gas molecules can be incorporated into the film during deposition [6.3]. Therefore, annealing to densify and outgas is necessary before CMP in order to achieve reliable bonding.

Before committing all the wafers to pre-CMP anneal, a 5 μm thick type I device wafer was annealed at 1000°C in N_2 ambient for one hour. After the wafer was taken out of the annealing tube, the scene was shocking: dense circles were created all over the wafer surface with film missing inside them. A surface profile measurement revealed that these circles were holes with diameters from 215 μm to 1.1 mm, with hole depths of 2.0 μm, exactly the thickness of the 8 pair DBR stack ($\frac{\lambda_B}{4}(\frac{1}{3.5}+\frac{1}{1.46})\times 8 = 1.549$ μm) plus the top 400 nm thick oxide. Fig. 6.4 (a) shows a picture of such DBR blister. Annealed DBR monitor wafers deposited at the same time also exhibited severe blistering. This did not happen during the DBR thermal stability study as presented in Chapter 2. Later, it was found that the PECVD machine in MTL was out of maintenance: the shower head was too dirty with residue. This residue could drop onto the wafer and be incorporated into the film, causing blistering during anneal, or could cause indirect effects related to the high surface area trapping contaminants, such as chamber cleaning gases, which then outgas during the deposition. Other users of the same machine reported similar problems at the same time. Unfortunately the DBR stacks were already deposited on all the SOI device wafers, which are expensive to buy, and given the effort of making gratings in New Mexico, we had to find a way to mitigate this problem.

According to reference [6.4], a 16-hour anneal at 350°C can drive the trapped gas out of PECVD oxide completely. However, this method only applies to PECVD films deposited under normal conditions, and we did not succeed with this approach because of

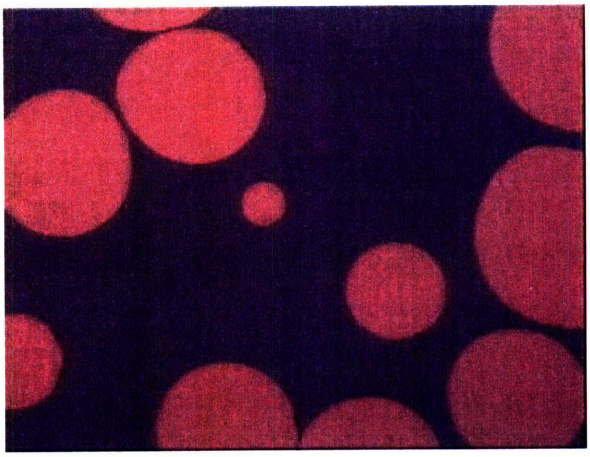

Fig. 6.4 (a) Severe DBR blistering after 1 hour anneal at 1000°C

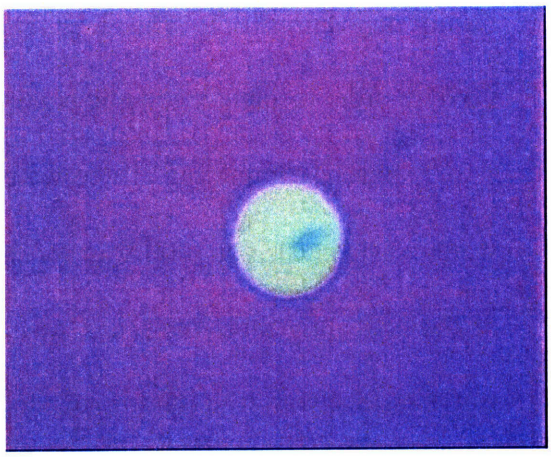

Fig. 6.4 (b) After 24-hour anneal process, DBR blistering was significantly reduced

the blister and hole defect failures.

After repeated trials, a 24-hour anneal process was developed, as shown in Fig. 6.5. This reduced the number of blisters by 90% (see Fig. 6.4 (b)), and they only appeared in a ring within one inch from the wafer edge, where none of the nine central dice with gratings are located.

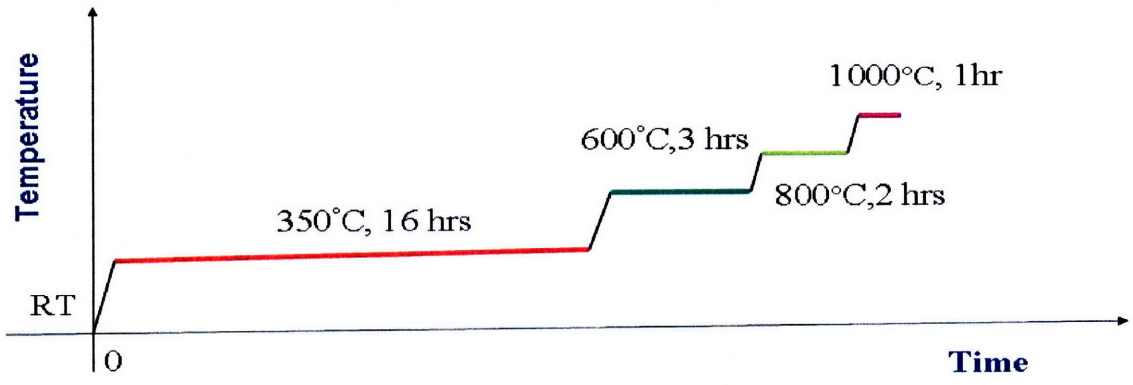

Fig. 6.5 A 24-hour anneal process which reduces DBR blister by 90%

II. CMP time determination

After outgassing anneal, the wafers were sent to a local company for CMP. For type I and II wafers, the desired oxide removal amount is 200 nm, leaving 200 nm for wafer bonding. For type III wafers, the target is to remove 200 nm from the 700 nm oxide, leaving 500 nm for wafer bonding and electrical isolation between the device layer and new handle wafer.

Accurate determination of the CMP polish time is critical to prevent damage to the grating and DBR under the oxide layer. However, determining the CMP oxide removal rate turned out to be challenging for type I wafers, and for type II wafers during the first CMP prior to DBR deposition. Because the CMP polish head applies a constant force to the wafer surface, when the surface is wavy, the force on the individual waves is greater than when the same force is distributed evenly across a whole wafer. Besides, in situ monitoring by optical means, which is used by the CMP comapny to determine the removal rate of a flat oxide layer on Si substrate, does not work on these wafers as both grating and DBR underneath the oxide to be removed are strong optical components. To tackle this issue, monitor wafers with a flat oxide layer on Si were used for a rough estimation of the polish time, and SEM analysis after CMP on monitor wafers with the same structure as type I wafers was used to determine the accurate polish rate. Fig. 6.5 is the SEM picture of a bonded monitor wafer pair mimicking the structure of 5 μm thick type I wafers. From bottom to top, it has a 600 μm thick Si substrate, with a grating etched into it, and 8 pairs of SiO_2/Si DBR deposited on top of the grating, and a 266 nm thick SiO_2 layer remaining after 7 minutes of CMP, which is then bonded to a 400 μm thick double-side polished Si wafer. The top layer oxide thickness reveals that the

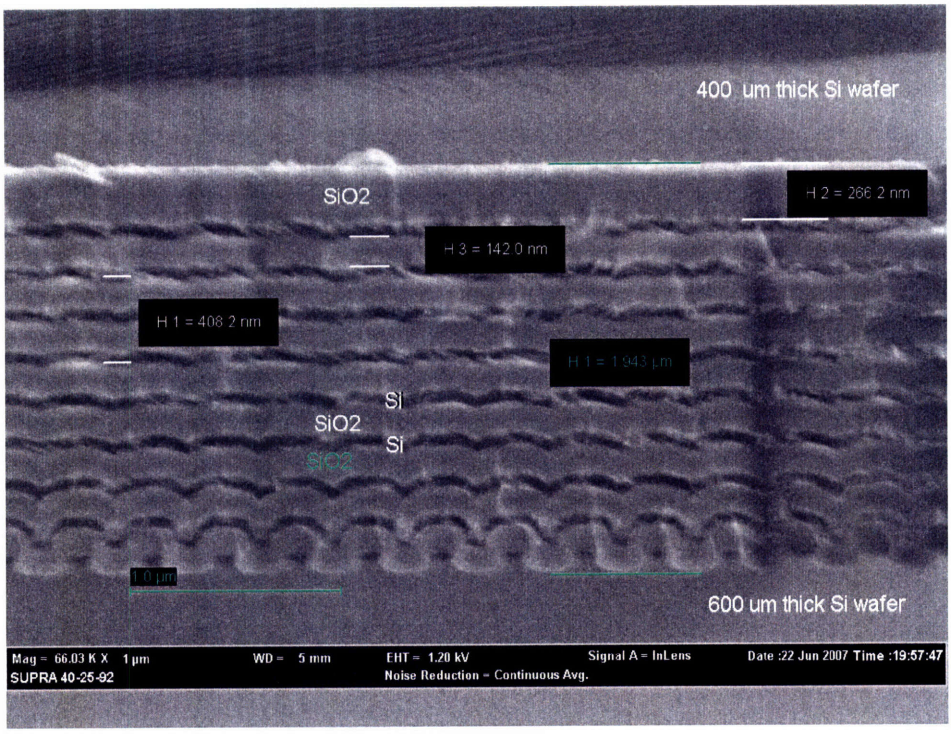

Fig. 6.6 SEM picture of a bonded pair mimicking the back structure of 5 µm thick type I SOI wafers

average polish rate is 5.4 $\mathring{A}$/s on the wavy surface, in contrast to the 4 $\mathring{A}$/s on flat surfaces. The actual time used for CMP is: type I wafers: 7 minutes; type 2 wafers: 4 minutes; type III wafers: 6 minutes.

Besides helping determine the CMP time, Fig. 6.6 reveals a lot of valuable information about the back reflector. It shows that the grating etch is uniform, and the DBR has periodic waviness in the plane of the film. For upper DBR layers, the waviness decreases gradually and levels out, before the 400 nm deposited oxide.

III. Wafer bonding

Three bonding parameters were reviewed: bonding interface, anneal condition and direct or fusion bonding.

(a) Bonding interface: during process development, to test bond strength, annealed CMP smoothed PECVD oxide was bonded to both bare Si wafers and wafers with a thermal oxide layer, and then was annealed. Both showed strong bonding, neither bonded pair could be separated using a razor blade. To simplify processing and reduce unnecessary steps, the SOI wafers will be bonded to bare Si wafers.

(b) Post-bonding anneal condition: successful bonding was achieved after anneal at both 1000°C for 1 hour and 800°C for 3 hours. Given that the DBR stopband might move in a high tempeature process, it is desirable to lower the anneal temperature to 800°C. Our tests showed good bonding strength from this lower anneal temperature, also.

(c) Direct vs. fusion bonding: there are two methods to van der waals bond wafers prior to annealing: direct bonding and fusion bonding. In direct bonding, the wafers are aligned and pressed together at atmospheric pressure, and then are annealed directly. In fusion bonding, the wafers are aligned as with direct bonding, but are separated by thin shims, called flags, and then transferred to a vacuum chamber. Only when the pressure reaches $1x10^{-2}$ mbar will the flags be removed and will the two wafers touch. Direct bonding works well for flat surfaces, while fusion bonding is good for bonding surfaces with deeply etched features, where trapped gas might otherwise cause explosion during post-bonding anneal. Since our DBR still had some blisters despite of the 24-hour anneal, it will be safer to use fusion bonding to deplete air in the defect areas.

After CMP, a double-piranha clean was performed to clean the wafers. The actual bonding sequence was: first, a RCA clean was done on both the device SOI wafers and the double-side polished, 600 μm thick Si new handle wafers right before bonding, to clean the wafers and activate the bonding surfaces. The next step was to align the bonding pair in an EV Group 620 aligner and then bond in an EV Group 501 bonder, at room temperature in $1x10^{-2}$ mbar vacuum, followed by an 800°C anneal for 3 hours. Fig. 6.7 is an infrared image of a bonded pair. Most areas are well bonded. The periodic squares are different dice created during grating formation; and the concentric white areas are not bonded regions due to defects. The outside black ring is the Teflon wafer holder of the imaging system.

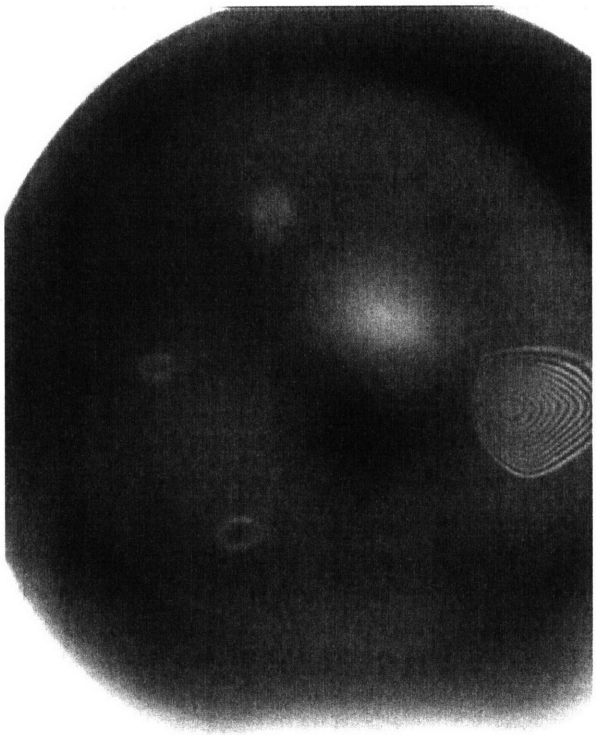

Fig. 6.7 Infrared image of a bonded pair between a type I SOI wafer and a double-side-polished Si wafer

6.2.5 Removal of original handle wafer and buried oxide

I. Old handle wafer removal

After bonding to the new handle wafer, the original handle wafer must be removed to expose the bottom surface of the SOI device layer so that active devices can be made there. In order to remove the entire 600 μm thick old handle wafer, several methods are available including wet etching methods like KOH and TMAH, and grinding/CMP. Wet etching is dangerous because if there are any defects in the typical nitride etch stop used to prevent unwanted etching, the inadvertent etching would be as deep as the original handle wafer, possibly creating holes in the SOI device layer, and certainly making the resulting wafer very fragile due to the inevitability of defects occurring at the outer edge of the wafer. Grinding alone without subsequent CMP is dangerous because there is mechanical damage transferred about 5 or 10 μm into the substrate past the extent of the grinding. To avoid these drawbacks, an alternate three-step removal procedure was developed:

(1) Mechanically grind the original handle wafer down to 50 μm thickness;

(2) CMP to remove damage caused by grinding and smooth the surface for subsequent plasma etching;

(3) Plasma etch using SF_6 to remove the remaining Si and stop on the buried oxide. The etch recipe flows SF_6 at 150 sccm under 45 mtorr pressure, and 250 W RF power. Since etch was performed across the whole 6-inch wafer surface, it was relatively slow with a removal rate of around 1.2 μm per minute.

For some wafers, especially the 5 μm thick ones, delamination occurred after wafer grinding and subsequent CMP. This is a sign of weak bond strength. Since our

wafer bonding procedure is commonly used and reproved solid during our process development, the most possible reason for the weak bonding is DBR blistering during pre- and post-bonding anneal, with its resulting topographical defects, some of which may be elastic under high temperature conditions, or the chemical irregularities at both the original handle and new handle interface weakening the bonding. During anneal, the wafers were put vertically in the furnace, and there was no gravity influence.

II. Stripping of the buried oxide

After removal of the old handle wafer, the wafers were dipped in 20% HF solution to remove the 500 nm thick buried oxide (BOX). Observation under microscope of the newly exposed surface of the Si device layer (former interface between the device

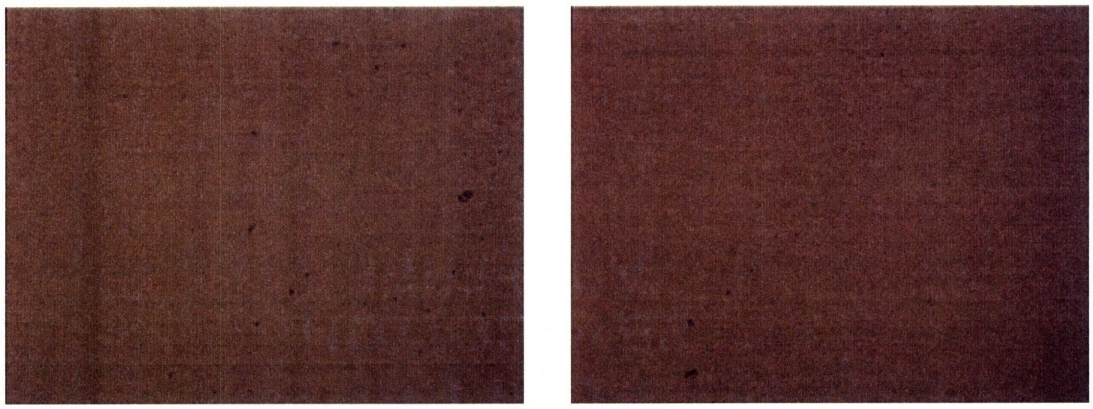

Fig. 6.8 Optical images of the surface of Si device layer after removal of buried oxide.

layer and BOX) showed non-uniform distribution of small holes scattered all over the surface, with diameter around 1 μm (see Fig. 6.8). Since HF solution has good selectivity between SiO_2 and Si, removal of the BOX would not cause damage to the device layer.

Therefore, these holes were pre-existing the processing, i.e., they came from the wafer vendor. Since the newly exposed Si device layer surface will be where our p-i-n junctions located, we expect significant influence on device performance. The carrier collection will be poor. This may also explain why the SOI wafer lifetime was below the detection limit (10 μs) during photoconductance decay measurement.

6.2.6 Front side processing

Once the device layer is transferred onto the new handle wafer, the front side processing is straightforward. It includes AR coating formation, etching alignment marks, ion implantation, and forming metal contacts. It is very similar to the thick solar cell processing presented in Chapter 3, except that this time we will use a double-layer ARC, contact lithography, thicker metal layer, and a sacrificial oxide layer to protect the ARC during metal etch.

I. AR coating formation

A 4 nm thick thermal oxide layer was grown with dry oxidation. Then low pressure chemical vapor deposition (LPCVD) was used to deposit a Si_3N_4 layer at 775°C at thicknesses between 65 nm to 72 nm, depending on the device layer thickness, as listed in Table 6.1.

II. Contact lithography mask design

The subsequent processing requires 5-level photolithography: put down alignment marks, two ion implantations, open contact window, and metal etch. Since the contact

aligner in MTL is more reliable than the stepper, especially in cases of non-uniform topography or low contrast alignment marks, an EV Group contact aligner will be used. The required 2.5 μm minimum feature size of the device cells, other than the previously patterned submicron grating, is achievable on a routine basis with contact lithography, so this method will be chosen for its robustness and reliability.

During grating lithography 9 dice were formed in the center of the wafer, so each mask will define these 9 big central dice, as well as the 3 dice close to each edge, with a unique label for each die, as shown in Fig. 6.9.

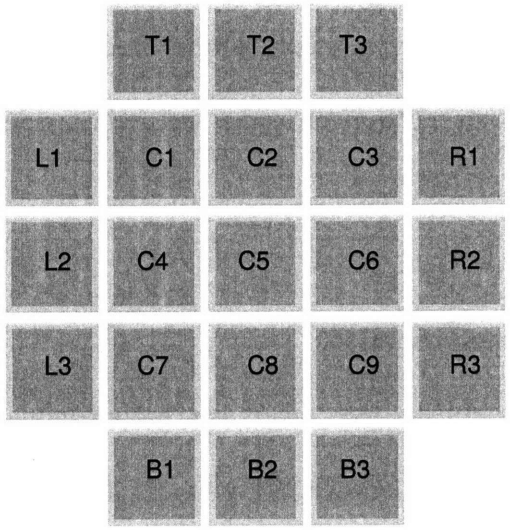

Fig. 6.9 Contact lithography mask die layout

III. Alignment marks formation

After Si_3N_4 deposition, photoresist was coated onto the wafers, and exposed using the first layer alignment mark mask. After photoresist patterning, a LAM490B plasma etcher was used to etch through the double-layer ARC, transferring the alignment marks

into the wafer. The plasma etch chemicals were SF_6 (190 sccm) and O_2 (19 sccm) under a pressure of 300 mtorr and RF power of 130 W, with an etch time of around 90 sec. After that, the photoresist was stripped using an asher.

IV. Ion implantation

The wafers were then photoresist patterned with the P-implantation layer mask, followed by boron implantation with the following specification: energy 40 keV, dose 2E15/cm^2, 7 degree tilt. Then the resist was stripped with an asher and piranha, and the wafers were patterned with the N-implantation layer mask, and implanted with phosphor at 100 keV, 5E15/cm^2, 7 degree tilt. Again, the resist was stripped, and then the wafers were annealed at 950°C for 20 minutes in N_2 ambient to activate the dopants. This will form junctions 0.47 μm deep with average doping $7.0x10^{19}$/cm^3 for phosphor, and a surface concentration of $8.0 x10^{19}$/cm^3 for boron.

V. Sacrificial oxide layer deposition

After implantation, the next step would be opening a contact window in the ARC and depositing metal on top of the ion implanted regions. However, because compared to our previous thick solar cell fabrication, the Al we want to use is twice as thick (2 μm), and our ARC is much thinner (~70 nm compared to 110 nm of SiO_2 used before), there is a new problem that during the Al over etch, the Si_3N_4 ARC will be destroyed. The Lam Rainbow 9600 metal dry etcher in MTL etches Al-2% Si at a rate of around 8000 $\mathring{A}$/min, and for 2 μm thick film, we will use a standard 20% over etch of 400 nm Al. Since the selectivity between Si_3N_4 and Al-2% Si might be 1:5, up to 80 nm of the Si_3N_4 film

would be removed, which is more than our Si_3N_4 film thickness. To protect ARC during this metal etch, a 200 nm thick PECVD SiO_2 layer was deposited as a sacrificial layer right after dopant anneal, which will be an RIE etch stop, and which can be removed later.

VI. Open contact window

The wafers were then photoresist patterned with the contact window mask and etched with an Applied Materials AME5000 plasma etcher to open windows through the sacrificial oxide layer and ARC for metal contacts.

VII. Metallization

A 2 μm thick Al-2% Si layer was then deposited, patterned and etched to define the metal lines and contact pads. 2 μm thick photoresist was used for metal patterning here, as opposed to 1 μm thick during previous 4-level lithography, to ensure sufficient protection during the Al etch.

VIII. Removal of sacrificial oxide layer

After metal etch, before removal of the photoresist, the top oxide layer was removed in a commercial solution "Silox Vapox III" to selectively remove oxide without damaging the Al or Si_3N_4 layer. The photoresist was then ashed, and the wafers annealed at 400°C for half an hour in an N_2 ambient.

This concludes our fabrication of SOI solar cells.

6.3 Solar cell characterization

Cell characterization involves three kinds of measurements: (1) I-V measurements in the dark to see whether theses solar cells are good diodes with small leakage currents and small series resistance; (2) I-V measurements under sun simulator (AM1.5 spectrum) to obtain power conversion efficiency; and (3) current-wavelength (I-λ) scan to measure external quantum efficiency.

6.3.1 Dark I-V measurements

Dark I-V measurements were carried out using a semiconductor analyzer probe station. The 14 solar cells within each of the 9 dice are numbered SC1 through 14. The small solar cells, such as SC14, with finger spacing 20 μm, and an area of 4.26 mm^2, mostly showed a small reverse bias current I_s of between 37 pA to 10 nA at -0.8 V bias, corresponding to a current density J_s of 0.87 to 235 nA/cm^2. For the big cells such as SC1, with finger spacing 20 μm, and an area of 40.3 mm^2, the I_s= 1 to 90 nA at -0.8 V bias, corresponding to Js=2.48 to 224 nA/cm^2. Solar cell 4, with finger spacing of 80 μm and an area of 40.0 mm^2 measured similar I_s (20 to 80 nA at -0.8 V). Note that since we have horizontal junctions, to compare with vertical junctions, the area used for J_s estimation equals solar cell area, not exactly the junction area. Fig. 6.10 shows the dark I-V curve of solar cell 14 on die C9, wafer I, designated solar cell IC9, #14. It has a 50 μm thick device layer, with both a 1D grating and wavy DBR on the backside. The log (I)-V curve shows a steep slope, indicating small series resistance, which will give a high fill factor.

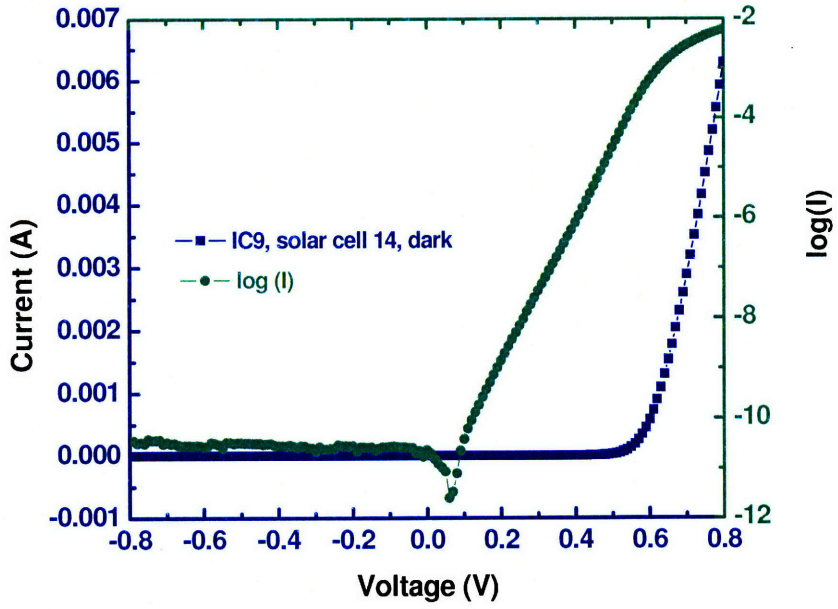

Fig. 6.10 dark I-V curve of solar cell 14 on wafer I, die C9

6.3.2 I-V measurements under sun simulator

I-V curves were measured under a homemade sun simulator, a copy of the solar cell tester in Evergreen Solar, Inc. Calibration cells were also provided by Evergreen. Almost all of the big solar cells (area ~40 mm^2), with different distances between adjacent doped p and n regions (finger spacing) on the 50 μm thick reference SOI wafer, were measured under the sun simulator to identify the best cells. These solar cells had already showed good dark response in previous measurements.

It was found that the short circuit current I_{sc} decreases exponentially as finger spacing d_f increases, as shown in Fig. 6.11. This means poor carrier collection. An exponential fit shows that

$$I_{sc} = 20.1e^{-0.0233 d_f} \qquad (6.3).$$

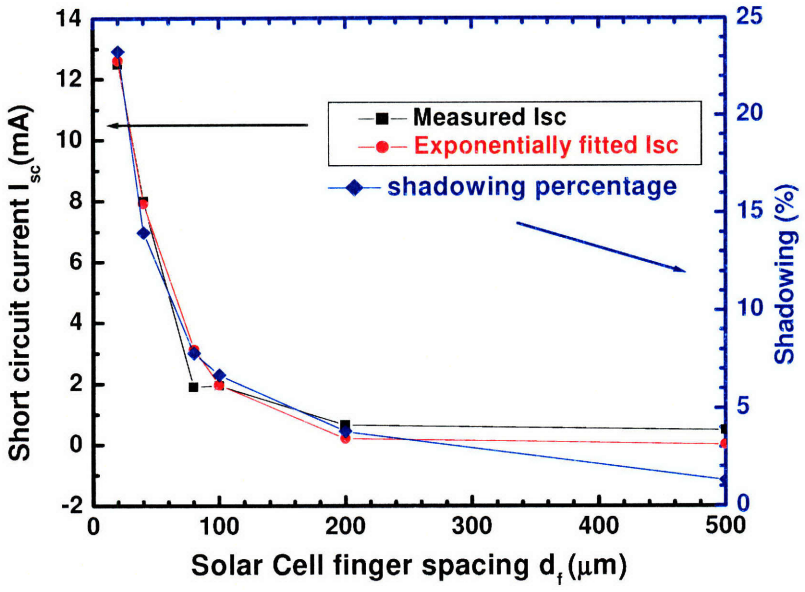

Fig. 6.11 solar cell finer spacing vs. short circuit current and shadowing

As a rough estimation, the diffusion length

$$L_D = \frac{1}{0.0233} = 42.9\,\mu\text{m} \qquad (6.4).$$

Since L_D is close to wafer thickness, this may indicate poor surface quality. As shown in Fig. 6.8, the interface between the device layer and buried oxide, which now becomes the front surface of the solar cells, has voids scattered, and they will act as recombination centers and significantly reduce the minority carrier lifetime, as evidenced by the photoconductance decay measurement. Moreover, the DBR blisters may increase the back surface recombination significantly. Its influence on 5 μm thick cells would be the most serious, as thinner cells are more sensitive to surface recombination.

Given the short diffusion length, in order to get good signal, we decided to concentrate our measurements on one of the small solar cells, solar cell 14, which has

implantation region width 6 μm and finger spacing 20 μm, area 4.26 mm^2 and shadowing of 20.4%.

I-V measurements under the sun simulator showed extremely high power conversion efficiency. As an example, Fig. 6.12 shows the J-V curve of solar cell 14 on 5 μm thick reference wafer S, die C6. In the figure, three curves are depicted which were obtained under three different conditions:

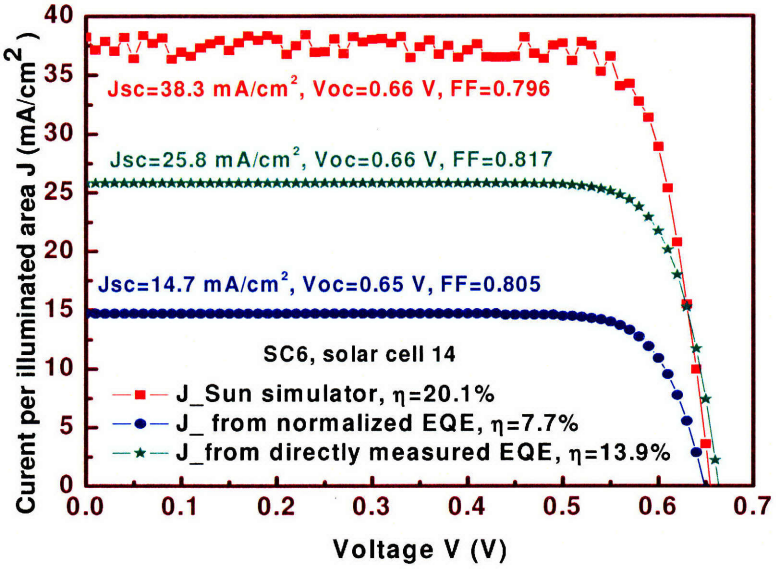

Fig. 6.12 J-V curve of solar cell 14 on a 5 μm thick reference wafer

(1) The top red curve represents the measurement under the sun simulator, showing Jsc=38.3 mA/cm^2, Voc=0.66 V, fill factor FF=0.796, and efficiency η=20.1%. Considering that SC14 has 20.4% shadowing, this Jsc is equivalent to 48.1 mA/cm^2 when no shadowing is considered. Simulation using scattering matrix method renders Jsc=19.8 mA/cm^2 for 5 μm thick reference cells with 100% carrier collection and no shadowing.

(2) The middle green curve is obtained by translation of the dark J-V curve of the same cell by the amount of Jsc which is calculated by integrating the measured external quantum efficiency (EQE) times the solar photon flux, as will be discussed in detail in the next section. This translation is based on the superposition approximation which works well for most photovoltaic materials [6.5]. This curve indicates a Jsc=25.8 mA/cm^2 and η=13.9%, both are more than 31% lower than the values obtained under condition (1). Interestingly, some cells exhibited more than 100% EQE in some regions within the wavelength range λ=430-890 nm, which we attributed to non-uniform illumination from the monochromator fiber. One cell, on wafer S die C6, also showed similar readings with the EQE between 100%-124% in λ=470-666 nm. Even so, the calculated Jsc is still 32.6% lower than the value obtained from direct measurements under the sun simulator.

(3) The lowest blue curve is acquired by translation of the dark J-V curve by the amount of Jsc that was obtained by integrating the normalized external quantum efficiency times the solar photon flux. As mentioned in the last paragraph, some cells showed more than 100% EQE. A normalization was done to compare the light absorption of cells with different back structures. After this normalization, the EQE of this cell dropped significantly, and consequently, the calculated Jsc is now only14.7 mA/cm^2, just 38% of the value in condition (1).

Given that the Jsc in condition (1) is even higher than that obtained in case (2) where EQE is more than 100% at some wavelengths, it seems like the sun simulator may gave out intensity of more than one sun. Although careful calibration was done, it may not be accurate because the calibration solar cell from Evergreen Solar, Inc. has solder bumps at the back for electrical contact wires for our I-V probe station, preventing

backside wafer cooling during the I-V scan. Without cooling, the cell temperature quickly rose to 50°C in one minute due to radiation heating of the sun simulator. As a result, the calibration measurements had to be done quickly using a multimeter, reading the Jsc and Voc within 1 minute after the simulator light shutter was opened. During the sun simulator calibration, the cell from Evergreen was held at progressively greater distances from the sun simulator, until it reached the Jsc (and Voc) value provided by Evergreen. Since no I-V curve could be collected, fill factor was unknown and we mainly relied on Jsc calibration. A more accurate method would be external quantum efficiency measurements, where we can measure the absorption more accurately at each wavelength, and reveal the relative efficiency enhancement provided by the back reflectors.

It is noteworthy that on the three curves, although Jsc changes greatly depending on the intensity of light source, Voc and fill factor remains almost constant.

6.3.3 External quantum efficiency measurements

External quantum efficiency (EQE) was measured using a Hewlett-Packard 4145A semiconductor analyzer coupled to an H20 IR Jobin Yvon monochromator. The monochromator light source generates multi-colored light from which a single wavelength is selected by a grating, and transmitted in optical fiber to the semiconductor analyzer chamber. The light comes out of the fiber and is incident vertically onto the sample. Depending on the desired wavelength, after the light passes the grating, a suitable filter is used to remove the 2^{nd} harmonic before the light is coupled into the fiber.

The photocurrent at zero bias voltage was measured at the interval of every 10 nm wavelength. Since the intensity of incident light at each wavelength was calibrated

beforehand, and the fiber spot size is known, one could calculate the total number of incident photons onto the solar cell. From the photocurrent, the number of photogenerated electrons can be obtained. EQE is found by dividing the number of electrons by the number of photons.

I. EQE normalization

Fig. 6.13 illustrates the EQE of SC14 at two different die positions, C6 and C9 on the same wafer S. From now on, without special statement, all the results shown will be on SC14. A remarkable feature of this figure is that although these two cells are both reference cells with the same back structure, and their EQE curves have the same shape, the EQE of SC6 is much higher than that of SC9. Note the discontinuity at 400 nm which is due to the change of filter in the monochromator at that wavelength. It is found that by

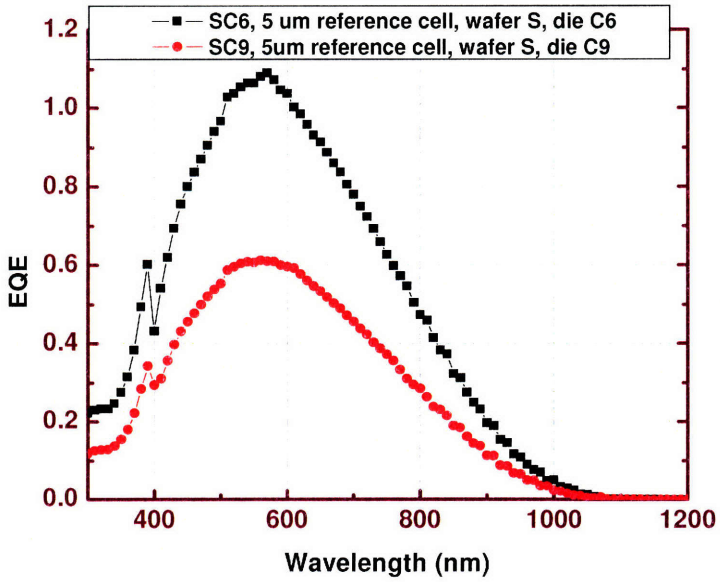

Fig. 6.13 EQE of 5 μm thick reference cells on the same wafer, SC6 and SC9

identifying the highest EQE points on the two curves (both points turned out to be at λ=570 nm), calculating their EQE ratio, and then multiplying one curve by the ratio, the two curves overlap exactly, as shown in Fig. 6.14! In this case, EQE of cell SC6 was multiplied by 0.559 at each λ. Both cells showed good dark response.

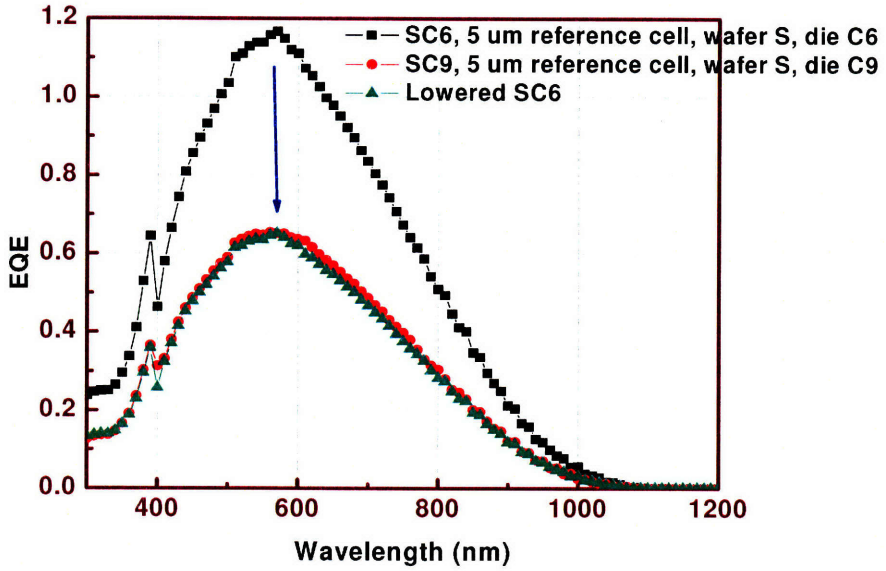

Fig. 6.14 After multiplying the EQE curve of SC6 by a simply factor, it overlaps with SC9 across the spectrum

Another interesting feature is that the EQE of SC6 before being normalized to that of SC9 was more than 1 between λ=505-605 nm. This happened to many other cells, and some cells even showed EQE=1.49, as we will see soon. Given that our cells have 20.4% shadowing, EQE should not be more than 0.796 at any λ. To make sure the measurements were accurate, the monochromator were recalibrated using two detectors, which showed almost identical photon intensity coming out of the fiber, same as the previous calibration values; the photocurrent was examined with a high accuracy pico-ammeter, which showed readings less than 8% off the value measured by the

semiconductor analyzer. It seems like the only possible reason is that the light coming out of the fiber is inhomogeneous, and its spot size (13.8 mm^2, 4.19 mm diameter) is much bigger than our solar cell size (4.26 mm^2, around 2 mm wide square). Depending on where the cell was positioned, from measurement to measurement, the total photon number impinging on the cell can be different by a same factor for each wavelength (solar cell position relative to fiber spot is fixed during the entire 300-1200 nm I-λ scan). This explains why we can scale the entire spectrum of cells with the same design by a single factor and make the two spectra overlap. Actually, for fibers with a parabolic index profile, the typical mode amplitude profile is Gaussian, with the fundamental mode having the pattern [6.6]

$$u_{00}(x,y) = \sqrt{\frac{2}{\pi}}\frac{1}{w}\exp(-\frac{x^2+y^2)}{w^2} \qquad (6.4),$$

where w is beam diameter determined by

$$w^2 = \frac{2h}{k_0} = \frac{h\lambda}{\pi}\sqrt{\frac{\varepsilon_0}{\varepsilon(0)}} \qquad (6.5).$$

Fig. 6.15 shows the schematic of intensity profile which is amplitude squared. Since in our EQE calculation, a constant intensity profile was assumed, as indicated by the dashed box, when the cell was placed in the center of the fiber spot, it could receive more than one time the average intensity; and when it was positioned off center, the intensity it received could be less then the average. This might be the reason why we measured more than 100% EQE on some cells. Since the cell size is small, although effort was made to cover the cell completely by the fiber spot, the cell's exact location relative to fiber spot will certainly differ for each measurement.

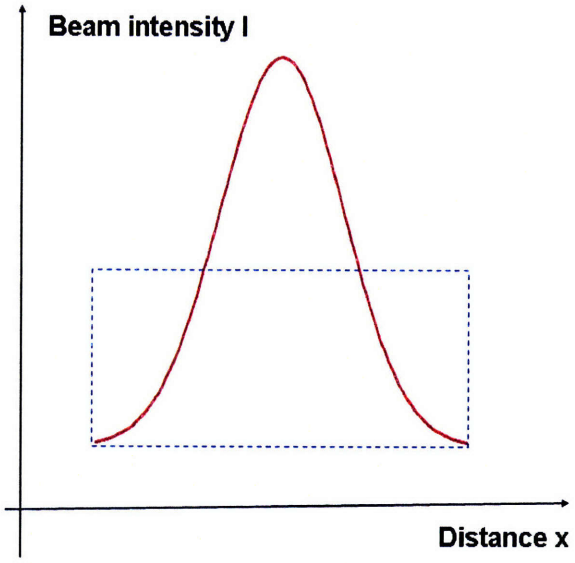

Fig. 6.15 Schematic of light intensity profile from a fiber

It was found that almost all EQE curves for cells with different thickness and back reflector design peak near λ=580 nm, and given that the EQE of shorter λ photons may differ due to different front surface quality, and that of longer λ photons will depend on path length (and therefore back structure) and carrier collection efficiency, it is reasonable to normalize all the EQE values at λ=580 nm to the same number. This will allow us to filter away the influence of non-uniform fiber emission and get useful information on the behavior of cells with different back reflector design.

Several pieces of evidence can be used as justification to this normalization method. First, some cells with same thickness and back reflector design have EQE overlapping before normalization. Second, if they do not overlap before normalization, after scaling, their EQE curves overlap completely throughout the entire λ=300-1200 nm spectrum. Thirdly, before normalization, some cells with the same thickness, but of differing back reflector design have EQE overlap in the range of λ between 300 nm and

somewhat more than 600 nm, but differ at longer wavelengths. Fig. 6.16 shows such an example. Solar cell BC4 has a wavy DBR plus grating on the back, and solar cell SC6

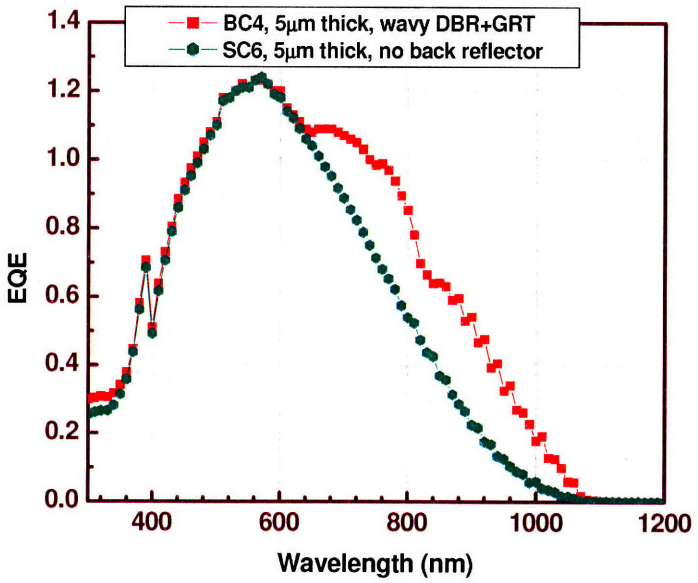

Fig.6.16 EQE curves of two 5 μm thick solar cells with different back structures before normalization. One cell has wavy DBR and grating on the back, the other does not have back structure

has no back reflector, except the 500 nm thick isolation oxide layer between the device layer and the new handle wafer. They exhibit almost identical EQE for λ between 300 nm and 640 nm. The small discrepancy near 300 nm could be caused by noise, as the total incident light intensity from the fiber around this wavelength is very weak, less than 0.2 μW on the whole spot. For λ>640 nm, however, the two curves show very different shapes. SC6 has smooth shape, and EQE decreases rapidly as λ increases, while BC4 is quite bumpy, having three obvious shoulders, one near 640 nm, the other two at 740 and 840 nm, respectively. This figure can be a strong support to the normalization method we use. For 20 and 50 μm thick cells, the EQE of cells with different back structures may start to diverge at longer λ than 640 nm. So it is reasonable to normalize EQE at λ=580

nm for all three cell thicknesses. In the following sections, we will present the EQE of all cells at three thicknesses, first EQE from direct measurements, then normalized EQE.

II. EQE of 5 μm thick cells

Fig. 6.17 displays the directly measured (original) EQE of 5 μm thick solar cells on three different wafers: B, N, S, with four different back structures. Wafer B has both wavy DBR and gratings on the 9 central dice. After grating etching, DBR film stack was deposited all over the wafer, so the peripheral dice, although having no gratings did get DBR. For wafers with 1D gratings on the central dice, since negative photoresist was used for grating lithography, all the peripheral area on the wafer was plasma etched during grating etching. For wafers with 2D gratings, because positive photoresist was used for grating lithography, the surrounding area was protected by the photoresist and remained intact during grating etching. Studying these DBR-only cells with different exposure to etching may tell us something about back surface passivation, for instance how useful the back surface field is, as well as how efficient DBR is by itself. Shown in the figure are two cells from two central dice, BC4 and BC7. Also shown is cell BL2 having DBR only and having received blanket plasma etching during grating fabrication. Cells NC3 and NC4 have a flat DBR and grating. For reference, cells SC6 and SC9 have no special back structure. We have seen SC6 and SC9 in Figs. 6.13 and 6.14 before; they overlap completely after multiplying one of them by a normalization factor. We have also seen in Fig. 6.16 the comparison between BC4 and SC6, which overlap for $\lambda<640$ nm.

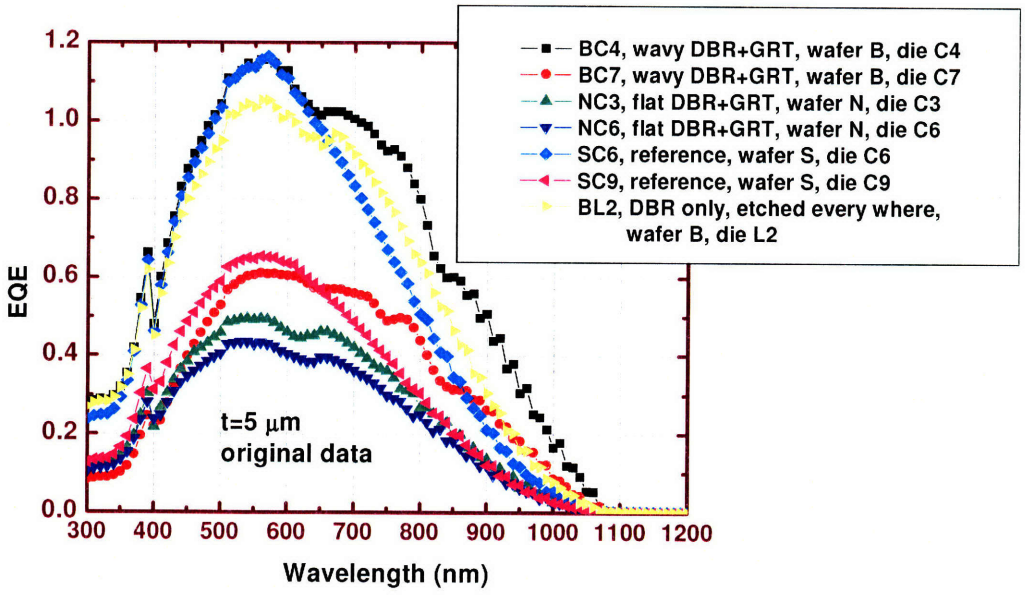

Fig. 6.17 Original EQE of 5 μm thick solar cells with different back structures

A quick observation of Fig. 6.17 reveals that cells with the same back reflector have the same shape of EQE curves, although the absolute value of EQE may differ: cells with no back reflector have smooth EQE curves; while cells with flat DBR and grating have at least one bump, located at λ=620 nm; cells with wavy DBR and grating have at least three bumps scattered between 640 nm and 1000 nm.

Normalizing these curves to EQE of cell SC9 at λ=580 nm (EQE=0.65) gives us Fig. 6.18. It is obvious that EQE of cells with the same back structure overlaps in most of the λ range. For easier inspection, Fig. 6.19 replots Fig. 6.18, depicting EQE of cells with different type of back structures, one curve for each type. It is obvious that all kinds of back reflectors enhances absorption significantly for λ>640 nm. Cells with flat DBR plus grating and those with DBR-only have one bump on the curve, and cells with wavy DBR plus grating have at least three bumps, rendering the highest absorption. It verified our

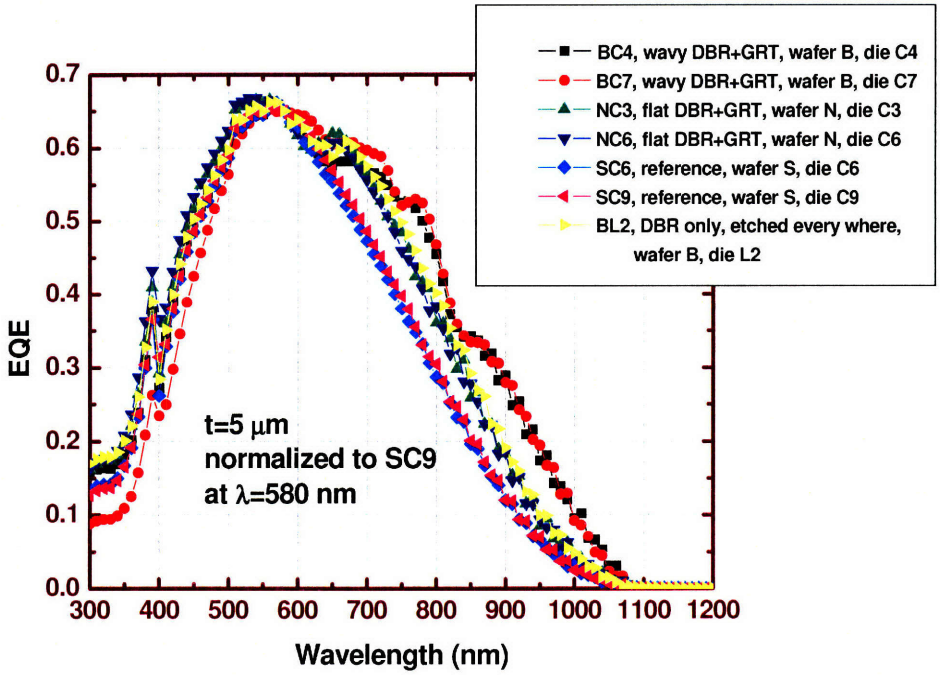

Fig. 6.18 EQE of 5 μm thick solar cells with different back structures after normalization at λ=580 nm

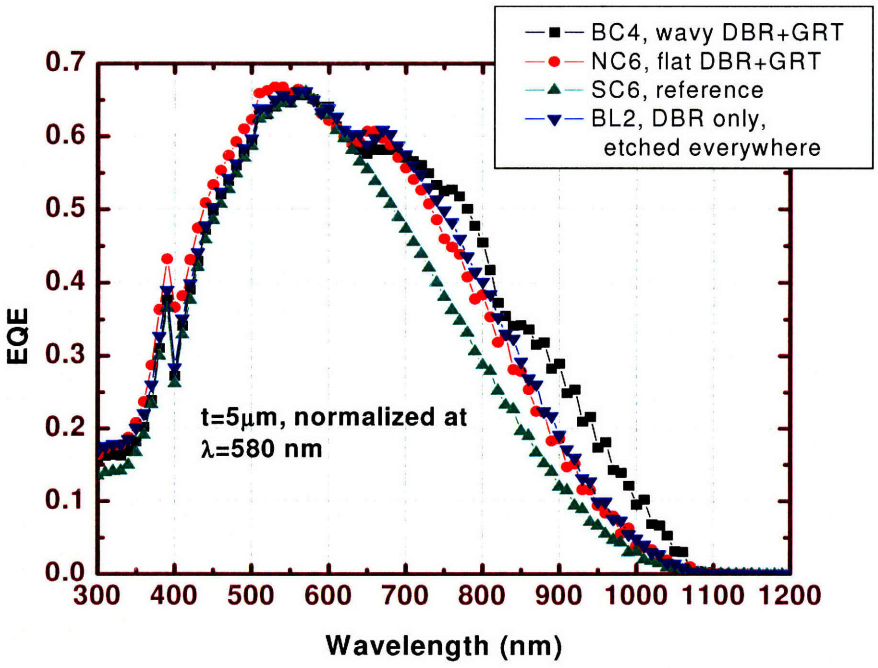

Fig. 6.19 Selected EQE curves for 5 μm thick SOI solar cells after normalization at λ=580 nm

previous assumption that the periodicity in the DBR film plane does improve absorption; textured photonic crystals (wavy DBR) are even better than flat ones. It is also observed that "DBR-only cell" has EQE almost identical to that of flat DBR plus grating.

Note that in t=5 μm thick cells, for photons that do enter the cell without being reflected, with wavelength at the normalization point λ=580 nm (absorption coefficient α=5.78x10^3/cm), a single trip from top to bottom surface of the cell will absorb photons by the probability

$$1-\exp(-\alpha t)=1-\exp(-5.78\times10^{3}\times5\times10^{-4})=94.4\% \qquad (6.6).$$

For cells with DBR and grating, at least two trips will be made, so the absorption probability is

$$1-\exp(-2\alpha t)=1-\exp(-5.78\times10^{3}\times10\times10^{-4})=99.7\% \qquad (6.7).$$

Considering the 20.4% shadowing, the highest EQE we can get is around

$$(1\text{-}20.4\%)\times 94.4\%=0.751 \qquad (6.8)$$

in the single trip case, and 0.794 in the double trip case, assuming no further photon absorption. Normalizing EQE to 0.65 at λ=580 nm is equivalent to assuming a carrier collection efficiency around 0.65/0.751= 86.5% for the single-trip case and 81.9% for the double-trip case.

From Fig. 6.19, one can calculate the relative efficiency enhancement rendered by the improvement of long λ photon absorption entailed by DBR and grating. The short circuit current density

$$J_{sc}=q\sum_{\lambda=300nm}^{1200nm}EQE(\lambda)s(\lambda) \qquad (6.9),$$

where q is the electron charge, and s(λ) is the number of incident photons per unit area at a certain wavelength for AM1.5 spectrum, which is well tabulated. By adding all the photogenerated electrons together, one can get J_{sc} and the relative enhancement caused by the back reflectors. Table 6.2 lists the calculation results. Relative Jsc enhancement was obtained from $\frac{J_{sc} - J_{sc\_ref}}{J_{sc\_ref}}$, where J_{sc_ref} is the value of the reference cell.

Table 6.2 Calculated J_{sc} of 5 μm thick solar cells with different back structures after EQE Normalization

Cell thickness (μm)	Solar cell identity	Description	Jsc (mA/cm^2)	relative Jsc enhancement
5	SC6	Reference cell	14.68	N/A
	NC6	Flat DBR+GRT	16.52	12.5%
	BC4	Wavy DBR+GRT	17.45	18.9%
	BL2	DBR only, etched	16.68	13.6%

Table 6.2 demonstrates that wavy DBR plus grating enhances Jsc the most, by 18.9%. Flat DBR plus grating renders an enhancement of 12.5%, almost the same as "DBR only". That flat DBR plus grating does not perform better than "DBR only" may result from the small dimension of our solar cells (2 mm x 2mm). For 5 μm thick cells, when light is diffracted by 45 degrees, assuming a "W" shaped path, the path length would be only $2\times(1/\cos 45^\circ + 1) = 4.85$ times the cell thickness. Therefore, for grating to

effectively enhance path length, big lateral dimension far more than 200 times cell thickness (as in this case) is important.

It is also noteworthy that DBR deposited on a blanket etched surface enhanced Jsc by 13.6%, which is evidence that our implanted back surface field and partially thermal oxidized first layer of DBR did improve back surface passivation.

Since the measurements under the sun simulator did not show obvious difference in Voc, and all the cells measured are good diodes with high fill factor, it is reasonable to assume that the total power conversion efficiency is enhanced by approximately the same relative amount as Jsc.

III. EQE of 20 μm thick cells

Fig. 6.20 shows the measured EQE of 20 μm thick cells with different back structures. For 20 μm thick wafers, we do not have wavy DBR plus 1D grating wafers measurements, because the yield decreases as we went through problematic grating exposure in New Mexico (laser intensity issue); the blistering DBR deposition in MIT cleanroom MTL (PECVD deposition issue), which caused a lot of difficulty during wafer bonding and created many bad dice; and the MTL metal etcher which broke several wafers. Fortunately, we got one wafer with wavy DBR plus 2D gratings, the only wafer with 2D gratings that has survived all the processing among wafers with all thicknesses. This also automatically gives us a few "DBR-only" cells on an un-etched back surface. Compared to the narrow EQE curves of 5 μm thick cells, the EQE of all the 20 μm thick cells broadens out. And collectively they also exhibit higher EQE than that of 5 μm cells, with the highest value 1.49 and lowest one 0.91 at λ=570 nm. Cells with the same back

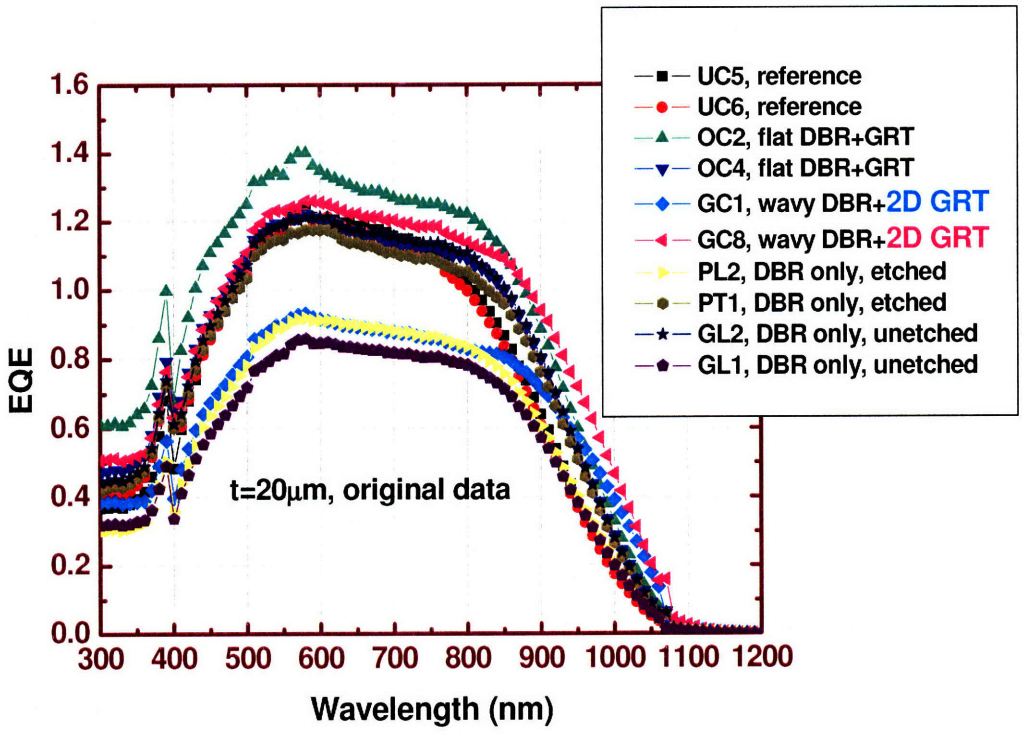

Fig. 6.20 Original EQE of 20 μm thick cells with different back structures

structure still have overlapping or vertically translated EQE curves. Cells with back reflectors still have around one bump on their EQE curves, but not as obvious compared to 5 μm thick cells.

Since at λ=570 nm, the lowest EQE=0.91, which is certainly unreasonable to be set as a target to normalize to, we normalize EQE at this wavelength to 0.725, as we will do for 50 μm thick cells. This is kind of arbitrary, but should not affect the accuracy of relative Jsc enhancement calculation, because if we decide to normalize to another value X, then each curve needs to be multiplied by the same value, the ratio between 0.725 and X, for every λ. For easier inspection, selected EQE curves after normalization are shown in Fig. 6.21, one for each back structure. All the curves overlap for λ<740 nm. For longer

λ, the cells can be divided into three groups: (1) the reference cell has the lowest EQE; (2) cells with flat DBR plus grating and etched or unetched DBR all have overlapping EQE, but wider and higher than that of the reference cell; (3) cells with wavy DBR plus 2D grating has the highest EQE, which becomes wider than the second group starting at λ=820 nm.

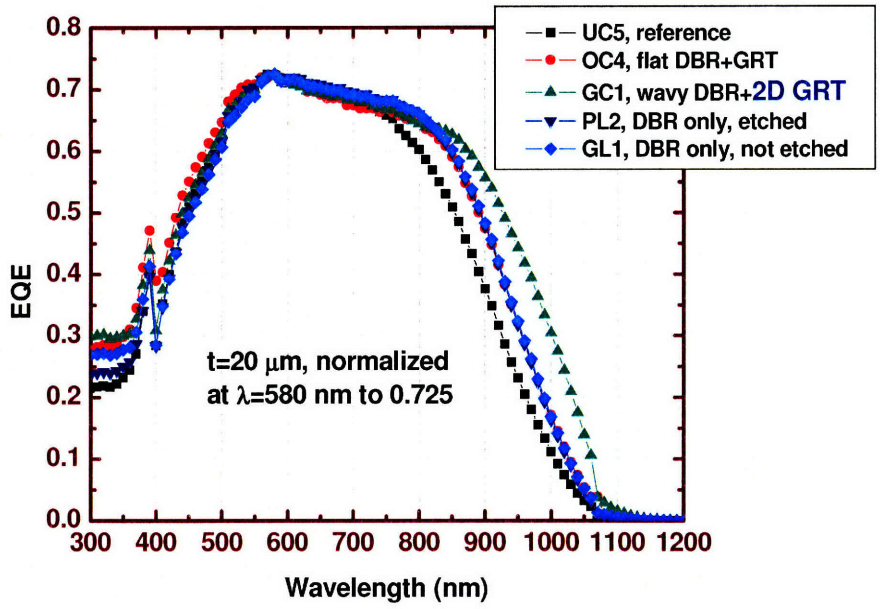

Fig. 6.21 Selected EQE curves of 20 μm thick cells with different back structures

Jsc calculation based on normalized EQE integration is listed in Table 6.3. Again, Wavy DBR plus grating renders the highest Jsc enhancement, 11.3% in this case; flat DBR plus grating, etched and unetched DBR are all similar, with flat DBR plus grating entails 6.74% enhancement, a little higher than both types of DBRs. Unetched DBR does not perform better than the etched one, further evidence that our back surface filed implantation and partial thermal oxidation of the first DBR layer did improve back surface quality.

Table 6.3 Calculated J_{sc} of 20 μm thick solar cells with different back structures after EQE normalization

Cell thickness (μm)	Solar cell identity	Description	Jsc (mA/cm^2)	relative Jsc enhancement
20	UC5	Reference cell	20.62	N/A
	OC4	Flat DBR+GRT	22.01	6.74%
	GC1	Wavy DBR+2D GRT	22.95	11.3%
	PL2	DBR only, etched	21.86	6.01%
	GL1	DBR only, not etched	21.80	5.72%

IV. EQE of 50 μm thick cells

The original data of EQE for 50 μm thick cells are shown in Fig. 6.22. The EQE curves broaden further than 20 μm thick cells. As with 5 and 20 μm thick cells, the EQE of cells with the same back structure has the same shape, and there are no obvious bumps on the curves of cells with DBR and grating. Fig. 6.23 illustrates the normalized EQE of selected cells, one for each back reflector type. As expected, all the cells with back reflectors outperform the reference cell: wavy DBR plus grating has the highest EQE; flat DBR plus grating has overlapping EQE with "DBR only" cells.

Note that for 50 μm thick cells, EQE was normalized to 0.725 at λ=580 nm, which is the EQE of reference cell WC1. For photons at this wavelength, after a single trip from top surface to bottom of the solar cell, the remaining light intensity is 2.8×10^{-13}

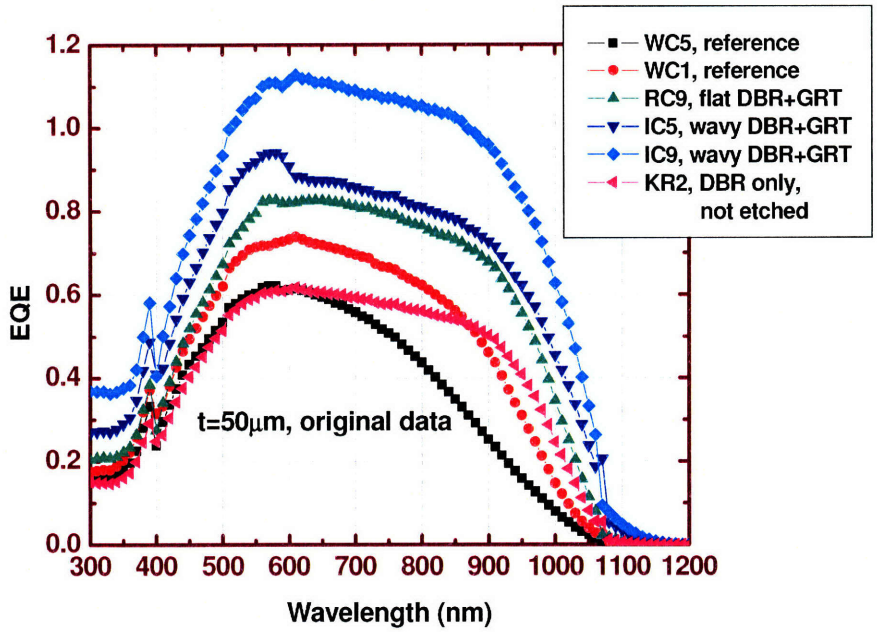

Fig. 6.22 Original EQE of 50 μm thick cells with different back structures

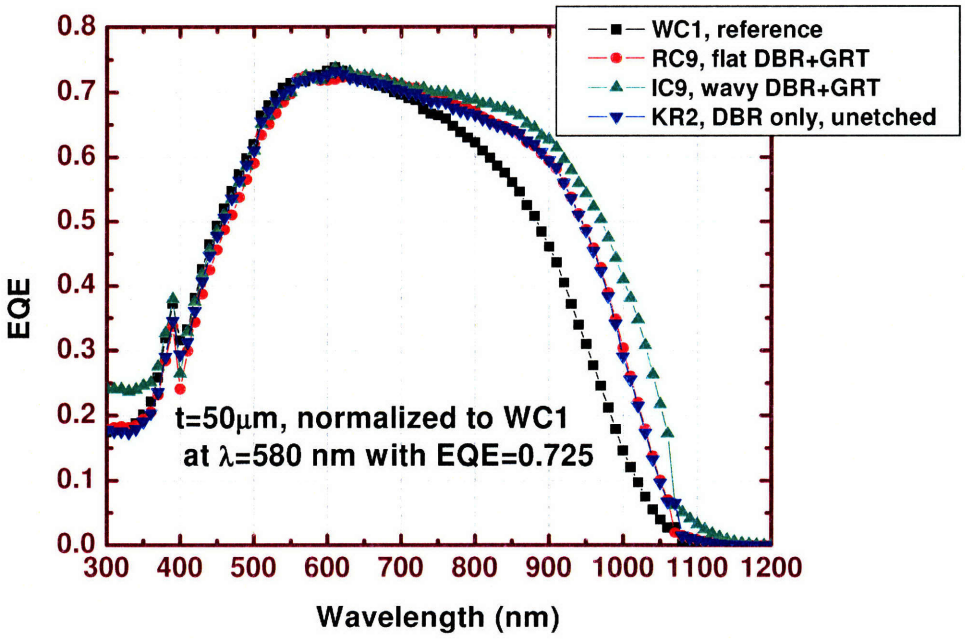

Fig. 6.23 Normalized EQE of 50 μm thick cells with different back structures

of the incident intensity. Therefore, this EQE corresponds to a carrier collection efficiency

$$\eta_c \approx \frac{EQE}{(1-shadowing)\times absorption} = \frac{0.725}{(1-0.204)\times 1} = 91.1\% \quad (6.10).$$

For comparison, our previous thick solar cells had a collection efficiency of more than 97.9% at this λ. For 20 μm thick SOI solar cells, a similar calculation revealed the same collection efficiency, as for both cell thicknesses, photons at λ=580 nm can be fully absorbed in a single trip.

Jsc calculated from normalized EQE of 50 μm thick cells is listed in Table 6.4. Wavy DBR plus grating enhances Jsc by 12.32%, flat DBR plus grating performs similarly as "DBR only" (not etched), with enhancement 6.65% and 7.16%, respectively.

Table 6.4 Calculated Jsc of 50 μm thick SOI solar cells with different back structures after EQE normalization

Cell thickness (μm)	**Solar cell identity**	**Description**	**Jsc (mA/cm^2)**	**relative Jsc enhancement**
50	WC1	Reference cell	21.51	N/A
	RC9	Flat DBR+GRT	22.94	6.65%
	IC9	Wavy DBR+GRT	24.16	12.32%
	KR2	DBR only, not etched	23.05	7.16%

V. EQE vs. cell thickness

In the earlier parts of this section, the EQE was normalized at λ=580 nm, to 0.65 for 5 μm thick cells (the measured value of reference cell SC9); and to 0.725 for 20 and 50 μm thick cells. To see the variation of EQE vs. cell thickness, perhaps all the EQE should be normalized to the same value at this wavelength. As mentioned earlier, compared to other wavelengths, EQE at this λ should receive little influence from surface effects and path length difference. However, as mentioned in Section 6.2.4 on wafer bonding and in section 6.3.2 on diffusion length, DBR blister may have the most severe influence on 5 μm thick cells. This is evidenced by their collectively low EQE, even before normalization. Meanwhile, their smaller device thickness also makes cells more sensitive to surface recombination. Our previous estimation on carrier collection efficiency η_c showed that at λ=580 nm, $\eta_c \approx 91.1\%$ for 20 and 50 μm thick cells, and ~82% for 5 μm thick cells. Because the 5 μm thick cells suffered more from DBR blistering, it makes sense to normalize their EQE to the same value as that of 20 and 50 μm thick cells. EQE for cells with the same kind of back structure, but different device layer thicknesses is shown in Figs. 6.24 (a)-(d). Here, EQE of 5 μm thick cells is also normalized to 0.725 at λ=580 nm.

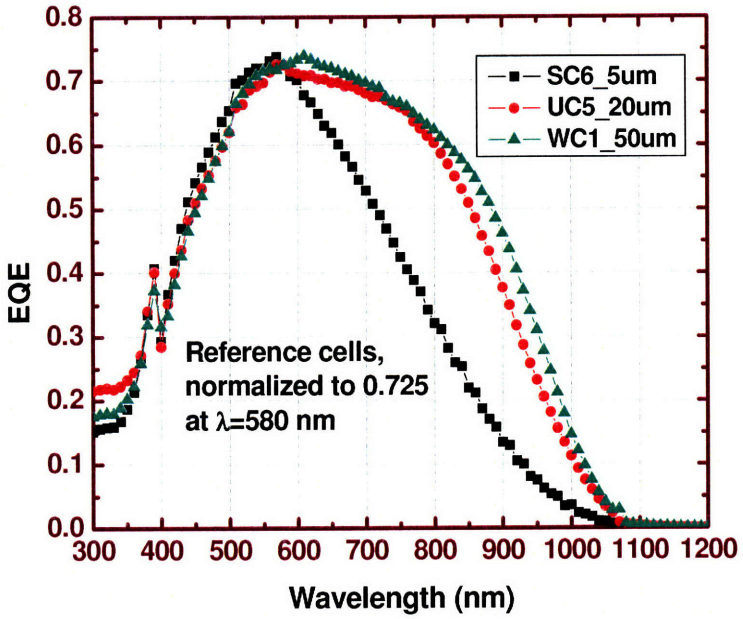

Fig. 6.24 (a) EQE of reference cells with different device layer thicknesses

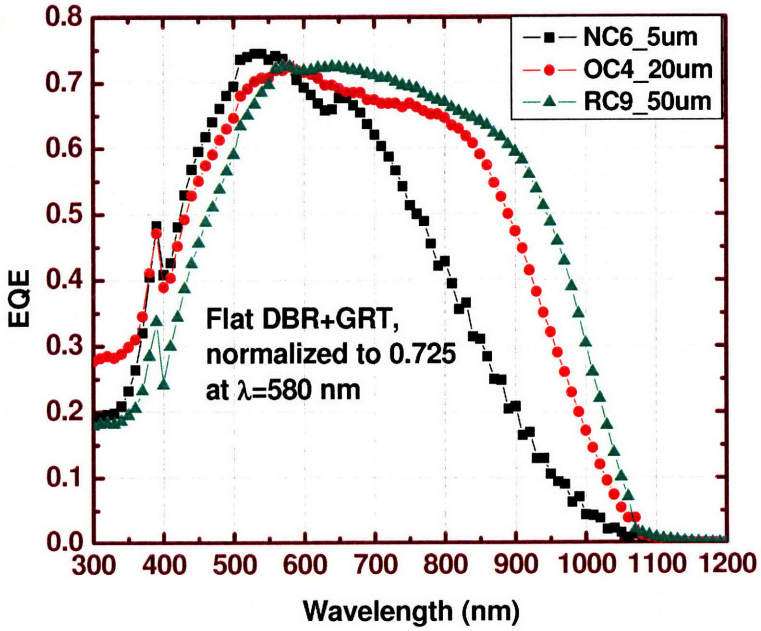

Fig. 6.24 (b) EQE of cells with flat DBR plus grating at different device layer thicknesses

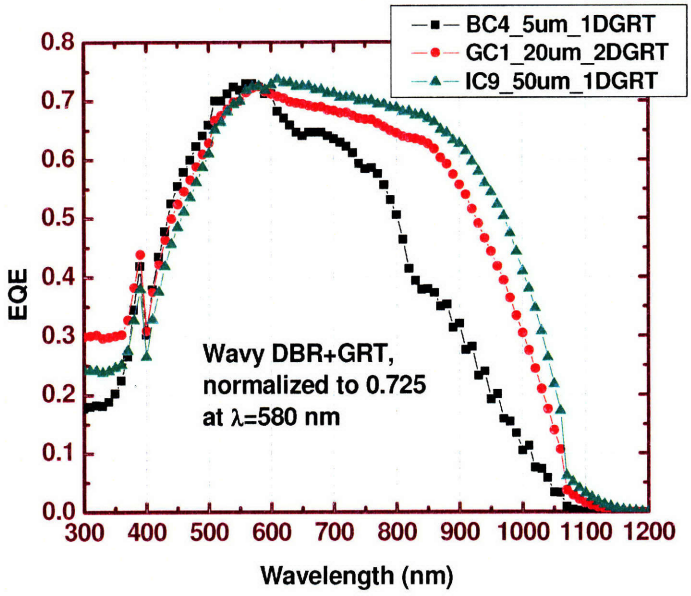

Fig. 6.24 (c) EQE of cells with wavy DBR plus grating at different device layer thicknesses

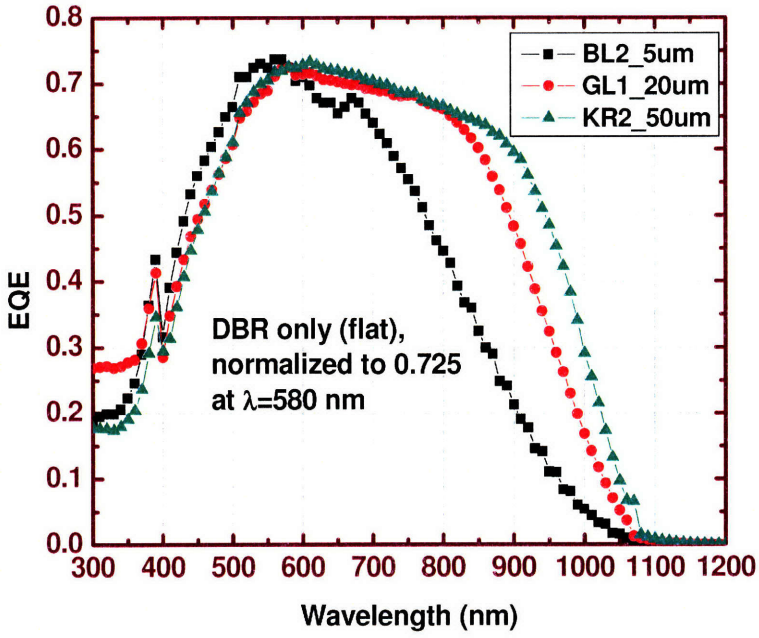

Fig. 6.24 (d) EQE of solar cells with "DBR only" at different device layer thicknesses

Fig. 6.24 clearly shows that the EQE of reference cells at all device layer thicknesses t have similar smooth shape, and widens as t increases. For cells with back reflectors, at t=5 μm, all the EQE curves display bumps, an sign of strongly enhanced absorption, with wavy DBR plus grating having 3 obvious bumps, flat DBR plus grating and "DBR only" having at least one bump. At t=20 μm, there seems to be just one bump on the EQE curves when there are back reflectors, and the bump is less obvious compared to t=5 μm cells. At t=50 μm, there are no appreciable bumps. Therefore, the thinnest cells benefit the most from the back reflectors, as expected.

Fig. 6.25 depicts the Jsc enhancement relative to reference cells $\frac{J_{sc} - J_{sc\_ref}}{J_{sc}}$, and it verifies the observation from EQE curves. While for t=20 and 50 μm, the Jsc

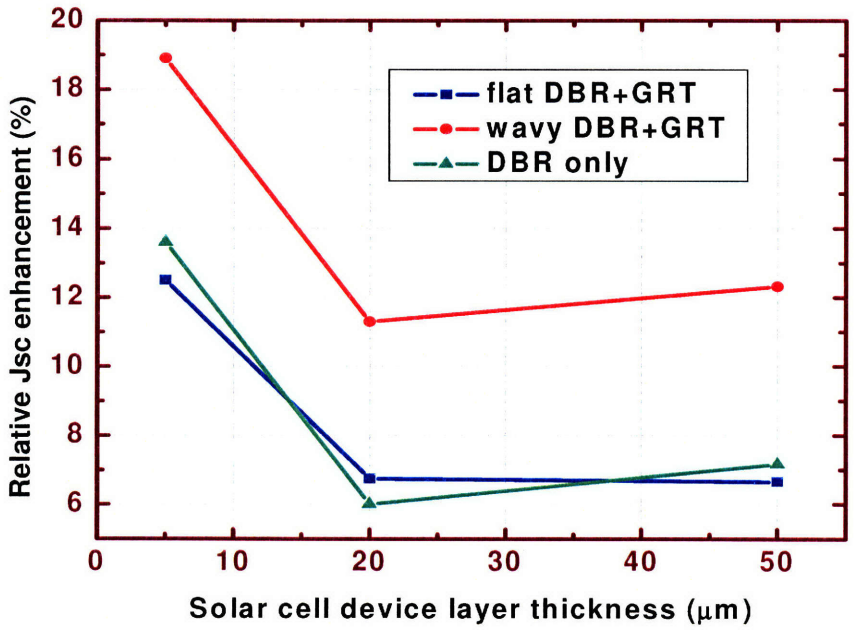

Fig. 6.25 Relative Jsc enhancement vs. cell thickness

enhancement is almost the same, when t is reduced to 5 μm, the enhancement dramatically increases, and jumps to 18.9% for cells with wavy DBR plus grating. Among all different back reflectors, wavy DBR plus grating performs the best at all cell thicknesses, far above flat DBR plus grating and "DBR only". In general, flat DBR plus grating does not gain more Jsc enhancement than "DBR only". The most possible reason may be that with the small lateral dimension of our cells (2 mmx2 mm), the benefit from grating is not obvious.

6.3.4 Power conversion efficiency deduced from EQE and dark I-V curves

Since our direct I-V measurements under the sun seemed to suffer from the light source accuracy, as an alternative, power conversion efficiency can be deduced from dark J-V curve translated by Jsc that is calculated from EQE. As shown in Fig. 6.12, although Jsc will change depending on the intensity of light source, Voc and fill factor remains almost constant. The fundamental reason is that according to the superposition approximation, which is reasonable for many photovoltaic materials [6.5],

$$\begin{aligned} J(V) &= J_{sc} - J_{dark}(V) \\ &= J_{sc} - J_0(e^{qV/nkT} - 1) \end{aligned} \qquad (6.11).$$

where J_0 is the reverse bias saturation current density, and n is the diode ideality factor. Therefore, J-V curve under illumination should just be a translation of the dark J-V curve by Jsc, which is determined by illumination intensity. Since fill factor measures the squareness of J-V curve and is determined by the shape of the curve, it should not depend on the amount of translation. As for Voc, it has the relation

$$V_{oc} = \frac{kT}{q} \ln\left(\frac{J_{sc}}{J_0} + 1\right) \qquad (6.12),$$

so it changes logarithmically with light intensity. Eqs. (6.11) and (6.12) show that translating the dark J-V curve by Jsc would be a good approximation to obtain the J-V curve under the sun and thereby the power conversion efficiency η. Since FF and Voc almost remain constant when the illumination intensity changes, as verified by the three curves in Fig. 6.12, η acquired this way may just be a factor off, depending on to which value we normalize EQE.

Fig. 6.26 illustrates the J-V curve translated from the dark J-V curve of 5 μm thick solar cells by Jsc, which is obtained from EQE normalized to 0.65 at λ=580 nm. The efficiency η varies from 7.68% for reference cell SC6 to 8.42% for cell BC4 with wavy DBR plus grating. Although the cell with wavy DBR plus grating has the highest Jsc, and the reference cell ranks the lowest in Jsc, the order of their Voc is reversed: the reference cell has the highest Voc=0.649 V, and the cell has wavy DBR plus grating has the lowest Voc=0.620 V. Fill factor varies from 0.805 for the reference cell and "DBR only" cell to 0.712 for the cell with flat DBR plus grating.

J-V curves of 20 μm thick cells are shown in Fig. 6.27. The reference cell still has the lowest efficiency, but the cell with flat DBR plus grating has the same η as the cell with wavy DBR plus grating. Here we see a bigger variation of V_{oc}, indicating a larger variation of minority carrier diffusion length. The reference cell and the cell with wavy DBR plus grating have almost the same V_{oc} around 0.70 V; the cell with flat DBR and grating has the highest Voc of 0.776 V, helping it achieve the same η as cell with wavy DBR plus grating.

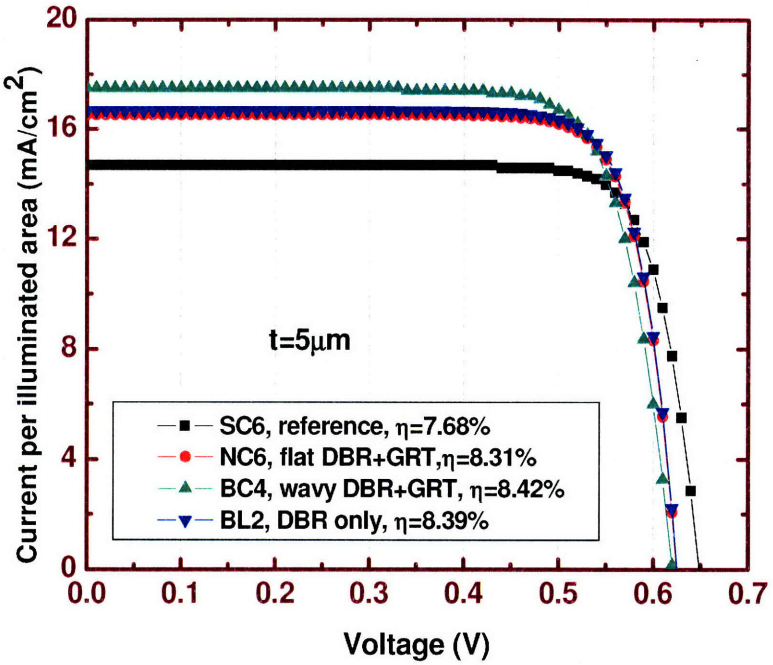

Fig. 6.26 J-V curves of 5 μm thick solar cells deduced from external quantum efficiency

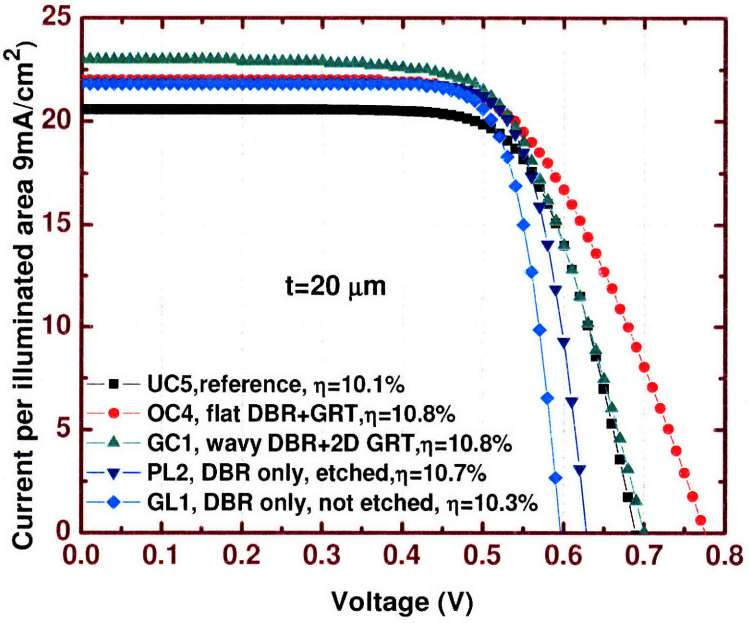

Fig. 6.27 J-V curves of 20 μm thick solar cells deduced from external quantum efficiency

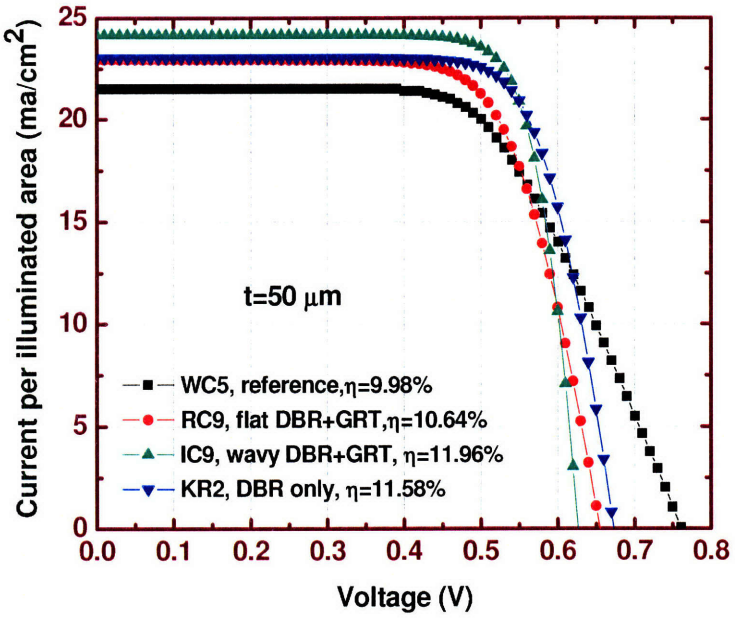

Fig. 6.28 J-V curve of 50 μm thick solar cells deduced from external quantum efficiency

Fig. 6.28 depicts the J-V curves of 50 μm thick cells. The cell with wavy DBR plus grating still performs the best, with η=11.96%, compared to the reference cell which has η=9.98%. Although the reference cell has the highest Voc=0.76 V, its fill factor is lower than that of other cells.

The relative efficiency enhancement $\frac{\eta - \eta_{ref}}{\eta_{ref}}$ vs. cell thickness is shown in Fig. 6.29. Surprisingly, although 5 μm thick cells have higher η enhancement than 20 μm thick cells as expected, 50 μm thick cell achieved the highest relative enhancement. This seems to result from the low fill factor of the 50 μm thick reference cell.

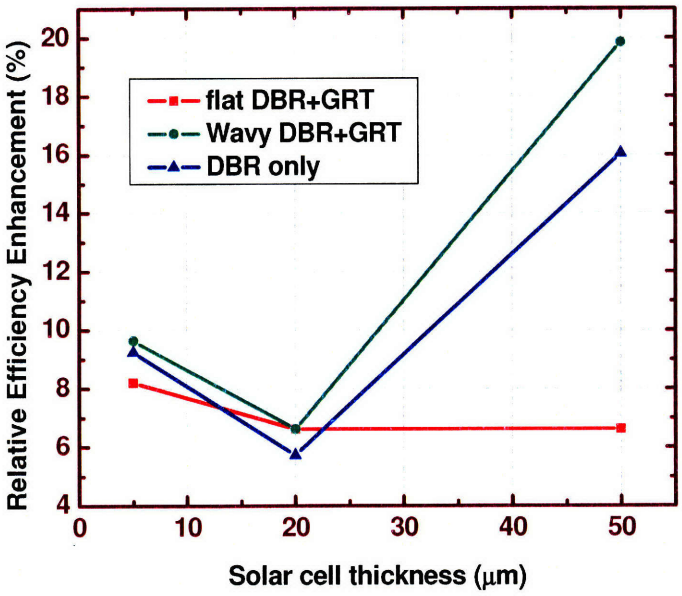

Fig. 6.29 Relative power conversion efficiency enhancement vs. cell thickness

6.4 Comparison between experiments and simulation

In this section, we will compare what we achieved experimentally with the theoretical predictions. Fig. 6.30 depicts the absorption spectra of 5 μm thick cells with different back structures, using scattering matrix simulation. It assumes no shadowing, and 100% carrier collection. The closely spaced sharp peaks at long wavelengths are interference or diffraction peaks that we have seen in Chapter 2. We could not see them experimentally because the accurate spectral resolution of our monochromator is more than 10 nm, and each step in our external quantum efficiency measurement was 10 nm. To better compare simulation with experiments, the narrow peaks in Fig. 6.30 are smoothed out in Fig. 6.31 using a moving averaging method which preserves the area under the curves. It records the average value of the absorption within some window of

fixed width but varying center. Fig. 6.31 clearly shows several absorption bumps on the curves for cells with DBR plus grating, starting at 600 nm; and for cells with DBR only, the bump starts at 640 nm. For comparison, Fig. 6.19 exhibits bumps on EQE curves starting at 640 nm for cells with all back structures. The oscillations in the long wavelength region in Fig. 6.31 are due to interference, and in the case of gratings, to diffraction also. Since the interference peak spacing is inversely proportional to cell thickness as discussed in Section 2.4.2 in Chapter 2, for 5 μm thick cells, due to the bigger peak spacing (~10 nm) compared to 20 and 50 μm thick cells, experimentally, we did observe oscillations on EQE curves, especially on curves representing DBR plus

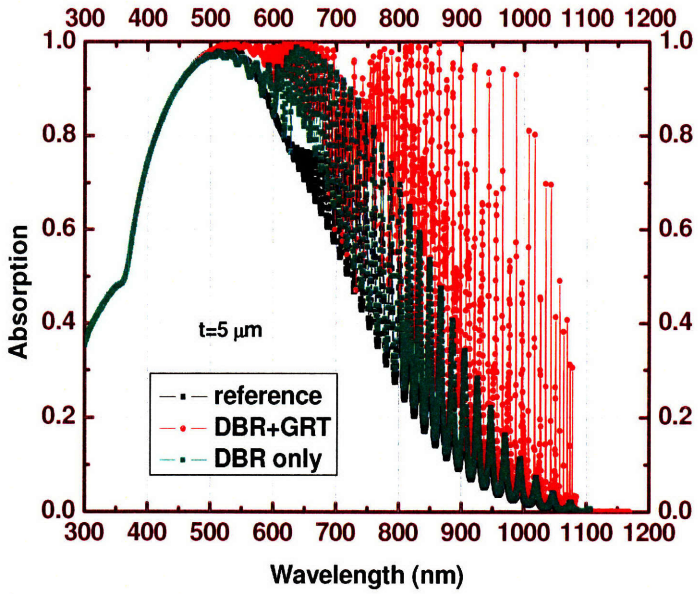

Fig. 6.30 Simulated absorption spectra of 5 μm thick solar cells with different back structures.

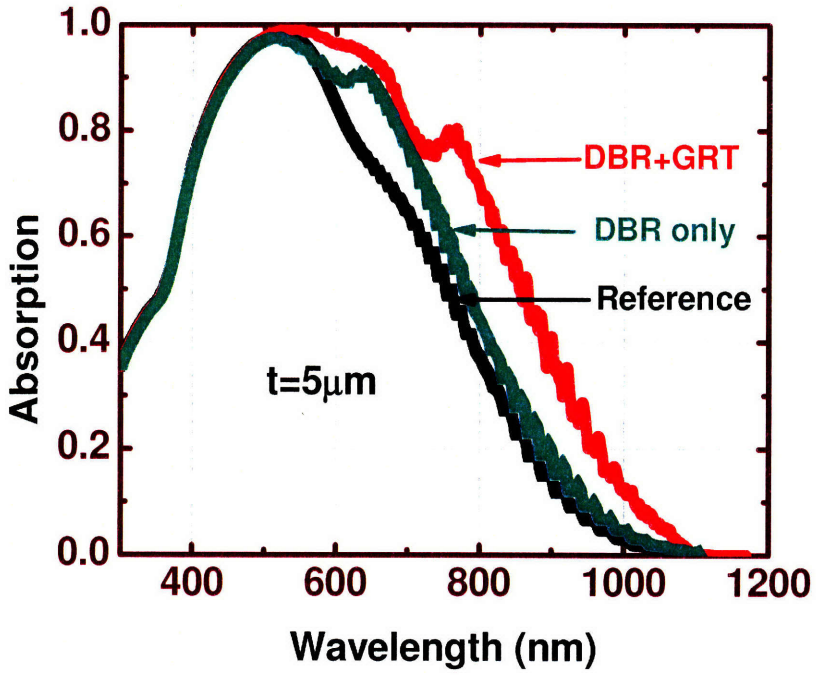

Fig. 6.31 Smoothed absorption spectra from simulation for 5 μm thick solar cells with different back structures

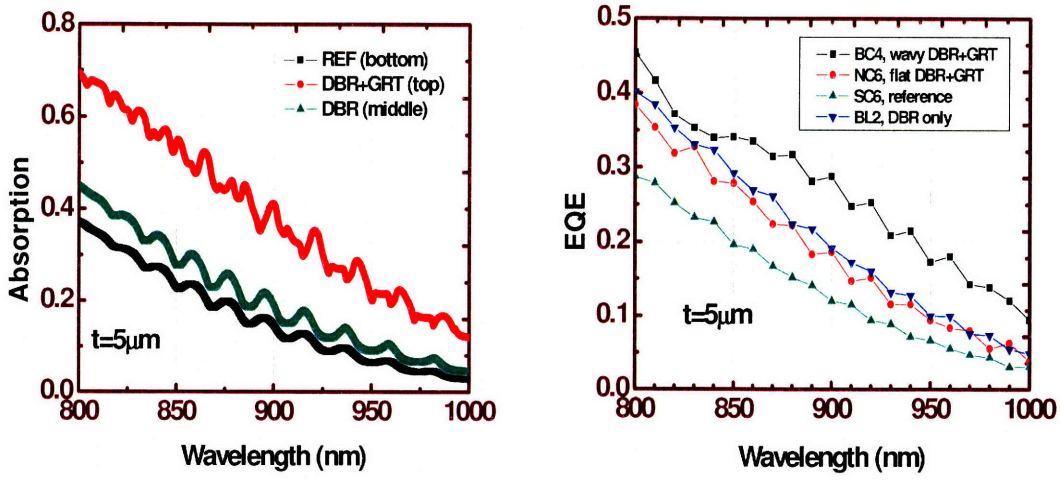

Fig. 6.32 Comparison between the simulated absorption spectra (left) and measured EQE curves (right) for 5 μm thick cells in the long wavelength region, showing oscillations due to interference

grating cells, as shown in Fig. 6.32, which consists of the middle wavelengths of view of Figs. 6.31 and 6.19. To quantitatively compare absorption in Fig. 6.31 with EQE in Fig. 6.19, we should consider 20.4% shadowing and 82% carrier collection efficiency at λ=580 nm, normalizing the absorption to 0.65 at 580 nm.

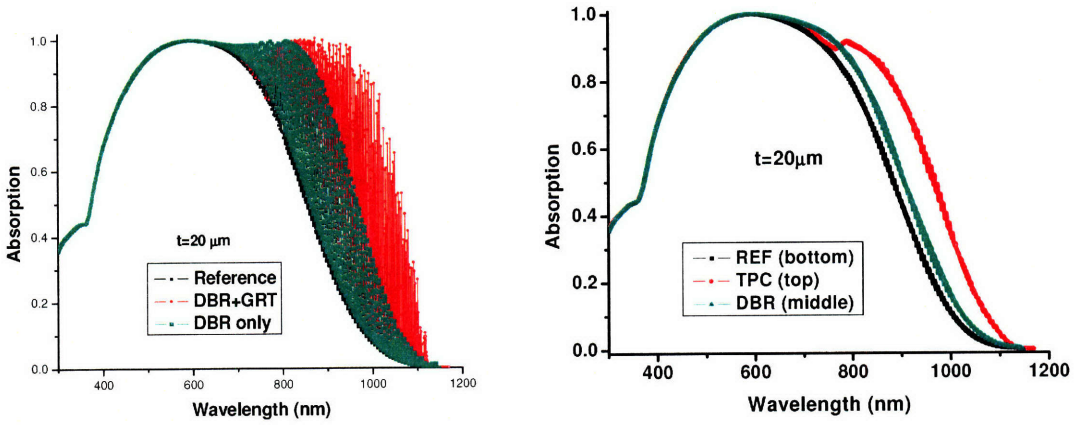

Fig. 6.33 Simulated absorption spectra of 20 μm thick solar cells with different back structures, before (left) and after (right) smoothing with moving average method

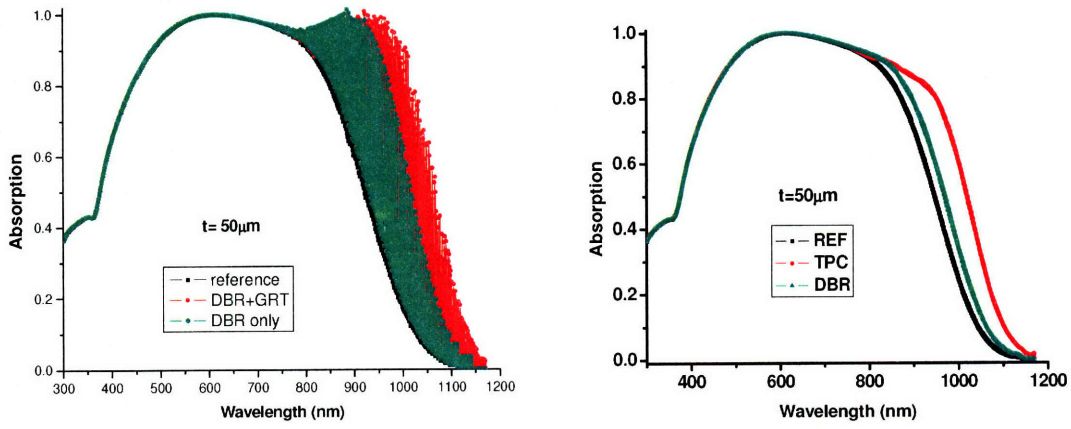

Fig. 6.34 Simulated absorption spectra of 50 μm thick solar cells with different back structures, before (left) and after (right) smoothing with moving average method

Figs. 6.33 and 6.34 illustrate the simulated absorption spectra of 20 and 50 μm thick cells before and after smoothing, which look very similar to the EQE curves we saw earlier in Figs. 6.21 and 6.23.

Relative Jsc enhancement from simulation and our experimental results is depicted in Fig. 6.35. Simulation results show the power conversion efficiency enhancement quite similar to the Jsc enhancement as it assumes an ideal diode and 100% carrier collection. Therefore, all the cells with the same thickness have almost identical Voc and fill factor. Fig. 6.35 shows that experimentally, DBR-only cells gained more enhancement than simulation; wavy DBR plus grating performed close to theory (assuming flat DBR) for 20 and 50 μm thick cells. Although wavy DBR plus grating just achieved 65% of simulation predicted increases for 5 μm thick cells, it gained 82.5% of

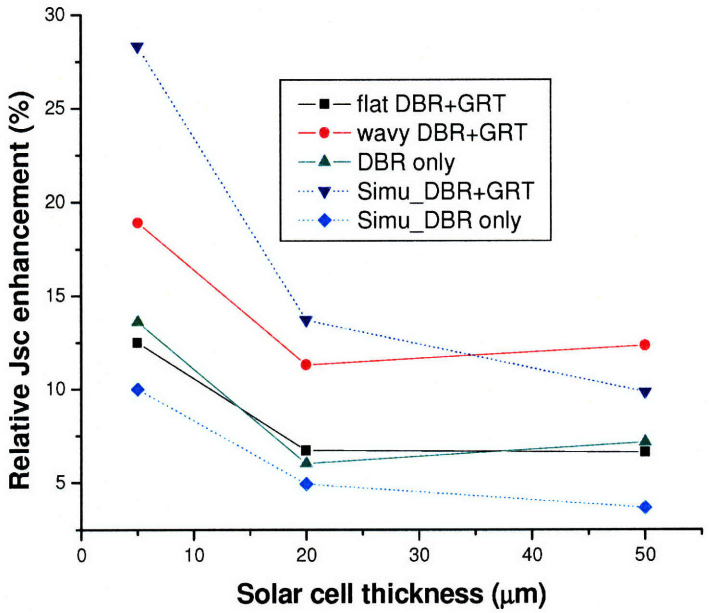

Fig. 6.35 Comparison between experimental and simulated Jsc enhancement vs. solar cell thickness

theoretical prediction for 20 μm thick cells. Flat DBR plus grating gained less enhancement than simulation for all cell thicknesses. The discrepancy between experimental results and simulation can result from many factors. For example, simulation assumes 100% carrier collection and ideal diode behavior with 86% fill factor, but experimentally that is never true. Furthermore, thinner cells are more sensitive to surface imperfections and fabrication errors. That might explain why the experimental results of 5 μm thick cells deviate the most from simulation. There are many materials, contamination and machine variations which would need to be studied and controlled to optimize the process. We have gone through a very complicated process flow with many possible causes of deviation from the ideal situation predicted by simulation.

References

[6.1] Robert F. Pierret, Semiconductor Device Fundamentals, Addison-Wesley Publishing Company, Reading, Massachusetts, Menlo Park, California, etc., 1996, p. 82.
[6.2] C. Yun, Ph.D. Thesis, University of California, Berkeley, CA (2000).
[6.3] J. D. Plummer, M. D. Deal, and P. B. Griffin, Silicon VLSI Technology, Prentice-Hall, New Jersey, 2000, p. 527.
[6.4] C. S. Tan, K. N. Chen, A. Fan, and R. Reif, Electrochemical and Solid-State Letters, 8 (1) G1-G4 (2005).
[6.5] Jenny Nelson, The Physics of Solar Cells, Imperial college Press, London, 2003, p. 9.
[6.6] H. A. Haus, Waves and Fields in Optoelectronics, Prentice Hall, Englewood Cliffs, New Jersey, 1984, p.162.

CHAPTER 7

Summary and Future Work

7.1 Summary of the thesis

In this thesis, a novel light trapping scheme, a textured photonic crystal (TPC) backside reflector, was invented, which can significantly enhance thin film Si solar cell efficiency through a wave optics approach. The light trapping principle of TPC was studied, and the design parameters as well as the antireflection coating were systematically optimized through simulation and experiments. The significant efficiency enhancement was verified by fabricating thin film Si solar cells integrated with the new back reflector.

The TPC backside reflector combines a one-dimensional photonic crystal and a reflection grating. By using high index contrast materials, the 1D photonic crystal achieves near 100% omnidirectional reflectivity in a wide stopband expanding more than 500 nm, completely covering the wavelength range needing light trapping, permitting

almost no transmission loss through the back surface of the cell. Careful selection of the grating parameters allows large angle light diffraction and causes total internal reflection at the front surface of the solar cell. The unique combination of 1D photonic crystal and grating tightly confines light inside the solar cell, and effectively changes the path length from the thickness of the cell to its lateral dimension, realizing path length enhancement up to several hundred times the cell thickness.

In order to prove the concept, thick Si solar cells integrated with the TPC back reflector were designed, fabricated, and characterized. The cells gained significant enhancement in external quantum efficiency of up to 135 times in the wavelength range of 1000-1200 nm, as well as notable power conversion efficiency improvement.

All the parameters of the TPC back reflector were systematically optimized for thin film solar cells through simulation. Scattering matrix method simulation shows that while the optimal grating duty cycle remains almost constant at 0.5, the optimal grating period, etch depth, DBR Bragg wavelength and antireflection coating thickness all decrease as the cell becomes thinner.

The best antireflection coating for thin film Si solar cells was identified through optical response simulation, surface passivation and dielectric strength measurements. It was found that an antireflection coating comprising two layers: a 4 nm thick thermal SiO_2 and a top layer of approximately 60 to 70 nm Si_3N_4, depending on cell thickness, offers the best light admission, surface passivation and dielectric strength. With the optimized back reflector and AR coating, a 2 μm thick cell can achieve a relative efficiency enhancement as high as 54%.

To prove the theory in the intended application, thin film Si solar cells with interdigitated top contacts and the TPC back reflector were successfully fabricated using Si-on-insulator material through an active layer transfer technique. Cells at all thicknesses exhibited strongly enhanced absorption, well matching simulation. The 20 and 50 μm thick cells achieved short circuit current density improvement of 10.8% and 12.0%, respectively, close to or even more than theoretical prediction. And the 5 μm thick cells gained 19% short circuit current density improvement, which is 65% of theoretical prediction, despite machine problems during fabrication.

The invention of textured photonic crystal back reflector can be directly applied to single and poly-crystalline Si solar cells; the principle of TPC can be used broadly to other materials systems.

7.2 Future directions

Several measures can be taken to further improve solar cell efficiency, and there are ways to reduce fabrication cost.

The important methods for solar cell efficiency improvement include reducing shadowing, combining the textured photonic crystal (TPC) back reflector with front surface random texturing, and increasing the waviness of the DBR stack.

First, we will discuss the reduction of shadowing. Since DBR is not conducting, we used interdigitated top contacts, which increased shadowing. The shadowing could be reduced by having bigger finger spacing, which would require better surface passivation. The exponential decay of I_{sc} vs. finger spacing under the sun simulator indicates poor surface quality perhaps due to the preexisting holes at the device layer and buried oxide

interface, blistering PECVD, or contaminants. It reminds us of the importance of surface passivation for thin cells. Methods to achieve better surface quality can be dry oxidation, better PECVD, or contaminants gettering. A second way to reduce shadowing is to use front and top contacts instead of interdigitated top contacts. Although DBR is not conducting, back contacts can be made by laser firing, as with Laser Fired Contact technology. The total DBR stack thickness is around 1.6 μm. If necessary, it can be reduced to ~1 μm by using 5 or 6 pairs of DBR with almost equal optical reflectivity, verses the 8 pairs used in our conservative first experiments. An even better way is to use all-back contact, like what is done with Crystalline-Si-on-glass (CSG). Significant shadowing reduction will certainly help the textured photonic crystal back reflector achieve more of its light trapping potential.

A second efficiency booster may be combining the TPC back reflector with front surface texturing. The angular distribution of light transmitted through a surface textured with 300 nm spheres shows that 72% of the light remains in the normal direction after passing through the textured surface, and the rest is dispersed into small angels [7.1], which makes it conceivable that one could combine the front surface random texturing with the textured photonic crystal, as most of the light will be normally incident on the back reflector.

The third approach is to make DBR more wavy by making the underlying grating less square. As shown by our experiments in Chapter 6, the wavy DBR plus grating back reflector enhances cell efficiency more than a flat DBR plus grating. A less square grating will keep the waviness of DBR through more of its top layers, and enhance large angle reflection.

In this thesis, we have proved that the textured photonic crystal back reflector can significantly enhance thin film solar cell efficiency. With the improvements discussed above, further efficiency enhancement is achievable. Steps toward practical application include developing cheap grating fabrication methodology to further reduce the cost. One possibility is nanoimprint lithography, which is suitable for large scale production. Another possibility is to use pre-made gratings. Certain liquid polymers can be spun onto a reusable grating template, cured, stripped from the template, and later attached to the backside of solar cells.

References

[7.1] R Windisch, S Schoberth, S Meinlschmidt, P Kiesel, A Knobloch, P Heremans, B Dutta, G Borghs and G H D¨ohler, J. Opt. A: Pure Appl. Opt. 1 512–516 (1999).